

# DISSERTATION

*Stress Signaling Heterogeneity in Normal and  
Malignant Hematopoiesis*

Abdul Rahman Itani

2024

Inaugural dissertation  
for  
obtaining the doctoral degree  
of the  
Combined Faculty of Mathematics, Engineering and Natural Sciences  
of the  
Ruprecht - Karls - University  
Heidelberg

Presented by  
M.Sc. Abdul Rahman Itani  
Born in: Riyadh, Saudi Arabia  
Oral examination: February 27<sup>th</sup>, 2024

*Stress Signaling Heterogeneity in Normal and Malignant Hematopoiesis*

Referees: Prof. Dr. Ralf Bartenschlager  
Dr. Steeve Boulant

## Summary

Hematopoietic stem cells (HSCs), positioned at the apex of the hematopoietic lineage, have long been considered a homogeneous population characterized by multipotency and self-renewal. Recent breakthroughs, however, have unveiled profound functional and molecular heterogeneity within this seemingly uniform group. Research from our group has identified a stable and heritable diversity in the intrinsic expression levels of interferon-stimulated genes (ISGs) in HSCs, termed intrinsic IFN signaling heterogeneity. Yet, it remains unclear whether this heterogeneity is established and sustained at the HSC level, and its potential role in the development and progression of clonal hematopoietic malignancies remains unexplored.

In my thesis, I explore the intrinsic IFN signaling signature in tissue-resident macrophages (TRMs) (aim 1). Utilizing flow cytometry and gene expression analysis, I demonstrated the presence of IFN signaling heterogeneity in TRMs. Importantly, as TRMs originate embryonically and precede HSC development, this finding suggests that IFN signaling heterogeneity in the hematopoietic system is established before the emergence of HSCs.

To assess the impact of intrinsic IFN signaling heterogeneity in disease (aim 2), I developed a humanized chronic myeloid leukemia (CML) mouse model on the background of a unique *ISRE-eGFP* reporter mouse. This reporter mouse features the interferon-stimulated response element (ISRE) upstream of eGFP, which enables the identification of HSCs expressing low or high levels of ISGs. In this context, the CML-ISG reporter mouse model facilitated the study of clonal expansion of CML leukemia stem cells (LSCs) relative to the intrinsic IFN signaling status of the parent HSC clone *in vivo*. Total BM transplantation experiments revealed a significant expansion of eGFP<sup>low</sup> leukemic clones in the peripheral blood, together with a quiescent eGFP<sup>low</sup> LSC pool in the BM suggesting a more aggressive leukemia clone. Survival analysis revealed that 100% eGFP<sup>low</sup> leukemic chimeras succumbed to leukemia significantly faster than eGFP<sup>high</sup> chimeras confirming my findings.

Additionally, I established a reliable method for isolating exosome-enriched small extracellular vesicles (sEVs) through serial centrifugation followed by size exclusion chromatography (SEC) (aim 3) in order to explore the role of sEV signaling in the BM (aim 4). My findings indicated a shift in sEV profile and content upon inflammatory stress, with specific sorting of inflammatory response proteins into vesicles exhibiting an inhibitory effect on

hematopoietic stem and progenitor cells (HSPCs) proliferation *in vitro*. Subsequent *in vivo* experiments I performed using different mouse models demonstrated a dynamic release of sEVs in response to acute inflammatory stress, suggesting the hematopoietic compartment as a major source of sEVs during such conditions.

In summary, my research has provided new insight on the origins of intrinsic IFN signaling heterogeneity and its consequential influence on disease progression in CML. Furthermore, it advanced our understanding of the intricate role played by sEV signaling in modulating the acute inflammatory response within the BM.

## Zusammenfassung

Hämatopoetische Stammzellen (HSZ), die an der Spitze der hämatopoetischen Abstammungslinie stehen, galten lange Zeit als homogene Population, die sich durch Multipotenz und Selbsterneuerung auszeichnet. Jüngste Erkenntnisse haben jedoch eine tiefgreifende funktionelle und molekulare Heterogenität innerhalb dieser scheinbar einheitlichen Gruppe ans Licht gebracht. Forschungsarbeiten unserer Gruppe haben eine stabile und vererbare Vielfalt in den intrinsischen Expressionsniveaus von Interferon-stimulierten Genen (ISGs) in HSCs identifiziert, die als intrinsische IFN-Signaltheterogenität bezeichnet wird. Es bleibt jedoch unklar, ob diese Heterogenität auf HSZ-Ebene etabliert und aufrechterhalten wird, und welche Rolle sie bei der Entwicklung und dem Fortschreiten klonaler hämatopoetischer Malignome spielt.

In meiner Dissertation untersuche ich die intrinsische IFN-Signalsignatur in gewebeansässigen Makrophagen (TRMs) (Ziel 1). Mithilfe von Durchflusszytometrie und Genexpressionsanalyse konnte ich die Heterogenität der IFN-Signalübertragung in TRMs nachweisen. Da TRMs embryonal entstehen und der Entwicklung von HSCs vorausgehen, deutet dieses Ergebnis darauf hin, dass die IFN-Signaltheterogenität im hämatopoetischen System bereits vor der Entstehung von HSCs etabliert ist.

Um die Zusammenhänge zwischen intrinsischer IFN-Signaltheterogenität und Erkrankung zu untersuchen (Ziel 2), habe ich ein humanisiertes Mausmodell für chronische myeloische Leukämie (CML) entwickelt, das ein einzigartiges ISRE-eGFP-Reporterkonstrukt verwendet. In diesem Mausmodell ist das Interferon-stimulierte Response-Element (ISRE) stromaufwärts von eGFP angeordnet, was die Identifizierung von HSCs ermöglicht, die niedrige oder hohe Mengen von ISGs exprimieren. In diesem Zusammenhang erleichterte das CML-ISG-Reportermausmodell die Untersuchung der klonalen Expansion von CML-Leukämie-Stammzellen (LSCs) im Verhältnis zum intrinsischen IFN-Signalstatus des Eltern-HSC-Klons in vivo. In Transplantationen des gesamten Knochenmarks wurde eine signifikante Expansion von eGFP<sup>low</sup>-Leukämieklonen im peripheren Blut festgestellt, zusammen mit einem ruhenden eGFP<sup>low</sup>-LSC-Pool im Knochenmark, der auf einen aggressiveren Leukämieklon hindeutet. Die Überlebensanalyse ergab, dass 100 % eGFP<sup>low</sup>-Leukämie-Chimären deutlich schneller an Leukämie erkrankten als eGFP<sup>high</sup>-Chimären, was meine Erkenntnisse bestätigt.

Darüber hinaus habe ich eine zuverlässige Methode zur Isolierung von kleinen extrazellulären mit Exosomen angereicherten Vesikeln (sEVs) etabliert (Ziel 3), mit der durch serielle Zentrifugation und anschließender Größenausschlusschromatographie (SEC) die Rolle der sEV-Signalübertragung im Knochenmark untersucht werden kann (Ziel 4). Meine Ergebnisse weisen auf eine Verschiebung des sEV-Profiles und -Anteil infolge entzündlichem Stress hin, wobei die spezifische Auslese von Entzündungsreaktionsproteinen in Vesikel eine hemmende Wirkung auf die Proliferation hämatopoetischer Stamm- und Vorläuferzellen (HSPCs) in vitro zeigte. Anschließende In-vivo-Experimente, die ich mit verschiedenen Mausmodellen durchgeführt habe, zeigten eine dynamische Freisetzung von sEVs als Reaktion auf akuten Entzündungsstress, was darauf hindeutet, dass das hämatopoetische Kompartiment unter solchen Bedingungen eine Hauptquelle für sEVs darstellt.

Zusammenfassend lässt sich sagen, dass meine Forschung neue Erkenntnisse über die Ursachen der intrinsischen IFN-Signaltheterogenität und deren Einfluss auf den Krankheitsverlauf bei CML liefert. Darüber hinaus hat sie unser Verständnis für die komplexe Rolle der sEV-Signalübertragung bei der Modulation der akuten Entzündungsreaktion im Knochenmark verbessert.

## Table of Contents

<b>Summary .....</b>	<b><i>i</i></b>
<b>Zusammenfassung .....</b>	<b><i>iii</i></b>
<b>1. Introduction .....</b>	<b>1</b>
<b>1.1 Heterogeneity and stress in the hematopoietic system .....</b>	<b>1</b>
1.1.1 Hematopoiesis and hematopoietic stem cells .....	1
1.1.2 Heterogeneity within HSCs .....	2
1.1.3 HSC heterogeneity and hematological disorders .....	3
1.1.4 HSCs and stress induced hematopoiesis .....	4
1.1.5 Stem cell based IFN signaling heterogeneity in the hematopoietic system.....	6
1.1.6 IFN signaling heterogeneity and chronic myeloid leukemia .....	8
<b>1.2 Extracellular vesicles (EVs).....</b>	<b>10</b>
1.2.1 EVs and cellular communication .....	10
1.2.2 sEV biosynthesis .....	11
1.2.3 sEV signaling.....	12
1.2.4 sEVs in stressed BM .....	13
<b>2. Aims of the thesis.....</b>	<b>15</b>
<b>2.1 Investigate intrinsic IFN signaling heterogeneity in non-HSC derived immune cells of adult mice .....</b>	<b>15</b>
<b>2.2 Explore the impact of IFN signaling in LSC on clonal expansion and disease progression in CML .....</b>	<b>15</b>
<b>2.3 Develop a reliable and reproducible method for isolating exosome-enriched sEVs .....</b>	<b>16</b>
<b>2.4 Investigate the role of sEV signaling in regulating system response to inflammatory stress in the BM .....</b>	<b>16</b>
<b>3. Results .....</b>	<b>17</b>
<b>3.1. Intrinsic IFN signaling heterogeneity in <i>ISRE-eGFP</i> reporter mouse model HSCs .....</b>	<b>17</b>
<b>3.2. Intrinsic IFN signaling heterogeneity in non-HSC derived immune cells.....</b>	<b>19</b>
<b>3.3. Impact of intrinsic IFN signaling heterogeneity in stem cells on leukemia progression .....</b>	<b>23</b>
3.3.1 A unique CML-ISG reporter mouse model as a tool to investigate the role of intrinsic IFN heterogeneity in a clonal hematopoietic malignancy .....	23
3.3.2 Generation and optimization of the CML-ISG reporter mouse model.....	23

3.3.2.1 No difference in baseline infectibility of eGFP <sup>low</sup> and eGFP <sup>high</sup> HSCs to murine stem cell vector (MSCV) retrovirus.....	23
3.3.2.2. <i>In vivo</i> 5-FU treatment response shows no difference between eGFP <sup>low</sup> and eGFP <sup>high</sup> HSCs ....	26
3.3.2.3 Comparable response of eGFP <sup>low</sup> and eGFP <sup>high</sup> HSCs to <i>in vitro</i> cytokine pre-stimulation and viral transduction.....	27
3.3.2.4 A CML-like disease is produced by MSCV-BCR::ABL1-IRES-mCherry retroviral construct <i>in vivo</i> .....	29
3.3.3 CML-ISG reporter mice in a total BM transplantation setting .....	32
3.3.3.1 MSCV-IRES-mCherry empty vector control does not induce a phenotype in mice .....	32
3.3.3.2 Leukemic ISG-CML mice .....	34
3.3.3.2.1 Untreated leukemic ISG-CML mice exhibit clonal expansion advantage of eGFP <sup>low</sup> leukemic cells in a total BM transplantation setting .....	34
3.3.3.2.2 Secondary ISG-CML mice exhibit clonal expansion advantage of eGFP <sup>low</sup> leukemic cells ....	37
3.3.3.2.3 Nilotinib successfully controlled leukemia progression .....	40
3.3.3.2.4 eGFP <sup>low</sup> leukemic cells expand in recipient mice derived from nilotinib-treated donors ....	42
3.3.3.2.5. Nilotinib treated ISG-CML mice didn't show obvious signs of relapse up to 32 days post-treatment cessation. ....	44
3.3.4 100% chimera CML-ISG reporter mice.....	46
3.3.4.1 Expression of <i>BCR::ABL1</i> in eGFP <sup>low</sup> HSCs results in a more aggressive leukemia <i>in vivo</i> .....	46
<b>3.4 The role of small extra cellular vesicle signaling in the stressed BM .....</b>	<b>50</b>
3.4.1 Size exclusion chromatography on top of sequential centrifugation increases the purity of isolated sEVs. ....	50
3.4.2 sEVs isolated from BM stromal cells <i>in vitro</i> .....	54
3.4.2.1 Differences in particle and protein quantities between sEVs isolated from PBS and IFN $\alpha$ treated stromal cells.....	54
3.4.2.2 sEVs derived from rMSCs do not affect proliferation or differentiation potential of HSPCs <i>in vitro</i> .....	57
3.4.3 sEVs isolated from BM <i>in vivo</i> .....	58
3.4.3.1 Inflammatory stress leads to alterations in the size distribution and abundance of sEVs in the BM .....	58
3.4.3.2 BM pl:C sEVs inhibit proliferation of LSKs <i>in vitro</i> .....	61
3.4.3.3 Dynamic increase in sEV production upon inflammation is primarily driven by hematopoietic cells <i>in vivo</i> .....	64
3.4.3.4. Administration of inflammatory sEVs impacts on the myeloid compartment <i>in vivo</i> .....	65
3.4.3.5 Modifications in the proteomic profile of sEVs isolated from murine BM in response to inflammatory stress .....	68
<b>4. Discussion and future direction .....</b>	<b>70</b>
<b>4.1 IFN signaling heterogeneity in non-HSC derived hematopoietic cells .....</b>	<b>70</b>
<b>4.2 IFN signaling heterogeneity and leukemia progression .....</b>	<b>71</b>

4.2.1 ISG-CML mouse model .....	72
4.2.2 Clonal expansion of eGFP <sup>low</sup> leukemic cells .....	73
4.2.3 Nilotinib Treatment.....	75
4.2.4 Future directions and other models .....	76
4.2.5 Translational studies .....	77
<b>4.3 sEV signaling in the BM.....</b>	<b>78</b>
4.3.1 sEV extraction, purification and characterization .....	78
4.3.2 sEV signaling in response to inflammatory stress .....	80
4.3.4 <i>In vitro</i> treatment of HSPCs with sEVs .....	81
4.3.5 <i>In vivo</i> treatment of mice with sEVs.....	83
4.3.6 Mouse models for sEV signaling. ....	84
<b>5. Materials and Methods.....</b>	<b>85</b>
<b>5.1 Materials.....</b>	<b>85</b>
5.1.1 Antibodies .....	85
5.1.2 qRT-PCR primers .....	87
5.1.3 Kits.....	90
5.1.4 Reagents and buffers .....	90
5.1.5 Additional Material .....	92
5.1.6 Cell lines and plasmids .....	93
5.1.7 Equipment.....	93
5.1.8 Programs and software.....	94
<b>5.2 Methods.....</b>	<b>95</b>
5.2.1 Mice .....	95
5.2.1.1 Mouse strains .....	95
5.2.1.2 Organ dissection and preparation of cell suspensions .....	95
5.2.1.2.1 Blood .....	95
5.2.1.2.2 Spleen.....	96
5.2.1.2.3 Bone marrow.....	96
5.2.1.3 ISG-CML mouse model .....	96
5.2.1.3.1 Isolation of BM from <i>ISRE-eGFP</i> mice.....	96
5.2.1.3.2 <i>In vitro</i> pre-stimulation.....	96
5.2.1.3.3 Viral transduction and transformation.....	97
5.2.1.3.4 Transplantation .....	97
5.2.1.3.5 Secondary transplantation .....	98
5.2.1.4 Forward and reverse Chimeras .....	98
5.2.1.5 <i>In vivo</i> treatments .....	98
5.2.2. Flow cytometry and cell sorting.....	99

5.2.3 Cell cycle analysis .....	100
5.2.4 Isolation of macrophages.....	100
5.2.5 Cell culture .....	101
5.2.6 Generation of MSCV-BCR::ABL1-IRES-mCherry by restriction cloning.....	102
5.2.7 Bacterial transformation .....	102
5.2.8 Generation of viral supernatant.....	102
5.2.9 Determination of viral titer .....	103
5.2.10 Viral infectibility studies.....	103
5.2.11 Generation of sEV-free FBS.....	104
5.2.12 Collection of sEVs .....	104
5.2.13 Purification of sEVs .....	104
5.2.14 Treatment of HSPC with sEV <i>in vitro</i> .....	105
5.2.15 Nanoparticle tracking analysis (NTA) .....	106
5.2.16 Transmission electron microscopy (TEM) .....	106
5.2.17 Protein extraction and western blot .....	106
5.2.18 RNA extraction, cDNA synthesis, and qRT-PCR .....	107
5.2.19 Microarray.....	108
5.2.20 Proteomic analysis .....	108
<b>6. Appendix.....</b>	<b>110</b>
<b>6.1 Supplementary tables.....</b>	<b>110</b>
<b>6.2 Abbreviations.....</b>	<b>118</b>
<b>6.3 List of figures.....</b>	<b>120</b>
<b>6.4 list of tables.....</b>	<b>122</b>
<b>7. Contributions .....</b>	<b>123</b>
<b>7.1 Technical support and expertise .....</b>	<b>123</b>
<b>7.2 Collaborative research efforts .....</b>	<b>123</b>
<b>8. Acknowledgment .....</b>	<b>125</b>
<b>9. Bibliography.....</b>	<b>127</b>

### 1. Introduction

#### 1.1 Heterogeneity and stress in the hematopoietic system

##### 1.1.1 Hematopoiesis and hematopoietic stem cells

Hematopoiesis, the process responsible for establishing and maintaining the blood system, has been the focus of extensive biomedical research for many decades (Eaves, 2015; Jagannathan-Bogdan & Zon, 2013). The hematopoietic system is highly regulated, and consists of a diverse array of specialized cell types, each with a distinct function crucial for proper operation and survival (Jagannathan-Bogdan & Zon, 2013; Pinho & Frenette, 2019). Numerous studies have invariably asserted that the rare population of cells residing within a complex niche in the bone marrow (BM), known as hematopoietic stem cells (HSCs), are essential for sustainable hematopoiesis (Essers et al., 2009; Osawa, Hanada, Hamada, & Nakauchi, 1996; Wilkinson et al., 2019; Wilkinson & Yamazaki, 2018). This is primarily attributed to their capacity to reconstitute and sustain the entire blood system for long-term upon HSC transplantation (Copelan, 2006; Pinho & Frenette, 2019). Consequently, and owing to their multipotency and self-renewing capacity, HSCs are believed to occupy the topmost position in the hematopoietic lineage hierarchy.

Even though HSCs are responsible for sustaining hematopoiesis over the entire life span of vertebrates, they are actually the last hematopoietic cell type to emerge during embryonic development (Dzierzak & Bigas, 2018). In murine embryos, hematopoietic development unfolds in three sequential waves: the primitive wave at embryonic day 7.5 (E7.5), followed by the pro-definitive wave at E8.5, and finally the definitive wave at around E10.5. Each of these hematopoietic waves generates cells with progressive blood lineage potential culminating in the emergence of the first definitive HSCs at around E10.5 (Dzierzak & Bigas, 2018). Consequently, not all hematopoietic cells that make up the adult mouse are derived from HSCs. Recent lineage tracing experiments have provided evidence that tissue-resident macrophages (TRMs), which colonize various organs, trace their origins directly back to the descendants of erythroid and myeloid progenitors (EMPs), which are produced during the 2<sup>nd</sup> embryonic wave (Dzierzak & Bigas, 2018; F. Ginhoux et al., 2010).

### 1.1.2 Heterogeneity within HSCs

Despite constituting only 0.01% of the total BM cell population (Challen, Boles, Lin, & Goodell, 2009), HSCs do not constitute a homogeneous population. They display significant intracellular heterogeneity, which extends across various physical, molecular, and functional aspects of HSCs (Donnelly, Zelterman, Sharkis, & Krause, 1999; Haas, Trumpp, & Milsom, 2018; Uchida, Fleming, Alpern, & Weissman, 1993). For instance, variations in HSC self-renewal capacity have led to their classification into distinct subgroups: short-term, intermediate-term, and long-term HSCs (Donnelly et al., 1999). Single-cell experiments have unveiled further aspects of HSC heterogeneity, such as lineage biases (Carrelha et al., 2018), reconstitution kinetics (Haas et al., 2018; Yohei Morita, Ema, & Nakauchi, 2010; Sieburg et al., 2006), and differential proliferative states (Anne Wilson et al., 2008). While these studies provide compelling evidence of functional and molecular heterogeneity within a seemingly phenotypically similar HSC pool, the underlying factors contributing to this heterogeneity remain poorly understood.

Understanding the origins of HSC heterogeneity is crucial, necessitating the consideration of both cell-extrinsic and intrinsic factors (Haas et al., 2018). Among the most investigated extrinsic factors is the spatial arrangement of HSCs within their specialized niche (Ehninger & Trumpp, 2011; Haas et al., 2018). Depending on the precise location of individual HSCs, their interactions with the different cellular components of the niche may vary significantly, influencing their behavior and contributing to intracellular heterogeneity (Anthony & Link, 2014). This includes direct interactions with mesenchymal stem cells (MSCs), osteoblast, or endothelial cells, as well as indirect regulation by sympathetic neurons or cytokines such as transforming growth factor beta (TGF- $\beta$ ) secreted by glial cells (Anthony & Link, 2014). Additionally, differences in biophysical and biochemical properties of the extracellular matrix in the immediate microenvironment surrounding HSCs have been implicated in regulating various aspects of HSC biology by modulating growth factor or cytokine accessibility (Uckelmann et al., 2016). This results in a diverse array of cell-extrinsic signals being delivered to HSCs, dependent on their location.

Intrinsic factors include inheritable elements, such as genetic and epigenetic modifications (Haas et al., 2018). Somatic mutations acquired in individual HSCs during the embryonic development can alter various aspects of HSC biology, resulting in emergence of heterogeneous HSC clones (Ju et al., 2017). To add to the complexity of the system, there is quite the striking difference between embryonic and adult HSCs in terms of gene signatures (Zhou et al., 2016) and self-renewing properties (Crisan & Dzierzak, 2016). Notably,

embryonic HSCs isolated from the fetal liver already exhibits clear heterogeneity in terms of lineage output, suggesting that some mechanisms governing HSC heterogeneity originate during embryogenesis (Benz et al., 2012). Furthermore, dynamic epigenetic alterations in chromatin configuration, mediated by histone modification or DNA methylation, coordinate chromatin accessibility during HSC lineage commitment, guiding and reinforcing lineage-specific gene expression programs (Haas et al., 2018; Yu et al., 2016).

Additional factors contributing to HSC heterogeneity involve their varying capacity to transition between diverse cellular or physiological states (Pauklin & Vallier, 2013), such as those related to proliferation. These transitions lead to changes in dynamic intracellular processes, including respiration and metabolism. Consequently, these transitions significantly impact the functional and molecular heterogeneity of HSCs, affecting aspects such as lineage bias, self-renewal capacity, and the maintenance of the hematopoietic system (Haas et al., 2018).

### **1.1.3 HSC heterogeneity and hematological disorders**

The HSC pool has been shown to accumulate mutations with time and aging. This causes the emergence of several HSC clones having a wide range of different somatic mutations. Some of these mutations are benign, and have no consequence on HSC function. On the other hand, other mutations are malignant, giving rise to conditions like chronic myeloid leukemia (CML) due to mutations like the *BCR::ABL1* reciprocal translocation. Furthermore, there are the so-called "driver mutations" such as *TET2* and *DNMT3A* (Zink et al., 2017) that are associated with the non-malignant expansion of individual HSC clones, a phenomenon known as clonal hematopoiesis (CH). The incidence of CH is closely tied to aging and carries an increased risk of developing hematologic malignancies (Bowman, Busque, & Levine, 2018; Haas et al., 2018; Zink et al., 2017).

As dysplastic or transformed progeny of HSCs retain certain characteristics or molecular signatures of the original cell, the heterogeneity within the HSC pool becomes a critical factor during malignant transformation. This becomes especially relevant when considering the various forms of HSC heterogeneity, as discussed in section 1.1.2. This heterogeneity can, in turn, have implications for multiple aspects of the disease, including its evolution, progression, prognosis, responsiveness to therapy, and the potential for disease relapse (Brianna M. Craver, Kenza El Alaoui, Robyn M. Scherber, & Angela G. Fleischman, 2018; Haas et al., 2018).

#### 1.1.4 HSCs and stress induced hematopoiesis

It is widely acknowledged that under normal homeostatic conditions, HSCs primarily reside in a dormant or quiescent state, which serves as a protective mechanism against genotoxic insults (Passegué, Wagers, Giuriato, Anderson, & Weissman 2005; Pinho & Frenette, 2019). In this setting, it is most likely that their progeny, the hematopoietic progenitors, sustain steady-state hematopoiesis (Caiado, Pietras, & Manz, 2021; Sun et al., 2014; Wilkinson & Yamazaki, 2018). However, under conditions of hematopoietic stress or injury, quiescent HSCs are reversibly activated to self-renew and proliferate in order to rapidly re-establish homeostasis (Essers et al., 2009; A. Wilson et al., 2008). This phenomenon is known as stress-induced hematopoiesis (Zhao & Baltimore, 2015) and has been recorded for HSCs under various stress conditions such as chemotherapeutic treatment, infection, inflammation and hemorrhage (Caiado et al., 2021; Essers et al., 2009; Zhao & Baltimore, 2015).

Key players involved in stress-induced hematopoiesis include a group of signaling proteins called interferons (IFNs), which belong to the cytokine family. IFNs are further classified into three families (type I, type II and type III) based on their receptors and signaling pathways (Lazear, Schoggins, & Diamond, 2019; J. M. Zhang & An, 2007). The widely studied and characterized Type I IFNs include IFN alpha (IFN $\alpha$ ) and IFN $\beta$ , among many others. These molecules are important regulators of innate and adaptive immunity (McNab, Mayer-Barber, Sher, Wack, & O'Garra, 2015) and can be produced by virtually all cell types (Trinchieri, 2010).

The heterodimeric receptor of type I IFNs, called IFNAR, is composed of the IFN alpha/beta receptor 1 (IFNAR1) and IFNAR2 chains. IFNAR1 is associated with tyrosine kinase 2 (TYK2), while IFNAR2 is associated with Janus-activated kinase 1 (JAK1). Upon binding of the receptor to its ligand, TYK2 and JAK1 are activated, initiating the activation of signal transducers and activators of transcription (STAT)1 and STAT2 through tyrosine kinase phosphorylation. STAT1 and STAT2 dimerize and join with IFN-regulatory factor 9 (IRF9) to create a trimeric complex known as IFN-stimulated gene factor 3 (ISGF3). ISGF3 then translocates to the nucleus and initiates the transcription of IFN-stimulated genes (ISGs) by binding to the IFN-Stimulated Response Element (ISRE) in ISG promoters (Negishi, Taniguchi, & Yanai, 2018). Furthermore, IFNAR activation can also lead to the formation of active STAT1 homodimers that translocate to the nucleus and initiate ISG transcription by binding to gamma ( $\gamma$ )-activated sequence (GAS) motifs (Decker, Müller, & Stockinger, 2005) (Fig. 1).

## Introduction

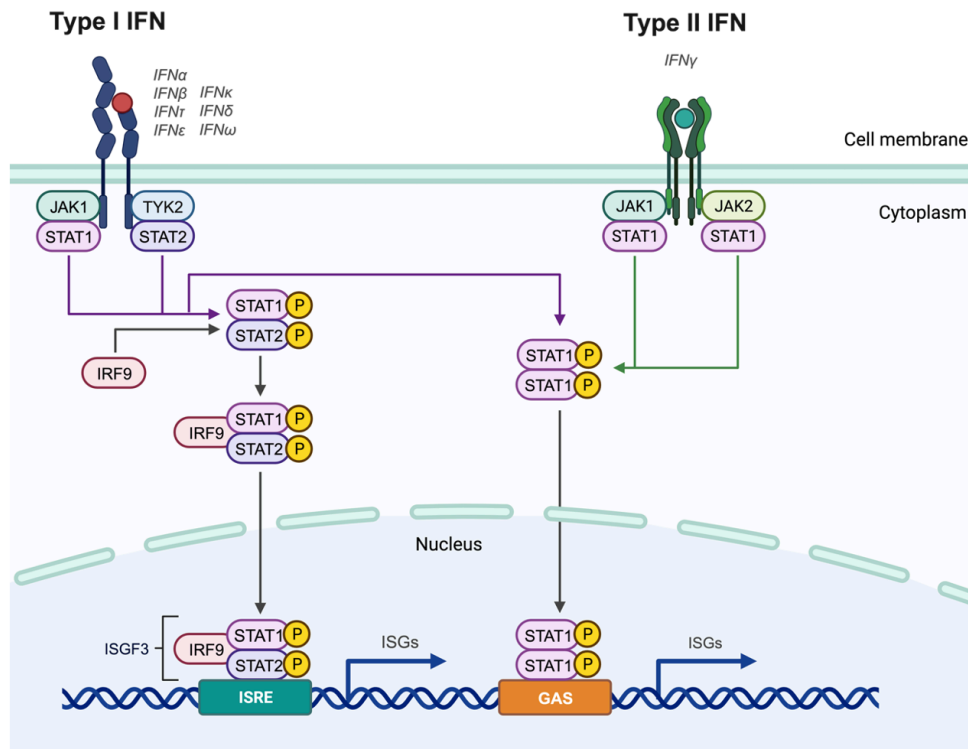


**Figure 1 | IFN type I and type II signaling pathway.**

Schematic representation of the canonical interferon type I (IFN I) and IFN II signaling pathway. Binding of type IFN I (IFN-  $\alpha$ , - $\beta$ , - $\tau$ , - $\epsilon$ , - $\kappa$ , - $\delta$ , and - $\omega$ ) to the IFN alpha/beta receptor (IFNAR) activates Janus-activated kinase 1 (JAK1) and tyrosine kinase 2 (TYK2) to phosphorylate signal transducers and activators of transcription (STAT)1 and STAT2 through tyrosine kinase phosphorylation. Activated STAT1 and STAT2 then associate with IFN-regulatory factor 9 (IRF9) to form the transcriptional complex known as IFN stimulated gene factor 3 (ISGF3). ISGF3 translocates to the nucleus and promotes the transcription of IFN stimulated genes (ISGs) by interacting with the IFN-stimulated response element (ISRE). IFN II (IFN- $\gamma$ ) binding to the IFN gamma receptor (IFNGR) activates JAK1 and JAK2, which phosphorylate STAT1. STAT1 forms a homodimer that translocates to the nucleus and activates ISG transcription by binding to  $\gamma$ -activated sequence (GAS) motifs. IFN I signaling can also generate STAT1 homodimers and lead to ISG transcription through binding to GAS. Adapted from "Interferon Pathway", by BioRender.com (2019). Retrieved from <https://app.biorender.com/biorender-templates/figures/all/t-5df2a193dbd96b0080ce673c-interferon-pathway>

Accordingly, signaling by IFN $\alpha$  or any of its inducers like Polyinosinic:polycytidylic acid (pl:C), leads to the altered expression of hundreds of ISGs. This causes profound system wide cellular changes associated with enhanced anti-tumor activity, increased resistance to viral infections, immune response modulation, regulation of cellular survival as well as activation of hematopoiesis (Essers et al., 2009; Schneider, Chevillotte, & Rice, 2014; Schreiber, 2017).

However, it is important to note that the response of HSCs to various proinflammatory cytokines can be heterogeneous (Eaves, 2015). In general, prolonged HSC activation in response to infection and inflammation is often accompanied by a reduction in HSC function, leading to diminished system reconstitution capacity and a notable shift toward myeloid-biased proliferation, especially in cases of chronic inflammation (Caiado et al., 2021; Essers et al., 2009).

### **1.1.5 Stem cell based IFN signaling heterogeneity in the hematopoietic system**

It has long been observed that pluripotent and multipotent cells of different systems and species are resistant to viral infections (Belzile, Stark, Yeo, & Spector, 2014; Wolf & Goff, 2009). However, this is not a shared property with their downstream differentiated cells. The mechanism by which this general characteristic of stem cells is maintained was largely unknown. It wasn't until fairly recently that this was explained by an intrinsically elevated level of ISGs in stem cells, that gradually decreases upon differentiation (Wu et al., 2018).

Indeed, upon systematically characterizing inter-cell type heterogeneity of intrinsic ISG expressions across hematopoietic stem and progenitor cells (HSPCs), our group showed that the majority of ISGs were highly expressed in HSCs, but gradually declined towards more differentiated progenitor populations with a few genes showing additional cell type-specific expression patterns (Fig. 2A). Interestingly, principal component analysis (PCA) of stem and progenitor populations, with ISGs as variables, auto-arranged the populations according to the hematopoietic differentiation hierarchy suggesting a tight correlation between HSC differentiation and intrinsic ISG expression (Fig. 2B). Single-cell transcriptional profiling confirmed the strong enrichment of intrinsic ISG expression in stem cells, but also revealed extensive intra-cell type variability of ISG expression in highly purified cell populations, which we refer to as intrinsic IFN-signaling heterogeneity (Fig. 2C) (Werner et al., in preparation)

## Introduction

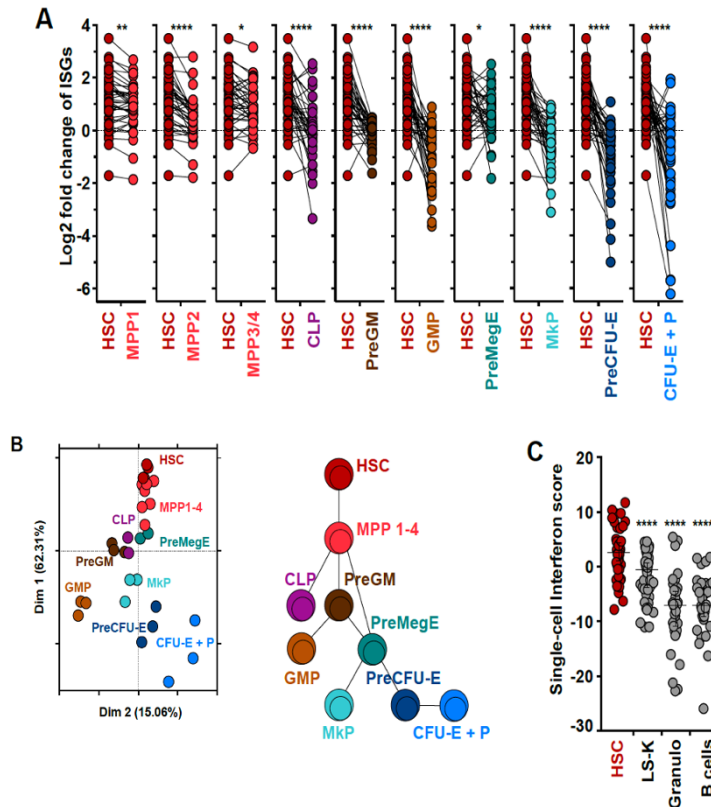


**Figure 2 | Intrinsic IFN signaling heterogeneity represents a powerful indicator of stemness in the hematopoietic system.**

(A) Transcriptional profiling by qRT-PCR of 40 interferon stimulated genes (ISGs) in stem and progenitor cells,  $n = 3$  per cell type, mean expression values relative to cKit<sup>+</sup> progenitors are indicated and corresponding genes are connected by lines. (B) Principal component analysis of cell populations of (A) with ISGs as variables (left panel), and comparative schematic illustration of the hematopoietic differentiation hierarchy (right panel). (C) Single-cell transcriptional profiling of 18 ISGs. Overall ISG expression of single cells was combined to form an “interferon score”.  $n=30-48$  cells per cell type. (Werner et al., in preparation)

To systematically characterize the functional consequence of intrinsic IFN signaling heterogeneity in the hematopoietic system, the group used an *ISRE-eGFP* reporter mouse in which eGFP expression directly correlates to ISG expression (Tovey, Lallemand, Meritet, & Maury, 2006) (Fig. 3A). Surprisingly, eGFP-reporter expression not only recapitulated the heterogeneity in baseline IFN signaling in different hematopoietic cell populations, but displayed an even more extreme picture compared to the wildtype (WT) with low or high intrinsic ISG expressing HSCs (eGFP<sup>low</sup> HSCs and eGFP<sup>high</sup> HSCs, respectively) (Fig. 3B). Transplantation of distinctly eGFP<sup>low</sup> or eGFP<sup>high</sup> HSCs into lethally irradiated WT recipients showed stable inheritance of reporter level status from HSCs to all downstream progeny, including mature blood cells, without obvious differences in self-renewal or differentiation bias (Fig. 3C&D). Remarkably, reporter-high expressing HSCs generated an exclusively reporter-high expressing hematopoietic system upon transplantation and reporter-low expressing HSCs vice versa, indicating stable inheritance of these specific gene expression patterns over a large number of cell generations (Fig. 3E). Furthermore, when *ISRE-eGFP* mice were

challenged with inflammatory stimuli using pl:C, eGFP<sup>high</sup> HSCs globally upregulated ISGs more efficiently than eGFP<sup>low</sup> HSCs, highlighting a differential response to inflammatory stimuli based on intrinsic IFN signaling status (Fig. 3F).

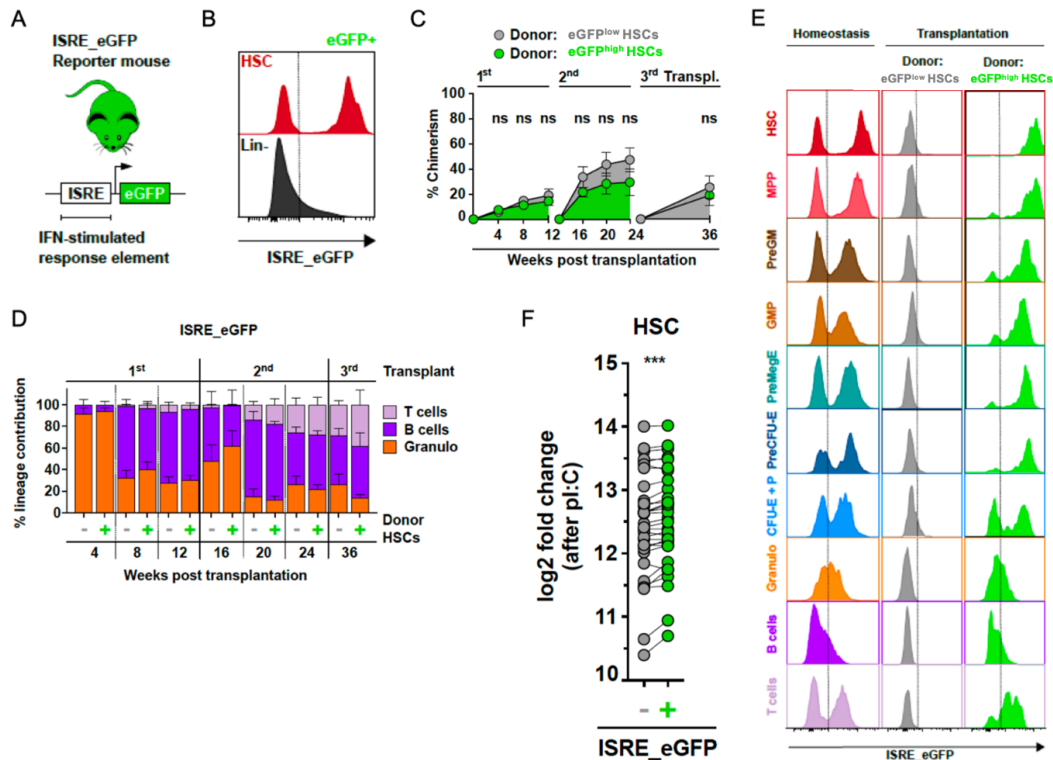


**Figure 3 | Stem cell based intrinsic IFN signaling heterogeneity in the hematopoietic system.**

(A) Schematic representation of the *ISRE-eGFP* reporter mouse model. (B) ISRE activity in HSCs (LSK CD150<sup>+</sup> CD48<sup>-</sup> CD34<sup>-</sup> EPCR<sup>+</sup>) and lineage-negative bone marrow (BM) as measured by flow cytometry. (C) 30 eGFP<sup>low</sup> or eGFP<sup>high</sup> HSCs were transplanted into lethally irradiated (2x500 Rad) WT mice. Blood chimerism was determined at the indicated time points. 12 weeks post-transplantation, re-transplantation of 3x10<sup>6</sup> unfractionated BM cells was performed. (D) Relative peripheral granulocyte (Gr-1<sup>+</sup> CD11b<sup>+</sup>), B (B220<sup>+</sup>), and T (CD3<sup>+</sup>) cell contributions from experiment (C). (E) 30 eGFP<sup>low</sup> or eGFP<sup>high</sup> HSCs were transplanted into lethally irradiated WT mice. 12 weeks post-transplantation, ISRE activity was determined by flow cytometry in indicated populations, and compared to homeostatic ISRE activity. (F) gene expression analysis by qRT-PCR of eGFP<sup>low</sup> or eGFP<sup>high</sup> HSCs from PBS or pl:C treated (24hrs) *ISRE-eGFP* mice. ISG genes were extracted and log<sub>2</sub> fold up-regulation relative to HSCs from untreated mice was calculated. Corresponding genes are connected by lines. Data are represented as mean and standard error of the mean, and statistics were calculated by a two-tailed student's *t*-test (ns, not significant; \*\*\* *p* ≤ 0.001;). (Werner et al., in preparation)

### 1.1.6 IFN signaling heterogeneity and chronic myeloid leukemia

CML is a clonal hematopoietic malignancy that belongs to the myeloproliferative neoplasm (MPN) family of hematological diseases. With an annual incidence of 1-2/10<sup>5</sup> population (Jabbour & Kantarjian, 2022), it accounts for 15-20% of new adult leukemia cases (median age of diagnosis 64 years) (Wintrobe & Greer, 2014), 2% of childhood leukemias (< 15 years), and 9% of adolescent leukemias (15 -19 years) (Hijiya, Schultz, Metzler, Millot, & Suttorp, 2016). It affects males more than females, however, there is no familial, geographic or ethnic predisposition (Wintrobe & Greer, 2014). CML is characterized by the presence of

the abnormal Philadelphia chromosome (Ph) (Hoffman, Benz, Furie, McClave, & Heslop, 2008), which is the product of a reciprocal translocation between the long arms of chromosome 9 and 22 [t(9;22)(q34;q11)] in which the *BCR* (breakpoint cluster region) gene on chromosome 22 fuses to the *ABL1* (Abelson leukemia virus) gene on chromosome 9, giving rise to the *BCR::ABL1* fusion oncogene. Since this Ph chromosome is detected in cells of all hematopoietic lineages, and *BCR::ABL1* does not confer self-renewal capacity, the original translocation event is believed to occur in a multipotent HSC (Hoffman et al., 2008; Wintrobe & Greer, 2014).

Unlike *ABL1*, which is a heavily regulated nuclear kinase, the replacement of the *ABL1* N-terminus with *BCR* fragments in the *BCR::ABL1* fusion oncoprotein generates a constitutively active tyrosine kinase that is exclusively localized in the cytoplasm (Hoffman et al., 2008; Wintrobe & Greer, 2014). Consequently, downstream signaling pathways such as *RAS*, *RAF*, *JUN* kinase, *MYC*, and *STAT* are affected by the kinase activity resulting in amplified cell growth, reduced growth factor dependence, impaired apoptosis and perturbed interactions with extracellular matrix and stroma (Hoffman et al., 2008; Jabbour & Kantarjian, 2022; Wintrobe & Greer, 2014). This affords the transformed malignant clones a proliferative advantage over normal cells allowing them to gradually displace residual normal hematopoiesis (Hoffman et al., 2008).

Today, targeted therapy by administration of tyrosine kinase inhibitors (TKIs) is the standard of care for CML patients owing to their impressive results in increasing the 10-year survival rate (from 20% to 80-90%) (Wintrobe & Greer, 2014). In general, TKIs function by efficiently obstructing the interaction between the *BCR::ABL1* fusion oncoprotein and adenosine triphosphate (ATP), therefore hindering the proliferation of the malignant clone (Hoffman et al., 2008; Jabbour & Kantarjian, 2022; Wintrobe & Greer, 2014).

The ultimate goal of any cancer therapy is achieving tumor-free remission (TFR). This is especially relevant in CML considering the cost and duration of treatment, associated side effects, and the increased risk of the emergence of resistant clones due to prolonged treatment periods. Data on TFR from clinical trials using different TKIs alone or in combination with other drugs vary greatly (from around 20 to 60%) (Annunziata et al., 2020; Baccarani, 2017; García-Gutiérrez & Hernández-Boluda, 2019; Hughes & Ross, 2016). This is consistent with various reports suggesting the persistence of CML leukemia stem cells (LSCs) upon TKI treatment, which has been explained by mechanisms such as maintenance of quiescence, lack of addiction to *BCR::ABL1* in LSCs, and heterogeneity within the LSCs (R. El Eit et al., 2019). When factoring in the clonal nature of CML, this necessitates a deeper understanding of the

heterogeneity in CML LSC biology in order to help optimize treatment strategies for achieving TFR.

In patients with myeloid malignancies like CML, a simultaneous overproduction of both inflammatory and anti-inflammatory cytokines creates a chronic cytokine storm, and thus an inflammatory milieu in the BM. This generates a selective pressure that plays a role in determining the mutant clones that will acquire a proliferative advantage and eventually out-compete normal cells (Brianna M. Craver et al., 2018). Recent reports on HSCs have focused on the immense functional and molecular heterogeneity present in these stem cells (Eaves, 2015; Haas et al., 2018). Building upon these findings, our group has recently identified intracellular heterogeneity of intrinsic IFN signaling in HSCs which influences their response to inflammatory stress signals such as those found in CML (Werner et al., in preparation). This raises the question of how this innate intrinsic IFN signaling heterogeneity in HSCs will influence transformation, clonal expansion, and response to treatment in CML LSCs.

### **1.2 Extracellular vesicles (EVs)**

#### **1.2.1 EVs and cellular communication**

Cell-to-cell communication is essential in multicellular organisms, serving a critical role in orchestrating developmental events, regulating routine cellular functions, and facilitating responses to environmental changes and stressors. This communication occurs through various mechanisms, including direct cell-to-cell contact, metabolites, hormones, and cytokines. However, an especially intriguing mode of communication is via small extracellular vesicles (sEVs). What sets sEVs apart from other communication methods is their ability to convey a vast array of specific messages to recipient cells, surpassing traditional molecular signaling. This capability arises from the fact that sEVs can carry a diverse range of bioactive molecules, such as surface receptors, proteins, and nucleic acids, all packaged within a single entity (Pitt, Kroemer, & Zitvogel, 2016).

Importantly, the content transported by sEVs is influenced by the physiological or pathological state of the cell of origin at the time of their synthesis and release (Raposo & Stoorvogel, 2013). Given that virtually all cell types are capable of engaging in sEV signaling, this field of research has gained increasing attention in various disciplines, spanning apoptosis, immune regulation, cancer progression, among others (Kalluri & LeBleu, 2020).

### 1.2.2 sEV biosynthesis

sEVs are a class of cell-derived membrane-bound structures that play an important role in cellular communication (Wiklander, Brennan, Lötval, Breakefield, & EL Andaloussi, 2019). Broadly speaking, sEVs can be categorized into two primary groups based on their origin and biosynthesis: ectosomes and exosomes. Exosomes represent a subset of sEVs typically ranging in size from approximately 40 to 160 nm, and are of endosomal origin. On the other hand, ectosomes are larger in size, ranging anywhere between ~50 nm to 1µm, and they are formed through direct outward budding of the plasma membrane. As such, ectosomes include a wider spectrum of vesicles, including microparticles, microvesicles (MVs), and larger vesicular structures (Kalluri & LeBleu, 2020).

The initial steps in the biosynthesis of exosomes and ectosomes differ significantly (Meldolesi, 2018). Exosome biosynthesis starts with the inward invagination of the cell membrane, giving rise to early-sorting endosomes (ESEs) in the cytoplasm. As a result, ESEs accumulate extracellular components such as soluble proteins, metabolites, lipids, and cell surface proteins which are incorporated into exosome synthesis. Subsequently, these ESEs mature into late-sorting endosomes (LSEs) through direct interactions with the trans-Golgi network (TGN), the endoplasmic reticulum (ER), or pre-existing ESEs originating from intracellular sources. At this stage, LSEs undergo a second invagination of the endosomal membrane transforming into multivesicular bodies (MVBs) that contain the precursors of exosomes known as intraluminal vesicles (ILVs). Finally, these multivesicular bodies can either fuse with lysosomes for degradation and recycling of their contents, or with the plasma membrane, releasing the enclosed ILVs as exosomes into the extracellular space (Kalluri & LeBleu, 2020; Meldolesi, 2018) (Fig. 4).

In contrast, ectosomes are generated much more rapidly. Their biosynthesis starts with the assembly of cargo on the cytosolic face of the plasma membrane. This is followed by the emergence of differentiated membrane microdomains at the cell surface, which manifest as outward bulges in the plasma membrane. Subsequently, vesicle fusion takes place, releasing ectosomes into the extracellular space (Kalluri & LeBleu, 2020; Meldolesi, 2018) (Fig. 4).

## Introduction

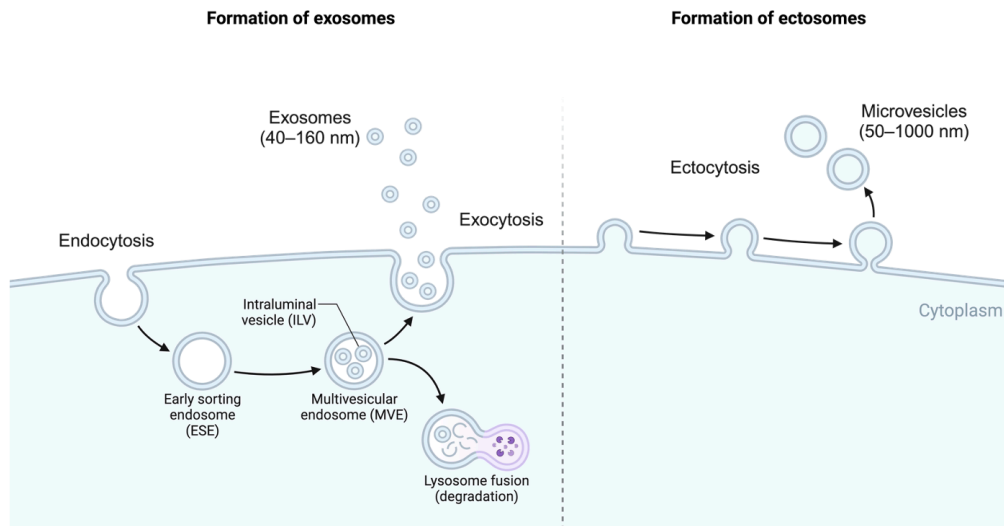


**Figure 4 | The biogenesis of sEVs.**

Simplified schematic representation of small extracellular vesicles (sEVs) biosynthesis: Exosome (40-160 nm) synthesis starts with the inward budding (endocytosis) of the plasma membrane giving rise to early sorting endosomes (ESE). A second invagination of the endosomal membrane results in the formation of intra-luminal vesicles (ILVs) within multivesicular bodies (MVB). MVBs either fuse with lysosomes for degradation, or with the plasma membrane to release the ILVs as exosomes by exocytosis. Microvesicles (50-1000nm) are formed by ectocytosis, directly pinching-off from the plasma membrane. Adapted from "Extracellular Vesicles", by BioRender.com (2023). Retrieved from <https://app.biorender.com/biorender-templates/figures/all/t-6489c5384c269a5dafd8ff0b-extracellular-vesicles>.

### 1.2.3 sEV signaling

The study of sEV signaling is a rapidly advancing field that dissects the role of sEVs in regulating both normal physiological processes and various pathological conditions (Kalluri & LeBleu, 2020). Moreover, growing evidence highlight the potential utilization of sEVs as diagnostic markers or therapeutic tools for various diseases, including cancer (Wiklander et al., 2019). This interest stems from compelling reports demonstrating the remarkable intrinsic, cell specific homing capabilities of sEVs, especially exosomes, that is driven by distinct vesicular surface proteins (Berumen Sánchez, Bunn, Pua, & Rafat, 2021; Hazan-Halevy et al., 2015; Rana, Yue, Stadel, & Zöller, 2012; Toda et al., 2015).

Importantly, sEV signaling can take on an autocrine or paracrine nature, either acting within the local cellular environment or impacting neighboring tissues (Asare-Werehene et al., 2020). It can also adopt an endocrine role, triggering phenotypic changes or functional responses in distant tissues (H. G. Zhang & Grizzle, 2014). The cargo of sEVs is quite diverse and complex, not always mirroring that of their cell of origin. However, it has been shown that the content changes in response to shifting environmental or physiological conditions (Wen et al., 2019). This cargo includes lipids, metabolites, cell surface and cytosolic proteins, DNA, messenger RNA (mRNA), as well as various non-coding RNAs (ncRNAs) (Kalluri & LeBleu, 2020) (Fig. 5).

## Introduction

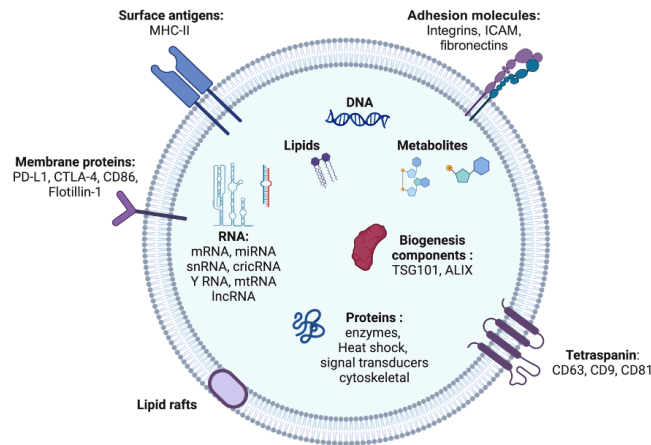


**Figure 5 | The composition and cargo of sEVs.**

Schematic representation of a typical extracellular vesicle. Extracellular vesicles are membrane enclosed entities that vary in size between 40 to 1000 nm with various surface and intra-vesicular components. Typical surface constituents include tetraspanins, adhesion molecules, surface antigens, membrane proteins and lipid rafts. Typical intra-vesicular constituents include coding and non-coding RNA, DNA, metabolites, lipids, sEV biosynthesis components and other proteins. mRNA; messenger RNA, miRNA; microRNA, circRNA; circular RNA, lncRNA; long non-coding RNA, PD-L1; Programmed death-ligand 1, CTLA-4; cytotoxic T-lymphocyte-associated protein 4, MHC-II; histocompatibility complex class II, TGS101; Tumor susceptibility gene 101, ALIX; ALG-2-interacting protein X, ICAM; Intercellular Adhesion Molecule. Created with BioRender.com. Adapted from (Kalluri & LeBleu, 2020)

Given their heterogeneous nature, the classification of sEVs remains an evolving challenge. The most recent recommendation by International Society for Extracellular Vesicles (ISEV) is to use “extracellular vesicle” as the generic term for naturally released lipid bilayer-enclosed particles that cannot replicate, modifying “EV” based on clear, measurable characteristics (Théry et al., 2018). Nonetheless, exosomes hold particular significance in signaling biology, primarily due to their distinct intracellular regulatory process that governs their composition (discussed in section 1.2.2). This, in turn, influences their functions within the specific physiological contexts and originating conditions of their biosynthesis and release into the extracellular space. Consequently, there has been several ongoing efforts over the years to isolate, purify, and characterize exosomes. However, a standardized protocol is still lacking, and marker selections continue to evolve (Berumen Sánchez et al., 2021; Kalluri & LeBleu, 2020; Théry et al., 2018).

### 1.2.4 sEVs in stressed BM

Challenges such as infections and inflammation represent a natural form of stress to the BM. As a result, various components of the BM system respond in a highly coordinated manner to restore homeostasis. A good example of this response is how HSCs react to inflammatory stress, leading to the reversible induction of cycling and division in otherwise quiescent HSCs. Interestingly, this response cannot be recapitulated *in vitro* (Essers et al., 2009). While the exact mechanisms behind HSC activation and their subsequent return to a

quiescent state remain incompletely understood, this highlights the interdependence of various cell types within the BM in regulating an appropriate response. Indeed, this has been shown in several settings such as the secretion of granulocyte colony-stimulating factor (G-CSF) by BM stromal cells in response to infection-induced neutrophil depletion, which, in turn, leads to the expansion of myeloid-committed progenitors (D. W. Cain, Snowden, Sempowski, & Kelsoe, 2011; Kwak et al., 2015).

Interestingly, a role for sEVs in BM regulation has only recently been described. In mouse models, sEVs released by MSCs have been shown to induce a loss of quiescence in HSPCs through the transfer of the MyD88 adaptor protein, ultimately resulting in the expansion of myeloid-committed progenitors (Goloviznina et al., 2016). Conversely, another study demonstrated that MSC-derived sEVs promote the maintenance of HSC stemness through the transfer of specific microRNAs (miRNAs or miRs), including miR-181, miR-21, and miR-27a (De Luca et al., 2016). These findings show the important role of sEVs released from MSCs in orchestrating the response of HSCs to inflammation, and help explain why this response cannot be obtained when attempting to replicate it in artificial *in vitro* settings.

Moreover, sEV signaling has also been found to significantly influence the remodeling of the BM microenvironment. For example, in acute myeloid leukemia (AML), sEVs released by leukemic cells were found to induce the reorganization of the BM niche into a pro-leukemic microenvironment. This occurred through the downregulation of normal hematopoietic support factors in stromal cells, either by inducing the expression of DKK1 (Kumar et al., 2018) or via the transfer of mRNA transcripts like NPM1 and FLT3 (Huan et al., 2013), which are implicated in AML pathogenesis.

Collectively, these findings confirm the bidirectional nature of sEV signaling between the BM stromal and hematopoietic compartments, playing a crucial role in maintaining homeostasis or mediating pathological changes in diseases. This highlights the need for further investigation into the multifaceted implications of sEVs in the BM microenvironment.

## **2. Aims of the thesis**

The identification of various forms of heterogeneity within the limited pool of HSCs has significantly reshaped our understanding of hematopoiesis. Our group has recently identified IFN signaling heterogeneity in HSCs, which is characterized by the intrinsic differential expression of ISGs in highly purified cells. Notably, this heterogeneity exhibits stable inheritance from parent to progeny and significantly influences cellular responses to extrinsic stress stimulation. Nonetheless, the question of whether this heterogeneity is exclusive to HSCs and their progeny within the hematopoietic system, or if it extends to non-HSC derived hematopoietic cells, remains to be explored. Furthermore, the potential contribution of this intrinsic IFN signaling heterogeneity to pathological conditions, such as malignancies, remains a subject requiring further investigation. To address these open questions in my thesis, I focused on the following aims:

### **2.1 Investigate intrinsic IFN signaling heterogeneity in non-HSC derived immune cells of adult mice**

TRMs are hematopoietic cells of embryonic origin, independent of definitive hematopoietic stem cells, that persist in the adult. To understand the origin of IFN signaling heterogeneity, this thesis investigates the intrinsic expression level of ISGs in TRMs of the central nervous system and the peritoneal cavity in WT and *ISRE-eGFP* mice.

### **2.2 Explore the impact of IFN signaling in LSC on clonal expansion and disease progression in CML**

To unravel the impact of IFN signaling heterogeneity on hematopoietic malignancies, this thesis presents an innovative CML-ISG reporter mouse model. This model enables a comprehensive investigation of the *in vivo* clonal expansion of LSCs, related to the intrinsic IFN signaling status of the parent HSC clone. It also provides valuable insights into disease progression relative to the ISG heterogenous LSC clones.

In addition to investigating intrinsic ISG signaling heterogeneity, in my thesis, I investigated communication in the stressed BM. Existing evidence strongly suggests extensive cross-talk among different BM elements in regulating homeostatic and inflammatory conditions. Nevertheless, mechanisms of crosstalk, particularly in terms of sEV signaling, remain largely unexplored. To investigate the role of sEV signaling in the stressed BM, I focused on the following aims:

### **2.3 Develop a reliable and reproducible method for isolating exosome-enriched sEVs**

Addressing the lack of standardized methods for sEV isolation, this thesis explores the benefits of combining serial centrifugation with SEC. The investigated method aims to provide a reliable and reproducible means for obtaining exosome-enriched sEVs, thus contributing to the advancement of sEV research.

### **2.4 Investigate the role of sEV signaling in regulating system response to inflammatory stress in the BM**

Recognizing the crucial role of sEV signaling in hematopoietic processes, particularly under inflammatory conditions, this thesis explores the impact of sEVs on HSPCs. Through *in vitro* and *in vivo* experiments, I aimed to unravel the regulatory role of sEVs in the BM during normal and inflammatory states, adding valuable insights to the understanding of systemic responses to stress.

In conclusion, the aims of my research are dedicated to unraveling the complexities surrounding intrinsic IFN signaling heterogeneity and its impact on disease progression in CML. Moreover, my work strives to deepen our comprehension of the role played by sEV signaling in shaping the acute inflammatory response within the BM.

### 3. Results

#### 3.1. Intrinsic IFN signaling heterogeneity in *ISRE-eGFP* reporter mouse model HSCs

Our research group has already uncovered intrinsic heterogeneity in IFN signaling within the hematopoietic system, a phenomenon that is established and maintained at the HSC level and stably inherited by differentiated immune cells (Werner et al., in preparation). Moreover, consistent with previous reports, our findings demonstrate a general high expression of intrinsic ISGs in HSC, with a gradual decline in expression as cells differentiate into progenitor populations (Wu et al., 2018).

To study IFN signaling heterogeneity, the lab used a general type I IFN (IFN I) signaling reporter mouse model known as the *ISRE-eGFP*. This transgenic model incorporates the IFN-Stimulated Response Element (ISRE), the key promoter sequence regulating the expression of IFN-stimulated genes (ISGs), upstream of the enhanced green fluorescence protein (eGFP) (Tovey et al., 2006). This enables the discrimination of hematopoietic stem cells (HSCs) based on their eGFP expression into intrinsic low or high ISG expressing HSCs (eGFP<sup>low</sup> or eGFP<sup>high</sup> HSCs, respectively) (Fig. 1A).

To validate that the ISRE-eGFP signal in HSCs from these reporter mice genuinely reflects heterogeneity in basal ISG expression and not the result of an artifact of the *ISRE-eGFP* reporter mouse model, I performed global gene expression profiling. In brief, I isolated reporter eGFP<sup>low</sup> or eGFP<sup>high</sup> HSCs from reporter mice using fluorescence activated cell sorting (FACS). Subsequently, I performed global gene expression utilizing Clariom™ S microarray chips following manufacturer's protocols with the full technical support of the Genomics and Proteomic Core facility in the DKFZ. I then filtered the profiling data for 404 mouse-specific ISGs (Table 11) (Wu et al., 2018), and analyzed the data by Ingenuity Pathway Analysis (IPA) to identify canonical pathways associated with the expression profiles. Remarkably, IPA analysis effectively detected inherent heterogeneity in IFN signaling, yielding a collection of differentially regulated canonical pathways between eGFP<sup>low</sup> and eGFP<sup>high</sup> HSC (Fig. 1B). Notably, all the top dysregulated canonical pathways were specific to inflammatory stimulation, such as "Activation of IRF by Cytosolic Pattern Recognition Receptors" and "Interferon signaling," and were upregulated in eGFP<sup>high</sup> HSCs compared to eGFP<sup>low</sup> HSCs. These findings affirm the efficacy, specificity, and sensitivity of our mouse model, providing a solid foundation for its utilization in subsequent experiments aimed at elucidating the role of intrinsic IFN signaling heterogeneity within the hematopoietic system.

## Results

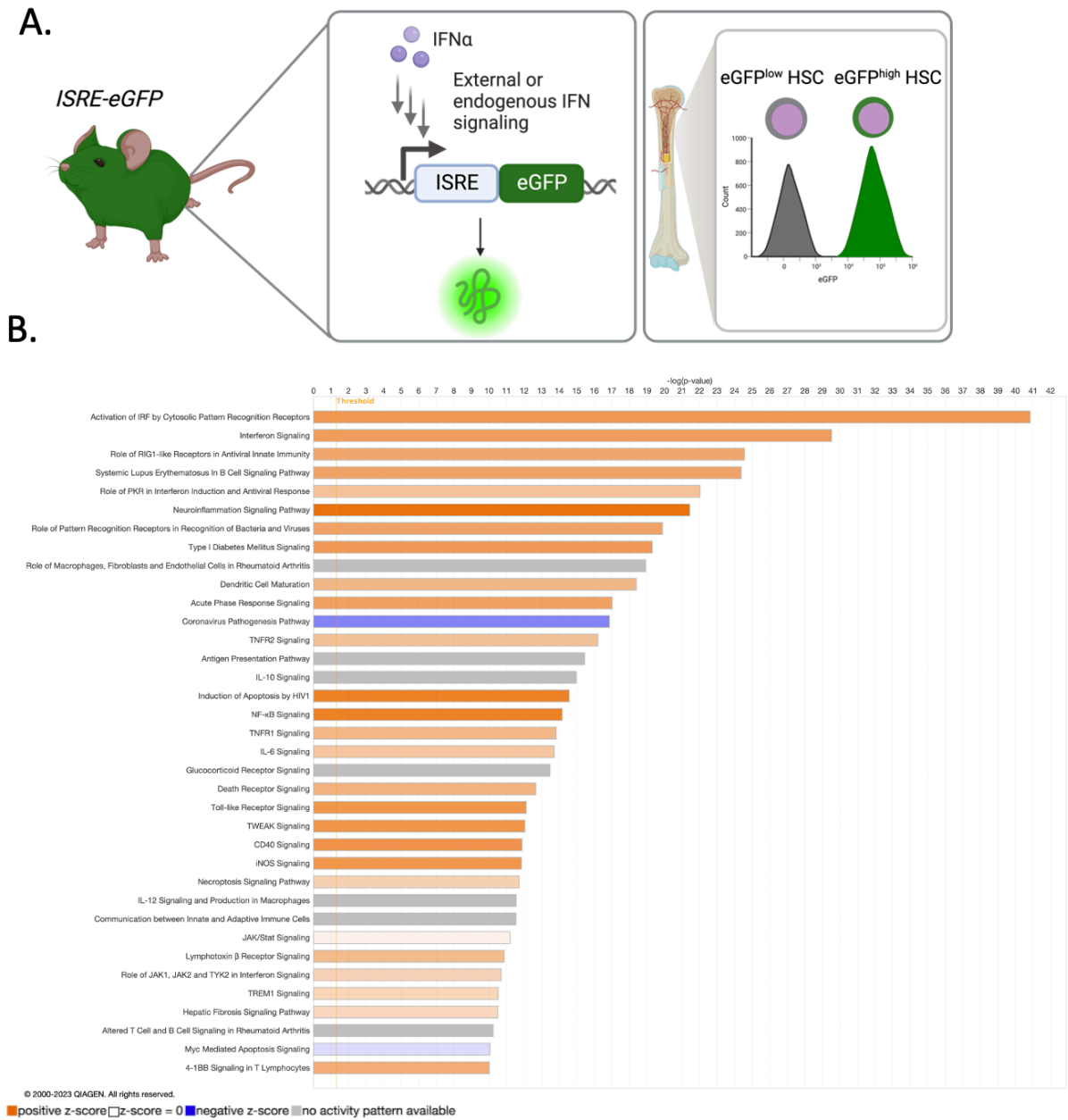


**Figure 6 | *ISRE-eGFP* reporter mouse model reveals intrinsic IFN signaling heterogeneity in HSCs.**

(A) Schematic representation of the *ISRE-eGFP* reporter mouse model showing the positioning of the IFN-Stimulated Response Element (ISRE) upstream of enhanced green fluorescent protein (eGFP). Consequently, activation of the ISRE, either intrinsically or extrinsically via INF signaling, leads to the expression of ISGs and eGFP. This design enables the distinction of HSCs, based on their eGFP expression, into low ISG expressing HSCs and high ISG expressing HSCs (eGFP<sup>low</sup> and eGFP<sup>high</sup> HSCs). (B) Top enriched canonical pathways in eGFP<sup>high</sup> HSCs compared to eGFP<sup>low</sup> HSCs (Lin<sup>-</sup> Sca-1<sup>+</sup> cKit<sup>+</sup> CD150<sup>+</sup> CD48<sup>-</sup> CD34<sup>-</sup> eGFP<sup>high/</sup> or eGFP<sup>low</sup>). The analysis was conducted using Ingenuity Pathway analysis (IPA) and filtered for 404 mouse-specific ISGs (Wu et al., 2018). The -log(p-value) cutoff was set at 10. Input data sets were derived from global gene expression profiles generated using Clariom™ S microarray chips following manufacturer's protocols. n=3.

### 3.2. Intrinsic IFN signaling heterogeneity in non-HSC derived immune cells

Our group has shown the presence of baseline IFN signaling heterogeneity in the earliest HSCs which emerge at E10.5, and this signature remains stable in their progeny (Werner et al., in preparation). However, in the adult, differentiated hematopoietic cells like tissue-resident macrophages (TRMs) originate independently of definitive hematopoiesis, stemming from the 2<sup>nd</sup> embryonic hematopoietic wave known as the pro-definitive wave (Dzierzak & Bigas, 2018) (Fig 7A).

To investigate whether these differentiated cells also show heterogeneity in ISG expression, I examined the intrinsic expression of ISGs in various TRMs in *ISRE-eGFP* mice. I tested diverse marker panels and isolation protocols for macrophages in the peritoneal cavity and the central nervous system (CNS). This effort resulted in the successful isolation of large peritoneal macrophages (LPMs) and microglia as TRMs from the peritoneal cavity and CNS, respectively. Simultaneously, I isolated small peritoneal macrophages (SPMs) and monocyte-derived macrophages (MDMs), representing their HSC-derived counterparts (Fig. 7B). Furthermore, I carried out a similar analysis in WT mice.

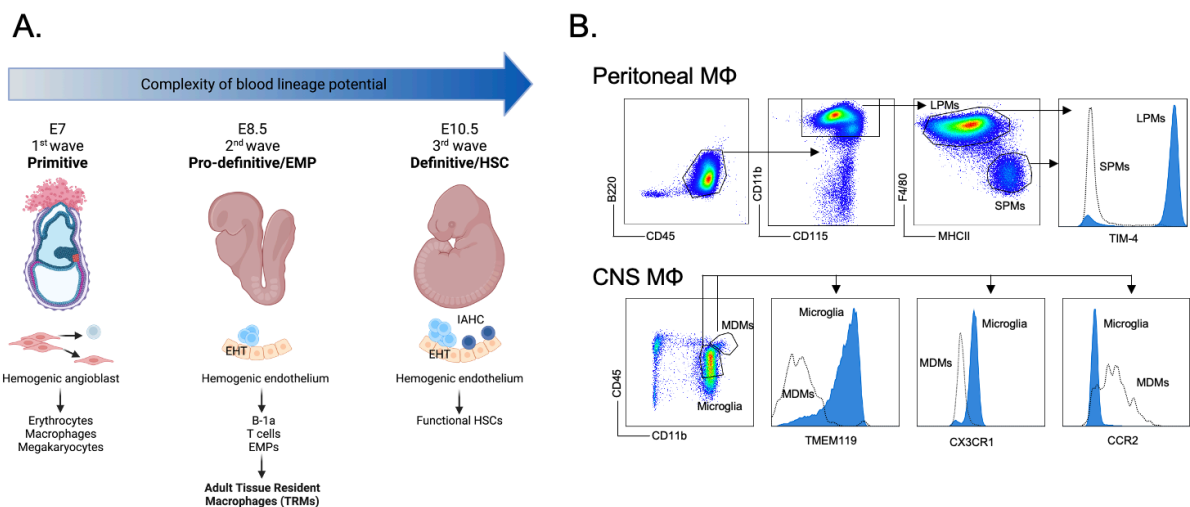


**Figure 7 | Identification of tissue resident macrophages in WT mice.**

(A) Schematic representation of murine embryonic hematopoietic developmental stages: The primitive stage, occurring at embryonic day 7 (E7), marks the genesis of hematopoietic cells from hemogenic angioblasts. Transitioning to the pro-definitive/EMP stage at E8.5, hematopoietic cells, including erythroid and myeloid progenitors (EMPs), originate from the hemogenic endothelium through endothelial-to-hematopoietic transition (EHT). These EMPs disperse throughout the developing embryo, ultimately contributing to the pool of tissue-resident macrophages (TRMs). The definitive/HSC stage, occurring at E10.5, results in the formation of definitive HSCs, originating both from the hemogenic endothelium via EHT and seen in intra-aortic hematopoietic cluster (IAHC). Created with BioRender.com, Adapted from (Dzierzak & Bigas, 2018). (B) Representative flow cytometry gating strategy for macrophages (MΦ) in the peritoneal cavity and the central nervous system (CNS): Top panel, gating strategy used to identify peritoneal MΦ, distinguishing between small peritoneal macrophages (SPMs) and large peritoneal macrophages (LPMs). Lower panel, gating strategy used to identify CNS MΦ, discerning between monocyte-derived macrophages (MDMs) and microglia.

## Results

Remarkably, flow cytometry analysis of reporter LPMs and microglia revealed a bimodal distribution of ISRE-activity, similar to HSC-derived hematopoietic cells (Fig. 8A). Notably, the ratio of eGFP<sup>high</sup> to eGFP<sup>low</sup> LPMs was 2.28, representing a 50.68% increase compared to the 1.51 ratio of eGFP<sup>high</sup> to eGFP<sup>low</sup> SPMs (Fig. 8B). This difference was even more pronounced in the CNS, where tissue-resident eGFP<sup>high</sup> microglia outnumbered eGFP<sup>low</sup> microglia by 4.4 times, marking a substantial 418.954% increase over the 0.8489 ratio of HSC-derived eGFP<sup>high</sup> to eGFP<sup>low</sup> MDMs (Fig. 8C).

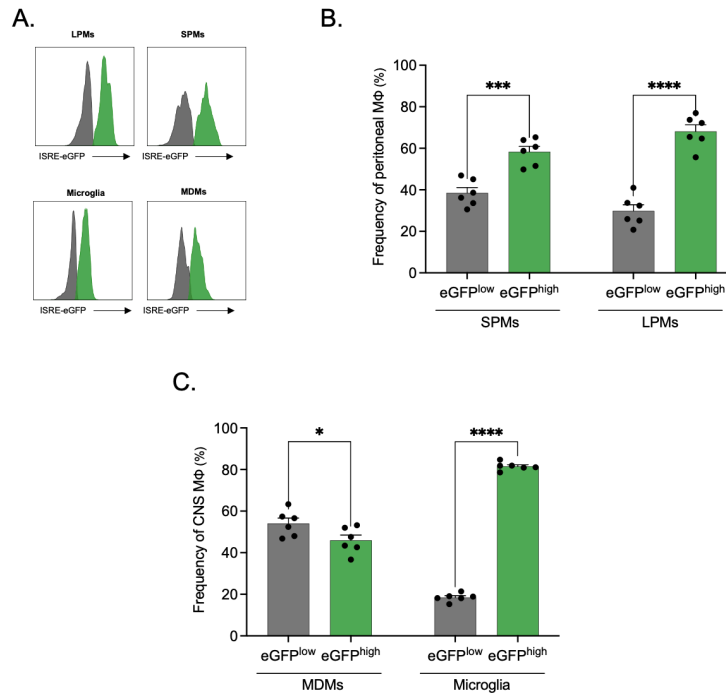


**Figure 8 | IFN signaling heterogeneity in tissue resident macrophages in *ISRE-eGFP* mice.**

(A) Representative flow cytometry histogram of eGFP expression in large peritoneal macrophages (LPMs) (B220<sup>-</sup> CD45<sup>+</sup> CD11b<sup>+</sup> CD115<sup>+</sup> F4/80<sup>high</sup> MHCII<sup>-/low</sup> TIM-4<sup>+</sup>), small peritoneal macrophages (SPMs) (B220<sup>-</sup> CD45<sup>+</sup> CD11b<sup>+</sup> CD115<sup>+</sup> F4/80<sup>-/low</sup> MHCII<sup>high</sup> TIM-4<sup>-</sup>), microglia (CD11b<sup>+</sup> CD45<sup>med</sup> Tmem119<sup>+</sup> CX3CR1<sup>+</sup> CCR2<sup>-</sup>) and monocyte derived macrophages (MDMs) (CD11b<sup>+</sup> CD45<sup>high</sup> Tmem119<sup>-</sup> CX3CR1<sup>-</sup> CCR2<sup>+</sup>). (B) Frequencies (%) of eGFP<sup>low</sup> versus eGFP<sup>high</sup> cells in SPM and LPM peritoneal macrophages (MΦ). (C) Frequencies (%) of eGFP<sup>low</sup> versus eGFP<sup>high</sup> cells in MDM and microglia central nervous system (CNS) MΦ. n=6 for (B-C). Data are represented as mean, and error bars as standard error of mean. Statistical significance was determined by two-way ANOVA using Tukey's multiple comparison test for (B-C) (\* p < 0.05; \*\*\* p < 0.001; \*\*\*\* p < 0.0001).

For the real-time quantitative polymerase chain reaction (qRT-PCR) analysis of ISGs, I used a panel of ISGs which I constructed by cross-referencing the M5911 (HALLMARK\_INTERFERON\_ALPHA\_RESPONSE) and M11929 (GO\_RESPONSE\_TO\_INTERFERON\_ALPHA) reference datasets from the Molecular Signature Database (MSigDB) to identify consistently up-regulated genes (Liberzon et al., 2015; Subramanian et al., 2005). This list was then cross-referenced with our previous global HSC gene expression analysis following IFNα treatment (Haas et al., 2015), yielding a final

## Results

list of 49 ISG genes (Table 3). The qRT-PCR analysis revealed that TRMs generally upregulated basal ISG expression levels compared to their HSC-derived counterparts in both the peritoneal cavity and the CNS. In WT mice, this upregulation was statistically significant in LPMs compared to SPMs ( $p=0.0091$ ) and microglia compared to MDMs ( $p=0.005$ ) (Fig. 9A). The same transcriptional analysis in *ISRE-eGFP* reporter cells further confirmed that, in both peritoneal and CNS macrophages, eGFP<sup>high</sup> subpopulations displayed a general upregulation of basal ISG expression compared to their eGFP<sup>low</sup> counterparts, although this difference was not statistically significant (Fig. 9B&C). However, these results underscore the specificity of the reporter signal. Moreover, in alignment with data from WT mice, reporter LPMs and microglia exhibited an upregulation of basal ISG expression in both eGFP<sup>low</sup> (significant,  $p=0.0292$  for LPMs and  $p=0.0091$  for microglia) and eGFP<sup>high</sup> subpopulations compared to their HSC-derived counterparts (Fig. 9B&C).

Collectively, this data suggests that the establishment of intrinsic IFN-signaling heterogeneity in the hematopoietic system likely precedes the formation of functional HSCs, possibly originating during the embryonic endothelial-to-hematopoietic transition phase of the second (pro-definitive) wave of hematopoietic cell generation. Furthermore, it highlights that hematopoietic cells of embryonic origin exhibit higher levels of ISG expression under homeostatic conditions compared to HSC-derived immune cells.

## Results

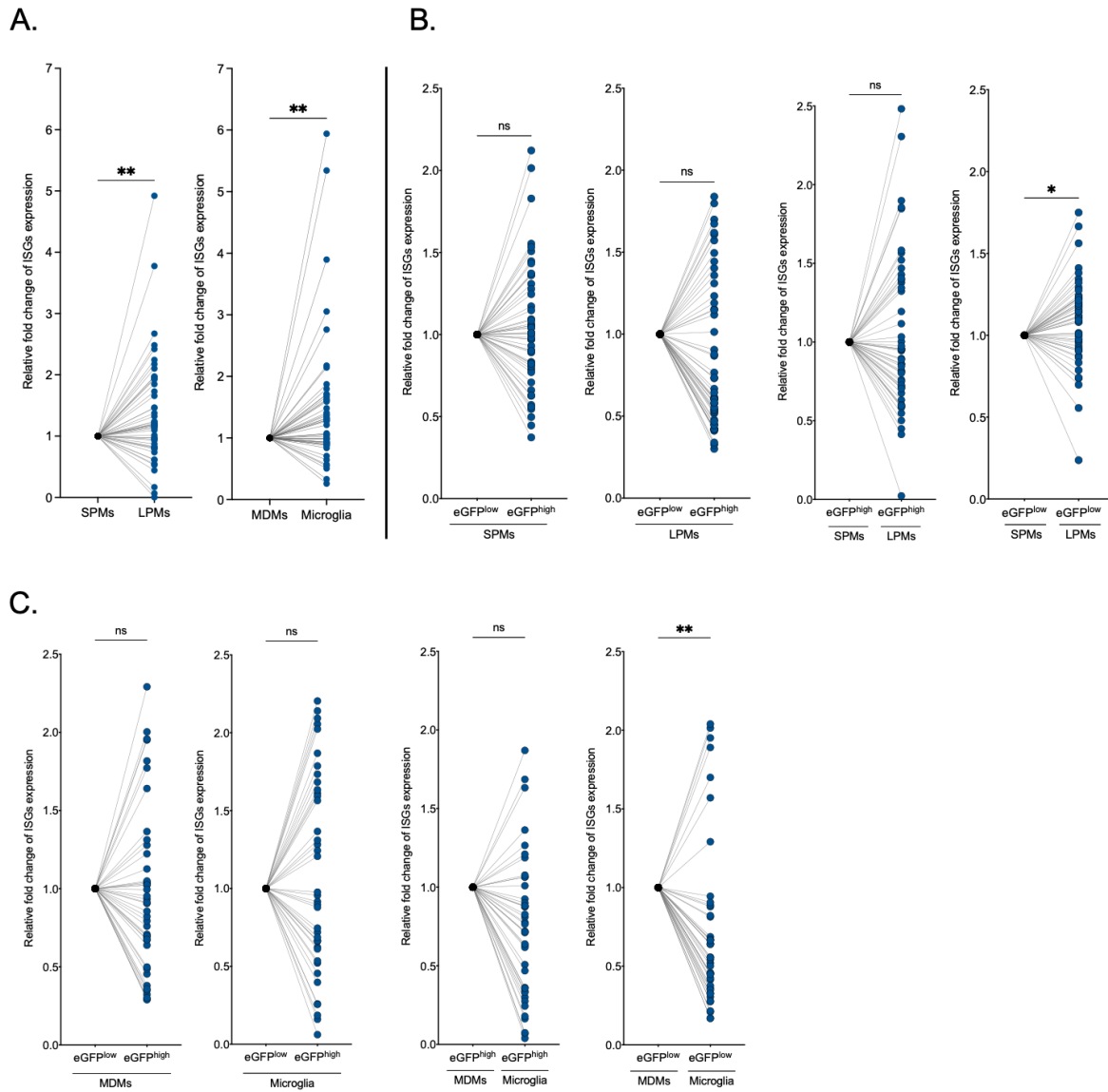


**Figure 9 | IFN signaling heterogeneity in TRMs confirmed by transcriptional profiling of ISGs.**

Transcriptional profiling of 49 ISGs in: (A) WT large peritoneal macrophages (LPMs) (B220<sup>-</sup> CD45<sup>+</sup> CD11b<sup>+</sup> CD115<sup>+</sup> F4/80<sup>high</sup> MHCII<sup>-/low</sup> TIM-4<sup>+</sup>) relative to small peritoneal macrophages (SPMs) (B220<sup>-</sup> CD45<sup>+</sup> CD11b<sup>+</sup> CD115<sup>+</sup> F4/80<sup>-/low</sup> MHCII<sup>high</sup> TIM-4<sup>-</sup>), left panel; WT microglia (CD11b<sup>+</sup> CD45<sup>med</sup> Tmem119<sup>+</sup> CX3CR1<sup>+</sup> CCR2<sup>-</sup>) relative to monocyte derived macrophages (MDMs) (CD11b<sup>+</sup> CD45<sup>high</sup> Tmem119<sup>-</sup> CX3CR1<sup>-</sup> CCR2<sup>+</sup>), right panel. (B) *ISRE-eGFP* reporter SPMs (eGFP<sup>high</sup> relative to eGFP<sup>low</sup>), first panel; *ISRE-eGFP* reporter LPMs (eGFP<sup>high</sup> relative to eGFP<sup>low</sup>), second panel; *ISRE-eGFP* reporter eGFP<sup>high</sup> LPMs relative to eGFP<sup>high</sup> SPMs, third panel; *ISRE-eGFP* reporter eGFP<sup>low</sup> LPM relative to eGFP<sup>low</sup> SPM, fourth panel. (C) *ISRE-eGFP* reporter MDMs (eGFP<sup>high</sup> relative to eGFP<sup>low</sup>), first panel; *ISRE-eGFP* reporter microglia (eGFP<sup>high</sup> relative to eGFP<sup>low</sup>), second panel; *ISRE-eGFP* reporter eGFP<sup>high</sup> microglia relative to eGFP<sup>high</sup> MDM, third panel; *ISRE-eGFP* reporter eGFP<sup>low</sup> microglia relative to eGFP<sup>low</sup> MDM. n=6. Each symbol represents the expression of a single ISG. Statistical significance was determined by Wilcoxon matched-pairs signed rank test for all panels (ns, not significant; \*  $p \leq 0.05$ ; \*\*  $p \leq 0.01$ ).

### **3.3. Impact of intrinsic IFN signaling heterogeneity in stem cells on leukemia progression**

Given the well-established correlation between an inflammatory milieu and the onset of various myeloid malignancies (Brianna M. Craver et al., 2018), the heterogeneity observed in the intrinsic inflammatory signature within HSCs holds potential biological significance in a malignant context. Therefore, I hypothesize that the heterogeneity in IFN signaling among stem cells may play a pivotal role in influencing the onset and progression of diseases when introducing an oncogene into stem cells with diverse baseline IFN signaling.

#### **3.3.1 A unique CML-ISG reporter mouse model as a tool to investigate the role of intrinsic IFN heterogeneity in a clonal hematopoietic malignancy**

To dissect the role of intrinsic IFN signaling heterogeneity in HSCs within the context of myeloid malignancies, I directed my research towards CML since it is a clonal hematopoietic malignancy that is believed to be driven by the *BCR::ABL1* mutation originating in HSCs (Hoffman et al., 2008; Wintrobe & Greer, 2014). To facilitate this investigation, I first developed and characterized a humanized CML mouse model on the background of the unique *ISRE-eGFP* reporter mouse.

#### **3.3.2 Generation and optimization of the CML-ISG reporter mouse model**

##### **3.3.2.1 No difference in baseline infectibility of eGFP<sup>low</sup> and eGFP<sup>high</sup> HSCs to murine stem cell vector (MSCV) retrovirus**

To create the CML-ISG reporter mouse model, I adapted the well-established retroviral transduction/transplantation CML mouse model (R. El Eit et al., 2019; R. M. El Eit et al., 2014; Pear et al., 1998) to introduce a reporter linked to *BCR::ABL1* expression, which did not interfere with eGFP. The vector used for my studies is a bicistronic retroviral construct that codes for the P210 *BCR::ABL1* oncoprotein with an associated mCherry tag. I generated it by restriction cloning using the MIGR1 plasmid as a backbone (Addgene plasmid #27490) which is extensively used in CML retroviral studies (R. El Eit et al., 2019; R. M. El Eit et al., 2014; Pear et al., 1998). Specifically, MSCV-*BCR::ABL1*-IRES-mCherry was constructed by ligating the 7005-pb *EcoRI* fragment containing the E14a2 (b3a2) version of the *BCR::ABL1* cDNA from NGFR P210 (Addgene plasmid #27486) into pMSCV-IRES-mCherry FP (Addgene plasmid #52114) (Fig. 10A). The latter also served as the control empty vector. The generated

## Results

construct was then verified by plasmid sequencing (data not shown) and used to produce retrovirus via transient transfection of a specialized ecotropic retroviral packaging cell line, Platinum-E (Plat-E) (Fig. 10B).

Through optimization of transfection conditions for both the empty vector and the BCR::ABL1 vector on Plat-E cells, I determined that 15 µg DNA of the BCR::ABL1 and the empty vector yielded the highest transfection rates (50% and 79%, respectively) (Fig. 10C). As expected, the virus titer from the empty vector was higher ( $4.8 \times 10^6$  IU/mL) compared to the BCR::ABL1 vector ( $3.6 \times 10^5$  IU/mL) (Fig. 10D). Both titers were sufficient for downstream infectibility studies, and quantifying the titers was crucial to ensure reproducibility, preventing bias by maintaining a uniform multiplicity of infection (MOI) in subsequent experiments.

Several ISGs are recognized for their role in shielding cells against viral infections. Given that the CML murine model is based on *in vitro* retroviral transduction of *ISRE-eGFP* donor BM, it was important to assay the inherent baseline infectibility of eGFP<sup>low</sup> and eGFP<sup>high</sup> HSCs. Thus, I used FACS to isolate eGFP<sup>low</sup> or eGFP<sup>high</sup> HSC subpopulations from *ISRE-eGFP* BM. These subsets were then individually exposed to the same empty vector virus with increasing viral MOIs, allowing the assessment of their infectibility (Fig. 10E). Both HSC subpopulations displayed similar levels of susceptibility, revealing only marginal differences particularly at high MOI levels which are not relevant for my research (Fig. 10F, left panel). Importantly, the baseline eGFP levels of eGFP<sup>low</sup> and eGFP<sup>high</sup> HSCs remained unchanged following *in vitro* retroviral infection at all tested MOIs (Fig. 10F, right panel). Thus, these data showed no differences in infectibility nor a change in eGFP signal, allowing me to use this retroviral transduction model in *ISRE-eGFP* cells for further experiments.

## Results

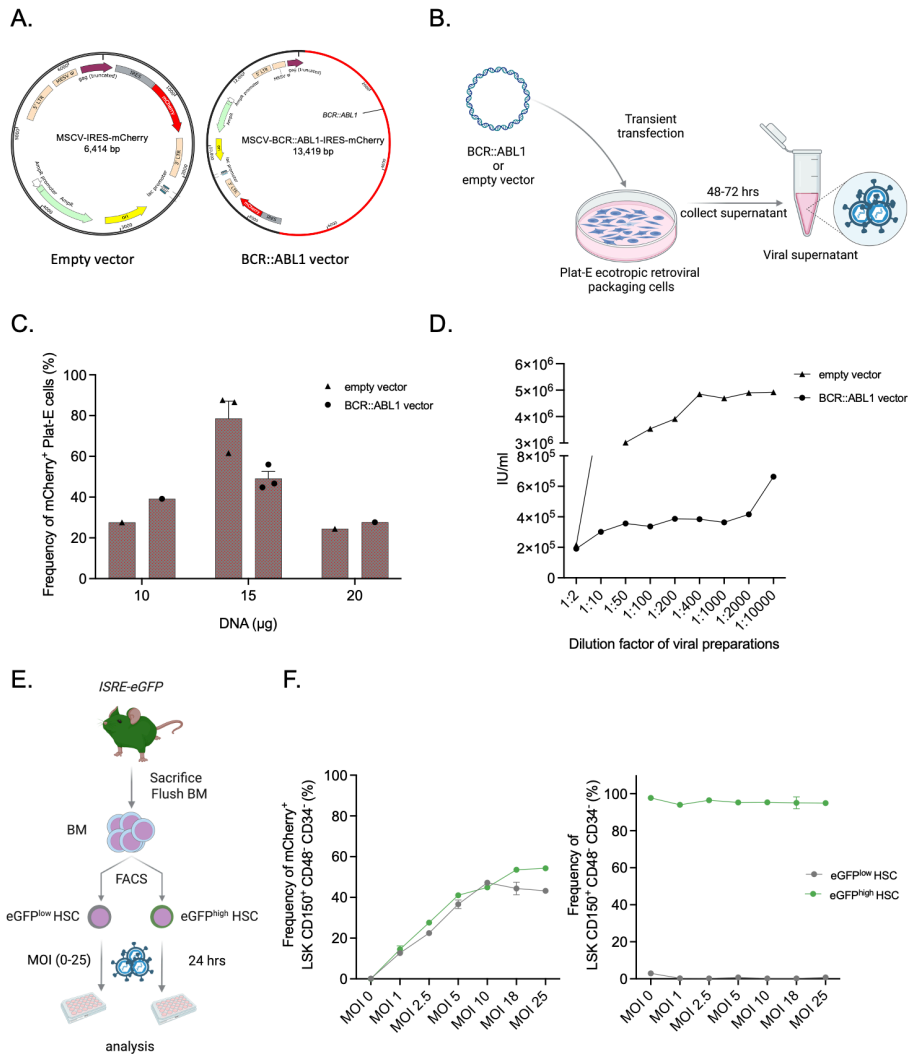


**Figure 10 | No difference in baseline infectibility of eGFP<sup>low</sup> and eGFP<sup>high</sup> HSCs with murine stem cell vector (MSCV) retrovirus.**

(A) Schematic representation of the empty vector MSCV-IRES-mCherry (left) and the BCR::ABL1 containing vector MSCV-BCR::ABL1-IRES-mCherry (right), which are bicistronic retroviral constructs with a mCherry<sup>+</sup> tag used for the generation of ISG-CML mice. (B) Schematic overview of experimental design: MSCV-IRES-mCherry or MSCV-BCR::ABL1-IRES-mCherry constructs were used to transfect Platinum-E cells (Plat-E), an ecotropic retroviral packaging cell line, using the calcium phosphate transient transfection method. Viral supernatants from each preparation were collected at 48hrs and 72hrs. Created with BioRender.com (C) Frequency (%) of mCherry<sup>+</sup> Plat-E cells transfected with indicated DNA amounts of MSCV-IRES-mCherry and MSCV-BCR::ABL1-IRES-mCherry. (D) Titer quantification of representative viral preparations (IU/mL) generated by the MSCV-IRES-mCherry or MSCV-BCR::ABL1-IRES-mCherry constructs on NIH/3T3 cells. (E) Schematic representation of experimental design: eGFP<sup>low</sup> and eGFP<sup>high</sup> HSCs (Lin<sup>-</sup> Sca-1<sup>+</sup> cKit<sup>+</sup> CD150<sup>+</sup> CD48<sup>+</sup> CD34<sup>-</sup> eGFP<sup>low</sup>/ or eGFP<sup>high</sup>) were isolated from *ISRE-eGFP* mice, and separately transduced with MSCV-IRES-mCherry virus at different MOIs. Created with BioRender.com. (F) Infectibility of eGFP<sup>low</sup> or eGFP<sup>high</sup> HSCs (left panel) and eGFP reporter signal (right panel) with MSCV-IRES-mCherry virus at indicated MOIs. n=1-3 for (C), and n= 2 for (F). Data are represented as mean, and error bars as standard error of mean. Experiments (B-D) performed jointly with Kalliopi-Anna Penteskoufi.

### 3.3.2.2. *In vivo* 5-FU treatment response shows no difference between eGFP<sup>low</sup> and eGFP<sup>high</sup> HSCs

With the retroviral CML model, the first step usually involves treating donor mice with 5-Fluorouracil (5-FU), which is a widely adopted practice in retroviral gene delivery protocols (Wertheim, Miller, Xu, He, & Pear, 2002). Acute *in vivo* 5-FU treatment results in a swift and efficient depletion of cycling progenitor cells, leading to a significant reduction in total BM counts while safeguarding quiescent HSCs (Hodgson & Bradley, 1979; Lerner & Harrison, 1990; Shaikh, Bhartiya, Kapoor, & Nimkar, 2016; Van Zant, 1984). This selective action creates favorable conditions for retroviral integration in stem cells, offering dual advantages. Firstly, it permits the utilization of lower viral MOIs due to the enrichment of primitive cells. Secondly, it renders HSCs susceptible to retroviral infection by stimulating them into cell cycle in order to replenish the system (D'Hondt et al., 2002). However, given the influence of intrinsic IFN signaling heterogeneity on modulating stress response, I first needed to test whether eGFP<sup>low</sup> and eGFP<sup>high</sup> HSC subpopulations might exhibit variant cycling patterns in response to 5-FU treatment. This could influence retroviral infection and potentially introduce a bias. Furthermore, the steady state ratio of eGFP<sup>low</sup> to eGFP<sup>high</sup> HSCs (40/60, respectively) could also be perturbed by this treatment, further obscuring results.

To effectively navigate these challenges, I first determined the optimal 5-FU dosage and BM harvesting technique that would yield the most reduction of total BM counts, along with maximum enrichment of cycling primitive cells in *ISRE-eGFP* mice. Accordingly, BM was harvested using either a flushing or a crushing technique, 96 hours post treatment of *ISRE-eGFP* mice with two distinct intravenous (i.v.) doses of 5-FU (100mg/kg or 200 mg/kg) (Fig. 11A). The combination of flushing and a 200 mg/kg 5-FU dose resulted in the maximal reduction of total BM counts (Fig. 11B). Using these conditions, I observed no significant alteration in the ratio between eGFP<sup>low</sup> and eGFP<sup>high</sup> HSCs (Fig. 11C) or cycling patterns of the 2 subpopulations of HSCs (Fig. 11D). This finding provided me the confidence to proceed with the utilization of 5-FU in our mouse model without the concern of introducing technical bias.

## Results

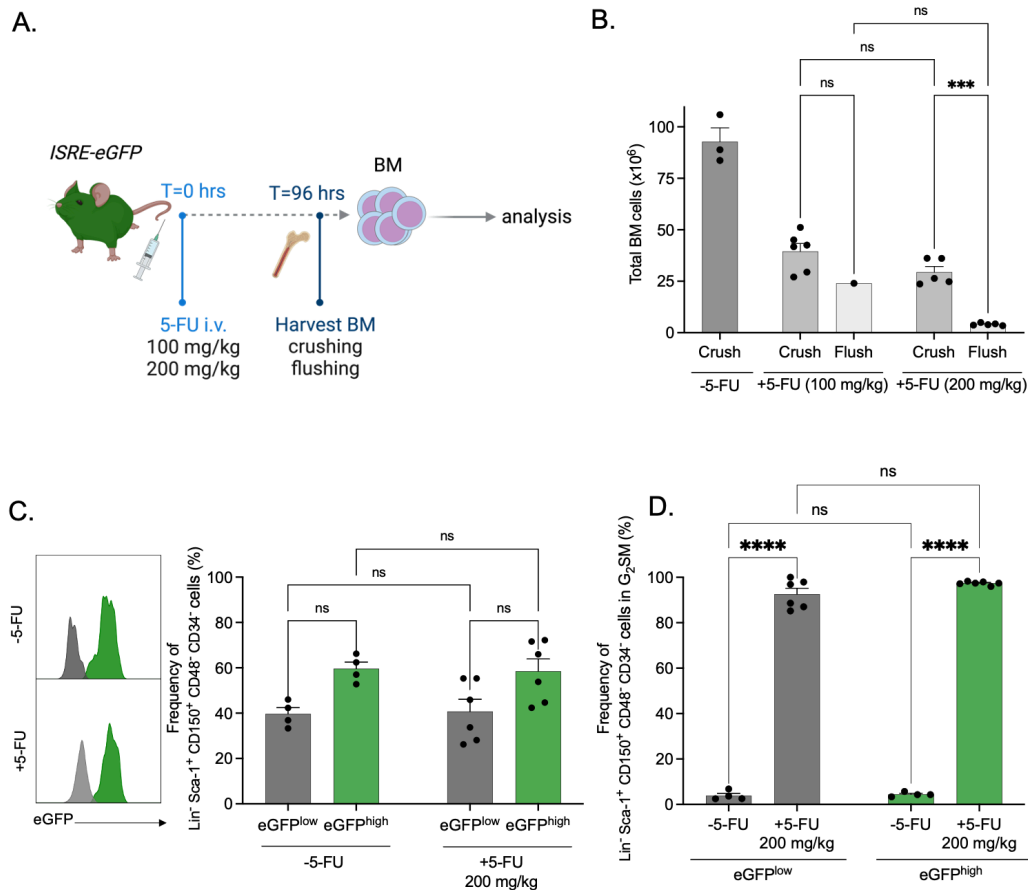


**Figure 11 | No difference in the response to *in vivo* 5-FU treatment between  $eGFP^{low}$  and  $eGFP^{high}$  HSCs.**

(A) Schematic representation of experimental design: BM was collected from untreated or 5-FU treated (100 or 200 mg/kg i.v.) *ISRE-eGFP* mice by flushing or crushing 96 hours post 5-FU treatment. Created with BioRender.com (B) Total BM counts of *ISRE-eGFP* mice at indicated harvesting methods and treatments. (C) Representative flow cytometry histograms of eGFP expression in HSCs ( $Lin^- Sca-1^+ CD150^+ CD48^- CD34^-$ ) of untreated controls and 5-FU (200 mg/kg) treated mice 96 hours post-treatment (left panel); and frequencies (%) of  $eGFP^{low}$  and  $eGFP^{high}$  HSCs at indicated experimental conditions (right panel). (D) Frequency (%) of  $eGFP^{low}$  and  $eGFP^{high}$  HSCs in the  $G_2SM$  phase at indicated experimental conditions.  $n=1-6$  for (B), and  $n=4$  (untreated controls) and  $n=6$  (5-FU, 200 mg/kg) for (C-D) from two independent experiments. Data are presented as mean and error bars as standard error of mean. Statistical significance was determined by ordinary one-way ANOVA using Tukey's multiple comparison test for (B), and by two-way ANOVA using Tukey's multiple comparison test for (C-D) (ns, not significant; \*\*\*  $p \leq 0.001$ ; \*\*\*\*  $p \leq 0.0001$ ).

### 3.3.2.3 Comparable response of $eGFP^{low}$ and $eGFP^{high}$ HSCs to *in vitro* cytokine pre-stimulation and viral transduction

In murine retroviral-mediated gene transfer protocols, *in vitro* cytokine pre-stimulation enhances HSC infection by increasing their abundance and promoting their cycling (Gavrilescu & Van Etten, 2008). It involves culturing HSCs in a medium containing 10 ng/ml interleukin (IL) 6 (IL-6) and IL-3 and 100 ng/ml murine stem cell factor (mSCF) for 24 hours. After pre-stimulation, cells are subjected to 2 rounds of viral transduction (24 hours apart) to deliver the gene of interest into HSCs. Given the potential for distinctive responses of  $eGFP^{low}$

## Results

and eGFP<sup>high</sup> HSC subpopulations to these *in vitro* manipulations, I performed a series of optimization experiments to elucidate and account for any differential outcomes.

In the initial experiment, I harvested and pooled BM from 5-FU treated *ISRE-eGFP* mice, and cultured these cells in pre-stimulation medium for 24 hours, followed by 2 rounds of retroviral transduction using empty vector viral preparations (Fig. 12A). The MOI in this, and all downstream experiments was maintained at 0.3. Under these conditions, 68.8% of the total HSCs were effectively infected (mCherry<sup>+</sup>) (Fig. 12B). Importantly, upon a closer examination of the HSC subpopulation after infection, it is evident that the ratios of mCherry<sup>-</sup> or mCherry<sup>+</sup> eGFP<sup>low</sup> or eGFP<sup>high</sup> HSCs remained consistent ( $\approx 40/60$ , respectively) (Fig. 12C), aligning with their proportions at the time of harvest (Fig. 11C). This data suggests that within these parameters, the protocol is efficient in targeting HSCs without any discernible bias linked to the intrinsic IFN signaling background of HSCs.

To test if this is a true system response, detached from the potentially confounding effects of 5-FU which substantially impacts HSCs, I replicated the experiment without 5-FU treatment using a BCR::ABL1 viral preparation. As anticipated, the efficiency of transduction for the collective HSC population drastically decreased to approximately 15% (Fig. 12B). Interestingly, the omission of 5-FU didn't disrupt the system's response, yielding results and HSC ratios as observed with 5-FU treatment (Fig. 12D).

This data suggests that our technique proficiently and impartially targets the distinct HSCs subpopulations, irrespective of 5-FU treatment. This presents an attractive technical angle in my CML-ISG model, since although 5-FU enhances transduction efficiency, its long-term ramifications on HSC subpopulations remain uncertain and cannot be disregarded especially in the context of a leukemia.

## Results

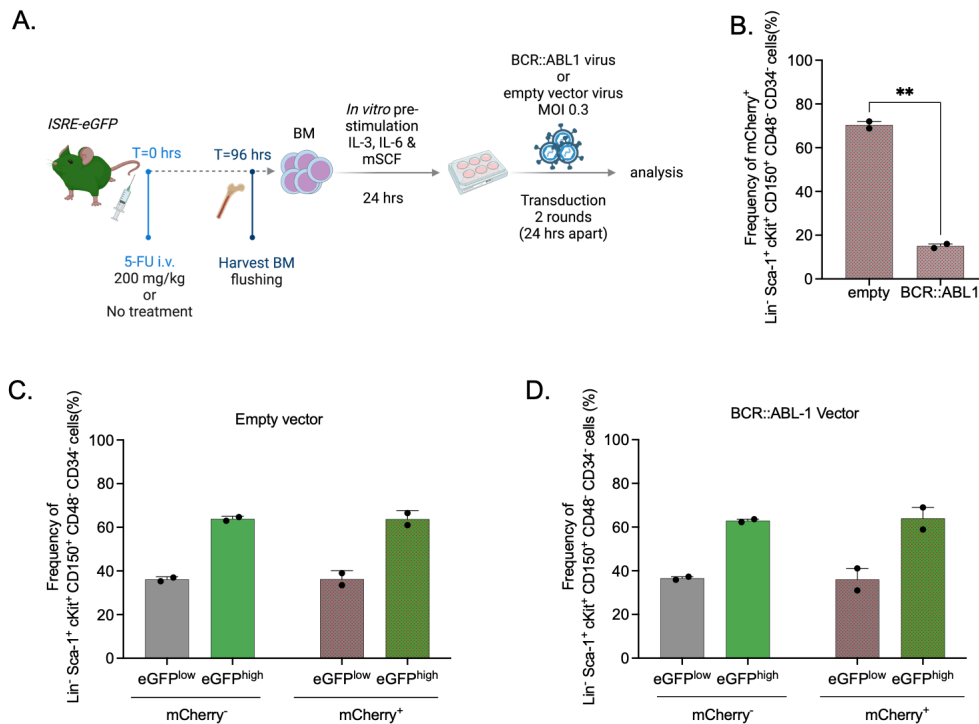


**Figure 12 | No difference between eGFP<sup>low</sup> and eGFP<sup>high</sup> HSC response to *in vitro* cytokine pre-stimulation and viral transduction.**

(A) Schematic representation of experimental design: BM from untreated or 5-FU treated (200 mg/kg 5-FU i.v. for 96 hours) *ISRE-eGFP* mice was pooled from at least 8 mice (8-36), and pre-stimulated *in vitro* for 24 hours in pre-stimulation medium containing IL-3, IL-6 and mSCF. The cells were then transduced twice (24 hours apart) with MSCV-IRES-mCherry (empty) or MSCV-BCR::ABL1-IRES-mCherry (BCR::ABL1) at MOI 0.3, and analyzed by flow cytometry. Created with BioRender.com (B) Frequency (%) of total mCherry<sup>+</sup> HSCs (Lin<sup>-</sup> Sca-1<sup>+</sup> cKit<sup>+</sup> CD150<sup>+</sup> CD48<sup>-</sup> CD34<sup>+</sup>) after viral transduction with indicated viral preparations. (C) Frequencies (%) of mCherry<sup>+</sup> or mCherry<sup>-</sup> labeled eGFP<sup>low</sup> or eGFP<sup>high</sup> HSCs after retroviral transduction with empty vector. (D) Frequencies (%) mCherry<sup>+</sup> or mCherry<sup>-</sup> labeled eGFP<sup>low</sup> or eGFP<sup>high</sup> HSCs after retroviral transduction with BCR::ABL1 vector. n=2 (B-E) from two independent experiments. Data are presented as mean and error bars as standard error of mean. Statistical significance for (B) was determined by a two-tailed student's *t*-test (\*\*  $p \leq 0.01$ ).

### 3.3.2.4 A CML-like disease is produced by MSCV-BCR::ABL1-IRES-mCherry retroviral construct *in vivo*

The MSCV-BCR::ABL1-IRES-mCherry retrovirus was assessed for its potential to induce the characteristic CML-like disease in WT mice according to standard protocol (R. El Eit et al., 2019; R. M. El Eit et al., 2014; Pear et al., 1998). Briefly, BM cells from 5-FU treated WT donor mice were pre-stimulated and subjected to two consecutive rounds of transduction with BCR::ABL1 retrovirus at MOI 0.3. Subsequently, I transplanted a total of  $2.5 \times 10^5$  transformed BM cells into 6 lethally irradiated ( $2 \times 500$  Rad) WT recipients (Fig. 13A). As expected, transduction efficiency was high, with 87.5% of the total HSCs effectively infected (mCherry<sup>+</sup>) (Fig. 13B).

Leukemia engraftment (>1% mCherry<sup>+</sup> cells in peripheral blood, PB) was already detectable in all recipient mice by day 7 (D7). By D17, these mice displayed an average of

## Results

approximately 80% mCherry<sup>+</sup> cells in their PB and were euthanized due leukemia burden (Fig. 13C). When analyzing different cell population in the PB, a characteristic significant increase in the frequency of mCherry<sup>+</sup> myeloid cells, neutrophils and macrophages, was observed at D12 and 17 (Fig. 13D&E). On the other hand, lymphoid cells (B cells and T cells) exhibited the expected reduced numbers at early timepoints following BM transplantation (Fig. 13F).

Furthermore, BM analysis revealed that the majority of primitive and committed progenitor cells were expressing BCR::ABL1 at the time of sacrifice, aligning with the observed CML-like phenotype (Fig. 13G&H). Notably, all mice exhibited the classical splenomegaly commonly associated with untreated advanced CML (Fig. 13I). Collectively, these data convincingly suggests that the generated BCR::ABL1 construct is indeed capable of generating a rapid CML-like disease in mice, while simultaneously enabling efficient mCherry labeling of leukemic cells across the entire hematopoietic hierarchy.

## Results

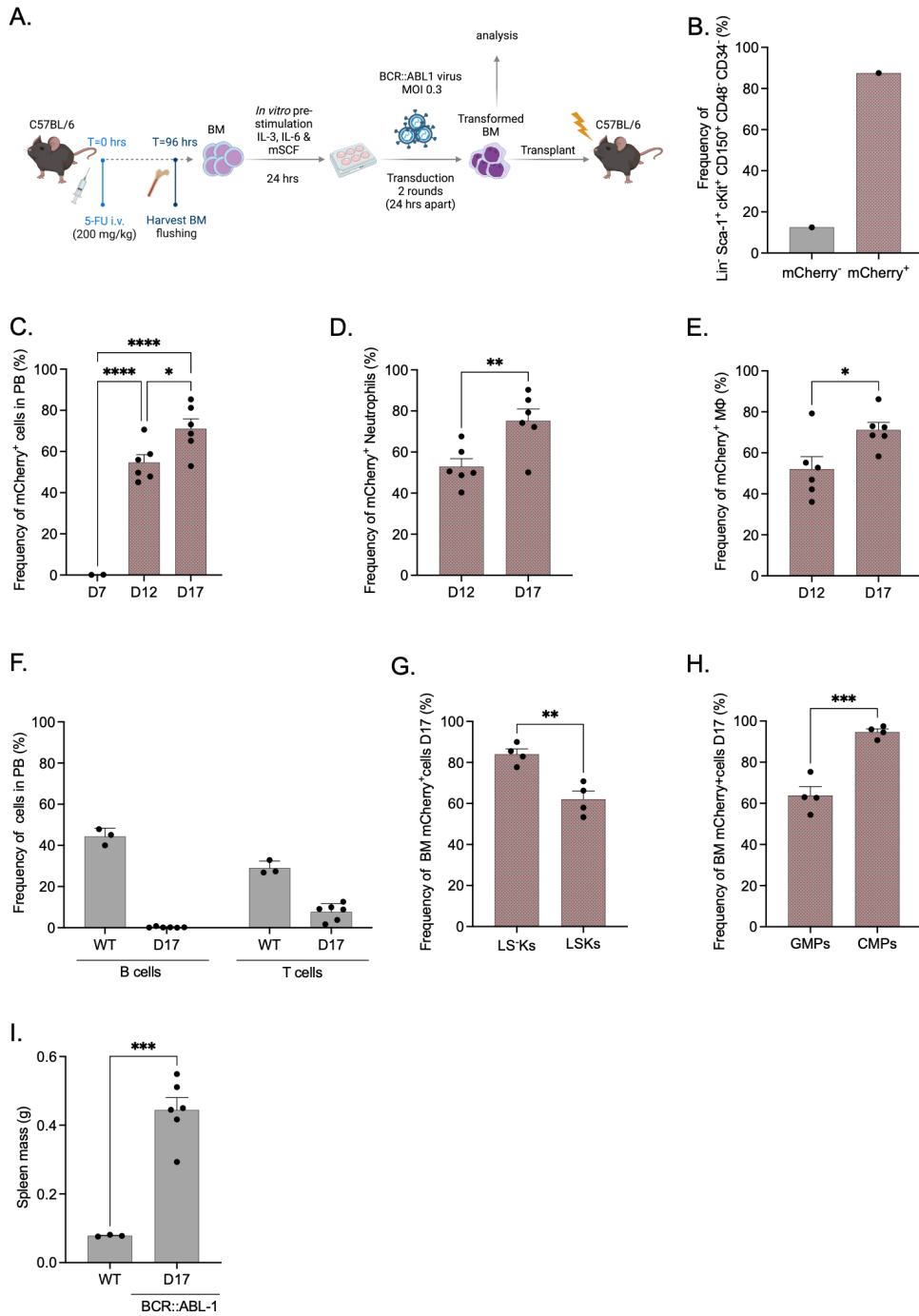


**Figure 13 | Transplantation of BCR::ABL1 transduced BM induced a CML-like disease *in vivo*.**

(A) Schematic representation of experimental design: pooled BM from 9 5-FU treated (200 mg/kg, i.v. for 96 hours) C57BL/6 WT was pre-stimulated *in vitro* (24 hours) and transduced twice (24 hours apart) with MSCV-BCR::ABL1-IRES-mCherry virus at MOI 0.3. Then,  $2.5 \times 10^5$  cells/mouse were transplanted i.v. into lethally irradiated ( $2 \times 500$  Rad) C57BL/6 WT mice. Created with BioRender.com. (B) Transduction efficiency (%) of HSCs (Lin<sup>-</sup> Sca-1<sup>+</sup> cKit<sup>+</sup> CD150<sup>+</sup> CD48<sup>-</sup> CD34<sup>-</sup>). (C-E) Frequency (%) of mCherry<sup>+</sup> cells (C), neutrophils (B220<sup>-</sup> CD4/8<sup>-</sup> CD11b<sup>+</sup> Ly6G<sup>+</sup>) (D), and macrophages (MΦ) (B220<sup>-</sup> CD4/8<sup>-</sup> CD11b<sup>+</sup> Ly6G<sup>-</sup> Siglec-F<sup>+</sup> F4/80<sup>+</sup>) (E) in the PB of recipient mice at indicated days post-transplantation. (F) Frequency (%) of B cells (B220<sup>+</sup>) and T cells (CD4/8<sup>+</sup>) in the PB. (G-H) Frequency (%) of mCherry<sup>+</sup> LSKs (Lin<sup>-</sup> Sca-1<sup>-</sup> cKit<sup>+</sup>) and LSKs (Lin<sup>-</sup> Sca-1<sup>+</sup> cKit<sup>+</sup>) (G), granulocyte-monocyte progenitors (GMPs) (Lin<sup>-</sup> Sca-1<sup>+</sup> cKit<sup>+</sup> CD16/32<sup>+</sup> CD34<sup>+</sup>) and common myeloid progenitors (CMPs) (Lin<sup>-</sup> Sca-1<sup>+</sup> cKit<sup>+</sup> CD16/32<sup>low</sup> CD34<sup>+</sup>) (H) in the BM at D17. (I) Spleen mass (g) of mice. For (B-H), frequencies (%) were determined by flow cytometry-based analysis.  $n=1$  (B), and  $n= 2-6$  for (C-I). Data are presented as mean and error bars as standard error of mean. Statistical significance was determined by ordinary one-way ANOVA using Tukey's multiple comparison test for (C and F), and by a two-tailed student's *t*-test for (D-E and G-I). Only statistically significant differences are shown (\*  $p \leq 0.05$ ; \*\*  $p \leq 0.01$ ; \*\*\*  $p \leq 0.001$ ; \*\*\*\*  $p \leq 0.0001$ ).

### 3.3.3 CML-ISG reporter mice in a total BM transplantation setting

#### 3.3.3.1 MSCV-IRES-mCherry empty vector control does not induce a phenotype in mice

Having optimized and validated the curtail stages of the mouse model generation process, I proceeded to create control CML-ISG mice utilizing the total transformed BM transplantation method as per established protocols (R. El Eit et al., 2019; R. M. El Eit et al., 2014; Pear et al., 1998) (Fig. 14A). These mice were not expected to develop leukemia, and the inclusion of 5-FU in this experimental design was intended to enhance transduction efficiency (Fig. 13B), thereby promoting higher chimerism levels. However, under these conditions, rescue BM was essential to ensure the survival of recipients during the critical initial 4-week post-transplantation period.

Evaluation of PB samples demonstrated consistently high and comparable chimerism levels at both D40 and D70, averaging at 72.2 and 74.2 respectively (Fig. 14B). No statistically significant differences were observed between mCherry<sup>+</sup> eGFP<sup>low</sup> or eGFP<sup>high</sup> donor cells (CD45.2<sup>+</sup>) at both time points (Fig. 14C). Importantly, there was no significant difference in the ratio of mCherry<sup>+</sup> eGFP<sup>low</sup> and eGFP<sup>high</sup> neutrophils (Fig. 14D) or mCherry<sup>+</sup> eGFP<sup>low</sup> and eGFP<sup>high</sup> macrophages (Fig. 14E). Throughout the entire experiment, the mice remained in good health, displaying no signs of leukemia burden until the study's conclusion at D300. Macroscopic examination of the mice further reaffirmed these findings, revealing normal spleen masses comparable to those of age-matched WT mice (Fig. 14F). Furthermore, a comprehensive assessment of both the BM and spleen indicated the presence mCherry<sup>+</sup> LS<sup>-</sup> Ks (Fig. 14G), with no significant differences evident in the frequencies of eGFP<sup>low</sup> or eGFP<sup>high</sup> LS<sup>-</sup> K populations (Fig. 14H).

Collectively, this control experiment confirmed that development of a leukemic phenotype is primarily driven by the introduction of the *BCR::ABL-1* oncogene itself, rather than being influenced by technical factors. Moreover, it shed light on the distribution patterns of various donor subpopulations in a non-leukemic experimental context following total transformed BM transplantation. These findings are essential to understand and interpret subsequent experiments employing of BCR::ABL1 viral preparations to induce leukemia.

## Results

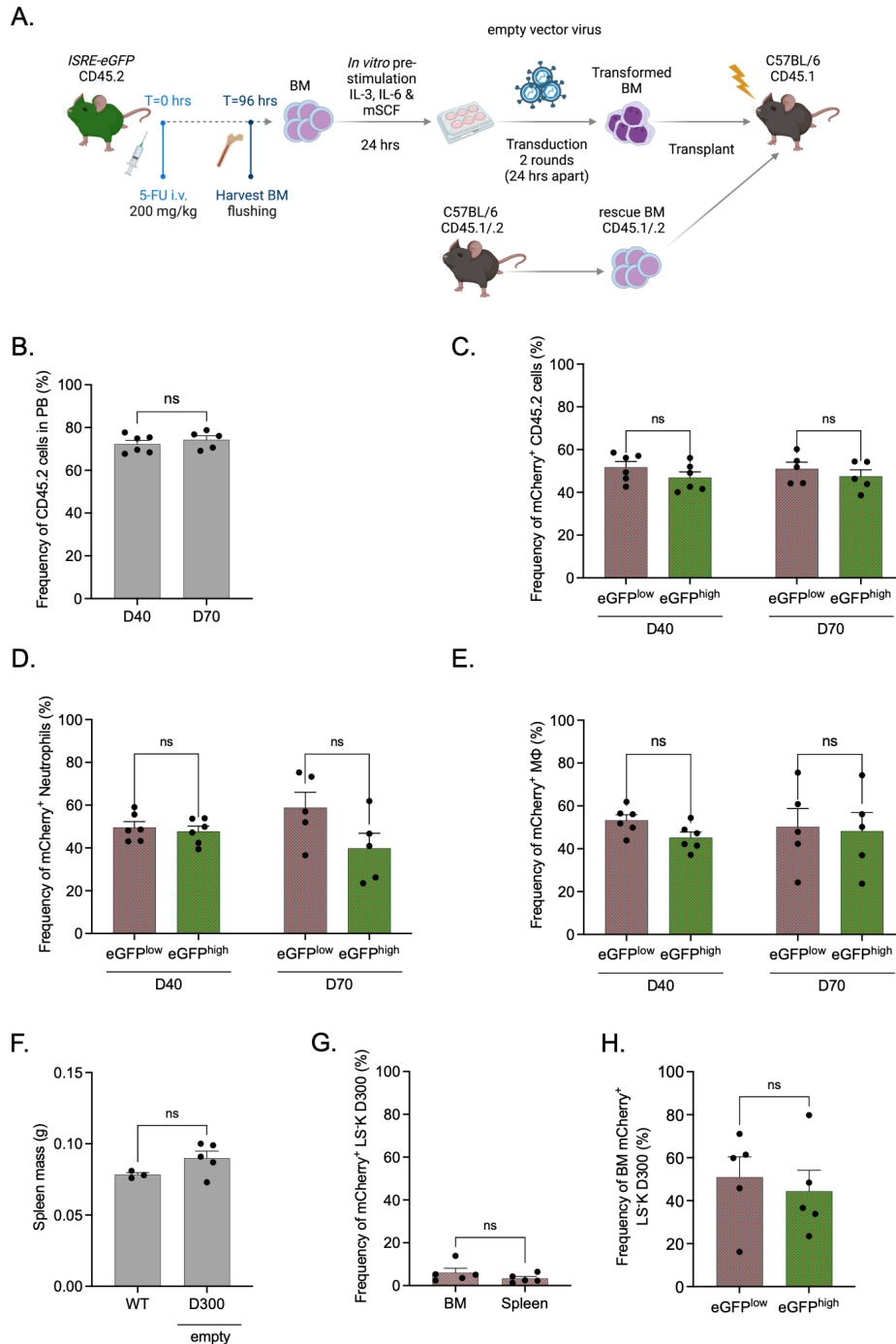


**Figure 14 | Mice transplanted with BM transduced with control MSCV-IRES-mCherry exhibit a normal phenotype *in vivo*.**

(A) Schematic representation of experimental design: BM from 11 5-FU treated (200 mg/kg, i.v. for 96 hours) CD45.2 ISRE-eGFP was pooled for *in vitro* pre-stimulation (24 hours) and transduction (twice, 24 hours apart) with MSCV-IRES-mCherry (empty vector) control virus at MOI 0.3. Subsequently,  $2.5 \times 10^5$  transformed cells were transplanted along with  $3 \times 10^5$  CD45.1/2 rescue BM cells into 6 lethally irradiated ( $2 \times 500$  Rad) CD45.1 C57BL/6 recipients. Created with BioRender.com. (B) Frequency (%) of CD45.2 cells in the PB of recipient mice at indicated timepoints. (C-E) Frequency (%) of mCherry<sup>+</sup> eGFP<sup>low</sup> or eGFP<sup>high</sup>: total CD45.2 cells (C), neutrophils (B220<sup>-</sup> CD4/8<sup>-</sup> CD11b<sup>+</sup> Ly6G<sup>+</sup>) (D), and macrophages (MΦ) (B220<sup>-</sup> CD4/8<sup>-</sup> CD11b<sup>+</sup> Ly6G<sup>-</sup> Siglec-F<sup>+</sup> F4/80<sup>+</sup>) (E) in the PB of recipient mice at indicated days. (F) Spleen mass (g) of mice at indicated experimental conditions and timepoints. (G) Frequency (%) of mCherry<sup>+</sup> LS-Ks (Lin<sup>-</sup> Sca-1<sup>-</sup> cKit<sup>+</sup>) at indicated organs and timepoint. (H) Frequency (%) of BM mCherry<sup>+</sup> eGFP<sup>low</sup> or eGFP<sup>high</sup> LS-Ks at indicated timepoint. For (B-E and G-H), frequencies (%) were determined by flow cytometry-based analysis.  $n=6$  for (B-E),  $n=3-5$  for (F), and  $n=5$  for (G-H). Data are presented as mean and error bars as standard error of mean. Statistical significance was determined by a two-tailed student's *t*-test for (B, F-H), and by two-way ANOVA using Tukey's multiple comparison test for (C-E) (ns, not significant).

### 3.3.3.2 Leukemic ISG-CML mice

#### 3.3.3.2.1 Untreated leukemic ISG-CML mice exhibit clonal expansion advantage of eGFP<sup>low</sup> leukemic cells in a total BM transplantation setting

For the generation of leukemic CML-ISG mice, I employed the total BM transplantation approach, similar to the experimental setup used for control mice (section 3.3.3.1). I started PB sampling at day D6 post-transplantation. On D9, I randomized the mice into two groups: one receiving no treatment (N=6) and the other receiving nilotinib treatment (N=12) (details on the nilotinib treatment group are discussed in section 3.3.3.2.3). At D14, untreated mice were sacrificed for analysis, and I performed secondary (2<sup>ry</sup>) transplantation of 5x10<sup>6</sup> splenocytes into sub-lethally irradiated (600 Rad) 2<sup>ry</sup> recipients (N=8), following the previously established protocol (R. El Eit et al., 2019; R. M. El Eit et al., 2014). I collected PB samples from 2<sup>ry</sup> mice at D55, and the experiment was concluded at D103 post-2<sup>ry</sup> transplantation (Fig. 15A). Notably, I excluded the use of 5-FU treatment to minimize the impact of extrinsic inflammatory factors on the eGFP<sup>low</sup> and eGFP<sup>high</sup> HSC responses, as such factors could potentially obscure results. Additionally, rescue BM was unnecessary and therefore omitted in this context, given that the transformed transplant material exhibit leukemic characteristics and had previously been demonstrated to efficiently re-establish the hematopoietic system without the need for rescue BM (R. El Eit et al., 2019; R. M. El Eit et al., 2014; Pear et al., 1998).

Leukemia engraftment was initially detected starting at D6, characterized by the presence of more than 1% mCherry<sup>+</sup> cells in the PB of all primary recipients. The levels of mCherry<sup>+</sup> cells in PB continued to rise rapidly, reaching an average of 32.28% by D14 (Fig. 15B), which was the endpoint for these mice. Intriguingly, a closer examination of PB samples at D14 unveiled a distinct and significant ( $p=0.0004$ ) clonal expansion advantage within eGFP<sup>low</sup> donor leukemic cells (Fig. 15C), despite the transplant material having fewer mCherry<sup>+</sup> eGFP<sup>low</sup> HSCs cells compared to mCherry<sup>+</sup> eGFP<sup>high</sup> HSCs cells (ratio of approximately 40/60, respectively) (Fig. 12D). Further analysis of neutrophils corroborated these findings, demonstrating substantial increase ( $p < 0.0001$ ) in leukemic mCherry<sup>+</sup> eGFP<sup>low</sup> neutrophils compared to mCherry<sup>+</sup> eGFP<sup>high</sup> neutrophils (Fig. 15D). Notably, this clonal expansion appeared to be specific to classic murine CML models, as it was observed primarily in neutrophils, the major affected population in murine CML (Hu, 2016; Scholar, 2007). Macrophages, another major myeloid population, exhibited comparable expansion levels between mCherry<sup>+</sup> eGFP<sup>low</sup> or eGFP<sup>high</sup> cells (Fig. 15E). Moreover, there were very few mCherry<sup>+</sup> lymphoid cells in these mice (data not shown). This is in line with the classic murine

## Results

CML models, in which neutrophils have been shown to be the major affected population (R. El Eit et al., 2019; R. M. El Eit et al., 2014; Hu, 2016)

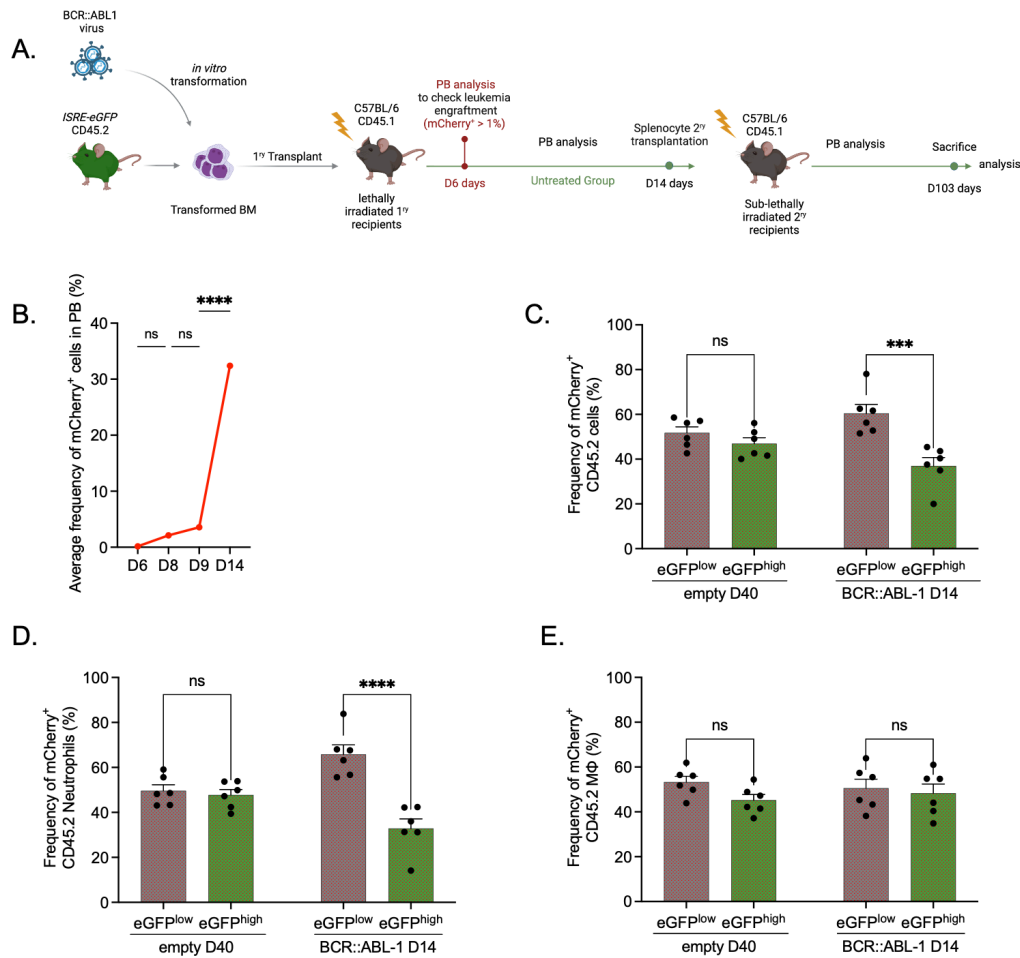


**Figure 15 | Clonal expansion advantage of eGFP<sup>low</sup> neutrophils in PB of leukemic mice.**

(A) Schematic representation of experimental design: BM from 36 *ISRE-eGFP* mice was pooled for *in vitro* pre-stimulation (24 hours) and transduction (twice, 24 hours apart) with MSCV-BCR::ABL1-IRES-mCherry virus (CML inducing) at MOI 0.3. Subsequently,  $2.5 \times 10^5$  transformed cells were then transplanted into 18 lethally irradiated ( $2 \times 500$  Rad) CD45.1 C57BL/6 recipients. PB was sampled starting at day 6 (D6). At D14, 6 mice were sacrificed for analysis and the  $2^{ry}$  transplantation of  $5 \times 10^6$  splenocytes into 8 sub-lethally irradiated (600 Rad)  $2^{ry}$  recipients. PB was sampled from  $2^{ry}$  recipients that were then sacrificed at D103 post  $2^{ry}$  transplantation for analysis. Created with BioRender.com. (B) Average frequency (%) of mCherry<sup>+</sup> CD45.2 cells in PB at indicated time points post-transplantation. (C-E) Frequency (%) of CD45.2 mCherry<sup>+</sup> eGFP<sup>low</sup> or eGFP<sup>high</sup>: total CD45.2<sup>+</sup> cells (C), neutrophils (B220<sup>-</sup> CD4/8<sup>-</sup> CD11b<sup>+</sup> Ly6G<sup>+</sup>) (D), and macrophages (MΦ) (B220<sup>-</sup> CD4/8<sup>-</sup> CD11b<sup>+</sup> Ly6G<sup>-</sup> Siglec-F<sup>-</sup> F4/80<sup>+</sup>) (E) in PB at indicated days and experimental conditions. For (B-E), frequencies (%) were determined by flow cytometry-based analysis.  $n=6-8$  for (B),  $n=6$  for (C-E). Data are presented as mean and error bars as standard error of mean. Statistical significance was determined by ordinary one-way ANOVA using Tukey's multiple comparison test for (B), and by two-way ANOVA using Tukey's multiple comparison test for (C-E) (ns, not significant; \*\*\*  $p \leq 0.001$ ; \*\*\*\*  $p \leq 0.0001$ ).

Macroscopic examination of primary leukemic mice revealed the characteristic splenomegaly associated with CML (Fig. 16A). When assessing the frequency of leukemic HSPCs in the BM and spleen, I observed an equal distribution of mCherry<sup>+</sup> HSCs and LS<sup>-</sup>Ks, indicating a balanced distribution of leukemic progenitors in both lymphoid organs (Fig. 16B). Importantly, the clonal expansion advantage of eGFP<sup>low</sup> leukemic clones was prominently

## Results

evident within the HSPCs; mCherry<sup>+</sup> eGFP<sup>low</sup> HSCs were 4.4 times ( $p= 0.0003$ ) more abundant in the BM and 8.8 times ( $p < 0.0001$ ) more abundant in the spleen compared to mCherry<sup>+</sup> eGFP<sup>high</sup> HSCs (Fig. 16C). Interestingly, cell cycle analysis of these populations revealed significantly higher cycling activity in mCherry<sup>+</sup> eGFP<sup>high</sup> HSCs in both the BM and spleen (Fig. 16D). A similar pattern was also observed in LS-Ks with a significant clonal expansion advantage of the mCherry<sup>+</sup> eGFP<sup>low</sup> LS-K in both the BM ( $p= 0.042$ ) and spleen ( $p= 0.0028$ ) (Fig. 16E), and higher cycling activity of mCherry<sup>+</sup> eGFP<sup>high</sup> LS-K in both organs (Fig. 16F). As expected LS-Ks exhibited higher cycling activity compared to HSCs in both the spleen and BM, and the cycling activity of was more pronounced in the spleen as compared to the BM (Y. Morita et al., 2011).

This observed higher cycling rate in eGFP<sup>high</sup> HSPCs, coupled with their elevated intrinsic inflammatory signature and heightened response to extrinsic inflammatory cues, could lead to their rapid exhaustion and depletion (Bogeska et al., 2022; Caiado et al., 2021; Demerdash, Kain, Essers, & King, 2021; Ho & Takizawa, 2022). This would provide a plausible explanation for the clear expansion advantages observed within the mCherry<sup>+</sup> eGFP<sup>low</sup> clones in PB.

## Results

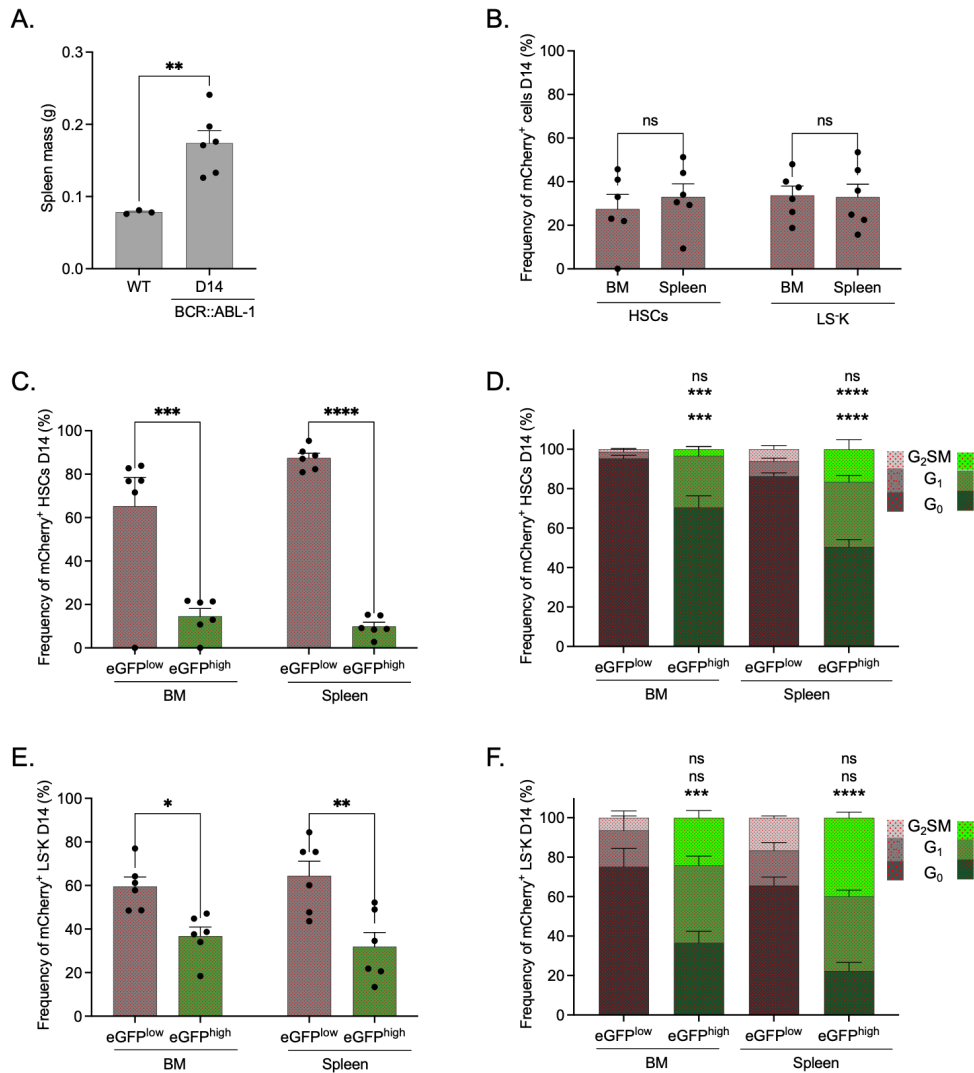


**Figure 16 | Leukemic eGFP<sup>low</sup> HSCs show increased chimerism and quiescence.**

(A) Spleen mass (g) of mice at indicated experimental conditions and timepoint. (B) Frequency (%) of mCherry<sup>+</sup> HSCs (Lin<sup>-</sup> Sca-1<sup>+</sup> cKit<sup>+</sup> CD150<sup>+</sup> CD48<sup>-</sup>) LS-Ks (Lin<sup>-</sup> Sca-1<sup>-</sup> cKit<sup>+</sup>) at indicated organs and timepoint. (C) Frequency (%) of mCherry<sup>+</sup> eGFP<sup>low</sup> or eGFP<sup>high</sup> HSCs at indicated organs and timepoint. (D) Cell cycle analysis using Ki-67 and DAPI to detect the frequency (%) of mCherry<sup>+</sup> eGFP<sup>low</sup> or eGFP<sup>high</sup> HSCs in G<sub>0</sub> (Ki-67<sup>neg</sup> DAPI<sup>low</sup>), G<sub>1</sub> (Ki-67<sup>high</sup> DAPI<sup>low</sup>) and G<sub>2</sub>SM (Ki-67<sup>high</sup> DAPI<sup>high</sup>) in indicated organs and timepoint. (E) Frequency (%) of mCherry<sup>+</sup> eGFP<sup>low</sup> or eGFP<sup>high</sup> LS-K at indicated organs and timepoint. (F) Cell cycle analysis using Ki-67 and DAPI to detect the frequency (%) of mCherry<sup>+</sup> eGFP<sup>low</sup> or eGFP<sup>high</sup> LS-Ks in G<sub>0</sub>, G<sub>1</sub> and G<sub>2</sub>SM in indicated organs and timepoint. For (B-F), frequencies (%) were determined by flow cytometry-based analysis. n=3-6 for (A), and n=6 for (B-F). Data are presented as mean and error bars as standard error of mean. Statistical significance was determined by a two-tailed student's *t*-test for (A), and by two-way ANOVA using Tukey's multiple comparison test for (B-F) (ns, not significant; \* *p* ≤ 0.05; \*\* *p* ≤ 0.01; \*\*\* *p* ≤ 0.001; \*\*\*\* *p* ≤ 0.0001).

### 3.3.3.2.2 Secondary ISG-CML mice exhibit clonal expansion advantage of eGFP<sup>low</sup> leukemic cells

To evaluate the self-renewal potential of eGFP<sup>low</sup> and eGFP<sup>high</sup> LSCs (mCherry<sup>+</sup> HSCs), I performed secondary transplantation using splenocytes from leukemic ISG-CML mice, following a well-established protocol (R. El Eit et al., 2019; R. M. El Eit et al., 2014). Analysis of PB samples from 2<sup>ry</sup> mice revealed low levels of mCherry<sup>+</sup> cells at both D55 and

## Results

D103 post-transplantation (Fig. 17A). Therefore, further analysis of subpopulations was not possible due to the limited number of cells. Upon macroscopic examination of the spleens, a wide spectrum of splenomegaly was observed, ranging from severely enlarged spleens to sizes comparable to age-matched WT mice (Fig. 17B).

Consistent with my observation in donor primary leukemic mice, a distinct and significant ( $p < 0.0001$ ) clonal expansion was evident within mCherry<sup>+</sup> eGFP<sup>low</sup> HSCs compared to mCherry<sup>+</sup> eGFP<sup>high</sup> HSCs in the BM of 2<sup>ry</sup> mice (Fig. 12C). Additionally, the cycling pattern of the HSC subpopulations in these 2<sup>ry</sup> mice closely mirrored that of the primary mice, with much higher cycling observed in mCherry<sup>+</sup> eGFP<sup>high</sup> HSCs compared to mCherry<sup>+</sup> eGFP<sup>low</sup> HSCs (Fig. 17D). A similar analysis in the spleen was not possible due to the limited number of mCherry<sup>+</sup> HSCs (data not shown). mCherry<sup>+</sup> eGFP<sup>low</sup> LS-Ks also showed a clear clonal expansion advantage in the BM ( $p < 0.0001$ ) (Fig. 17E). However, this advantage was not as pronounced in the spleen, likely due to the variability in splenomegaly (Fig. 17B&E). Cell cycle analysis indicated an increase in cycling activity of mCherry<sup>+</sup> eGFP<sup>low</sup> LS-K subpopulation, surpassing that of the mCherry<sup>+</sup> eGFP<sup>high</sup> LS-K subpopulation, with a higher frequency of cells in the G<sub>2</sub>SM phase of the cell cycle observed in both the BM and spleen ( $p = 0.3282$  and  $p = 0.0376$ , respectively) (Fig. 17F).

As expected, mCherry<sup>+</sup> common myeloid progenitors (CMPs), which are known to accumulate in CML (Bruns et al., 2009; Bühner et al., 2022), were significantly enriched in the spleen as compared to the BM (Bühner et al., 2022) ( $p < 0.0001$ ) (Fig. 17G). These CMPs also exhibited a clonal expansion advantage of mCherry<sup>+</sup> eGFP<sup>low</sup> clone in both the BM and spleen ( $p < 0.0001$  for both) (Fig. 17H). Importantly, cell cycle analysis of CMPs indicated that mCherry<sup>+</sup> eGFP<sup>low</sup> CMPs were cycling more than mCherry<sup>+</sup> eGFP<sup>high</sup> CMPs, with a higher frequency of cells in the G<sub>2</sub>SM phase in both the BM and spleen ( $p = 0.008$  and  $p = 0.9$ , respectively) (Fig. 17I). Given that clonal expansion in CML is believed to initiate at the CMP stage (Miyawaki et al., 2013), these findings provide valuable insights into the dominance of the leukemic eGFP<sup>low</sup> clone observed in the peripheral blood.

Data from both primary and 2<sup>ry</sup> leukemic ISG-CML mice collectively suggest that introducing *BCR::ABL1* into HSCs with low basal intrinsic IFN signaling may enhance leukemic potency, leading to the development of a more aggressive leukemia with faster progression.

## Results

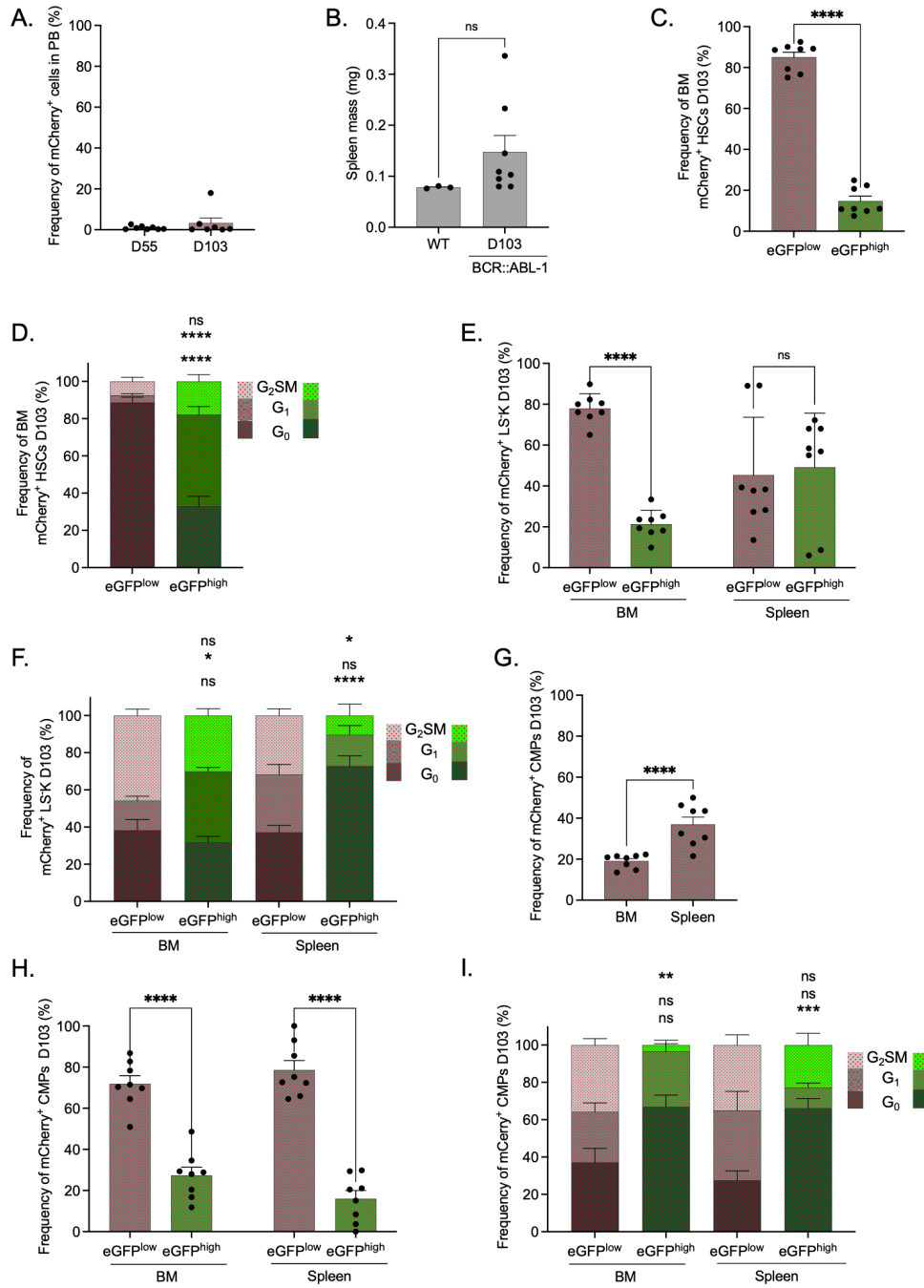


**Figure 17 | Clonal expansion advantage of eGFP<sup>low</sup> leukemic cells in 2<sup>ry</sup> ISG-CML mice.**

(A) Frequency (%) of total mCherry<sup>+</sup> cells in PB at indicated timepoints. (B) Spleen mass (g) of mice at indicated experimental conditions and timepoint. (C) Frequency (%) of BM mCherry<sup>+</sup> eGFP<sup>low</sup> or eGFP<sup>high</sup> HSC (Lin<sup>-</sup> Sca-1<sup>+</sup> cKit<sup>+</sup> CD150<sup>+</sup> CD48<sup>-</sup>) at indicated timepoint. (D) Cell cycle analysis using Ki-67 and DAPI to detect the frequency (%) of BM mCherry<sup>+</sup> eGFP<sup>low</sup> or eGFP<sup>high</sup> HSCs in G<sub>0</sub> (Ki-67<sup>neg</sup> DAPI<sup>low</sup>), G<sub>1</sub> (Ki-67<sup>high</sup> DAPI<sup>low</sup>) and G<sub>2</sub>SM (Ki-67<sup>high</sup> DAPI<sup>high</sup>) at indicated timepoint. (E) Frequency (%) of mCherry<sup>+</sup> eGFP<sup>low</sup> or eGFP<sup>high</sup> LS-K (Lin<sup>-</sup> Sca-1<sup>-</sup> cKit<sup>+</sup>) at indicated organs and timepoint. (F) Cell cycle analysis to detect the frequency (%) of mCherry<sup>+</sup> eGFP<sup>low</sup> or eGFP<sup>high</sup> LS-Ks in G<sub>0</sub>, G<sub>1</sub> and G<sub>2</sub>SM in indicated organs and timepoints. (G) Frequency (%) of mCherry<sup>+</sup> CMPs (Lin<sup>-</sup> Sca-1<sup>-</sup> cKit<sup>+</sup> CD16/32<sup>low</sup> CD34<sup>+</sup>) at indicated organs and timepoint. (H) Frequency (%) of mCherry<sup>+</sup> eGFP<sup>low</sup> or eGFP<sup>high</sup> CMPs at indicated organs and timepoints. (I) Cell cycle analysis to detect the frequency (%) of mCherry<sup>+</sup> eGFP<sup>low</sup> or eGFP<sup>high</sup> CMPs in G<sub>0</sub>, G<sub>1</sub> and G<sub>2</sub>SM in indicated organs and timepoints. For (A and C-I), frequencies (%) were determined by flow cytometry-based analysis. n=8 for (A, C-I), and n=3-8 for (B). Data are presented as mean and error bars as standard error of mean. Statistical significance was determined by a two-tailed student's *t*-test for (B-C and G), and by two-way ANOVA using Tukey's multiple comparison test for (D-F and H-I) (ns, not significant; \*  $p \leq 0.05$ ; \*\*  $p \leq 0.01$ ; \*\*\*  $p \leq 0.001$ ; \*\*\*\*  $p \leq 0.0001$ ).

### 3.3.3.2.3 Nilotinib successfully controlled leukemia progression

The standard treatment for CML involves tyrosine kinase inhibitors (TKIs) like nilotinib. Despite its remarkable efficacy, TKI therapy is frequently associated with treatment resistance and relapse upon discontinuation (R. El Eit et al., 2019; Wintrobe & Greer, 2014). This resistance may stem from the persistence of LSCs during TKI treatment (R. El Eit et al., 2019). To assess how eGFP<sup>low</sup> and eGFP<sup>high</sup> leukemic cells respond to frontline TKI therapy, I administered a daily dose of 75 mg/kg nilotinib to primary ISG-CML mice (N=12), starting at day 9 post-transplantation when approximately 5% of PB cells were mCherry<sup>+</sup>. This treatment continued for a duration of 21 days (N21), at which point I sacrificed 6 mice for detailed analysis. Additionally, I transplanted 5x10<sup>6</sup> splenocytes into WT recipients (N=8 mice), while the remaining 6 mice were left untreated to observe potential relapse (Fig. 18A).

Notably, the administration of nilotinib successfully maintained low levels of mCherry<sup>+</sup> cells in the PB throughout the treatment period. Specifically, at N11 and N21, PB samples exhibited an average of only 12% mCherry<sup>+</sup> PB cells, in contrast to untreated mice at D14, which displayed an average of 32.28% ( $p=0.003$ ) mCherry<sup>+</sup> PB cells (Fig. 18B). Furthermore, most mice exhibited sustainably reduced levels of mCherry<sup>+</sup> neutrophils, confirming the effectiveness and specificity of the treatment (Fig. 18C).

However, due to the limited number of cells available, analysis of the mCherry<sup>+</sup> eGFP<sup>low</sup> and eGFP<sup>high</sup> neutrophils was only feasible in 2 mice at N11 and 4 mice at N21 (indicated by colored points on the graphs Fig. 18C-E). In these mice, which could also be considered resistant to treatment, frequency analysis revealed a significant clonal expansion advantage of eGFP<sup>low</sup> cells at N21 ( $p=0.0059$ ) (Fig. 18D). I also investigated mCherry<sup>+</sup> eGFP<sup>low</sup> and eGFP<sup>high</sup> macrophages in the same mice, which indicated similar clonal expansion advantage, however this finding did not reach statistical significance (Fig. 18E).

In sacrificed animals, nilotinib treatment effectively minimized splenomegaly (Fig. 18F). Due to the limited number of mCherry<sup>+</sup> cells in the BM samples, I was only able to analyze the frequency distribution of eGFP<sup>low</sup> and eGFP<sup>high</sup> subpopulations, as well as their cycling activity, in LS-Ks. While there was a slight increase in mCherry<sup>+</sup> eGFP<sup>low</sup> LS-K compared to mCherry<sup>+</sup> eGFP<sup>high</sup> LS-K cells, this difference didn't reach statistical significance (Fig. 18G). Furthermore, no substantial differences were observed in the cycling behavior of both LS-K subpopulations (Fig.18H).

## Results

This data suggests that nilotinib treatment successfully controlled leukemia progression, minimizing the presence of both differentiated and immature mCherry<sup>+</sup> cells. In cases where mCherry<sup>+</sup> cell populations were sufficient for the analysis of eGFP<sup>low</sup> and eGFP<sup>high</sup> clonal expansion and distribution, a residual clonal expansion advantage of the eGFP<sup>low</sup> subpopulation was noted. This observation may imply that resistance to frontline CML treatment could potentially be associated with a disease originating from eGFP<sup>low</sup> LCSs. It is crucial to emphasize that increasing the cohort of mice is imperative to augment the data points and comprehensively validate these findings.

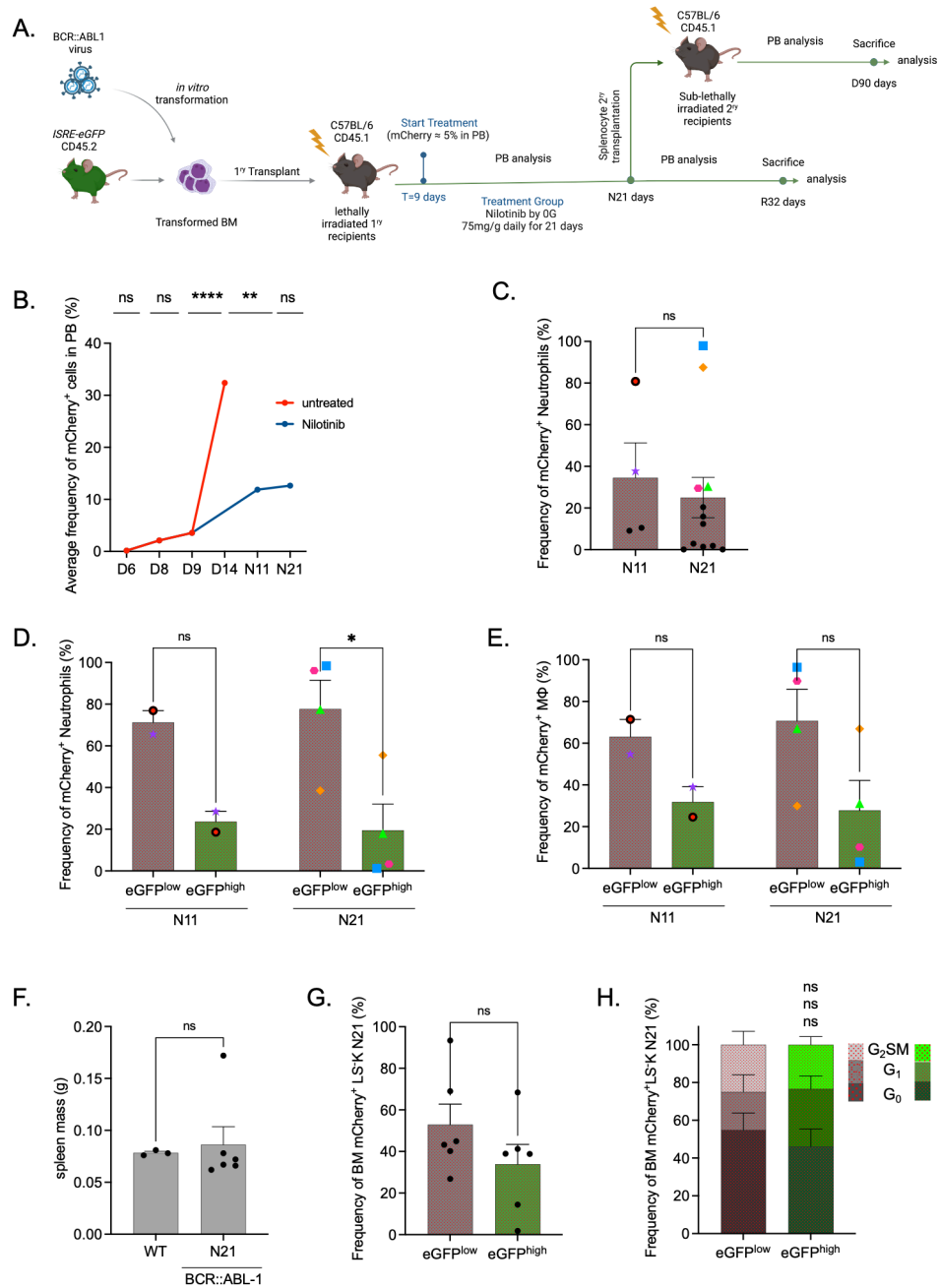


**Figure 18 | Effective leukemia progression control with frontline nilotinib TKI therapy.**

(A) Schematic representation of experimental design: BM from 36 *ISRE-eGFP* mice was pooled for *in vitro* pre-stimulation (24 hours) and transduction (twice, 24 hours apart) with MSCV-BCR::ABL1-IRES-mCherry virus (CML inducing) at MOI 0.3. Transformed cells ( $2.5 \times 10^5$ ) were transplanted into 18 lethally irradiated ( $2 \times 500$  Rad) CD45.1

## Results

C57BL/6 recipients. PB sampling started at day 6 (D6), and at D9, when mCherry<sup>+</sup> cells reached approximately 5%, 12 mice received daily oral nilotinib (75 mg/kg) for 21 days (N21). At N21, 6 mice were sacrificed for analysis, and 5 x 10<sup>6</sup> splenocytes were transplanted into 8 sub-lethally (600 Rad) irradiated secondary recipients. PB sampling from secondary recipients continued until sacrifice at D90 post-transplantation. The remaining 6 primary mice monitored for relapse and sacrificed at day 32 (R32). Created with BioRender.com (B) Average frequency (%) of mCherry<sup>+</sup> CD45.2 cells in the PB blood of 1<sup>ry</sup> recipients at indicated time points and experimental conditions. (C) Frequency (%) of mCherry<sup>+</sup> neutrophils (B220<sup>-</sup> CD4/8<sup>-</sup> CD11b<sup>+</sup> Ly6G<sup>+</sup>) in PB at indicated timepoints. Colored data points represent samples with frequency higher than 20%. (D-E) Frequency (%) of mCherry<sup>+</sup> eGFP<sup>low</sup> and eGFP<sup>high</sup>: neutrophils (D) and macrophages (MΦ) (B220<sup>-</sup> CD4/8<sup>-</sup> CD11b<sup>+</sup> Ly6G<sup>-</sup> Siglec-F<sup>-</sup> F4/80<sup>+</sup>) (E) in the PB of the 1<sup>ry</sup> nilotinib treated mice that were represented with colored data points from (C) at indicated days. (F) Spleen mass (g) of mice at indicated experimental conditions and timepoints. (G) Frequency (%) of mCherry<sup>+</sup> eGFP<sup>low</sup> or eGFP<sup>high</sup> LS-K (Lin<sup>-</sup> Sca-1<sup>-</sup> cKit<sup>+</sup>) at indicated organ and timepoints. (H) Cell cycle analysis using Ki-67 and DAPI to detect the frequency (%) of mCherry<sup>+</sup> LS-K-eGFP<sup>low</sup> or LS-K-eGFP<sup>high</sup> in G<sub>0</sub> (Ki-67<sup>neg</sup> DAPI<sup>low</sup>), G<sub>1</sub> (Ki-67<sup>high</sup> DAPI<sup>low</sup>) and G<sub>2</sub>SM (Ki-67<sup>high</sup> DAPI<sup>high</sup>) in indicated organs and timepoint. For (B-E and G-H), frequencies (%) were determined by flow cytometry-based analysis. n=4-12 biological replicates for (B-C), n=2-4 biological replicates for (D-E), n=3-6 for (F) and n=6 for (G-H). Data are presented as mean and error bars as standard error of mean. Statistical significance was determined by ordinary one-way ANOVA using Tukey's multiple comparison test for (B), and by a two-tailed student's *t*-test for (C and F-G), and by two-way ANOVA using Tukey's multiple comparison test for (D-E, and I) (ns, not significant; \*  $p \leq 0.05$ ; \*\*  $p \leq 0.01$ ; \*\*\*\*  $p \leq 0.0001$ ).

### 3.3.3.2.4 eGFP<sup>low</sup> leukemic cells expand in recipient mice derived from nilotinib-treated donors

To evaluate the impact of nilotinib treatment on the self-renewal potential of eGFP<sup>low</sup> and eGFP<sup>high</sup> LSCs (mCherry<sup>+</sup> HSCs) derived from the primary cohort, secondary mice were left untreated. PB sampling from these 2<sup>ry</sup> consistently showed low levels of chimerism, except for three mice at D39, one of which did not survive until D90 (Fig. 19A). With a limited number of mCherry<sup>+</sup> cells in the remaining secondary recipients, a comprehensive blood analysis was conducted only on those specific mice. Notably, these mice exhibited a high frequency of mCherry<sup>+</sup> cells indicating a substantial leukemia burden (Fig. 19B). I didn't observe any evident clonal expansion advantage of either mCherry<sup>+</sup> eGFP<sup>low</sup> or eGFP<sup>high</sup> cells, possibly due to advanced leukemia (Fig. 19C). Furthermore, splenomegaly associated with CML was also only present in the same two mice with high mCherry<sup>+</sup> cells (Fig. 19D).

Due to the limited number of mCherry<sup>+</sup> HSCs in the spleen, the analysis of leukemic HSCs was restricted to the BM. It revealed a slight increase in the frequency of mCherry<sup>+</sup> eGFP<sup>low</sup> HSCs compared to mCherry<sup>+</sup> eGFP<sup>high</sup> HSCs, although this difference did not reach statistical significance (Fig. 19E). In terms of cell cycle analysis, there was significantly higher cycling activity in mCherry<sup>+</sup> eGFP<sup>high</sup> HSCs, which was similar to what I observed in 2<sup>ry</sup> mice from untreated 1<sup>ry</sup> mice (Fig. 19F & Fig. 17D).

Analysis of LS-Ks showed a clear clonal expansion advantage in mCherry<sup>+</sup> eGFP<sup>low</sup> LS-Ks, particularly in the spleen but not in the BM (Fig. 19G). Cell cycle analysis showed increased cycling activity of mCherry<sup>+</sup> eGFP<sup>low</sup> LS-Ks compared to mCherry<sup>+</sup> eGFP<sup>high</sup> LS-Ks, with a higher frequency of cells in the G<sub>2</sub>SM phase, both in the BM and spleen.

## Results

Together, these results indicate that mice that were transplanted with cells from either treated or untreated primary mice develop a similar leukemic phenotype, mainly originating from the eGFP<sup>low</sup> leukemic cells. This observation suggests the potential superiority of the eGFP<sup>low</sup> LSC clones in initiating disease in a 2<sup>ry</sup> transplantation setting, possibly due to their higher quiescent state. Moreover, this increased quiescence can render eGFP<sup>low</sup> LSC clones less susceptible to frontline TKI therapy (Tanaka et al., 2022), potentially explaining the observed clonal expansion advantage in mice transplanted with cells from nilotinib-treated mice. However, a larger cohort of mice is necessary to validate these findings.

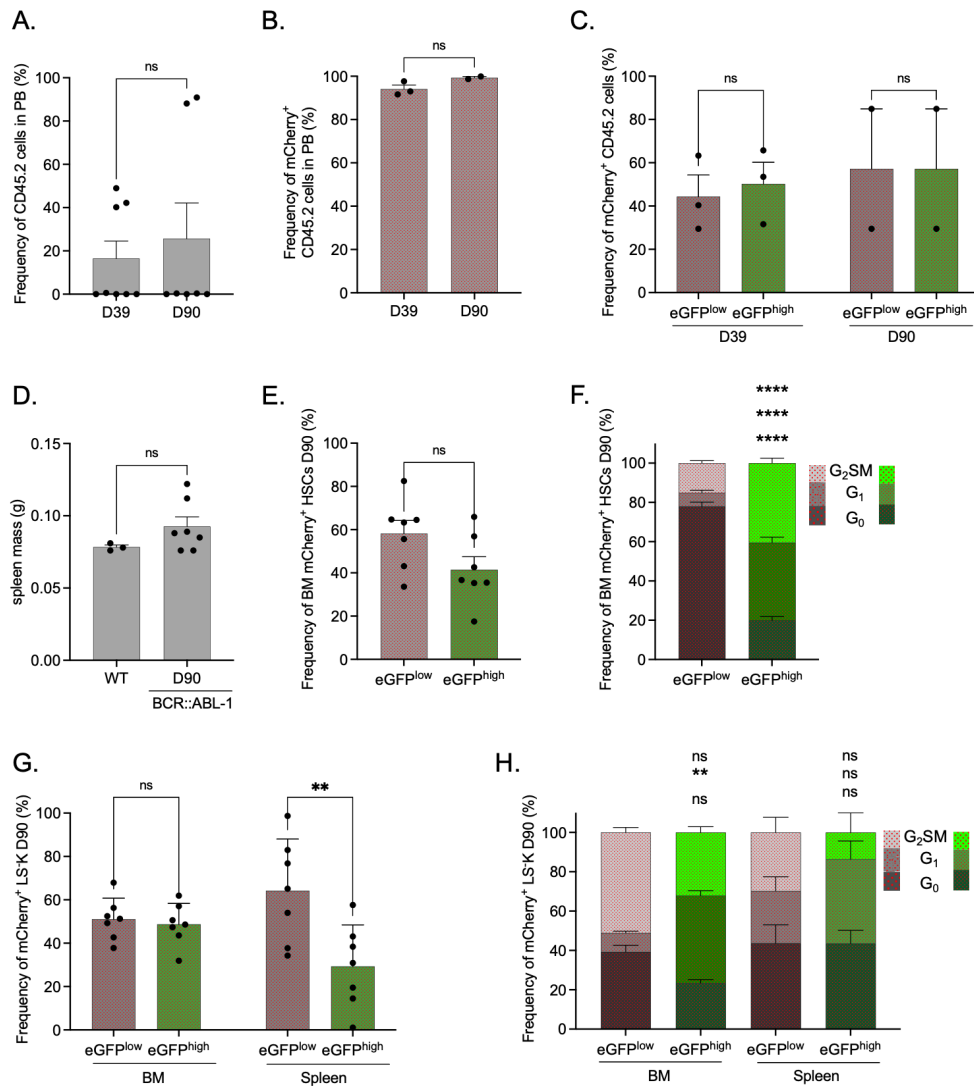


**Figure 19 | eGFP<sup>low</sup> leukemic cells expand in mice generated by 2<sup>ry</sup> transplantation from nilotinib treated mice.**

(A) Frequency (%) of CD45.2 cells in the PB at indicated timepoints. (B) Frequency (%) of mCherry<sup>+</sup> CD45.2 cells in PB at indicated time points. (C) Frequency (%) of mCherry<sup>+</sup> eGFP<sup>low</sup> or eGFP<sup>high</sup> CD45.2 cells in PB at indicated timepoints. (D) Spleen mass (g) of mice at indicated experimental conditions and timepoint. (E) Frequency (%) of mCherry<sup>+</sup> eGFP<sup>low</sup> or eGFP<sup>high</sup> HSC (Lin<sup>-</sup> Sca-1<sup>+</sup> cKit<sup>+</sup> CD150<sup>+</sup> CD48<sup>-</sup> eGFP<sup>low</sup>/or eGFP<sup>high</sup>) at indicated organ and timepoint. (F) Cell cycle analysis using Ki-67 and DAPI to detect the frequency (%) of mCherry<sup>+</sup> eGFP<sup>low</sup> or eGFP<sup>high</sup> HSCs in G<sub>0</sub> (Ki-67<sup>neg</sup> DAPI<sup>low</sup>), G<sub>1</sub> (Ki-67<sup>high</sup> DAPI<sup>low</sup>) and G<sub>2</sub>SM (Ki-67<sup>high</sup> DAPI<sup>high</sup>) in indicated organs and timepoint. (G) Frequency (%) of mCherry<sup>+</sup> eGFP<sup>low</sup> or eGFP<sup>high</sup> LS-K (Lin<sup>-</sup> Sca-1<sup>-</sup> cKit<sup>+</sup> eGFP<sup>low</sup>/ or eGFP<sup>high</sup>) at indicated organs and timepoint. (H) Cell cycle analysis to detect the frequency (%) of mCherry<sup>+</sup> eGFP<sup>low</sup> or eGFP<sup>high</sup>

## Results

LSK in G<sub>0</sub>, G<sub>1</sub>, and G<sub>2</sub>SM in indicated organs and timepoint. For (A-C and E-H), frequencies (%) were determined by flow cytometry-based analysis. n=7-8 for (A), n=2-3 for (B-C), n=3-7 for (D), and n=7 for (E-H). Data are presented as mean and error bars as standard error of mean. Statistical significance was determined by a two-tailed student's *t*-test for (A-B and D-E), and by two-way ANOVA using Tukey's multiple comparison test for (C and F-H) (ns, not significant; \*\*  $p \leq 0.01$ ; \*\*\*\*  $p \leq 0.0001$ ).

### **3.3.3.2.5. Nilotinib treated ISG-CML mice didn't show obvious signs of relapse up to 32 days post-treatment cessation.**

A small cohort of nilotinib-treated mice was kept alive and closely monitored for relapse beyond the 21-day treatment period (N21). The average frequency of mCherry<sup>+</sup> cells in the PB remained consistently low and stable for up to 10 days after the cessation of treatment (relapse day 10, R10), with an average of 10.8%. This level closely resembles what was recorded at N21 (12%). However, a noticeable increase in the average frequency was observed thereafter, reaching 17% and 22% at R25 and R32, respectively, hinting at the potential onset of relapse in these mice (Fig. 20A, left panel). Subsequently, the experiment was terminated at R32, and in-depth analysis was conducted.

Upon close examination of individual mice, only one mouse exhibited significant elevated levels of mCherry<sup>+</sup> cells (Fig. 20A, right panel, red datapoint). However, this mouse already had a relatively high percentage (21%) of total mCherry<sup>+</sup> cells in the PB at N21 (data not shown), thus suggesting that the recorded effect is more likely attributed to treatment resistance rather than relapse. Further analysis revealed relatively low levels of mCherry<sup>+</sup> neutrophils in the entire cohort except for this particular mouse (Fig. 20B). Notably, the overwhelming majority of mCherry<sup>+</sup> neutrophils in this mouse were eGFP<sup>low</sup>, which confirmed my previous findings (Fig. 20C). The same mouse also had high levels of mCherry<sup>+</sup> macrophages at R25 and R32, but not R10 (Fig. 20D), also predominantly eGFP<sup>low</sup> (Fig. 20E). Unfortunately, an analysis of immature populations in the spleen and BM was not feasible due to the limited number of mCherry<sup>+</sup> cells (data not shown).

Collectively, this data suggests that the selected time point for sacrifice may have been too early to accurately assess relapse following the discontinuation of treatment. Additionally, it raises the possibility that treatment resistance might be driven by eGFP<sup>low</sup> leukemic clones. Nevertheless, to substantiate these findings, a more extensive mouse cohort is essential with sampling at different time points.

## Results

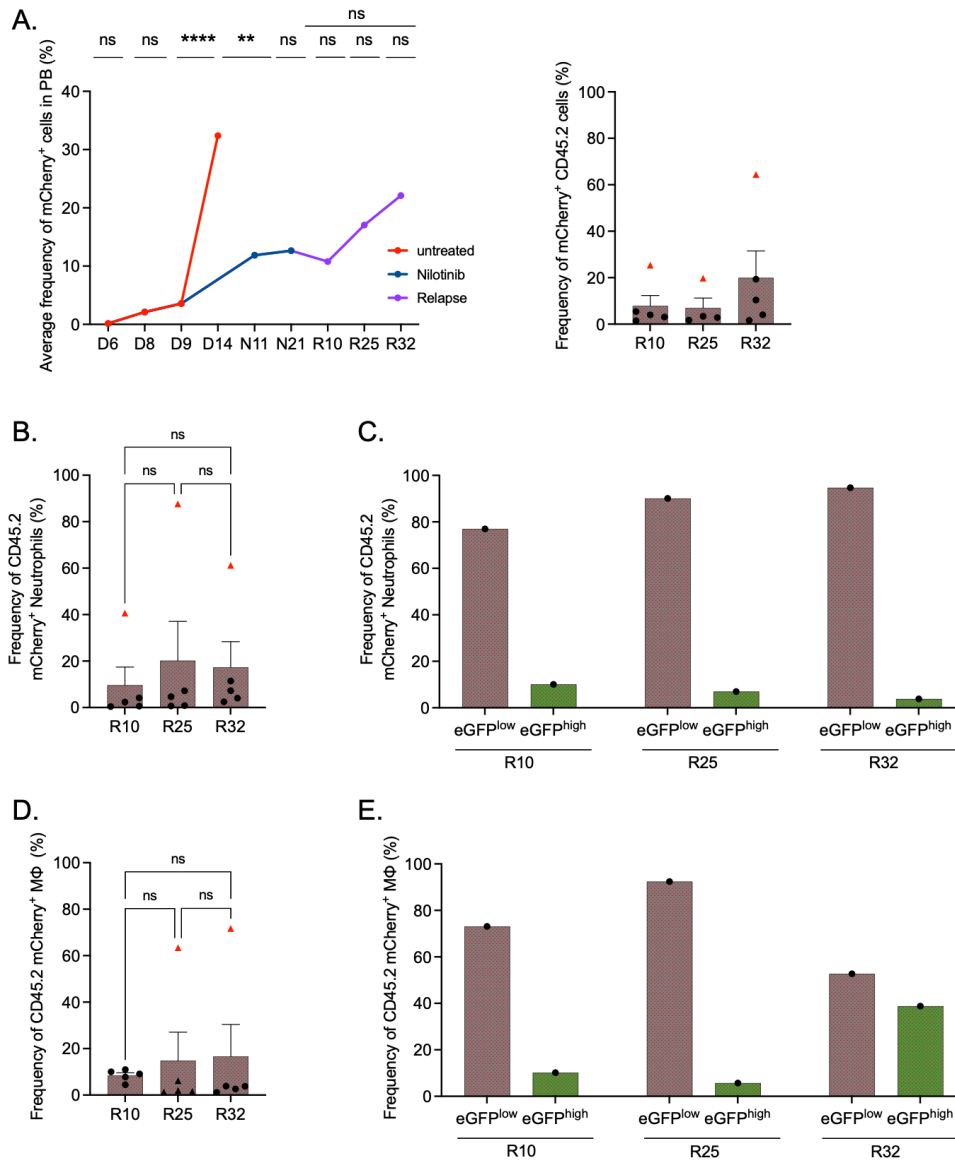


**Figure 20 | Absence of apparent relapse in nilotinib-treated ISG-CML mice up to 32 days post-treatment cessation.**

(A) Average frequency (%) of mCherry<sup>+</sup> CD45.2 cells in the PB blood of 1<sup>ry</sup> recipients at indicated time points and experimental conditions, left panel. Frequency (%) of mCherry<sup>+</sup> CD45.2 cells in the PB blood of relapse mice shown as individual data points at indicated timepoints, right panel. Colored data points represent samples with frequency higher than 20%. (B) Frequency (%) of CD45.2 mCherry<sup>+</sup> neutrophils (B220<sup>-</sup> CD4/8<sup>-</sup> CD11b<sup>+</sup> Ly6G<sup>+</sup>) in PB at indicated time points. Colored data points represent samples with frequency higher than 20%. (C) Frequency (%) of CD45.2 mCherry<sup>+</sup> eGFP<sup>low</sup> or eGFP<sup>high</sup> neutrophils at indicated timepoints. (D) Frequency (%) of CD45.2 mCherry<sup>+</sup> macrophages (MΦ) (B220<sup>-</sup> CD4/8<sup>-</sup> CD11b<sup>+</sup> Ly6G<sup>-</sup> Siglec-F<sup>-</sup> F4/80<sup>+</sup>) in PB at indicated time points. Colored data points represent samples with frequency higher than 20%. (E) Frequency (%) of CD45.2 mCherry<sup>+</sup> eGFP<sup>low</sup> or eGFP<sup>high</sup> MΦ at indicated timepoints. Frequencies (%) were determined by flow cytometry-based analysis for all panels. N=4-14 for (A), n=5 for (B and D), and n=1 for (C and E). Data are presented as mean and error bars as standard error of mean. Statistical significance was determined by ordinary one-way ANOVA using Tukey's multiple comparison test for (A-B and D) (ns, not significant; \*\*  $p \leq 0.01$ ; \*\*\*\*  $p \leq 0.0001$ ).

### 3.3.4 100% chimera CML-ISG reporter mice

#### 3.3.4.1 Expression of *BCR::ABL1* in eGFP<sup>low</sup> HSCs results in a more aggressive leukemia *in vivo*

To assess the system's response in a non-competitive setting, and to create conditions that closely resemble native CML, I established a model of 100% chimeric CML-ISG leukemic mice. Briefly, BM collected from *ISRE-eGFP* donor mice was sorted into eGFP<sup>low</sup> or eGFP<sup>high</sup> LKs (lin<sup>-</sup> cKit<sup>+</sup>) subsets. I transformed each subset separately *in vitro* and transplanted them into lethally irradiated recipients, resulting in the generation of 100% eGFP<sup>low</sup> or 100% eGFP<sup>high</sup> chimeric CML-ISG leukemic mice. I sampled PB from these mice and analyzed them at different time points, and at day 17 (D17), I sacrificed 5 mice from each group for detailed analysis. The remaining mice from each group were monitored for survival (Fig. 21A).

I analyzed transformed cells prior to transplantation. Importantly, more than 96% of HSCs in each fraction exhibited the eGFP signature of its respective subset (Fig. 21B). Furthermore, the frequency of transformed mCherry<sup>+</sup> HSCs was nearly identical (9.65% and 10.3% for eGFP<sup>low</sup> and eGFP<sup>high</sup> subsets, respectively) (Fig. 21C).

Analysis of PB in transplanted mice revealed similar frequencies of mCherry<sup>+</sup> cells in both chimeric groups at D7. However, a faster increase in the frequency of mCherry<sup>+</sup> cells in the eGFP<sup>low</sup> mice compared to the eGFP<sup>high</sup> mice was observed starting at D11. This difference continued to escalate until it reached statistical significance at D19 ( $p=0.0022$ ), which was the time point when I sacrificed 5 mice from each chimeric group for analysis (Fig. 21D). A similar trend was noted in the frequency of mCherry<sup>+</sup> neutrophils ( $p=0.0377$ ) (Fig. 21E).

## Results

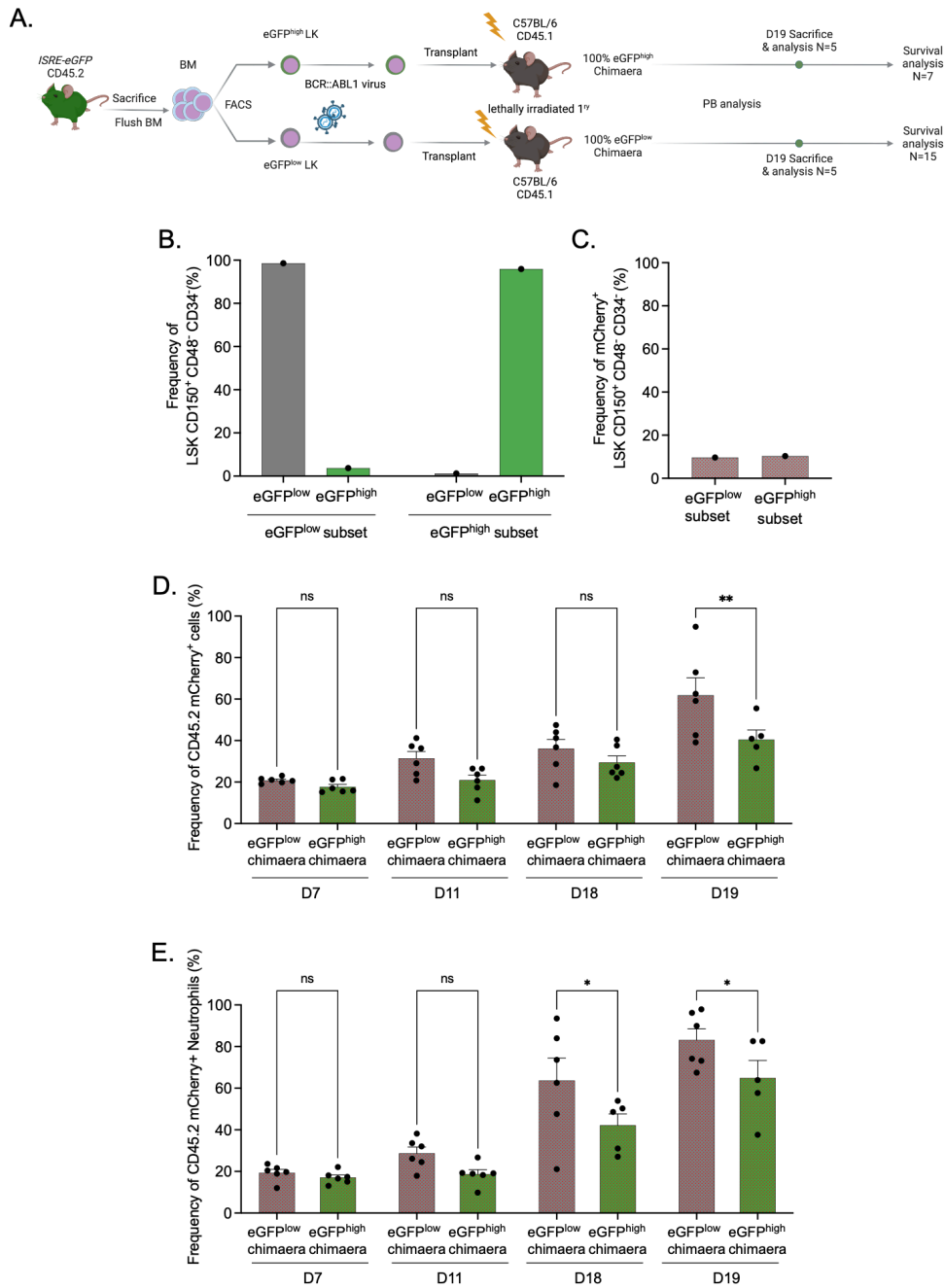


**Figure 21 | Faster rate of leukemia progression in eGFP<sup>low</sup> chimeric ISG-CML mice.**

(A) Schematic representation of experimental design: BM from 50 *ISRE-eGFP* mice was pooled and sorted for eGFP<sup>low</sup> or eGFP<sup>high</sup> LK (*lin*<sup>-</sup> *cKit*<sup>+</sup>) subsets which were transformed separately *in vitro* with MSCV-BCR::ABL1-IRES-mCherry virus (CML inducing) at MOI 0.3. Subsequently,  $2.5 \times 10^5$  transformed cells from each subset were then transplanted separately into lethally irradiated ( $2 \times 500$  Rad) CD45.1 C57BL/6 recipients generating  $n=12$  100% ISG-CML eGFP<sup>low</sup> chimaeras and  $n=20$  100% ISG-CML eGFP<sup>high</sup> chimaeras. PB from 1 <sup>$\nu$</sup>  recipients was sampled starting at day 7 (D7). At D19, 5 mice from each group were sacrificed for analysis while the remainder of the mice were followed for survival. Created with BioRender.com. (B) Frequencies (%) of eGFP<sup>low</sup> and eGFP<sup>high</sup> HSCs (*Lin*<sup>-</sup> *Sca*-1<sup>+</sup> *cKit*<sup>+</sup> *CD150*<sup>+</sup> *CD48*<sup>-</sup> *CD34*<sup>-</sup> eGFP<sup>low</sup>/ or eGFP<sup>high</sup>) after retroviral transduction with CML construct at indicated experimental conditions. (C) Frequency (%) of mCherry<sup>+</sup> HSCs in indicated experimental conditions. (D) Frequency (%) of mCherry<sup>+</sup> eGFP<sup>low</sup> or eGFP<sup>high</sup> CD45.2 cells in the PB at indicated timepoints and experimental conditions. (E) Frequency (%) of CD45.2 mCherry<sup>+</sup> eGFP<sup>low</sup> or eGFP<sup>high</sup> neutrophils (*B220*<sup>-</sup> *CD4/8*<sup>+</sup> *CD11b*<sup>+</sup> *Ly6G*<sup>+</sup> eGFP<sup>low</sup>/ or eGFP<sup>high</sup>) at indicated timepoints and experimental conditions. For (B-F), frequencies (%) were determined by flow cytometry-based analysis.  $n=1$  for (B-D), and  $n=6$  for (E-F). Data are presented as mean and error bars as standard error of mean. Statistical significance was determined by two-way ANOVA using Šidák's multiple comparison test for (E-F) (ns, not significant; \*  $p \leq 0.05$ ; \*\*  $p \leq 0.01$ ).

## Results

Interestingly, I did not observe the pronounced difference in clonal expansion between mCherry<sup>+</sup> eGFP<sup>low</sup> and eGFP<sup>high</sup> HSCs, LSKs, or CMPs in these 100% chimeric mice (Fig. 22 A, B & C, respectively), which was seen in the previous mice with the total transplantation setting. Instead, in these 100% chimeric mice, the frequency of mCherry<sup>+</sup> HPSCs was similar between both chimeric groups in the BM and spleen. Furthermore, cell cycle activity in mCherry<sup>+</sup> HSCs or CMPs was high and comparable between both groups (Fig. 22D&F). On the other hand, mCherry<sup>+</sup> LSKs showed a significant increase in the frequency of cells in the G<sub>2</sub>M phase of the cell cycle in the eGFP<sup>low</sup> chimeric group compared to the eGFP<sup>high</sup> group in the BM, but not in the spleen (Fig. 22E). These differences between transplanting eGFP<sup>low</sup> and eGFP<sup>high</sup> leukemic cells into the same recipient (competitive) or separate recipients (100% chimera) could indicate a delicate interaction between eGFP<sup>low</sup> and eGFP<sup>high</sup> leukemic cells that regulates their cycling. Separating the clones seemed to disrupt this regulation and led to increased cycling.

Despite minimal differences in HSC chimerism or cell cycle distribution at the selected timepoints, there was a striking difference in the survival of eGFP<sup>low</sup> and eGFP<sup>high</sup> chimeras (Fig. 22G). The eGFP<sup>low</sup> group exhibited a median survival of merely 21 days, compared to 41 days in the eGFP<sup>high</sup> group ( $p < 0.0001$ ). These results further support my previous findings, suggesting that *BCR::ABL1* expression in eGFP<sup>low</sup> stem cells results in a faster development of leukemia in recipient mice.

## Results

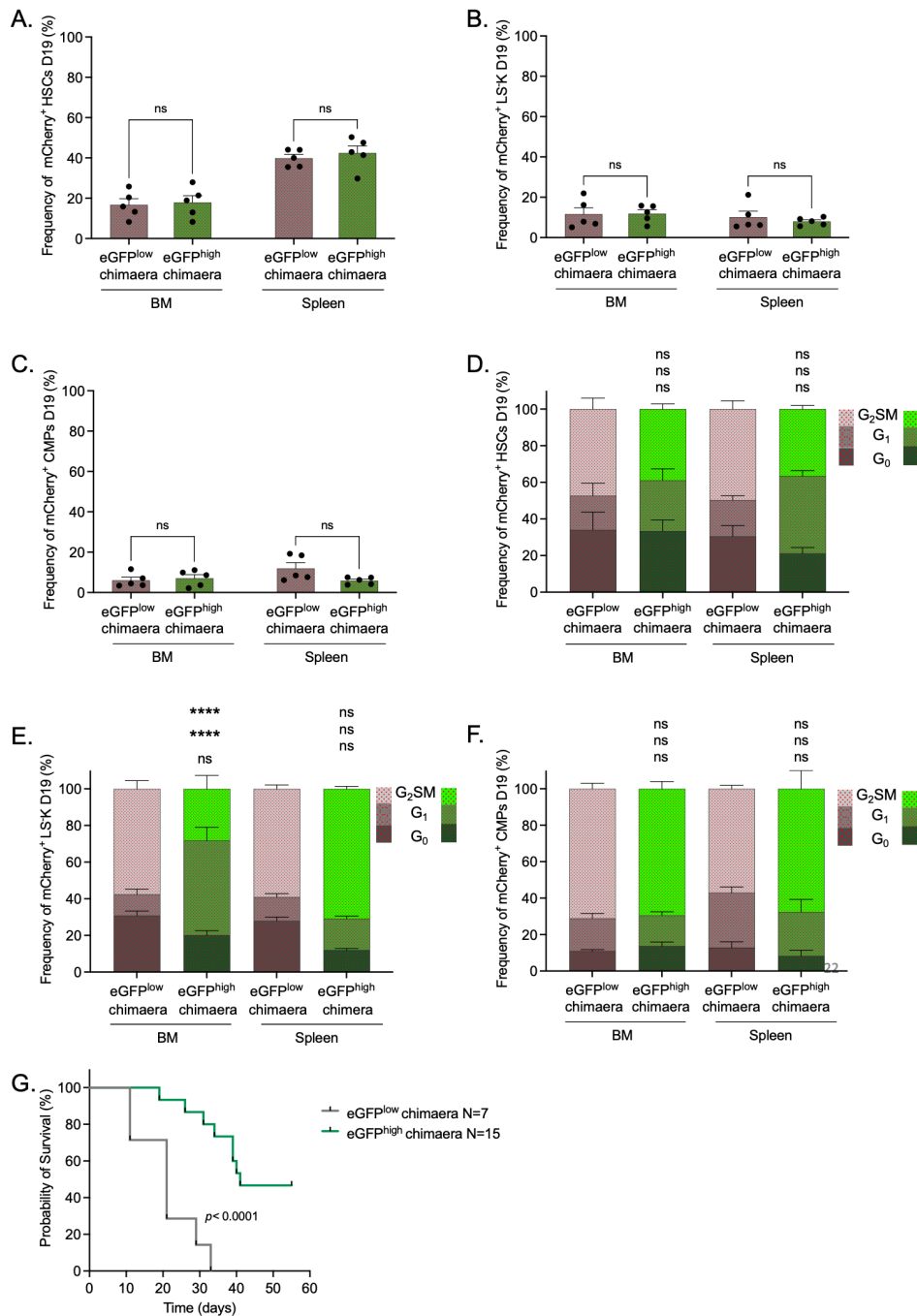


**Figure 22 | Expression of *BCR::ABL1* in eGFP<sup>low</sup> HSCs promotes aggressive leukemogenesis *in vivo*.**

(A-C) Frequency (%) of mCherry<sup>+</sup> eGFP<sup>low</sup> or eGFP<sup>high</sup>: HSCs (Lin<sup>-</sup> Sca-1<sup>+</sup> cKit<sup>+</sup> CD150<sup>+</sup> CD48<sup>-</sup>) (A), LS-Ks (Lin<sup>-</sup> Sca-1<sup>-</sup> cKit<sup>+</sup>) (B), and CMPs (Lin<sup>-</sup> Sca-1<sup>+</sup> cKit<sup>+</sup> CD16/32<sup>low</sup> CD34<sup>+</sup>) (C) in indicated groups and organs. Cell cycle analysis using Ki-67 and DAPI to detect the frequency (%) of cells in G<sub>0</sub> (Ki-67<sup>neg</sup> DAPI<sup>low</sup>), G<sub>1</sub> (Ki-67<sup>high</sup> DAPI<sup>low</sup>) and G<sub>2</sub>SM (Ki-67<sup>high</sup> DAPI<sup>high</sup>) in: mCherry<sup>+</sup> eGFP<sup>low</sup> or eGFP<sup>high</sup> HSCs (D), mCherry<sup>+</sup> eGFP<sup>low</sup> or eGFP<sup>high</sup> LS-K (E), and mCherry<sup>+</sup> eGFP<sup>low</sup> or eGFP<sup>high</sup> CMPs (F). (G) Kaplan-Meier survival curve showing the probability of survival (%) of the indicated experimental groups with a follow up duration of 56 days. At the end of the follow up period, the remaining 7 eGFP<sup>high</sup> chimeric mice were sacrificed and the experiment was terminated. Frequencies (%) were determined by flow cytometry-based analysis for (A-F). n=5 for (A-F) and n=7-15 for (G). Data are presented as mean and error bars as standard error of mean. Statistical significance was determined by two-way ANOVA using Tukey's multiple comparison test for (A-F), and by Log-rank (Mantel-Cox) test for (G) (ns, not significant; \*\*\*\* p ≤ 0.0001).

### **3.4 The role of small extra cellular vesicle signaling in the stressed BM**

Cells within multicellular organisms employ a variety of mechanisms to interact with their surroundings in order to uphold cellular functions and maintain tissue balance (Caruso Bavisotto et al., 2019). One such mechanism involves the use of small extracellular vesicles (sEVs), like exosomes. Signaling mediated by sEVs is gaining recognition as a major means of cellular communication in various tissues, both during normal functioning and in response to stress conditions. sEVs accomplish this by delivering their cargo to recipient cells or by influencing the external environment (Caruso Bavisotto et al., 2019).

Inflammatory insult represents a natural form of stress in the BM. Consistent with existing literature (Butler, Abdelhamed, & Kurre, 2018; Morrison & Scadden, 2014), our group has documented extensive intercellular communication within diverse cell populations regulating the stress response. However, the specific mechanisms of this communication remain largely unresolved. Nevertheless, increasing evidence suggests that sEVs signaling may play a significant role in facilitating this intercellular dialogue.

#### **3.4.1 Size exclusion chromatography on top of sequential centrifugation increases the purity of isolated sEVs.**

While serial centrifugation followed by a final ultracentrifugation step is regarded as the 'gold standard' for sEVs isolation (Théry, Amigorena, Raposo, & Clayton, 2006), it typically yields a heterogeneous mixture of sEVs along with unwanted contaminants, notably proteins. To enhance the purity of our sEV isolation, we conducted a comparative analysis. Specifically, we compared sEV preparations obtained through the conventional method with those obtained after incorporating an additional size-exclusion chromatography (SEC) purification step. This supplemental purification, achieved using commercially available columns from IZON after the ultracentrifugation step, serves a dual purpose in our experiment. Firstly, it allows the differentiation of various sEV sub-populations based on size as they pass through the chromatography column. Secondly, it facilitates the separation of potential contaminants, such as protein aggregates.

To ensure a fair comparison, both protocols were executed simultaneously using the same initial material: fetal bovine serum (FBS), which is known for its abundance of sEVs (Lehrich, Liang, Khosravi, Federoff, & Fiandaca, 2018). After ultracentrifugation, the resulting pellet was reconstituted in 400  $\mu$ L of PBS and divided into two equal portions. One portion, designated as the '100K pellet,' was retained in 200  $\mu$ L of PBS, while the other portion

## Results

underwent purification through SEC, resulting in the collection of multiple fractions labeled as F0 to F15, each contained within 200  $\mu$ L of PBS. This collection of 16 fractions aimed to encompass a wide spectrum of the elution process, ensuring comprehensive capture of eluting sEVs (Fig. 23).

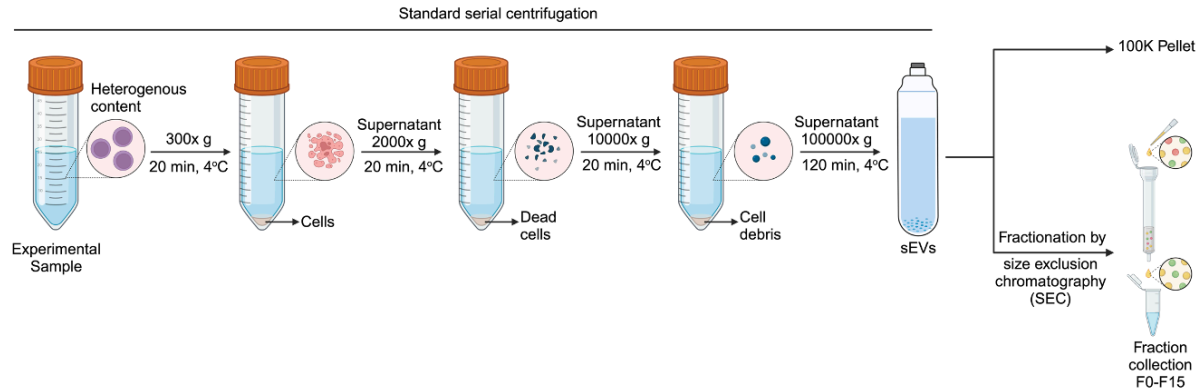


**Figure 23 | Isolation of sEVs through sequential centrifugation and SEC.**

Schematic representation of experimental design: For the isolation of sEVs, experimental samples were subjected to serial centrifugation at indicated speeds, durations and temperatures. During the initial three centrifugation steps, the resulting pellets, comprising cells, nonviable cells, and cellular debris respectively, were discarded. Following the final centrifugation step (100,000x g), the pellet was resuspended in 400  $\mu$ L of PBS and divided into two separate 200  $\mu$ L aliquots. One of these aliquots was kept in 200  $\mu$ L of PBS and designated as the '100K pellet.' Conversely, the other aliquot underwent purification using size-exclusion chromatography (SEC), leading to the isolation of multiple fractions denoted as F0 (void), progressing through to F15. These fractions were collected in an equivalent volume of PBS (200  $\mu$ L), allowing for a direct comparison with the 100K pellet. Created with BioRender.com. Experiments performed jointly with Marie-Elen Tichel.

To evaluate the effectiveness of both isolation methods, we conducted a comprehensive assessment of the respective sEV preparations, aligning with the 'Minimal Information for Studies of Extracellular Vesicles' guidelines (MISEV2018). These guidelines were established by the International Society for Extracellular Vesicles (ISEV) with the principal objective of enhancing the robustness and reproducibility of research findings within the field (Théry et al., 2018).

For the physical characterization of the isolated sEVs, we utilized nanoparticle tracking analysis (NTA), a dark-field microscopy technique that observes the Brownian motion of particles using laser light-scattering (Dragovic et al., 2011). NTA was specifically designed to quantify the size distribution and concentration of nanoparticles, such as sEVs. Our NTA analysis revealed a significant enrichment of particles in SEC fractions 6-11 (F6-11) compared to the 100K pellet, with F8 and F9 exhibiting the highest abundance (Fig. 24A). Conversely, protein quantification of the SEC fractions demonstrated a substantial reduction in protein concentration compared to the 100K pellet (Fig. 24B). This, combined with the higher particle enrichment, indicates a superior purification of sEVs in SEC compared to the 100K pellet.

## Results

Upon comparing SEC fractions, F8 displayed much lower protein quantification than F9, while maintaining a very similar particle concentration, suggesting higher sEV purity with less contaminating protein (Fig. 24B). Consequently, F8 was identified as the most purified SEC fraction, showing a 3.22-fold increase in absolute particle amount over the 100K pellet (Fig. 24C). Additionally, SEC F8 exhibited a significant 61.2-fold reduction in absolute protein content compared to the 100K pellet (Fig. 24D), resulting in a 196.8-fold increase in the particle-to-protein ratios (Fig. 24E). As expected, due to their smaller size, co-isolated protein complexes experienced prolonged retention time in the column, leading to later elution. This is evident from the higher protein concentration in the later fractions (F10-F15), which are poor in particles.

Furthermore, the mean particle size of SEC F8 closely matched the expected size for exosome-enriched fractions. In contrast, the observed mean particle size in the 100K pellet was much larger than that of the SEC fractions (Fig. 24F). A more in-depth examination of these results revealed that the particle size distribution profile of SEC F8 displayed greater uniformity, with the main peak falling within the 40-160 nm range, indicating an enrichment of smaller particles (Figure 24G, left panel). In contrast, the size distribution profile of the 100K pellet exhibited a broader range of particles, highlighting the substantial heterogeneity of the isolated particles (Figure 24G, right panel).

To corroborate our findings, we performed transmission electron microscopy (TEM) to examine both SEC F8 and the 100K pellet sEVs. While sEVs were identifiable in both samples, SEC F8 exhibited a lower background and a higher incidence of exosomes, recognizable by their distinctive cup-shaped appearance (Fig. 24H).

For a more in-depth characterization of the isolated sEVs and to illustrate exosome enrichment, Western blotting was performed. Given the high compositional heterogeneity of exosomes and the association of different protein markers with exosomes from different biological sources, establishing a universally standardized marker panel presented a challenge. As a starting point, we selected two positive markers: CD81, a transmembrane tetraspanin, and TSG101, a cytosolic marker. In contrast, we used the mitochondrial marker Cytochrome C and the Golgi marker GM130 as negative markers (Lötvald et al., 2014). Our results revealed a notably high presence of the classical exosome enrichment marker, TSG101, in the SEC F8 sEV preparation, with only a faint band observed in the 100K pellet sEV preparation. Furthermore, the negative marker GM130 exhibited significantly lower detection in the SEC F8 fraction compared to the 100K pellet sEV preparation. Both CD81 and Cytochrome C were undetectable in our analysis.

## Results

Collectively, these findings emphasize the added value of incorporating the SEC step after ultracentrifugation, as it leads to sEV preparations with enhanced sample purity, reduced contaminating proteins, and a more homogenous size profile indicative of exosome enrichment.

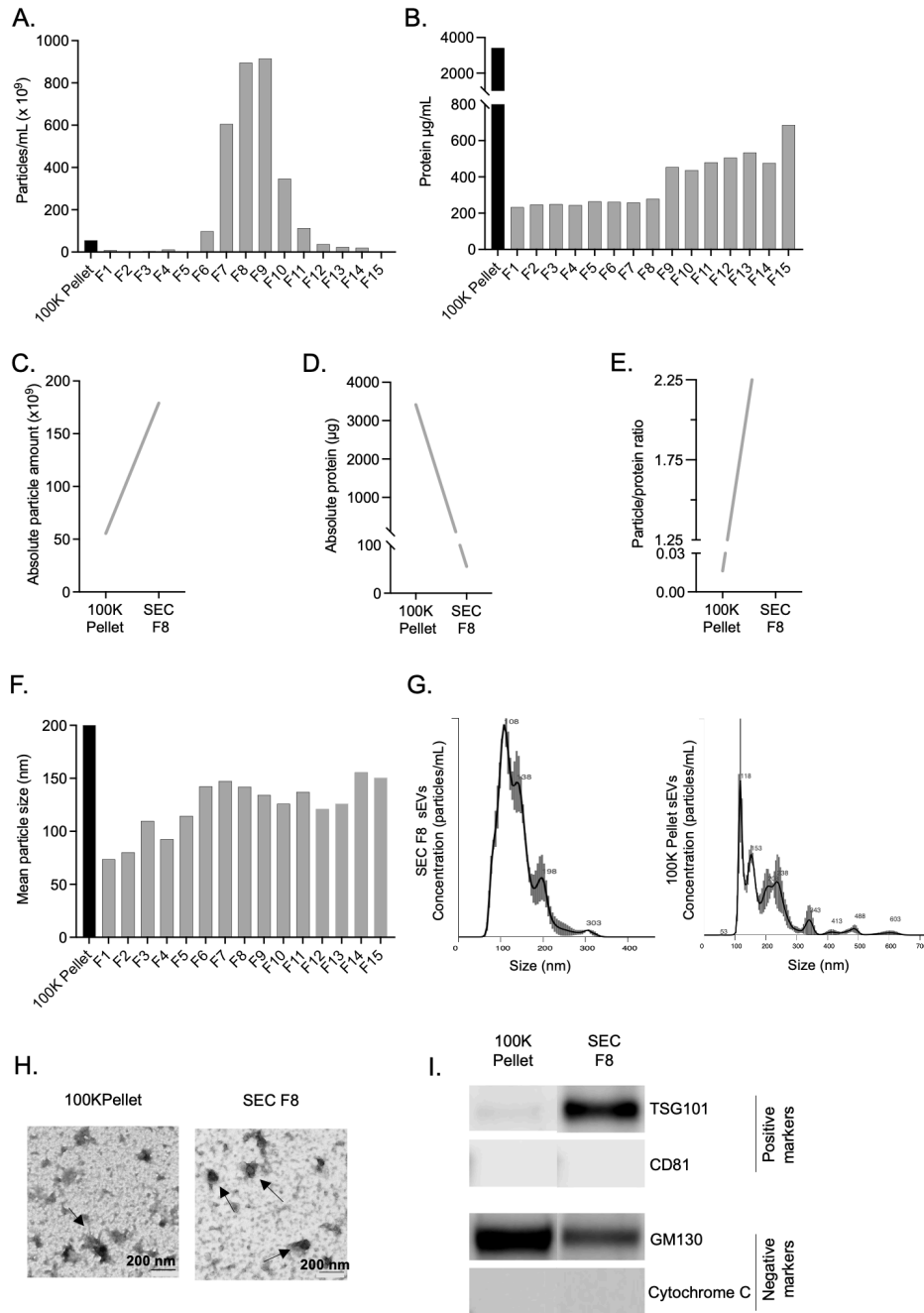


**Figure 24 | Incorporating SEC to sEV isolation enhances purity.**

(A) Particle concentration (particle/mL  $\times 10^9$ ) as determined by nanoparticle tracking analysis (NTA) in indicated fetal bovine serum (FBS) sEV samples. (B) Protein quantification ( $\mu\text{g/mL}$ ) as determined by Qubit™ in indicated FBS sEV samples. (C) Absolute number of detected particles ( $\times 10^9$ ) as determined by NTA in indicated FBS sEV samples. (D) Absolute amount of protein ( $\mu\text{g}$ ) as determined by Qubit™ in indicated FBS sEV samples. (E) Particle-to-protein ratio in indicated FBS sEV samples. (F) Mean particle size (nm) as determined by NTA in indicated FBS sEV samples. (G) Particle distribution profile for FBS sEVs in the F8 (left panel) and in the 100K pellet (right panel)

## Results

as determined by NTA. (H) Transmission electron micrograph of FBS sEVs in the 100K pellet (left panel) and in SEC F8 (right panel). Arrows point to examples of exosomes. Scale bar: 200 nm. (I) Western blot analysis of TSG101 and CD81 (positive sEVs/exosome markers) and GM130 and Cytochrome C (negative sEVs/exosome markers) in FBS sEVs in indicated FBS sEV samples. (C-E), absolute numbers are normalized to final volume. All panels are representative analysis panels. Experiments performed jointly with Marie-Elen Tüchel.

### 3.4.2 sEVs isolated from BM stromal cells *in vitro*

#### 3.4.2.1 Differences in particle and protein quantities between sEVs isolated from PBS and IFN $\alpha$ treated stromal cells

With a reliable sEV extraction protocol in place, our next focus was to investigate the role of sEV signaling in coordinating the BM stress response. We initiated our studies *in vitro* by isolating sEVs from a well-defined and homogenous population of murine bone-lining stromal cells, which we have recently characterized as "reinvigorating mesenchymal stem cells" (rMSCs). These rMSCs have demonstrated their capacity to sustain and expand HSCs in co-culture, while also modulating their response to inflammatory stimulation, specifically via IFN $\alpha$  (Sood, Klein et al., in preparation).

rMSCs were cultured in sEV-depleted medium for 48 hours with or without 100 IU/mL IFN $\alpha$ . Following incubation, we collected the supernatant for sEV extraction with the protocol of serial centrifugation followed by SEC. In all subsequent experiments, we made a slight modification to the above outlined SEC protocol (Section 3.4.1) by altering the fraction collection volumes. This adjustment allowed us to collect exosome-enriched sEVs in an earlier fraction, specifically in fraction F5 instead of the usual F8 (Fig. 25A). Simultaneously, we conducted an assessment of the rMSCs' viability and apoptotic state using the Annexin V/DAPI assay to confirm that the IFN $\alpha$  treatment did not induce significant cell death, which might lead to the accumulation of apoptotic bodies in the culture supernatant. Our results verified that the proportion of Annexin V<sup>+</sup> cells, indicative of apoptosis, remained minimal and comparable between both treatment conditions, thus reducing the likelihood of substantial apoptotic body accumulation (Fig. 25B).

## Results

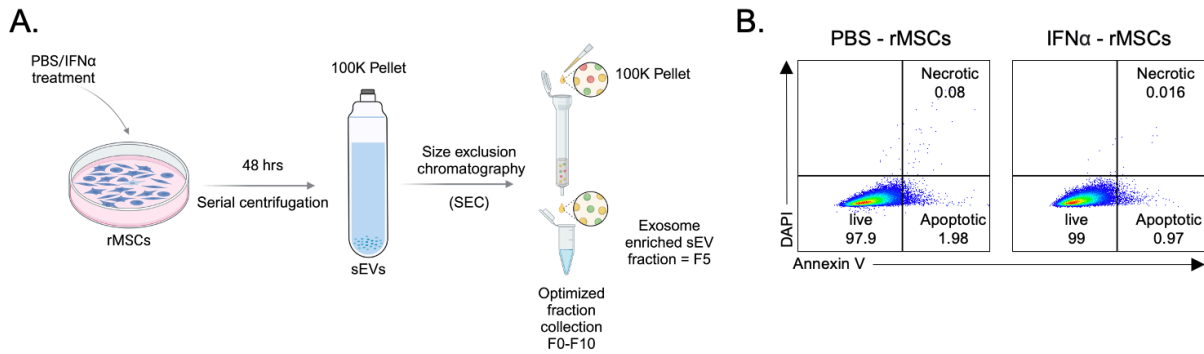


**Figure 25 | Isolation of *in vitro*-generated exosome-enriched rMSC sEVs**

(A) Schematic representation of experimental design:  $2 \times 10^6$  rMSC were cultured in sEV free medium, and treated with either 100 units/mL of IFN $\alpha$  (IFN $\alpha$  sEVs) or PBS (PBS sEVs) for 48 hours. Following the treatment period, 100 mL of culture supernatant from each condition was used for the isolation of sEVs by serial centrifugation, followed by the implementation of a modified SEC protocol. Exosome-enriched sEVs elute in F5. Created with BioRender.com. (B) Representative flow cytometry gating strategy to assess apoptosis in PBS or IFN $\alpha$  (100 units/mL) treated rMSCs using the Annexin V/DAPI assay, allowing differentiation between necrotic (Annexin $V^+$  DAPI $^+$ ), live (Annexin $^-$  DAPI $^-$ ), and apoptotic cells (Annexin $V^+$  DAPI $^-$ ). Data is representative of three replicates. Experiments performed jointly with Marie-Elen Tüchel.

NTA of isolated sEVs revealed a notable enrichment of particles in fraction F5 for both treatment conditions (Fig. 26A, left and middle panels). Nevertheless, treatment with IFN $\alpha$  led to a 1.35-fold increase in the absolute particle count (Fig. 26A, right panel). Moreover, there was a general increase in protein content in response to IFN $\alpha$  treatment (Fig. 26B, left and middle panels). Notably, the absolute protein quantity recovered in F5, the fraction enriched with particles, was 1.5 times higher in the IFN $\alpha$ -treated rMSC supernatant compared to that of the PBS treated supernatant (Fig. 26B, right panel). Nonetheless, the calculated particle-to-protein ratios in F5 did not display significant differences (Fig. 26C).

The mean particle size remained comparable between the PBS and IFN $\alpha$  treatments and corresponded to the expected size range for exosome-enriched sEV preparations (Fig. 26D). The size distribution profiles of F5 exhibited the characteristic distribution of peaks corresponding to the mean particle size of sEVs. However, it was observed that upon IFN $\alpha$  treatment, additional peaks of larger sizes atop the primary peak (40-160 nm) also appeared (Fig. 26E). In both conditions, TEM analysis of F5 confirmed the enrichment of morphologically cup-shaped sEVs, a typical feature of exosomes, with minimal backgrounds (Fig. 26F).

For Western blot analysis, we followed the MISEV2018 guidelines, this time incorporating a broader panel of positive and negative markers. The guidelines advise for the inclusion of at least three positive protein markers for sEVs, including at least one transmembrane protein (e.g., CD81) or lipid-bound protein (e.g., Flotillin-1), a cytosolic protein (e.g., TSG101), and at least one negative protein marker (e.g., GM130 for the Golgi apparatus, Cytochrome C for mitochondria, and Calnexin for the endoplasmic reticulum) (Lötvalld et al.,

## Results

2014; Théry et al., 2018). In our analysis, all the positive markers were detected in F5 for both treatment conditions, which is the fraction of interest owing to its enrichment with sEVs (Fig. 26A). Notably, the negative marker Cytochrome C was absent in F5 for both conditions, whereas GM130 and Calnexin were detected at very low intensities in both samples (Fig. 26G).

Collectively, the data suggests that the exosome-enriched sEVs obtained from both treatment conditions elute within the same fraction (F5). Nevertheless, the data also indicate notable distinctions in both the overall particle and protein quantities between the PBS and IFN $\alpha$  treatments. Additionally, the IFN $\alpha$ -treated samples display variations in size distribution, implying potential difference in the sEVs released by rMSCs when subjected to PBS or IFN $\alpha$  treatment.

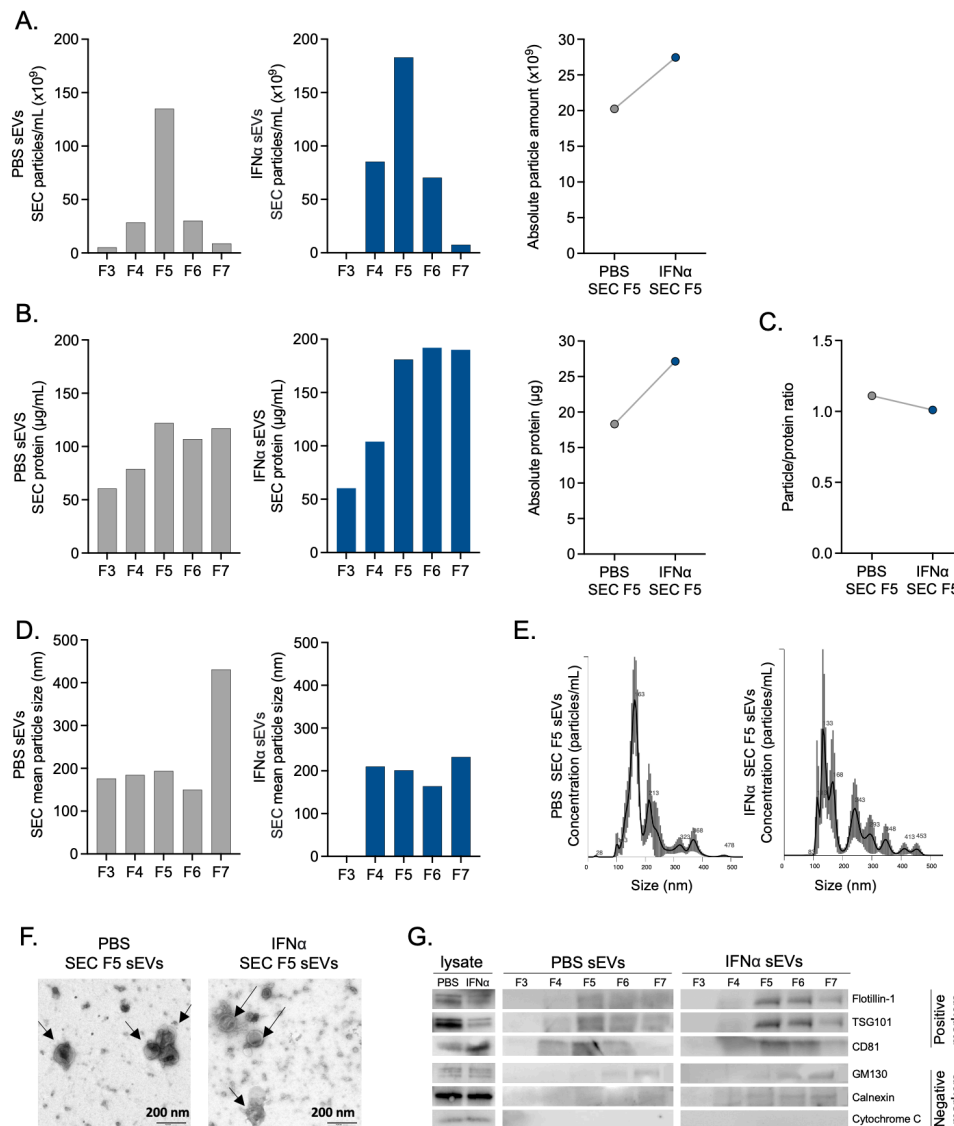


**Figure 26 | Variations in particle and protein quantities of sEVs derived from from PBS and IFN $\alpha$  treated stromal cells**

## Results

(A) Particle concentration (particle/mL  $\times 10^9$ ) of rMSC sEVs as determined by nanoparticle tracking analysis (NTA) following treatment with either PBS (PBS sEVs, left panel), or 100 IU/mL of IFN $\alpha$  (IFN $\alpha$  sEVs, middle panel) for 48 hours, and absolute number of detected particles in indicated SEC fractions, right panel. (B) Protein quantification ( $\mu\text{g/mL}$ ) as determined by Qubit<sup>TM</sup> for PBS sEVs (left panel) and IFN $\alpha$  sEVs (middle panel) in indicated SEC fractions, and absolute amount of protein ( $\mu\text{g}$ ) in indicated SEC fractions, right panel. (C) Particle-to-protein ratio in indicated SEC fractions. (D) Mean particle size (nm) as determined by NTA for PBS sEVs (left panel) and IFN $\alpha$  sEVs (right panel) in indicated SEC fractions. (E) Particle distribution profile for PBS sEVs F5 (left panel) and in IFN $\alpha$  sEVs F5 (right panel). (F) Transmission electron micrograph of PBS sEVs F5 (left panel) and in IFN $\alpha$  sEVs F5 (right panel). Arrows point to examples of exosomes. Scale bar: 200 nm. (G) Western blot analysis of indicated PBS or IFN $\alpha$  sEVs fractions along with parental cell lysates for Flotillin-1, TSG101 and CD81 (positive sEV/exosome markers) and GM130, Calnexin and Cytochrome C (negative sEV/exosome markers). For (A-B), absolute numbers are normalized to final volume. All panels are representative analysis panels. Experiments performed jointly with Marie-Elen Tüchel.

### 3.4.2.2 sEVs derived from rMSCs do not affect proliferation or differentiation potential of HSPCs *in vitro*

To investigate the influence of rMSC sEVs on hematopoietic cells, we isolated LSKs and HSCs from the BM of WT mice. These cells were subsequently cultured in a medium devoid of sEVs. In parallel, sEVs were isolated from cultured rMSCs that were either treated with PBS or 100 IU/mL IFN $\alpha$  (Fig. 27A).

As an initial assessment, we monitored the proliferation of LSKs following treatment with PBS- or IFN $\alpha$ -induced rMSC-derived sEVs for 48 hours, utilizing the Cell Trace Violet (CTV) assay. In this assay, LSKs were pre-labeled with the fluorescent CTV dye before culture. This dye equally divides between daughter cells, resulting in its dilution with each division. Consequently, a lower CTV signal correlates with higher proliferation. Flow cytometric analysis of CTV dilution revealed that the proliferation of LSKs remained unaffected when exposed to 0.5-2  $\mu\text{g/mL}$  of PBS or IFN $\alpha$  rMSC sEVs for 48 hours (Fig. 27B). Higher sEV doses were cytotoxic to the cells and were therefore excluded from testing (data not shown).

Subsequently, we assessed the effect of prolonged sEV treatment on HSC differentiation. HSCs were treated with 0.5  $\mu\text{g/mL}$  of sEVs for 10 days, with replenishment of sEVs every third day. We used the lowest sEV dose to prevent potential cell toxicity due to sEV accumulation or prolonged exposure. Flow cytometry analysis of HSPCs revealed no discernible differences in the differentiation potential of HSCs when treated with PBS- or IFN $\alpha$ -rMSC sEVs, although a slight increase in the frequency of MPP2 cells could be observed (Fig. 27C).

In summary, these analyses indicate that sEVs derived from rMSCs did not affect proliferation or differentiation potential of HSPCs *in vitro*.

## Results

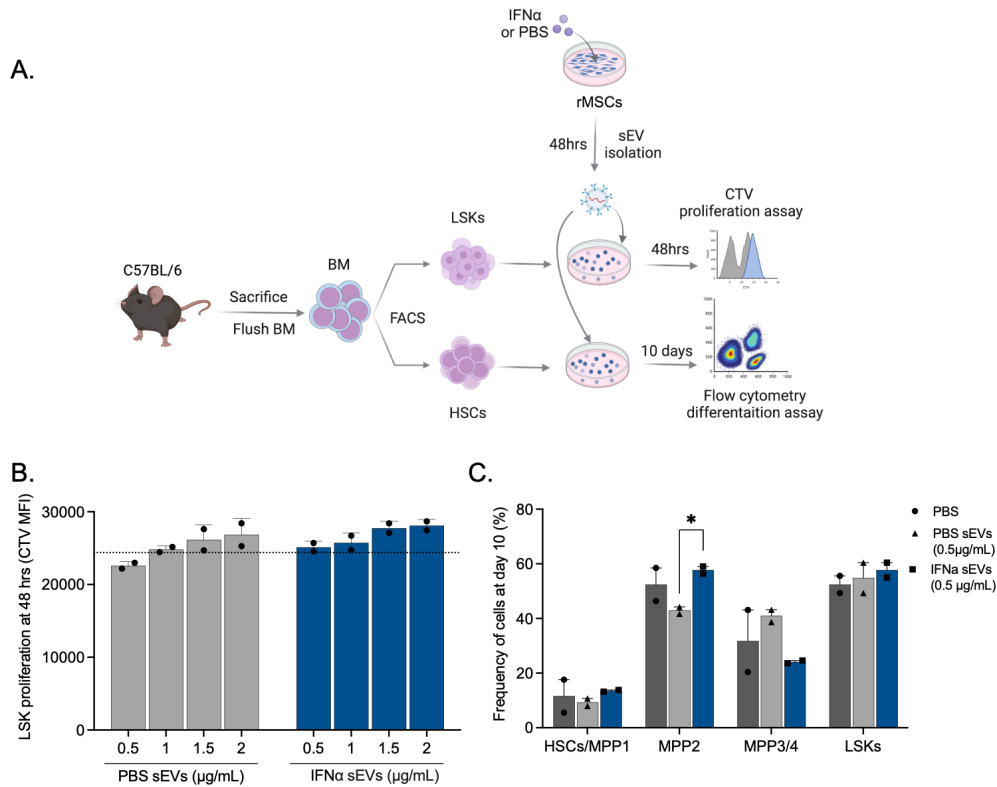


**Figure 27 | rMSC derived sEVs do not affect proliferation or differentiation potential of HSPCs *in vitro*.**

(A) Schematic representation of experimental design: LSKs ( $\text{Lin}^- \text{Sca-1}^+ \text{cKit}^+$ ) or HSCs ( $\text{Lin}^- \text{Sca-1}^+ \text{cKit}^+ \text{CD150}^+ \text{CD48}^- \text{CD34}^-$ ) were isolated via FACS from BM of WT mice and cultured in 96-well plates at a density of  $2 \times 10^4$  LSKs per well, or  $2.5 \times 10^3$  HSCs per well, both in sEV free medium. These cultures were subjected to treatment with SEC F5 sEVs, derived from either PBS or 100 IU/mL IFN $\alpha$ -treated rMSCs (48 hours) (referred to as PBS sEVs and IFN $\alpha$  sEVs, respectively). LSK cultures were maintained for 48 hours, after which their proliferation was evaluated using the cell trace violet (CTV) proliferation assay. HSC cultures were sustained for a duration of 10 days, and HSC differentiation was assessed by flow cytometry. For HSCs, sEV treatment was replenished every third day. Created with BioRender.com. (B) Proliferation of LSKs upon treatment with indicated concentrations of PBS sEVs or IFN $\alpha$  sEVs as determined by the median fluorescence intensity (MFI) of the CTV dye. Dashed line represents PSB treated LSKs as control. (C) Frequency (%) of indicated progenitor cells after 10-day HSC culture with indicated treatments and conditions as determined by flowcytometry. For all panels,  $n=2$ . Data are presented as mean and error bars as standard error of mean. Statistical significance was determined by a two-tailed student's *t*-test. Only statistically significant differences are shown (\*  $p \leq 0.05$ ). Experiments performed jointly with Marie-Elen Tüchel.

### 3.4.3 sEVs isolated from BM *in vivo*

#### 3.4.3.1 Inflammatory stress leads to alterations in the size distribution and abundance of sEVs in the BM

rMSCs constitute a well-defined stromal cell population that does not fully capture the complexity of the *in vivo* stromal system. Additionally, the first step in biosynthesis of certain sEVs, particularly exosomes, involves the incorporation of soluble proteins associated with the extracellular milieu (Kalluri & LeBleu, 2020), which are absent in an *in vitro* system. Keeping this in mind, we proceeded with the isolation and characterization of sEVs directly from the BM supernatant under normal and inflammatory conditions.

## Results

Inflammatory stress was induced by administering 5mg/kg Polyinosinic:polycytidylic acid (pI:C) intraperitoneally (i.p.) to WT mice for 18 hours, followed by the isolation of exosome-enriched sEVs. Similarly, mice were treated with an equivalent volume of PBS to collect exosome-enriched sEVs under normal conditions (Fig. 28).

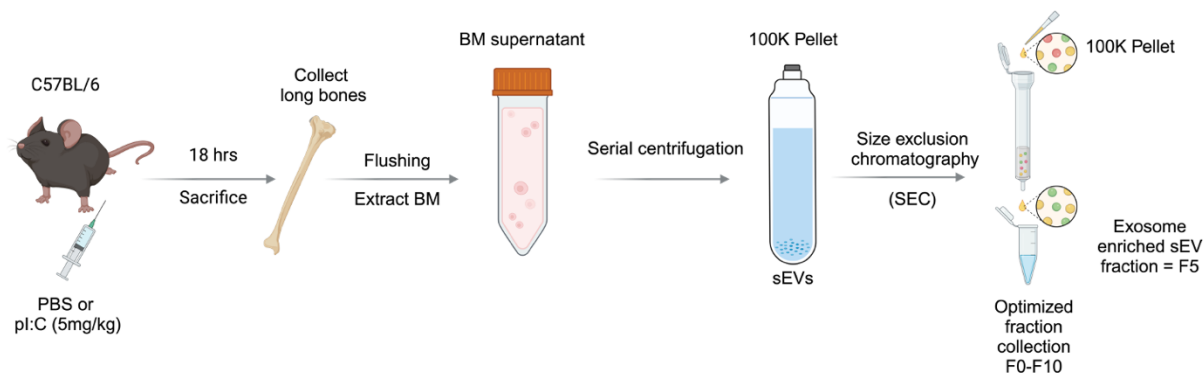


**Figure 28 | Isolation of exosome-enriched sEVs from murine BM**

Schematic representation of experimental design: WT mice were treated with either 5 mg/kg of pI:C (pI:C sEVs) or PBS (PBS sEVs) intraperitoneally (i.p.) for 18 hours. Following the treatment period, mice were sacrificed and the BM was flushed and used for the isolation of sEVs by serial centrifugation, followed by the implementation of a modified SEC protocol. In this adapted protocol void fraction (F0) was increased to 600  $\mu$ L, while the remaining fractions were collected in 150  $\mu$ L portions instead of the previous 200  $\mu$ L. Exosome-enriched sEVs elute in F5. Created with BioRender.com. Experiments performed jointly with Marie-Elen Tüchel.

Following the isolation of sEVs from the BM, NTA indicated that F5 contained the highest particle concentration in both samples (Fig. 29A, left and middle panels). Moreover, under inflammatory conditions, the absolute number of particles in F5 was 1.36 times higher compared to the PBS (Fig. 29A, right panel). Protein quantification also revealed the highest protein concentration in F5 of both samples (Fig. 29B, left and middle panels), and the absolute protein amount was 1.71 times higher in the pI:C sample compared to the PBS (Fig. 29 B, right panel). Nevertheless, the calculation of the particle-to-protein ratios indicated a slight decrease in the ratio after the pI:C treatment (Fig. 29C).

Moreover, the mean particle size correlated with an exosome-enriched sEV preparation in F5, but there was a noticeable increase in mean particle size upon pI:C treatment (Fig. 29D). Indeed, particle size distribution profile for F5 of the pI:C sample showed several minor peaks with larger sizes that were not observed in F5 of the PBS sample, indicating the heterogenous release of particles in response to inflammation (Fig. 29E).

TEM confirmed the presence of sEVs with a characteristic cup-shaped morphology typical of exosomes in both conditions (Fig. 29F). Western blot analysis of sEV markers Flotillin-1, TSG101, and CD81 confirmed their presence in F5 and adjacent fractions in both samples with minimal detection of negative markers (Fig. 29G).

## Results

In summary, this data validates the successful isolation of exosome-enriched sEVs from BM supernatant with high purity. Furthermore, the data indicate that the induction of inflammatory stress in the BM leads to alterations in the size distribution and abundance of sEVs *in vivo*.

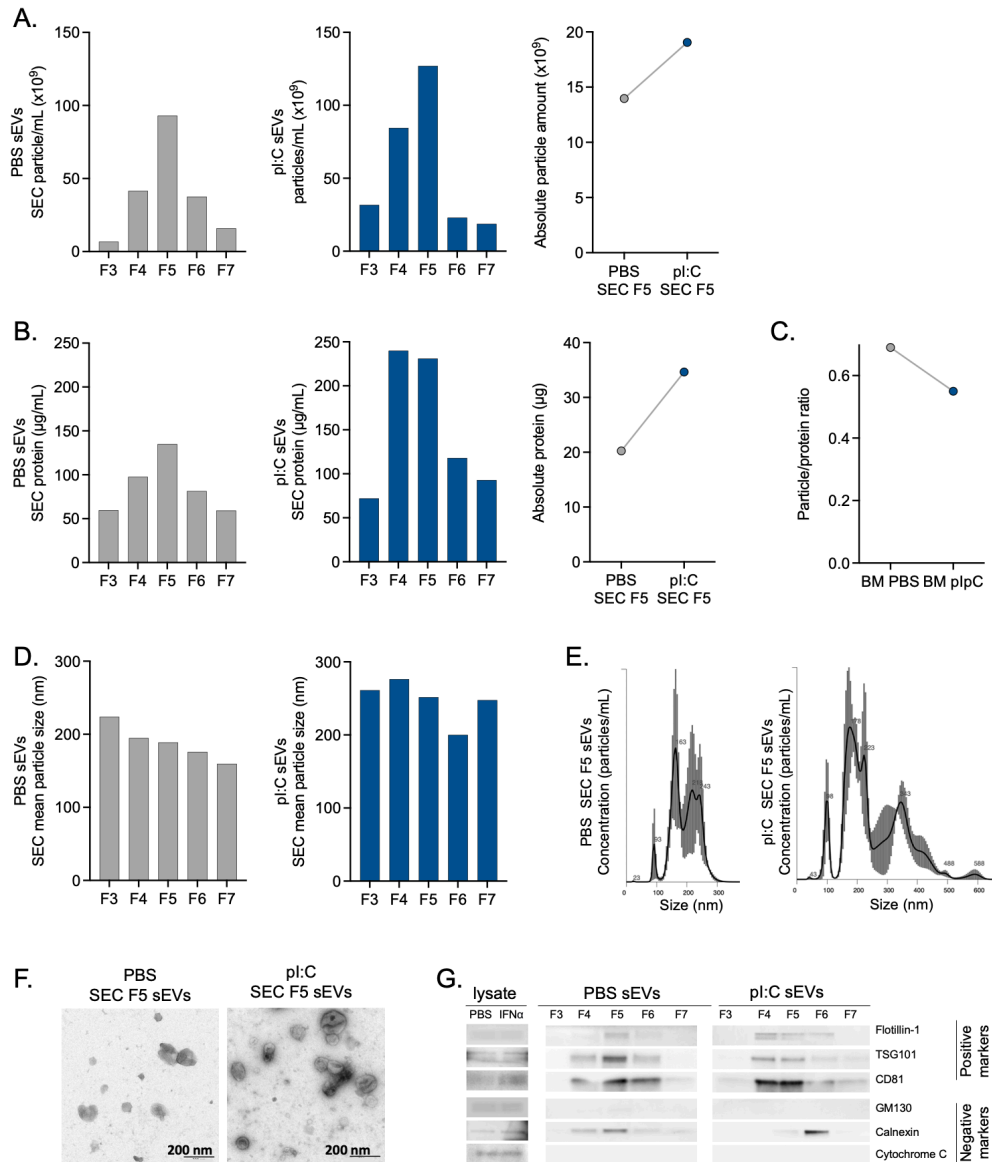


**Figure 29 | Inflammatory stress induces changes in the size distribution and abundance of BM sEVs *in vivo*.**

(A) Particle concentration (particle/mL  $\times 10^9$ ) of murine BM sEVs as determined by nanoparticle tracking analysis (NTA) following treatment with either PBS (PBS sEVs, left panel), or 5 mg/kg of pl:C (pl:C sEVs, middle panel) for 18 hours. The line graph on the right illustrates the absolute number of detected particles in indicated SEC fractions. (B) Protein quantification ( $\mu\text{g/mL}$ ) as determined by Qubit™ for PBS sEVs (left panel) and pl:C sEVs (middle panel) in indicated SEC fractions. The line graph on the right illustrates the absolute amount of protein ( $\mu\text{g}$ ) in indicated fractions. (C) Particle-to-protein ratio in indicated SEC fractions. (D) Mean particle size (nm) as determined by NTA for PBS sEVs (left panel) and pl:C sEVs (right panel) in indicated SEC fractions. (E) Particle distribution profile for PBS sEVs F5 (left panel) and in pl:C sEVs F5 (right panel) as determined by NTA. (F) Transmission electron micrograph of PBS sEVs F5 (left panel) and in pl:C sEVs F5 (right panel). Arrows point to examples of exosomes. Scale bar: 200 nm. (G) Western blot analysis for Flotillin-1, TSG101 and CD81 (positive sEV/exosome markers) and GM130, Calnexin and Cytochrome C (negative sEV/exosome markers) in PBS or pl:C sEVs fractions along with parental cell lysates. For (A-B), absolute numbers were normalized to final volume. All panels are representative analysis panels. Experiments performed jointly with Marie-Elen Tichel.

### 3.4.3.2 BM pl:C sEVs inhibit proliferation of LSKs *in vitro*

To investigate the influence of BM derived exosome-enriched sEVs on HSPCs *in vitro*, freshly sorted LSKs or HSCs from WT mice were cultured with sEVs isolated from the BM of WT mice treated with either PBS or pl:C. However, this time, we also included LSKs and HSCs that were treated with only IFN $\alpha$  (without sEVs) as a positive control. LSK cultures were maintained for either 12 hours to assess apoptosis using Annexin V/DAPI staining, or 72 hours for CTV proliferation analysis. HSC cultures were maintained for either 3 or 24 hours for gene expression profiling (Fig. 30A).

Treatment of LSKs with PBS sEVs resulted in a dose-dependent increase in apoptotic cells after 12 hours of LSK treatment, with no significant effect on proliferation after 72 hours (Fig.30 B&C). On the other hand, treatment with pl:C sEVs led to a dose-dependent increase in apoptotic cells accompanied by an anti-proliferative effect at higher doses (Fig.30 B&C).

Previously generated data from our lab and others in the field have consistently demonstrated that the *in vivo* responses of HSPCs to inflammatory treatments, including pl:C or IFN $\alpha$ , cannot be fully replicated *in vitro* (Essers et al., 2009). This highlights the critical role of the BM microenvironment in mediating inflammation-induced effects. Thus, in the next step, we combined IFN $\alpha$  treatment with sEV treatment *in vitro* to explore potential synergistic effects on HSPCs.

Analysis of apoptosis after 12 hours of treatment with IFN $\alpha$  and either PBS sEVs or pl:C sEVs concurrently resulted in a significant increase in apoptosis compared to any of the single treatments (Fig. 30D). Single pl:C sEV or IFN $\alpha$  treatment induced an anti-proliferative effect compared to single PBS sEV treatment (Fig. 30E). However, when combining IFN $\alpha$  treatment with pl:C sEVs, an even stronger anti-proliferative effect was observed, as was also observed for PBS sEVs in combination with IFN $\alpha$  treatment. This indicates that the combined treatment of sEVs with IFN $\alpha$  synergize to induce apoptosis of LSKs, and blocks their proliferation *in vitro*.

An additional approach to assess the influence of inflammatory sEVs on HSPC biology is to examine the expression levels of specific genes known to be upregulated in HSCs under inflammatory stress *in vivo* (Demerdash et al. in preparation). Consequently, the expression levels of these genes were analyzed in HSCs after *in vitro* sEV treatment for 3 and 24 hours. Interestingly, all the tested genes were found to be downregulated in the pl:C sEV-treated

## Results

HSCs after 24 hours, but not in the PBS sEV-treated HSCs (Fig. 30F). This observation could explain the anti-proliferative effect observed in pl:C-treated LSKs.

In summary, these experiments suggest that BM-derived sEVs, particularly those enriched in response to inflammatory stimuli, synergize with IFN $\alpha$  to induce apoptosis and block proliferation of HSPCs *in vitro*. Additionally, the downregulation of specific genes in response to inflammatory sEVs may contribute to the observed anti-proliferative effects, highlighting the crucial role of sEV signaling in mediating stress response.

## Results

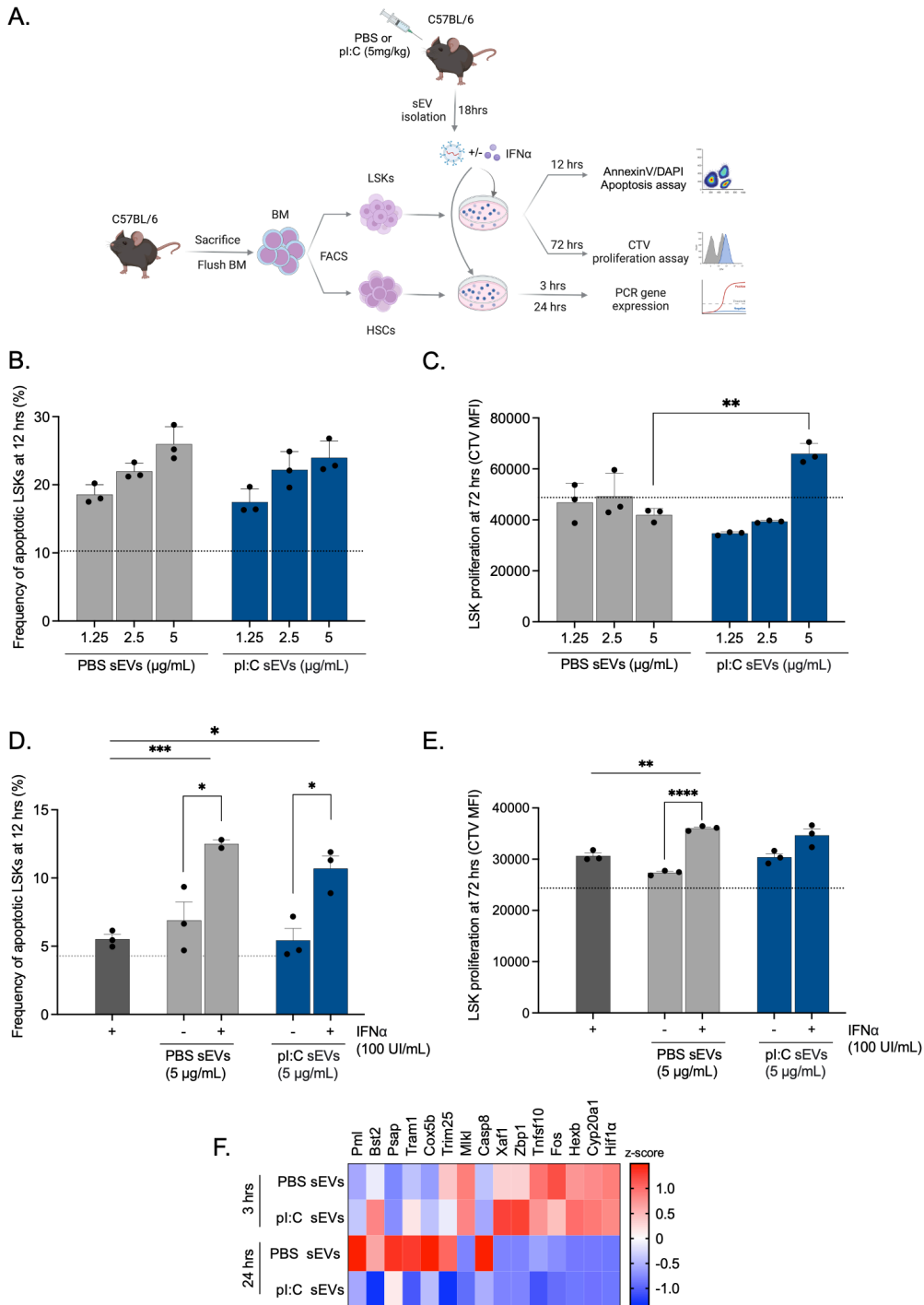


**Figure 30 | *In vitro* suppression of HSPC proliferation by BM pl:C-induced sEVs.**

(A) Schematic representation of experimental design: LSKs (Lin<sup>-</sup> Sca-1<sup>+</sup> cKit<sup>+</sup>) or HSCs (Lin<sup>-</sup> Sca-1<sup>+</sup> cKit<sup>+</sup> CD150<sup>+</sup> CD48<sup>-</sup> CD34<sup>-</sup>) were isolated via FACS from BM of WT mice and cultured in 96-well plates at a density of  $2 \times 10^4$  LSKs per well, or  $2.5 \times 10^3$  HSCs per well, both in sEV free medium. These cultures were subjected to treatment with SEC F5 sEVs, derived from either PBS or 5 mg/kg pl:C treated mice for 18 hours (referred to as PBS sEVs and pl:C sEVs, respectively). LSK cultures were maintained for either 12 hours, during which their viability was assessed using the AnnexinV/DAPI assay, or for 72 hours, at which point their proliferation was evaluated through the cell trace violet (CTV) proliferation assay. On the other hand, HSC cultures were kept for either 3 or 24 hours for the purpose of gene expression analysis through real time quantitative polymerase chain reaction (qRT-PCR). Created with BioRender.com. (B) Frequency (%) of apoptotic LSKs upon treatment with indicated concentrations of PBS sEVs or pl:C sEVs for 12 hours. (C) Proliferation of LSKs upon treatment with indicated concentrations of PBS sEVs or pl:C sEVs for 72 hours. (D) Frequency (%) of apoptotic LSKs upon treatment with indicated concentrations of PBS sEVs or pl:C sEVs for 12 hours, both with and without co-treatment with 100 IU/mL IFN $\alpha$ . (E) Proliferation of LSKs upon treatment with indicated concentrations of PBS sEVs or pl:C sEVs for 72 hours, both with and without co-treatment with 100 IU/mL IFN $\alpha$ . (F) Heatmap showing the z-scores of genes that are

## Results

consistently upregulated in response to inflammatory stress within HSCs. This response is observed after either 3 or 24 hours of treatment with either 2.5 µg/mL PBS sEVs or pl:C sEVs. The scale for the heatmap is set to row-normalized units, and the values represent the mean from a sample size  $n=4$ . For (B-E), dashed line represents PSB treated LSKs as control. For (B-D), frequencies (%) were determined by flow cytometry-based analysis. For (C-E), proliferation was determined by flow cytometry based on the median fluorescence intensity (MFI) of the CTV dye in pre-labeled LSKs.  $n=3$  for biological replicates for (B-E). Data are presented as mean and error bars as standard error of mean. Statistical significance was determined by a two-tailed student's *t*-test. Only statistically significant differences are shown (\*  $p \leq 0.05$ ; \*\*  $p \leq 0.01$ ; \*\*\*  $p \leq 0.001$ ; \*\*\*\*  $p \leq 0.0001$ ). Experiments performed jointly with Marie-Elen Tüchel.

### 3.4.3.3 Dynamic increase in sEV production upon inflammation is primarily driven by hematopoietic cells *in vivo*

Given that the acute inflammatory response within the BM is a dynamic process that ultimately culminates in peak activation and proliferation of HSCs at around the 24-hour mark, I chose to monitor the *in vivo* production of sEVs during this specific timeframe. Intriguingly, I noticed a rise in sEV protein content within the BM supernatant in response to inflammatory stimuli, peaking at the 9-hour mark, which is 2.2 times higher than that observed in PBS-treated mice ( $p=0.0001$ ) (Fig. 31A). Subsequently, this value begins to decline, returning to almost baseline levels at the 24-hour mark.

To validate that this alteration in sEV composition is indeed correlated with an inflammatory response, I compared the BM sEV protein content in WT mice and mice lacking the IFN $\alpha$  receptor (IFNAR) (*Ifnar*<sup>-/-</sup>). Interestingly, the results reveal that *Ifnar*<sup>-/-</sup> mice already exhibit elevated sEV protein levels even in the absence of inflammatory stimuli, which are 2.12 times higher than those in WT mice ( $p=0.003$ ) (Fig. 31B). Furthermore, the sEV protein content in *Ifnar*<sup>-/-</sup> mice does not increase upon pl:C treatment, in contrast to the substantial increase observed in WT mice, thereby confirming that this increase is indeed linked to an inflammatory response.

To investigate this further, I generated two types of chimeric mice: forward (*WT/Ifnar*<sup>-/-</sup>) and reverse (*Ifnar*<sup>-/-</sup>/WT) chimeras. Forward chimeras consist of *Ifnar*<sup>-/-</sup> hematopoietic cells within a WT niche environment, while reverse chimeras comprise WT hematopoietic cells within an *Ifnar*<sup>-/-</sup> niche environment. Consequently, when subjected to inflammatory stress, only the niche compartment can respond in forward chimeras, whereas only the hematopoietic compartment can respond in the reverse chimeras. Interestingly, in the absence of inflammatory stimulation, forward chimeras exhibited an elevated sEV protein content similar to that of *Ifnar*<sup>-/-</sup> mice. However, upon stimulation, this level decreased to approximately half (Fig. 31C). In contrast, reverse chimeras display a profile resembling that of WT mice, with sEV protein content initially low (around 18µg) but increasing by more than 2-fold upon inflammatory stimulation (Fig. 31C).

## Results

Taken together, this data indicates that the release and content of sEVs are dynamic in response to inflammation, evolving across different phases of the inflammatory response. Furthermore, it suggests that the lack of IFNAR receptor in the hematopoietic compartment results in an increased sEV signaling, likely as a compensatory mechanism to regulate inflammatory response in the absence of a major inflammatory receptor. Importantly, this data also suggests that during inflammation, the increase in sEV profile may primarily be driven by the hematopoietic compartment.

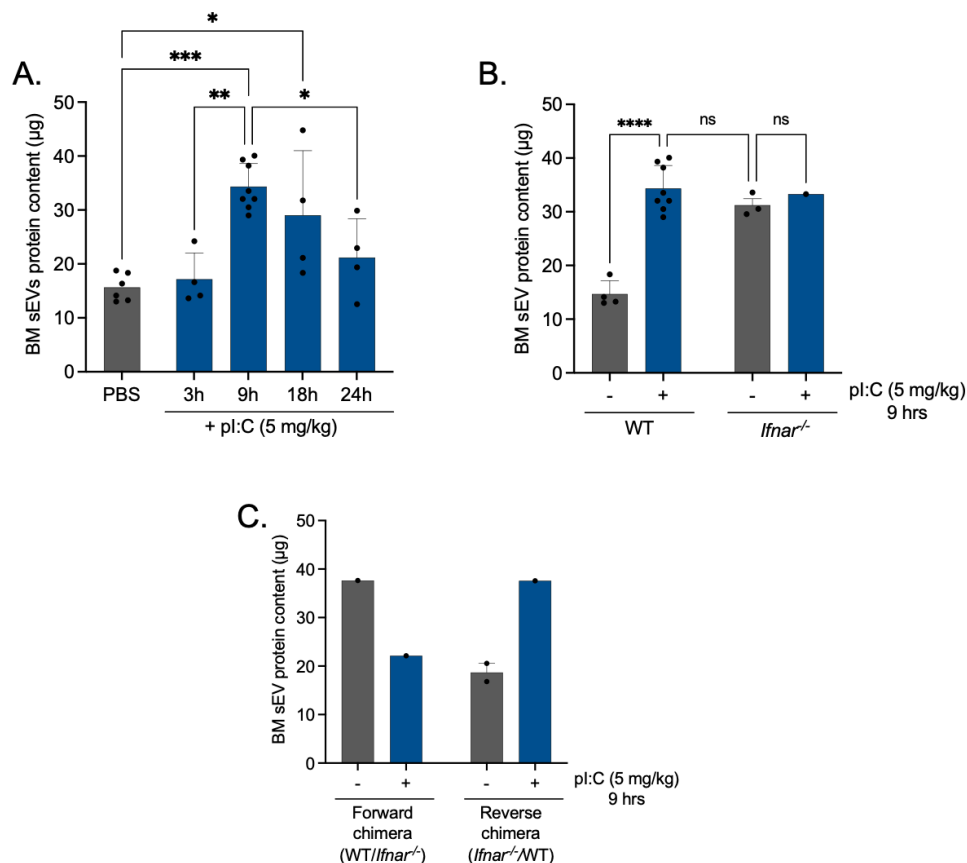


**Figure 31 | Dynamic increase in sEV production during inflammation is predominantly orchestrated by hematopoietic cells *in vivo*.**

Quantification of total protein content (µg) in BM sEVs under the specified treatment conditions for: WT mice treated with pl:C over time (A), WT and IFNα receptor knockouts (*Ifnar*<sup>-/-</sup>) treated with PBS or pl:C (B), forward (WT/*Ifnar*<sup>-/-</sup>) and reverse (*Ifnar*<sup>-/-</sup>/WT) chimeras treated with PBS or pl:C (C). Treatment of chimeric mice was performed 12 weeks after they were generated. Protein quantification was determined by Qubit™. For (A-B), individual data points represent biological replicates (from 1 mouse). For (C-D), individual points represent the average of pooled data from 12 biological replicates. Statistical significance was determined by ordinary one-way ANOVA using Tukey's multiple comparison test for (A-B) (ns, not significant; \*  $p \leq 0.05$ ; \*\*  $p \leq 0.01$ ; \*\*\*  $p \leq 0.001$ ; \*\*\*\*  $p \leq 0.0001$ ).

### 3.4.3.4. Administration of inflammatory sEVs impacts on the myeloid compartment *in vivo*

After demonstrating the influence of BM sEVs on HSPCs *in vitro*, I progressed to investigate the role of BM sEVs released in response to inflammatory stress in an *in vivo*

## Results

context. To accomplish this, sEVs were extracted from the BM of pl:C treated WT mice. Subsequently, these isolated sEVs were transplanted into recipient WT mice through tail vein injections (i.v.), testing various sEV dosages. Transplanted mice were then euthanized 18 hours post-transplant for a comprehensive analysis. To establish appropriate benchmarks, control groups were included, consisting of WT mice treated with PBS or pl:C (5 mg/kg for 24 hours) to serve as negative and positive controls, respectively (Fig. 32).

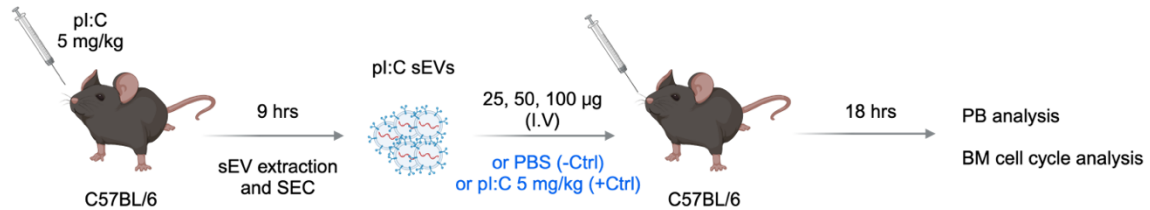


### Figure 32 | Optimization of the *in vivo* treatment dose of inflammatory BM sEVs

Schematic representation of experimental design: WT mice treated IP with 5 mg/kg pl:C to induce an inflammatory response. After 9 hours, the mice were euthanized for the extraction of inflammatory sEVs (pl:C sEVs). These pl:C sEVs were then administered i.v. at varying doses (25, 50, and 100 µg) to treatment mice. After 18 hours, the treated mice were sacrificed for the analysis of peripheral blood and the cell cycle status of immature bone marrow cell populations. Additionally, mice treated i.p. with 5 mg/kg pl:C or equivalent volume of PBS were taken as controls. Created with BioRender.com.

Analysis of PB samples from positive controls at the 24-hour time point revealed a robust acute inflammatory response induced by pl:C treatment, characterized by a reduction in the frequency of B cells, CD4 cells, CD8 cells, eosinophils, and macrophages, alongside an increase in neutrophils compared to the PBS control (Fig. 33A-F). In contrast, treatment with inflammatory sEVs had minimal impact on lymphocytes, specifically B cells, CD4, and CD8 cells (Fig. 33A-C). However, it did lead to a decrease in the frequency of myeloid cells across all tested dosages compared to the PBS control (Fig. 33D-F). Intriguingly, a detailed analysis of the cell cycle status in LSK cells revealed no significant alteration following sEV treatment.

Collectively, this data suggests that treatment with inflammatory sEVs alone was sufficient to simulate a response within the myeloid compartment of peripheral blood across all tested doses, emphasizing the crucial role of sEV signaling during acute inflammation. Notably, no discernible impact on the cell cycle status of LSKs was observed, possibly due to considerations related to the route of administration and its associated hepatic and renal clearance (Ha, Yang, & Nadiathe, 2016; Muthu, Bapat, Jain, Jeyaraman, & Jeyaraman, 2021).

## Results

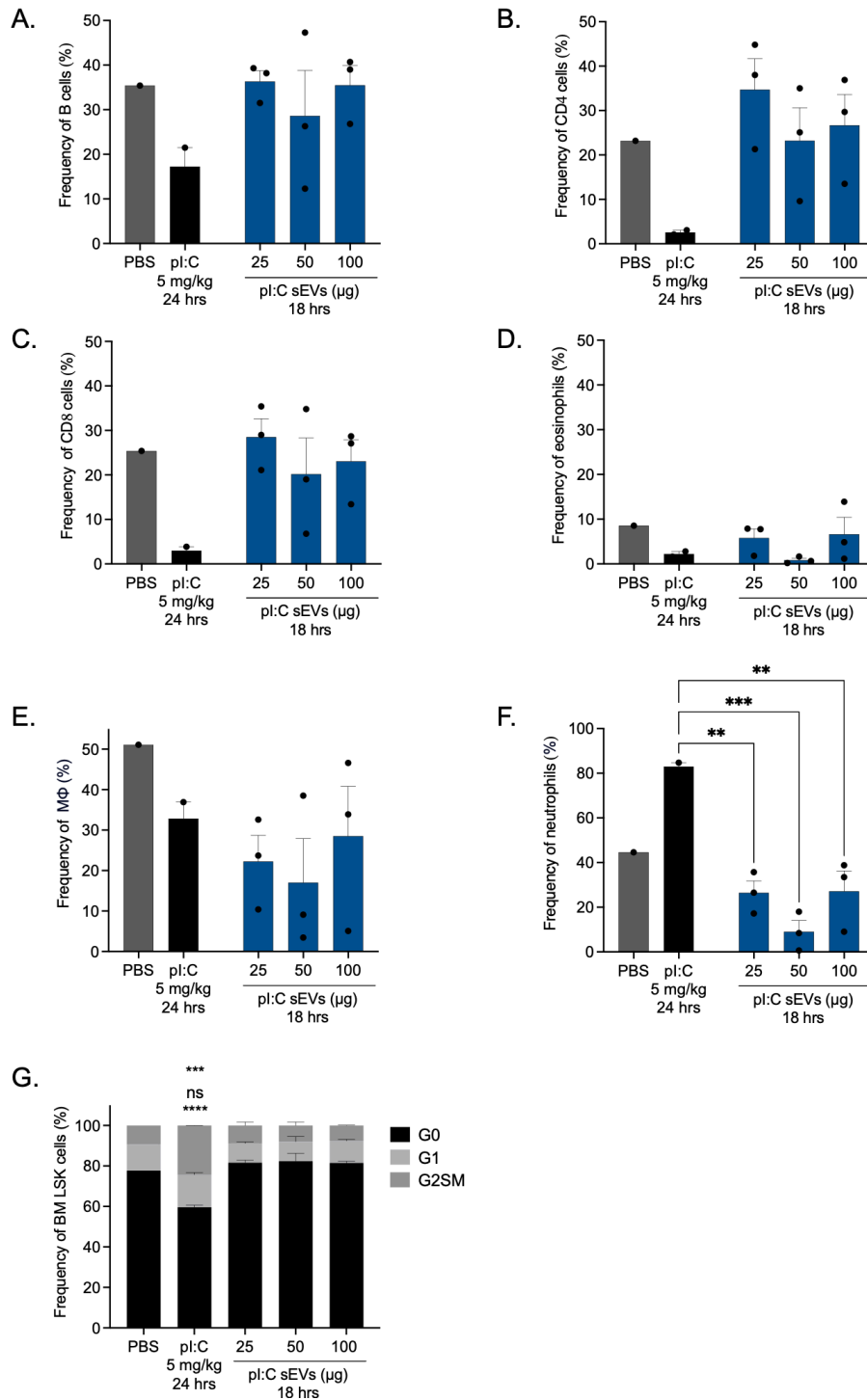


**Figure 33 | Inflammatory sEV administration impacts the myeloid compartment *in vivo*.**

(A-F) Frequency (%) of: B cells (B220<sup>+</sup>) (A), CD4 cells (CD4<sup>+</sup>) (B), CD8 cells (CD8<sup>+</sup>) (C), eosinophils (B220<sup>-</sup> CD4/8<sup>-</sup> CD11b<sup>+</sup> Ly6G<sup>-</sup> Siglec-F<sup>+</sup>) (D), macrophages (MΦ) (B220<sup>-</sup> CD4/8<sup>-</sup> CD11b<sup>+</sup> Ly6G<sup>-</sup> Siglec-F<sup>-</sup> F4/80<sup>+</sup>) (E), and neutrophils (B220<sup>-</sup> CD4/8<sup>-</sup> CD11b<sup>+</sup> Ly6G<sup>+</sup>) (F) in the peripheral blood of treated mice at indicated time points and treatment conditions. (G) Cell cycle analysis using Ki-67 and DAPI to detect the frequency (%) of LSKs (Lin<sup>-</sup> Sca-1<sup>+</sup> cKit<sup>+</sup>) in G<sub>0</sub> (Ki-67<sup>neg</sup> DAPI<sup>low</sup>), G<sub>1</sub> (Ki-67<sup>high</sup> DAPI<sup>low</sup>) and G<sub>2</sub>SM (Ki-67<sup>high</sup> DAPI<sup>high</sup>) at indicated time points and treatment conditions. Frequencies (%) were determined by flow cytometry-based analysis. For all panels, n=1-3 biological replicates. Data are represented as mean, and error bars as standard error of mean. Statistical significance was determined by ordinary one-way ANOVA using Tukey's multiple comparison test for (A-F), and by two-way ANOVA using Tukey's multiple comparison test for (G) (ns, not significant; \*\*  $p \leq 0.01$ ; \*\*\*  $p \leq 0.001$ ; \*\*\*\*  $p \leq 0.0001$ ).

### **3.4.3.5 Modifications in the proteomic profile of sEVs isolated from murine BM in response to inflammatory stress**

After observing dynamic changes in the protein composition of sEVs during the course of an acute inflammatory response, our study aimed to perform a comprehensive analysis of sEV cargo (protein, RNA and DNA) at various time points during inflammation. To initially assess the feasibility of this approach, we initiated the process with a singular time point, focusing on proteomic analysis, given its technical complexity with the nature of our samples.

We induced an inflammatory response in WT mice by administering either PBS or 5 mg/mL pl:C. Following an 18-hour period, we extracted sEVs and conducted label-free mass spectrometry-based proteomic analysis with the full technical support of the Genomics and Proteomics Core Facility, DKFZ (Fig. 34A). For each condition, we performed three biological replicates, with each replicate corresponding to sEVs isolated from the BM of an individual mouse.

Our proteomic analysis revealed a total of 3,737 proteins detected in at least one of the groups (PBS sEVs or pl:C sEVs) across all three biological replicates. Remarkably, within our samples, we identified 90 out of the top 100 frequently reported exosome proteins listed in the ExoCarta database. The ExoCarta database serves as a comprehensive repository documenting the molecular cargo of exosomes identified in studies aimed at characterizing exosome content (Keerthikumar et al., 2016). This finding further substantiates the enrichment of exosomal content within our sEV preparations.

Principal component analysis (PCA) revealed clear clustering of replicates from the two experimental groups, with distinct separation along the first principal component (Fig. 34B). This outcome aligns with our initial hypothesis, which anticipated differences in sEV content between the two conditions. Differential enrichment analysis identified 43 proteins that were consistently upregulated in pl:C-induced sEVs compared to PBS-induced sEVs across all biological replicates (Fig. 34C). To categorize these 43 differentially quantified proteins in terms of their biological functions and pinpoint significantly enriched processes, we conducted Gene Ontology (GO) enrichment analysis (Fig. 34D). This analysis highlighted the overrepresentation of processes related to immune responses, such as defense against viruses (GO:0051607; involving Bst2, Ifit1, Oasl2, and Oasl1) and the type I IFN signaling pathway (GO:0060337; involving Stat1 and Stat2). This firmly established that inflammation-specific proteins are indeed significantly enriched in BM sEVs during inflammation.

## Results

In summary, our dataset confirms the feasibility of conducting proteomic analyses on sEV samples and highlights specific changes in the cargo of BM exosomes in response to inflammatory stress. Nevertheless, these findings represent preliminary data, and further analyses are required to validate these observations.

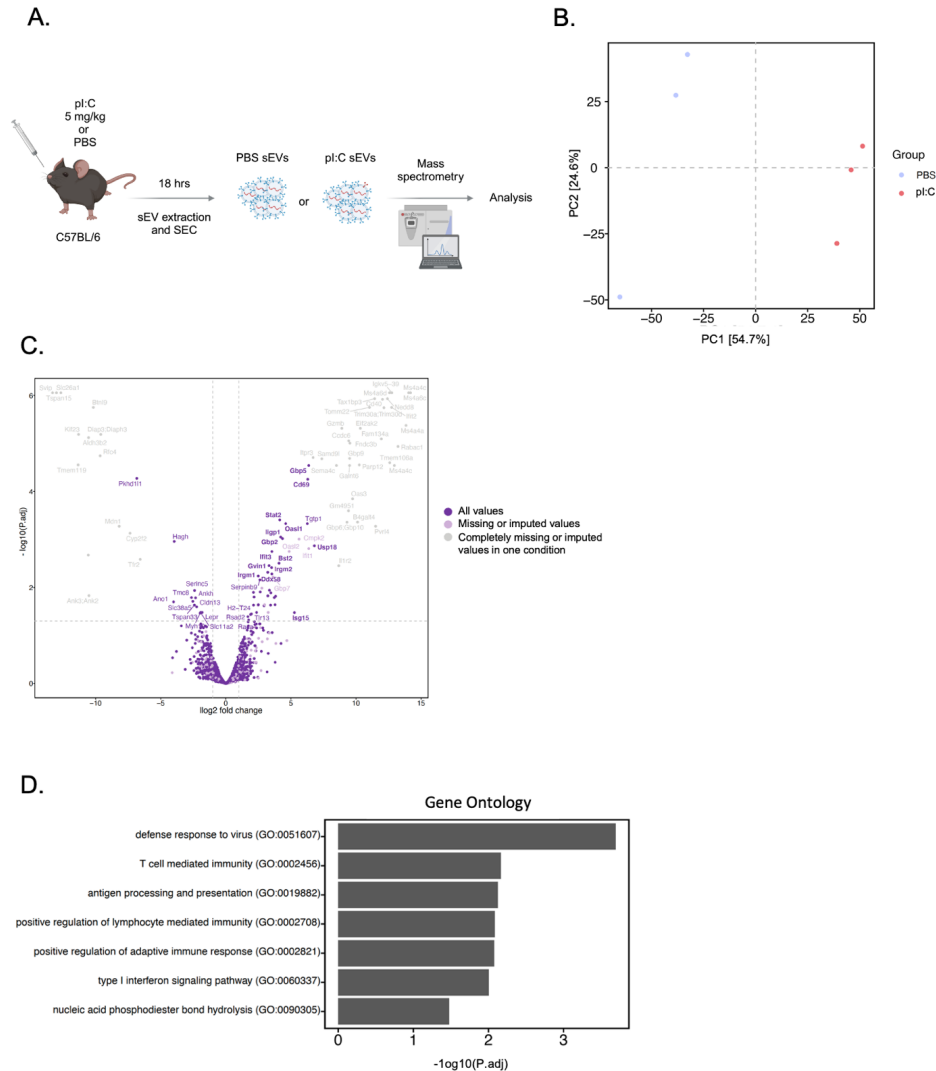


**Figure 34 | Alterations in the proteomic composition of sEVs isolated from murine BM in response to inflammatory stress.**

(A) Experimental design overview: WT mice received i.p. treatment with either 5 mg/kg pl:C (pl:C sEVs) or an equivalent volume of PBS (PBS sEVs). After 18 hours, the mice were euthanized for the isolation of sEVs. The collected sEVs were subsequently subjected to label-free mass spectrometry-based proteomic analysis. Created with BioRender.com. (B) Principal Component Analysis (PCA) on PBS sEVs and pl:C sEVs using intensity-based absolute quantification (iBAQ) values for quantified proteins. iBAQ values were normalized to the theoretical peptide count for each protein. (C) Volcano Plot showing the differential protein expression between PBS sEVs and pl:C sEVs. A total of 3,737 variables were plotted, with data obtained from three replicates. The analysis considered a Log<sub>2</sub> fold change cutoff of 1 and a *p*-value cutoff of 0.05. *P*-values were adjusted using the Benjamin-Hochberg method. (D) Representation of top Gene Ontology (GO) terms related to "biological processes" among the significantly differentially expressed proteins detected in all samples of each condition. The analysis was performed with three replicates. Experiments performed jointly with Marie-Elen Tichel.

## 4. Discussion and future direction

### 4.1 IFN signaling heterogeneity in non-HSC derived hematopoietic cells

Stem cells exhibit resistance to viral infections (Wu et al., 2018; Wu, Kwong, & Rice, 2019), a remarkable feature absent in their differentiated progeny. This intriguing property, previously unexplained, has recently been attributed to an inherently high level of ISGs, which serve as a natural innate defense mechanism against viral infections (Wu et al., 2018).

Our laboratory has confirmed the elevated intrinsic expression of ISGs in HSCs, which decreases upon differentiation. Furthermore, research within our group has identified intrinsic IFN signaling heterogeneity within the hematopoietic system, present at the HSC level and inherited by all subsequent populations. However, the source of this heterogeneity remains an open question. Recent findings from our group suggest that this heterogeneity emerges with the development of the first definitive HSCs at E10.5, hinting at its origin prior to definitive hematopoiesis (Werner et al., in preparation).

In my thesis, I investigated the intrinsic ISG expression levels in TRMs from two distinct sites: the CNS and the peritoneal cavity. I selected these two sites due to the substantial evidence suggesting that microglia in the CNS (Florent Ginhoux et al., 2010) and the large LPMs in the peritoneal cavity (Cassado, D'Império Lima, & Bortoluci, 2015; Yona et al., 2013) originate from embryonic precursors. My data revealed an upregulation of ISG expression in TRMs from both sites in adult mice. Given the evidence from our group that baseline IFN signaling is a stable and inheritable property, this suggests that the relatively high intrinsic IFN signature of TRMs originates during embryonic development and persists into adulthood. The biological relevance of this high baseline IFN signaling in TRMs can be attributed to their original role in protecting the developing embryo against infections (Dzierzak & Bigas, 2018). This intrinsic high expression of ISGs is critical in ensuring innate protection against infections (Wu et al., 2018), and facilitating a rapid and efficient response to stress conditions (Werner et al., in preparation). However, ISG signature in embryonic TRMs remains unexplored, representing a crucial area for further investigation

Moreover, my research has uncovered heterogeneity in IFN signaling within both microglia and LPMs. This constitutes initial evidence suggesting that IFN signaling heterogeneity may originate earlier in embryonic development than previously anticipated. To gain a deeper understanding of this phenomenon, one could explore whole embryo or embryonic organ imaging in *ISRE-eGFP* mice at various developmental time points. This

imaging could be complemented with the use of surface markers specific to TRMs or embryonic HSCs to ascertain the exact point in development in which IFN signaling heterogeneity emerges or is established.

Interestingly, the ratio of cells expressing a higher intrinsic level of ISG expression (ISRE-eGFP<sup>high</sup>) to those with a lower expression (ISRE-eGFP<sup>low</sup>) was significantly higher in microglia and LPMs compared to their monocyte-derived counterparts. Both microglia (Thompson & Tsirka, 2017) and LPMs (Derek W. Cain et al., 2013) have been demonstrated to participate in tissue repair and maintenance, as well as play a role in response to infection and inflammation. Notably, these cell types have the capacity to adopt both an M1 phenotype, which is pro-inflammatory, and an M2 phenotype, which is anti-inflammatory, depending on the specific experimental conditions (Cassado et al., 2015; Ghosn et al., 2010; Thompson & Tsirka, 2017). In light of these findings regarding the intrinsic IFN signaling heterogeneity in TRMs, this raises the intriguing possibility that the M1 and M2 phenotypes could be linked to the differential IFN signaling heterogeneity observed. This potential correlation warrants further in-depth investigations and analysis.

Another promising avenue for the study of IFN signaling heterogeneity is the exploration of epigenetic factors that regulate the high and low intrinsic expression of ISGs. The stable inheritance of the intrinsic signaling status hints towards epigenetic regulation, which warrants further investigation. This can be achieved through global methylome analysis by tagmentation-based whole genome bisulfide sequencing (TB-WGBS) (Lu et al., 2015), histone modification analysis by chromatin immunoprecipitation followed by massively parallel DNA sequencing (ChIP-seq) (Landt et al., 2012), or chromatin accessibility by assay for transposase-accessible chromatin using sequencing (ATAC-seq) (Buenrostro, Wu, Chang, & Greenleaf, 2015). Insights derived from such an analysis would bring us one step closer to understanding how IFN signaling heterogeneity is maintained, its origin, and the full spectrum of its biological relevance.

### **4.2 IFN signaling heterogeneity and leukemia progression**

Cellular heterogeneity plays a crucial role in complex biological systems, contributing to developmental processes, maintaining normal system functions, and even influencing pathological states. The emergence of single-cell omics along with sophisticated tools designed for high-throughput analysis has been the driving force in uncovering intracellular heterogeneity, especially within rare cells such as HSCs. This is not possible with traditional

bulk analyses since it only provides an average reading of a particular population, obscuring differences present in individual cells ("A focus on single-cell omics," 2023).

With single-cell technologies simultaneously diving into various avenues such as the genomics, proteomics, or epigenomics, we now possess a detailed, multilayered overview of single cells or cellular states at an impressive resolution. However, the consequence of many of the uncovered heterogeneities are yet to be fully explained. One such example is intrinsic IFN signaling heterogeneity within HSCs. While our group has extensively characterized IFN heterogeneity in the hematopoietic system, its contribution in pathological states, such as in clonal hematopoietic malignancies remains unexplored.

### 4.2.1 ISG-CML mouse model

My research is dedicated to addressing this question in the context of CML. CML presents an ideal subject for investigation due to its nature as a clonal hematopoietic malignancy primarily driven by the *BCR::ABL1* mutation within HSCs (Hoffman et al., 2008; Wintrobe & Greer, 2014). Much of our current knowledge about CML biology *in vivo* is derived from pioneering studies utilizing various mouse models, such as the *BCR::ABL1* retroviral murine CML model (R. El Eit et al., 2019; Pear et al., 1998). These studies were predominantly based on total bone marrow transplantation of transformed donor cells into lethally irradiated recipient mice. At that time, HSCs were largely perceived as a homogenous population, and little was known about HSC heterogeneity and its potential role in clonal expansion under normal or disease conditions.

To facilitate my research, I adapted the well-established *BCR::ABL1* retroviral mouse model, which involves viral delivery of the oncogene into HSCs, leading to the rapid and efficient induction of a CML-like disease in mice (R. El Eit et al., 2019; R. M. El Eit et al., 2014; Pear et al., 1998). The underlying principle was to introduce the *BCR::ABL1* mutation into eGFP<sup>high</sup> and eGFP<sup>low</sup> HSCs, taken from *ISRE-eGFP* donors, thereby transforming them into LSC with corresponding intrinsic ISG expression. Resulting eGFP<sup>low</sup> or eGFP<sup>high</sup> LSC populations were subsequently transplanted into WT recipients, leading to the generation of a CML-ISG double reporter mouse model.

Although my results demonstrate that eGFP<sup>high</sup> and eGFP<sup>low</sup> HSCs respond similarly within the selected experimental parameters, 5-FU treatment had a profound impact on the system, driving the majority of HSCs into the cell cycle. While this may increase retroviral transduction efficiency, the long-term consequences of this robust extrinsic inflammatory

challenge cannot be overlooked. This is especially relevant when considering that severe inflammation, such as that induced by the 5-FU treatment, has been shown to result in an irreversible HSC function depletion (Bogeska et al., 2022) while simultaneously favoring the development of mutant clones resistant to an inflammatory microenvironment, thereby promoting the onset of myeloid hematologic malignancies (B. M. Craver, K. El Alaoui, R. M. Scherber, & A. G. Fleischman, 2018). Therefore, it is possible that the 5-FU treatment, combined with intrinsic IFN heterogeneity, could favor the clonal expansion of one LSC clone over the other, a factor that cannot be accounted for in my model. As a result, I decided to exclude 5-FU treatment in all leukemic transplantation experiments.

### 4.2.2 Clonal expansion of eGFP<sup>low</sup> leukemic cells

In total BM transplantations, my results reveal a clear and pronounced clonal expansion of leukemic cells expressing a low intrinsic inflammatory signature (mCherry<sup>+</sup> eGFP<sup>low</sup>) in the PB, spleen and BM of primary mice. This aligns with recent studies indicating downregulation of ISGs, such as *IFIT2* (Z. Zhang et al., 2020) and *IRF8* (Miyawaki et al., 2013), in BM samples of CML patients. Further support is provided by a study reporting a general downregulation of ISGs in *BCR::ABL1*-expressing cells in mice and humans, which was attributed to the downregulation of genes specific to the IFN signaling pathway, such as *STAT1*, *STAT2* and *IRF9* (Schubert et al., 2019).

Interestingly, despite being the dominant clone, leukemic eGFP<sup>low</sup> HSCs showed a significantly reduced cycling activity compared to GFP<sup>high</sup> HSCs, with eGFP<sup>low</sup> HSCs in the BM being mostly quiescent. Given that these cells share the same marker selection and responded similarly to 5-FU and *in vitro* pre-stimulation, the difference in their cycling behavior is particularly intriguing. Our research group has previously demonstrated that eGFP<sup>high</sup> cells are more sensitive to inflammatory stimuli, such as viral infections, resulting in a more significant increase in ISG expression compared to their eGFP<sup>low</sup> counterparts (Werner et al., in preparation). In the context of CML, it is possible that *BCR::ABL1* expression in eGFP<sup>high</sup> cells, combined with the inflammatory milieu associated with CML, drives these cells to cycle at a high rate, leading to their exhaustion and depletion (Bogeska et al., 2022; Caiado et al., 2021; Demerdash et al., 2021; Ho & Takizawa, 2022).

These findings were further validated in secondary mice. Serial transplantation is the gold standard for assessing HSC self-renewal and multilineage potential (Harrison, Astle, & Delaitre, 1978; Harrison, Stone, & Astle, 1990; Ramkumar, Gerstein, & Zhang, 2013). Accordingly, it was expected that eGFP<sup>low</sup> LSCs would out compete eGFP<sup>high</sup> LSCs, given their

lower activity in the cell cycle in donor primary leukemic mice (Bogeska et al., 2022; Caiado et al., 2021; Demerdash et al., 2021; Ho & Takizawa, 2022). In these mice, the analysis CMPs was also performed since they are believed to initiate the overexpansion of cells in CML (Miyawaki et al., 2013). The analysis revealed clonal dominance of eGFP<sup>low</sup> clones, concurrent with significantly increased cycling activity compared to eGFP<sup>high</sup> clones in both the BM and spleen.

It is important to note that the clonal expansion and cell cycle analysis of HSPCs in the bone marrow and spleen in both primary and secondary mice represent a snapshot of a single time point. Future experiments should incorporate multiple time points, allowing for a longitudinal analysis of clonal expansion and cycling, commencing from early time points post-transplantation and concluding at euthanasia due to leukemia burden. Furthermore, single cell experiments with the transplantation of a single eGFP<sup>low</sup> or eGFP<sup>high</sup> LSCs should also be considered. Assays such as terminal deoxynucleotidyl transferase (TdT) dUTP Nick-End Labeling (TUNEL) assay should be employed to evaluate cell death in eGFP<sup>low</sup> and eGFP<sup>high</sup> HSPCs at different sites and timepoints. These experiments would provide a better understanding of the kinetics of clonal expansion of eGFP<sup>low</sup> and eGFP<sup>high</sup> clones, revealing the exact time when clonal dominance occurs at the progenitor level, and confirming that eGFP<sup>high</sup> HSCPs are indeed depleted due to their high proliferation rates.

100% chimeric eGFP<sup>low</sup> or eGFP<sup>high</sup> mice further confirmed my findings. Analysis of PB revealed that the eGFP<sup>low</sup> chimeras exhibited a notably faster expansion of leukemic cells compared to the eGFP<sup>high</sup> chimeras. Furthermore, survival analysis between these two groups yielded a striking difference. Despite both groups being transplanted with equal numbers LSCs and the detection of leukemia in all mice within each group, eGFP<sup>low</sup> chimaeras succumbed to leukemia significantly faster than eGFP<sup>high</sup> chimaeras. These findings strongly suggest that LSCs with a low intrinsic IFN signaling (eGFP<sup>low</sup> LSCs) tend to generate a more aggressive form of leukemia. Interestingly, unlike in the total BM transplantation setting, there was no noticeable differences in cycling activity or clonal expansion of HSPCs between the two groups. This observation hints at a delicate interplay between the two clones in orchestrating the disease. To address this intriguing observation, it would be essential to replicate these experiments while incorporating normal WT rescue BM while generating 100% eGFP<sup>low</sup> and eGFP<sup>high</sup> chimaeras. This would create a setting that more closely resembles what is observed in patients, generating a scenario that is less extreme and artificial. Histopathological analysis of the spleen and liver at different time points would also be essential to explain differences in observed kinetics and pathologies.

### 4.2.3 Nilotinib Treatment

Treatment with the TKI nilotinib was successful in suppressing leukemia expansion in most of the treated mice. Mice that didn't respond well to nilotinib showed clonal expansion of eGFP<sup>low</sup> leukemic cells, suggesting that treatment resistance in CML may be attributed to clones originating from LSCs with a low intrinsic IFN signaling signature. This aligns with previous reports showing that successful TKI treatment reverses the downregulation of ISGs in patients (Schubert et al., 2019), and patients who retain low ISG expression levels in response to anti-leukemic therapies fail to achieve cytogenetic responses (Kawakubo et al., 1996).

Secondary mice generated from nilotinib treated donor mice showed a similar pattern to that of secondary mice from untreated leukemic donors, demonstrating the dominance of eGFP<sup>low</sup> LSCs. Resistance to TKI therapy and the clonal expansion of eGFP<sup>low</sup> clones may be attributed to the quiescent state of eGFP<sup>low</sup> LSCs. This is in line with data suggesting that relapse and resistance in CML are mediated by quiescent LSCs which are less susceptible to TKI therapy (Tanaka et al., 2022). It's important to note that a larger sample size for both primary and secondary mice, along with comprehensive gene expression analysis, is required to substantiate these conclusions.

Several combination-based treatment protocols have been suggested to target LSC and increase the rate of sustained deep molecular response (DMR), a prerequisite for drug discontinuation (Branford, 2020). The most notable of these combinations includes TKIs with venetoclax (ABT-199, highly selective BCL-2 inhibitor) (Jabbour & Kantarjian, 2022), decitabine (DAC, hypomethylation agent) (Jabbour & Kantarjian, 2022) or IFN (Jabbour & Kantarjian, 2022). Given the potential differences in disease progression indicated by my preliminary data, it is conceivable that there would also be differences in the response to these treatments, with some therapies better suited for one LSC clone over the other. Therefore, it would be intriguing to test the efficacy of nilotinib alone (Weisberg et al., 2005), or in combination with venetoclax (Carter et al., 2016), decitabine, or IFN against leukemia driven by eGFP<sup>low</sup> or eGFP<sup>high</sup> LSCs in 100% chimeras. This approach takes into consideration the potential variations in treatment response based on LSC clone characteristics.

#### 4.2.4 Future directions and other models

My current findings open up new insights into the role of IFN signaling heterogeneity in CML LSC clonal expansion and disease progression. This knowledge holds the potential to significantly enhance our understanding of CML and, consequently, our ability to manage this disease effectively. However, it is essential to acknowledge that my current approach introduces several extrinsic inflammatory signals during the transduction and irradiation steps, which could potentially influence the results. To address this concern, it is crucial to validate these findings using another independent CML-ISG reporter model based on *SCLtTA/BCR::ABL1* transgenic mice. These mice allow for the inducible expression of the *BCR::ABL1* oncogene in stem and progenitor cells of the BM using a tetracycline-off (tet-off) system, where tTA is under the control of the *SCL* gene 3' enhancer (Koschmieder et al., 2005). Therefore, crossing *SCLtTA/BCR-ABL1* with our *ISRE-eGFP* reporter will generate a second CML-ISG reporter (*SCLtTA/BCR-ABL1flo<sub>x2</sub>/ISRE-eGFP*) that doesn't depend on *in vitro* viral transduction of *ISRE-eGFP* donors. In this model, BM from *SCLtTA/BCR-ABL1flo<sub>x2</sub>/ISRE-eGFP* mice will be sorted into the eGFP<sup>low</sup> and eGFP<sup>high</sup> fractions and transplanted into NSGW41 recipients with continuous supply of tetracycline. These NSGW41 mice harbor the spontaneous *Kit<sup>W-41J</sup>* allele, which induces the loss of *Kit* function. Consequently, endogenous HSCs within the NSGW41 mice are impaired, allowing the engraftment of donor HSCs without the need for irradiation (Cosgun et al., 2014). Eight weeks post-transplantation, tetracycline will be removed to induce eGFP<sup>low</sup> or eGFP<sup>high</sup> LSC production and leukemia development. Another added advantage of this model is that it produces a disease more closely resembling the chronic phase (CP)-CML observed in patients (Koschmieder et al., 2005).

Another potential approach to investigate the loss of eGFP<sup>high</sup> LSCs in a total transplantation setting would involve crossing *ISRE-eGFP* reporters with *SCLCreERT Bax<sup>flx/flx</sup>Bak<sup>-/-</sup>* mice. The latter is a transgenic mouse line that allows for the conditional deletion of *Bax*, combined with the *Bak1* null allele, in stem and progenitor cells of the BM upon tamoxifen treatment (Takeuchi et al., 2005). This strategy would generate an IFN signaling mouse line (*SCLCreERTBaxflo<sub>x2</sub>/Bak<sup>-/-</sup>/ISRE-eGFP*) with HSPCs that are incapable of undergoing apoptosis due to the *Bax<sup>-/-</sup>/Bak<sup>-/-</sup>* double knock out. Accordingly, BM from these mice would be transduced with MSCV-BCR::ABL1-mCherry viral preparations to transform HSCs into LSCs. These LSCs would then be transplanted into NSGW41 recipients, leading to leukemia development. Analyzing the frequency of eGFP<sup>low</sup> and eGFP<sup>high</sup> LSCs in the BM and spleen would help confirm whether the loss of eGFP<sup>high</sup> LSC clones is indeed driven by cell death resulting from high proliferation and an intrinsically high IFN signaling signature.

CML, like many malignancies, manifests as a heterogeneous disease. This variability can be attributed to the diverse nature of the original malignant CML clones or the influence of the inflammatory signature within the BM niche. My preliminary data strongly indicates that CML arising eGFP<sup>low</sup> LSCs presents with a more rapid and aggressive phenotype. Therefore, there is a compelling need to uncover the molecular mechanisms that underlie this phenotype. To comprehensively dissect the molecular mechanism driving the distinct phenotypes of eGFP<sup>low</sup> and eGFP<sup>high</sup> LSCs, a temporal multi-omics approach is instrumental. This strategy combines global gene expression analysis through RNA sequencing (RNA-seq), epigenetic profiling via the assay for transposase-accessible chromatin with high-throughput sequencing (ATAC-seq), and proteomic analysis by mass spectrometry (mass spec) at various time points throughout disease progression. Employing this multi-omics approach enables us to track and compare the dynamic changes in transcriptional, epigenetic, and translational profiles under different experimental conditions as leukemia evolves. The integration of data across these multiple parameters over time offers a more comprehensive understanding of the underlying mechanisms and their evolution throughout the course of the disease.

Given that CML is associated with a chronic inflammatory state that likely fosters the development of mutant clones, it becomes crucial to characterize the inflammatory signature linked to the expansion of eGFP<sup>low</sup> and eGFP<sup>high</sup> LSCs in the BM of leukemic mice. This analysis will aid our comprehension of the mechanisms governing the clonal expansion of each clone and could potentially improve treatment outcomes. This can be achieved by characterizing the BM inflammatory signature of 100% eGFP<sup>low</sup> or eGFP<sup>high</sup> chimaeras or leukemic mice generated by total BM transplantation. Different time points of the disease development can be selected for analysis using assays such as the Immune Monitoring 48-plex Mouse ProcartaPlex Panel with a Bio-Plex 200 system.

### **4.2.5 Translational studies**

Perhaps the most intriguing future prospect of this project is to corroborate these findings in humans and investigate IFN signaling heterogeneity in CML patients. Clinical material from CML patients, such as blood and bone marrow aspirates whenever possible, could be obtained for this purpose. This is possible for my purposes since simultaneous peripheral blood and marrow qRT-PCR studies show a high level of concordance in patients (Jabbour & Kantarjian, 2022), and because our data shows a stable inheritance of the ISG signature from stem to differentiated cells. The material collected from newly diagnosed CML patients would be used to evaluate ISG expression levels in leukemic cells to check for ISG

heterogeneity in CML patients' leukemic cells. Furthermore, the ISG signature from patients responding to, or resistant to frontline TKI therapy, as well as patients relapsing or achieving treatment-free remission (TFR), would be determined. These results would be compared to our preclinical studies to identify patterns and validate our findings.

Finally, since chronic inflammatory conditions are associated with the development of various myeloid hematologic malignancies, it would be interesting to investigate the contribution of IFN signaling heterogeneity in other hematological diseases and myeloproliferative neoplasms (MPNs) such as polycythemia vera. This broadens the scope of our understanding of the impact of IFN signaling heterogeneity on pathologies and may lead to the development of more targeted and effective therapies for such conditions.

### **4.3 sEV signaling in the BM**

#### **4.3.1 sEV extraction, purification and characterization**

sEVs play a pivotal role in cell-to-cell communication across various cell types (Kalluri & LeBleu, 2020). Their distinguishing feature lies in the remarkable capability of sEVs, particularly exosomes, to transport a diverse and dynamic cargo to target cells with high precision (Berumen Sánchez et al., 2021; Hazan-Halevy et al., 2015; Rana et al., 2012; Toda et al., 2015). Notably, the messages conveyed by sEVs exhibit a remarkable adaptability to environmental and physiological cues, surpassing the capabilities of traditional soluble molecules and proteins as signaling agents (Pitt et al., 2016). These properties make sEV-based communication appealing in nanomedicine applications, offering the potential for innovative therapeutics that could revolutionize the field.

Recent years have witnessed a surge in interest in sEV-based therapeutics, particularly focusing on exosomes, prompting numerous pharmaceutical companies to initiate manufacturing processes (Ahn et al., 2022). As a result, research in the field has pivoted towards refining the classification of sEVs and enhancing collection and purification protocols, aiming to adhere to good manufacturing practices (Ahn et al., 2022; Chen, Lin, Chiou, & Harn, 2020).

However, challenges persist in the field, primarily the lack of standardized methods for isolating and purifying sEVs, coupled with the ongoing evolution of EV classification and associated markers (Kalluri & LeBleu, 2020; Théry et al., 2018). Serial centrifugation has

traditionally been considered the gold standard for sEV isolation due to its reasonable purity (Konoshenko, Lekchnov, Vlassov, & Laktionov, 2018; Théry et al., 2006). Nevertheless, it tends to co-isolate contaminants such as protein aggregates which significantly impacts reproducibility and reliability. The major caveats would lie in factoring out the influence of co-precipitated contaminants as well as replicating consistent sEV yields between experiments.

To overcome these challenges, researchers have explored additional purification steps in conjunction with serial centrifugation. One such attempt involved the inclusion of a 30% sucrose density gradient ultracentrifugation step aimed to better separate sEV subclasses and eliminate protein contaminants. Although this approach showed some promise, it was overshadowed by low yields and poor reproducibility (Kalluri & LeBleu, 2020; Théry et al., 2018). Immunogenic assays based on immunocapturing of vesicles have also been proposed, but the elution of sEVs from the bead surface posed challenges that also compromised yields and reproducibility. Furthermore, these methods were subject to criticism due to the choice of markers, which is an ever-changing factor introducing bias in isolation (Clayton et al., 2001).

Our research addresses these challenges, revealing that incorporating SEC after serial centrifugation positively impacts sEV isolation and purification. This approach efficiently minimizes the co-sedimentation of contaminating proteins during ultracentrifugation, addressing one of the most significant limitations in sEV isolation. Notably, particle-enriched SEC fractions exhibited a considerably low particle-to-protein ratio, and the reduced protein background in TEM micrographs, indicating enhanced purity. Moreover, it enables the enrichment of exosomes, which are of great interest in the field due to their well-established role as mediators of cell-to-cell communication (Jia et al., 2022; Kalluri & LeBleu, 2020; Wang et al., 2021). Indeed, particle-enriched SEC fractions showed enrichment for sEVs in the size range of 40-160 nm, characteristic of exosomes. These findings were further corroborated by a notable increase in the frequency of cup-shaped vesicles in TEM micrographs and higher band intensity of exosome protein markers determined through Western blotting. Our results align with recent reports highlighting the benefits of incorporating SEC into sEV isolation, showing improvements in yield, purity, particle number, particle-to-protein ratio, and sEV marker signals (Diaz et al., 2018; Takov, Yellon, & Davidson, 2019). Importantly, our method demonstrates consistency and reliability, allowing for the reproducible production of similar yields and purity in replicate experiments, facilitating meaningful comparisons and robust conclusions.

While our method addresses current challenges, emerging techniques such as nano-scale flow cytometry, imaging flow cytometry, immunoelectron microscopy, and digital immune

assays for absolute protein quantification are promising avenues for advancing sEV characterization. Future experiments should consider incorporating these evolving techniques to meet the growing demands for comprehensive sEV quality assessment.

### 4.3.2 sEV signaling in response to inflammatory stress

In the BM, sEVs have emerged as pivotal regulators of both the hematopoietic and stromal compartments (De Luca et al., 2016; Goloviznina et al., 2016; Huan et al., 2013; Kumar et al., 2018). Particularly under inflammatory stress, HSCs display a reversible activation, transitioning from quiescence to active division to replenish depleted cells before returning to a quiescent state (Essers et al., 2009). Despite the vital nature of this response, attempts to recapitulate it *in vitro* using inflammatory cytokines have proven challenging. This observation reveals the intricate nature of this response, highlighting the requirement for the collective involvement of various components within the BM niche. In light of the recent discoveries regarding the extensive intracellular crosstalk between BM elements in response to stress (Butler et al., 2018; Morrison & Scadden, 2014), coupled with the recognized role of sEV signaling in stressed BM (De Luca et al., 2016; Goloviznina et al., 2016), we propose that sEV signaling plays a crucial role in orchestrating the systemic response to inflammation.

Examination of both rMSC and total BM sEVs revealed similar patterns in response to inflammatory challenge. In both cases, inflammatory stimulation led to an increase of absolute particles number, which was congruent with an increase of absolute protein. Longitudinal analysis of BM sEVs demonstrated a dynamic increase in protein content, peaking at 9 hours before gradually returning to near-homeostatic levels at 24 hours. This dynamic release of sEVs in response to inflammation suggests a potential functional role in inflammation regulation. Indeed, GO enrichment analysis of the global protein cargo identified an enrichment of ISGs, indicating a correlation with processes related to immune response and inflammation. Furthermore, proteomic analysis further unveiled the enrichment of Stat2 protein in BM sEVs at 18 hours post pl:C treatment. Considering that HSC proliferation in response to inflammation peaks at 24 hours and is Stat-dependent (Essers et al., 2009), this suggests a potential role for sEVs in orchestrating the inflammatory response of HSCs *in vivo*.

Given that the recorded response is specific to pl:C, a double-stranded RNA complex mimicking viral infections (Kawai & Akira, 2006), this implicates sEVs in actively regulating anti-microbial immune responses, consistent with reports demonstrating their role in modulating both innate and adaptive immunity. For instance, EVs in sepsis have been found to have a pro-inflammatory effect inducing leukocyte chemotaxis, macrophage polarization to

an M1-type phenotype, cytokine secretion, and differentiation of naive T cells into T helper. This was accomplished by their rich cargo encompassing high-mobility group box 1 (HMGB1), histones, and cytokines among others (Burgelman, Vandendriessche, & Vandenbroucke, 2021; Buzas, 2023).

While the mean particle size remained comparable between homeostatic and inflammatory conditions, a discernible variation in particle size distribution in the enriched fractions hinted at the release of larger particles, potentially influencing inflammatory responses. This aligns with recent findings demonstrating that large EVs derived from activated platelets can modulate adaptive immunity by transferring MHC class I complexes, co-stimulatory molecules (OX40L, CD40L, and CD40), as well as 20S proteasomes into T cells. This leads to the proliferation of antigen-specific CD8<sup>+</sup> T cells by enabling them to process exogenous antigens and load the resulting peptides onto MHC class I molecules (Marcoux et al., 2021).

Considering the dynamic nature of the inflammatory response in the BM, which involves the intricate crosstalk among different components of the microenvironment (Butler et al., 2018; Morrison & Scadden, 2014), a comprehensive longitudinal analysis of total BM sEV cargo (DNA, RNA, protein, metabolites, and lipids) spanning the entire acute inflammatory response (0 to 72 hours) becomes imperative. Such a longitudinal analysis, encompassing the entire spectrum of bio-molecules, would elucidate the role of sEV signaling and identify precise molecular players in orchestrating HSC activation and re-entry into quiescence. Subsequent functional experiments involving the overexpression or silencing of identified candidates could validate these findings, providing a deeper understanding of the regulatory mechanisms governing the inflammatory response

#### **4.3.4 *In vitro* treatment of HSPCs with sEVs**

Treatment of LSKs with sEVs *in vitro* revealed a block in proliferation only with pl:C-induced BM sEVs, and not with PBS-induced BM sEVs. However, co-treatment of PBS-induced BM sEVs with IFN $\alpha$  led to a pronounced proliferation block compared to individual treatments. This raises the possibility that BM sEVs help maintain HSCs in a quiescent state. This aligns with existing reports demonstrating that MSC-derived sEVs suppress inflammation by targeting toll-like receptor 4 and programmed cell death 4 through the delivery of miR-21-5p (Niu et al., 2023). Additionally, MSC-derived vesicles were found to preserve HSC functions by delivering transforming growth factor- $\beta$  (TGF- $\beta$ ) signal transducer Smad2 (Gautheron, Georgievski, Garrido, & Quéré, 2023), and miR-21, miR27a and miR-181 (De Luca et al.,

2016) to HSCs. The treatment of HSCs with pl:C-induced BM sEVs further supported these findings, revealing a downregulation of genes known to be overexpressed in HSCs upon inflammatory stimulation, such as *Pml*, *Bst2*, and *Psap* (Demerdash et al., in preparation).

Prolonged treatment of HSCs with IFN $\alpha$ -induced rMSCs sEVs revealed a slight bias towards MPP2. This finding aligns with a prior study demonstrating that MSC-derived EVs mediate HSPC expansion toward myeloid progenitors (Goloviznina et al., 2016). Another study also suggested that osteoblast-derived EVs increased myeloid differentiation, cellular proliferation, and protein translation in HSPCs via the transfer of processed transfer RNA (tiRNA) 5'-ti-Pro-CGG-1 (Kfoury et al., 2021).

Furthermore, total BM sEVs resulted in a dose-dependent increase in apoptotic cell death in LSKs, a phenomenon dramatically accentuated when combined with IFN $\alpha$ . This hints at an over sensitization of cells in response to this artificial setting.

It is crucial to acknowledge the preliminary nature of these results. While they highlight the potential involvement of sEVs in directly modulating the inflammatory response of HSPCs, it is essential to acknowledge that certain critical aspects remain unexplored. This limitation is primarily attributed to the current constraints inherent with *in vitro* culture systems. For instance, the impact of sEVs on HSCs may be indirect, affecting other elements or components of the niche, subsequently influencing HSPC function. The effect may also be additive, depending on sEV signaling, combined with direct cellular interactions with other niche components (such as MSCs, endothelial cells, or the extracellular matrix). Other environmental cues, including pH, oxygen levels, cellular density, and external factors, may also contribute to the overall effect. A good example on this is clearly described in myeloma, where myeloma-derived EVs remodel the extracellular matrix by digesting heparan sulfate proteoglycans, promoting tumor invasion and metastasis (Patel, Ashraf, & Chung, 2023; Sanderson, Bandari, & Vlodaysky, 2019). Along these lines, IL-8 within CML sEVs promote angiogenesis and tumor development by increasing the expression of intercellular adhesion molecule-1 (ICAM-1) and vascular cell adhesion molecule-1 (VCAM-1) by endothelial cells (Taverna et al., 2012). These complexities underscore the need for more sophisticated *in vitro* systems to decipher the interplay between sEVs, HSPCs, and the intricate BM microenvironment during inflammatory response.

#### 4.3.5 *In vivo* treatment of mice with sEVs.

Administering mice with inflammatory BM sEVs successfully replicated the impact of pl:C treatment on myeloid cell parameters in the blood. This is consistent with reports indicating the heightened responsiveness of myeloid cells to sEVs due to their receptor compatibility and robust phagocytic and pinocytotic capabilities (Makhijani & McGaha, 2022). However, no effect was seen on the cycling of LSKs in the BM. Preliminary *in vitro* data hint at the antiproliferative potential of pl:C-induced BM sEVs on HSPCs. Thus, a critical next step involves investigating the simultaneous treatment of mice with pl:C and inflammatory sEVs to ascertain whether pl:C-induced sEVs can counteract the proliferative effects of pl:C treatment on LSKs (Essers et al., 2009). Additionally, exploring alternative administration routes, such as intrafemoral injection, is warranted to overcome potential loss of sEV activity due to hepatic and renal clearance (Ha et al., 2016; Muthu et al., 2021).

An essential consideration in evaluating the effects of BM sEVs *in vivo* is the timing of analysis post-treatment. Given the diverse cargo of sEVs, they are capable of triggering both rapid and delayed responses. Accordingly, a longitudinal evaluation of blood parameters and the response of HSPCs should be considered for a comprehensive understanding of the temporal dynamics involved.

The role of sEV signaling in remodeling the BM microenvironment has been described in many reports, especially in the context to malignancies promoting invasion and metastasis (Patel et al., 2023; Sanderson et al., 2019) as well as angiogenesis (Taverna et al., 2012). Therefore, simultaneously investigating the impact of BM sEVs on both the hematopoietic and stromal compartments is essential. Understanding the delicate cross-talk between different elements in executing these effects offers a closer glimpse into the mechanisms of action and the role of sEVs in orchestrating the acute inflammatory response.

Furthermore, the contribution of sEV signaling in modulating the inflammatory response should be explored using various inflammatory models, such as those induced by lipopolysaccharide (LPS), interferon gamma (IFN $\gamma$ ), or tumor necrosis factor-alpha (TNF- $\alpha$ ). While these major inflammatory molecules operate through distinct signaling pathways, potential overlapping components prompt an intriguing investigation into whether sEVs maintain certain aspects of the signaling and how these responses differ or align across various inflammatory stimuli. This multifaceted exploration promises to provide valuable insights into the role of sEVs in shaping the inflammatory response.

#### 4.3.6 Mouse models for sEV signaling.

Insights derived from *Ifnar*<sup>-/-</sup> and forward chimeras hint at a potential augmentation in homeostatic sEV signaling, likely acting as a compensatory mechanism for the absence of IFNAR in the hematopoietic compartment. This is conceivable considering that *Ifnar*<sup>-/-</sup> mice exhibit no apparent hematologic defects (Essers et al., 2009; Matatall, Shen, Challen, & King, 2014), and that other inflammatory signaling pathways, particularly IFN type II via IFN $\gamma$ , exhibit overlap and synergy with type I signaling. The interplay between these pathways is significant, as IFN $\gamma$  signaling has the capability to induce the production of IFN $\alpha$  (Demerdash et al., 2021). Moreover, data from reverse chimeras suggest that a predominant proportion of sEVs released during the inflammatory response emanates from the hematopoietic compartment. This aligns with existing studies highlighting elevated release of sEVs from stressed HSCs, such as in CML, where the vesicles play a crucial role in enhancing HSC survival and reshaping the BM niche into a pro-leukemic environment (Gao et al., 2019).

A major experimental limitation in the field of EV research lies in the challenge of tracking and imaging sEVs *in vivo* at a reliable resolution (Kalluri & LeBleu, 2020). Despite this constraint, recent efforts have been directed towards developing mouse models tailored to enable the *in vivo* study of EVs. A noteworthy example is the Cre-dependent CD63<sup>flag</sup>-EGFP co-expressed with mCherry protein system (Li et al., 2022). CD63 is expressed at low levels in the plasma membrane, which makes it a suitable specific marker for EVs of endosomal origin. Simultaneously, the incorporation of the mCherry protein co-expression system facilitates the detection and confirmation of specific production sites. This innovative mouse model represents a potent tool to validate and extend my findings. Crossing these mice with *Leptin*, *Pdgfr* or *SCL* Cre mice, for instance, could provide invaluable insights into the *in vivo* origin, quantity, specific targets, and dynamics of released sEVs under inflammatory stress conditions which otherwise is technically challenging. This strategic intersection of advanced mouse models with precise Cre-driven expression systems opens avenues for a deeper understanding of sEV signaling in a multitude of complex *in vivo* scenarios and will significantly contribute to advancing the field.

## 5. Materials and Methods

### 5.1 Materials

#### 5.1.1 Antibodies

**Table 1 | List of flow cytometry antibodies and stains**

Antigen	Label	Clone	Supplier
CD115 (c-fms)	APC	AFS98	eBioscience™
CD117 (cKit)	PE	2B8	eBioscience™
CD117 (cKit)	BV786	2B8	BD Horizon™
CD117 (cKit)	Brilliant Violet 711™	2B8	BioLegend®
CD11b	PE-Cyanine7	M1/70	eBioscience™
CD11b	Brilliant Violet 711™	M1/70	BioLegend®
CD11b	Alexa Fluor™ 700	M1/70	eBioscience™
CD11b	eFluor™ 450	M1/70	eBioscience™
CD11b	PE	M1/70	BD Pharmingen™
CD11b	FITC	M1/70	eBioscience™
CD150	Brilliant Violet 785™	TC15-12F12.2	BioLegend®
CD150	PE-Cyanine7	TC15-12F12.2	BioLegend®
CD150	PE-Cyanine5	TC15-12F12.2	BioLegend®
CD16/32	BUV737	2.4G2	BD Horizon™
CD16/32	BUV496	2.4G2	BD OptiBuild™
CD192 (CCR2)	Brilliant Violet 421™	SA203G11	BioLegend®
CD34	Alexa Fluor™ 700	RAM34	eBioscience™
CD34	BV650	RAM34	BD OptiBuild™
CD34	BV421	RAM34	BD Horizon™
CD4	PE-Cyanine7	GK1.5	eBioscience™
CD4	Biotin	GK1.5	eBioscience™
CD4	Alexa Fluor™ 700	GK1.5	eBioscience™
CD4	FITC	GK1.5	eBioscience™
CD4	PE	GK1.5	eBioscience™
CD45	APC-eFluor™ 780	30-F11	eBioscience™
CD45	Alexa Fluor™ 700	30-F11	eBioscience™
CD45.1	Pacific Blue™	A20	BioLegend®
CD45.2	V500	104	BD Horizon™
CD45.2	Alexa Fluor™ 700	104	eBioscience™
CD45R (B220)	PE-Cyanine7	RA3-6B2	eBioscience™
CD45R (B220)	APC	RA3-6B2	eBioscience™
CD45R (B220)	Alexa Fluor™ 700	RA3-6B2	eBioscience™
CD45R (B220)	FITC	RA3-6B2	eBioscience™
CD45R (B220)	PE	RA3-6B2	eBioscience™
CD48	BUV395	HM48-1	BD OptiBuild™

## Materials and Methods

CD48	BUV737	HM48-1	BD OptiBuild™
CD48	PE	HM48-1	eBioscience™
CD8a	PE-Cyanine7	53-6.7	eBioscience™
CD8a	Biotin	53-6.7	BD Pharmingen™
CD8a	Alexa Fluor™ 700	53-6.7	eBioscience™
CD8a	FITC	53-6.7	eBioscience™
CD8a	PE	53-6.7	eBioscience™
CX3CR1	PE	Q9Z0D9	R&D SYSTEMS
DAPI	350/465nm		Thermo Scientific™
Donkey anti-Rabbit IgG	Alexa Fluor™ 647	polyclonal	Invitrogen
F4/80	PE	T45-2342	BD Pharmingen™
F4/80	PE-Cyanine7	BM8	BioLegend®
FVS780	759/780nm		BD Horizon™
Gr-1 (Ly6G/Ly-6C)	PE-Cyanine7	RB6-8C5	eBioscience™
Gr-1 (Ly6G/Ly-6C)	Alexa Fluor™ 700	RB6-8C5	eBioscience™
Gr-1 (Ly6G/Ly-6C)	FITC	RB6-8C5	eBioscience™
Gr-1 (Ly6G/Ly-6C)	PE	RB6-8C5	eBioscience™
Ki-67	Alexa Fluor® 647	B56	BD Pharmingen™
MHC Class II (I-A/I-E)	Brilliant Violet 786™	M5/114.15.2	eBioscience™
Sca-1 (Ly6A/E)	Brilliant Violet 421™	D7	BioLegend®
Sca-1 (Ly6A/E)	APC-Cy™7	D7	BD Pharmingen™
Sca-1 (Ly6A/E)	PE-Cyanine7	D7	eBioscience™
Siglec-F	BV421	E50-2440	BD Horizon™
Streptavidin	BUV737		BD Horizon™
TER-119	PE-Cyanine7	TER-119	eBioscience™
TER-119	BV786	TER-119	BD OptiBuild™
TER-119	Alexa Fluor™ 700	TER-119	BioLegend®
TER-119	FITC	TER-119	eBioscience™
TIM-4	PE	RMT4-54	BD Pharmingen™
TMEM119	unconjugated	106-6	Abcam

**Table 2 | List of Western Blot antibodies**

Antigen	Source	Supplier	Identifier
<b>Primary antibodies</b>			
Calnexin	Rabbit, monoclonal	Abcam	ab213243
CD81	Rabbit, monoclonal	Cell Signaling TECHNOLOGY®	10037
Cytochrome c	Rabbit, monoclonal	Cell Signaling TECHNOLOGY®	11940
Flotillin-1	Mouse, monoclonal	BD Transduction Laboratories™	610820
GM130	Mouse, monoclonal	BD Transduction Laboratories™	610823
TSG101	Rabbit, monoclonal	Abcam	ab125011
<b>Secondary antibodies</b>			
Anti-mouse IgG1, HRP-linked	Goat	SouthernBiotech	1070-5
Anti-rabbit IgG, HRP-linked	Goat	Cell Signaling TECHNOLOGY®	7074S

## 5.1.2 qRT-PCR primers

Table 3 | List of qRT-PCR primers and sequences

Gene	Primer	Sequence
Reference genes		
<i>β-actin</i>	Forward	CTAAGGCCAACCGTGAAAAG
	Reverse	ACCAGAGGCATACAGGGACA
<i>Oaz1</i>	Forward	TTTCAGCTAGCATCCTGTACTCC
	Reverse	GACCCTGGTCTTGTCGTTAGA
<i>Sdha</i>	Forward	AAGTTGAGATTTGCCGATGG
	Reverse	TGGTTCTGCATCGACTTCTG
ISG genes used in TRM gene expression analysis		
<i>Adar</i>	Forward	TCTGCGCCCTAACCATTGAT
	Reverse	TGTGTCTGGTGAGGGAACAC
<i>Agri</i>	Forward	GTGCAGCACACCTACTCCTG
	Reverse	ACCATCCAGCAGGCTCTCT
<i>Bst2</i>	Forward	GAAGTCACGAAGCTGAACCA
	Reverse	CCTGCACTGTGCTAGAAAGTCTC
<i>Ddx58</i>	Forward	GAGAGTCACGGGACCCACT
	Reverse	CGGTCTTAGCATCTCCAACG
<i>Dhx58</i>	Forward	AGAGACGGTAGACAGAGGCAAG
	Reverse	TCAGGGTTGTTACAGTCCAGTG
<i>Dtx3l</i>	Forward	CAAGTTTGGAGGACCAGCA
	Reverse	TCCTTACTCAATGCCTTTTGC
<i>Eif2ak2</i>	Forward	CCGGGAAAACGAAACAGAAGAG
	Reverse	CCCAGTGGCCAAAGTTTCTG
<i>Gbp6</i>	Forward	CAGGAAGAAGGTTGAACAGGA
	Reverse	GCTCTGAAGGACATGATTTGC
<i>H2-Eb1</i>	Forward	CCTCCAGTGGCTTTGGTC
	Reverse	CTGCGTCCCGTTGTAGAAAT
<i>H2-T10</i>	Forward	CCTCAGATCTCTCAGCACCTG
	Reverse	CGGGTCACATGTGCCTTT
<i>H2-T22</i>	Forward	TGCTGCAGAAATACCTGGAA
	Reverse	TGCCTTTGGAGGGTCTGA
<i>H2-T24</i>	Forward	CATTCCGGCAATACTACAACAGC
	Reverse	TGTGAACTGGAGGGTGTGAG
<i>Ifi44</i>	Forward	CTGATTACAAAAGAAGACATGACAGAC
	Reverse	AGGCAAACCAAAGACTCCA
<i>Ifit2</i>	Forward	CTCTTTTATCCAGAACCACCC
	Reverse	CAGAGTTGAGAGGTTGTGGGA
<i>Ifit3</i>	Forward	GAGATTTCTGAACTGCTCAGCC
	Reverse	ATTCCCGGTTGACCTCACTC
<i>Ifitim1</i>	Reverse	TGACCCAGTACAACCACCT
	Forward	GCTCCTCGACCACACCTCT

Materials and Methods

<i>Ifitm2</i>	Forward	ATTCTAGCTGCCCTGTGCTC
	Reverse	GCGTAGGGTAAAGGGTTCGAG
<i>Ifitm3</i>	Forward	AACATGCCCAGAGAGGTGTC
	Reverse	ACCATCTTCCGATCCCTAGAC
<i>Iigp2</i>	Forward	GCCTGGATTGCAGTTTTGTAA
	Reverse	TCAAATTCTTTAACCTCAGGTGACT
<i>Irf7</i>	Forward	CTTCAGCACTTTCTTCCGAGA
	Reverse	TGTAGTGTGGTGACCCTTGC
<i>Irgb10</i>	Forward	CCCTGAACATCGCTGTGAC
	Reverse	GGGCATTAATGAACGTGGAC
<i>Irgm</i>	Forward	AAGGCCACTAACATCGAATCA
	Reverse	TGCCTTATCTCACTTAATACTCCTCA
<i>Isg20</i>	Forward	GCGCCTGCTACACAAGAAC
	Reverse	CTGAGAGATTTTGTAGAGCTCCATT
<i>Lamp3</i>	Forward	GCTTGGTGTTCTTGGTGTTT
	Reverse	CCACTGTTGTGTGCTTGAGTC
<i>Ly6a</i>	Forward	TGGATTCTCAAACAAGGAAAGTAAAGA
	Reverse	ACCCAGGATCTCCATACTTTCAATA
<i>Nampt</i>	Forward	GGCAGAAGCCGAGTTCAA
	Reverse	TGGGTGGGTATTGTTTATAGTGAG
<i>Oas1</i>	Forward	TCAACTGTGTAAGGAGAAGCTGA
	Reverse	CCCGTATTCCCAGACGTAGA
<i>Oas1g</i>	Forward	GCATCAGGAGGTGGAGTTTG
	Reverse	GGCTTCTTATTGATACTACCATGACC
<i>Oas2</i>	Forward	TAGACCAGGCCGTGGATG
	Reverse	GTTTCCCGGCCATAGGAG
<i>Oas3</i>	Forward	AACACTGGTACCGCCAGGT
	Reverse	AGGAGCTCCAGGGCGTAG
<i>Oasl1</i>	Forward	GGCCAACCAGTGTCTGAAA
	Reverse	TGGATATCGGGTGCTCTCTT
<i>Oasl2</i>	Forward	AGGTGGCTGCAGAAGCTG
	Reverse	TGTTTCACTCTCACCTGAACATC
<i>Plac8</i>	Forward	CAGACCAGCCTGTGTGATTG
	Reverse	TCCAAGACAAGTGAAACAAAAGG
<i>Rbm6</i>	Forward	TTTCTCAGGGCAAATGTCC
	Reverse	TGGGCCAGTCCTATAATCTTG
<i>Rnf213</i>	Forward	CAGCTCTTCGAACTGTGTGG
	Reverse	GGAACACAGACTCAGCAGTGG
<i>Rsad2</i>	Forward	GTGGACGAAGACATGAATGAAC
	Reverse	TCAATTAGGAGGCACTGGAAA
<i>Samd9L</i>	Forward	TTGCAGAATGAGGAAACTGAAA
	Reverse	AATGCATTTTGTGGGAATCG
<i>Samhd1</i>	Forward	CAAGCGGTCAGGATCAATAAA
	Reverse	TGAGCTGCTCTGCAAATTTCT

Materials and Methods

<i>Scotin</i>	Forward	CTGTGGACCCTATTGCTGCT
	Reverse	GGGATCGAATTGTCTTCACC
<i>Sp100</i>	Forward	GAAACTCCACGAAACCCAAG
	Reverse	AGATAGTCAAAGAAGCAGTTCACAT
<i>Stat1</i>	Forward	TGAGATGTCCCGGATAGTGG
	Reverse	CGCCAGAGAGAAATTCGTGT
<i>Stat2</i>	Forward	GGAACAGCTGGAACAGTGGT
	Reverse	GTAGCTGCCGAAGGTGGA
<i>Tgtp</i>	Forward	CCAGATCAAGGTCACCACTG
	Reverse	GAGATGATTTTGCTTTCCCTTTT
<i>Trafd1</i>	Forward	GTGCTGCTGACGAGATTCTG
	Reverse	GAGAAGGGTTGCAGCTTGTC
<i>Trim30</i>	Forward	GAGCTGGAGGATCAGACAGAGT
	Reverse	GTTGCAGGCTTAAGGACTGACT
<i>Ube2L6</i>	Forward	ATGCTCCTGCTGCCAGAC
	Reverse	CTCCCTGGGGAAATCAATC
<i>Usp18</i>	Forward	TGACTCCGTGCTTGAGAGG
	Reverse	CGGGAGTCCACAACCTCACT
<i>Zbp1</i>	Forward	CAGGAAGGCCAAGACATAGC
	Reverse	GACAAATAATCGCAGGGGACT
<i>Znfx1</i>	Forward	CTGTTGGCCATGAGACTGG
	Reverse	TCTGGCCACGCTGAGTCT
<b>Other primers</b>		
<i>Casp8</i>	Forward	GGCTCAGGTAACAAGGGAGAC
	Reverse	GAATCCAGTGATTGGCCAGGA
<i>Cox5b</i>	Forward	GCTTCAAGGTTACTTCGCGG
	Reverse	ATGGGTCCAGTCCCTTCTGT
<i>Cyp20a1</i>	Forward	GCCTGTGGTCTCTTTCTGGTT
	Reverse	TCCGCCAGACTGATACCCTAA
<i>Fos</i>	Forward	GGAATGGTGAAGACCGTGTCA
	Reverse	GTTGATCTGTCTCCGCTTGGA
<i>Hif1a</i>	Forward	TCTCCTGTAAGCAAGGAGCC
	Reverse	GGGGAAGTGGCAACTGATGA
<i>Hexb</i>	Forward	TCGACCACAGTCCCAATTCC
	Reverse	ACTAGGGAAGGACTCGCACT
<i>Mkl1</i>	Forward	GACGGTAGGAGTCTTTCTGGC
	Reverse	TGTCCGTGGATTCTTCAACCG
<i>Pml</i>	Forward	AGGAACCCTCCGAAGACTATG
	Reverse	TTCCTCCTGTATGGCTTGCT
<i>Psap</i>	Forward	TCCGAGGTCTGTGTCCAGAT
	Reverse	CAGATTCTGCTCATAGGGGTCC
<i>Tnfsf10</i>	Forward	TCATCAGTGGAACCTTGCCC
	Reverse	TTGGGCTGCCCTCATTATT
<i>Tram1</i>	Forward	GGTGGAGGGAACATTCTGCC

	Reverse	TTTCCTGTTCCGAGGGGAGT
<i>Trim25</i>	Forward	AAGCAACTTCCCCTGATGCC
	Reverse	AGGCGGTGGTGTACTTGTTT
<i>Xaf1</i>	Forward	CCCAGAATGTGAAGAGCCCA
	Reverse	CCAGCTCACAGAACTTGACAC
<i>Zbp1</i>	Forward	CAGGAAGGCCAAGACATAGC
	Reverse	GACAAATAATCGCAGGGGACT

### 5.1.3 Kits

**Table 4 | List of kits**

<b>Kits</b>	<b>Supplier</b>	<b>Identifier</b>
Agilent RNA 6000 Pico Kit	Agilent	5067-1513
Annexin V-APC Assay Kit	Abcam	ab236215
Calcium Phosphate Transfection Kit	Invitrogen™	K278001
CellTrace™ Violet Cell Proliferation Kit	Invitrogen™	C34557
EasySep™ Mouse Hematopoietic Progenitor Cell Isolation Kit	STEMCELL™ TECHNOLOGIES	19856
FITC Annexin V Apoptosis Detection Kit with 7-AAD	BioLegend®	640922
Fixation/Permeabilization Kit	BD Cytofix/Cytoperm™	554714
GFP BrightComp eBeads™ Compensation Bead Kit	Invitrogen™	A10514
mCherry BrightComp eBeads™ Compensation Bead Kit	Invitrogen™	A54743
NucleoBond Xtra Maxi EF, Maxi kit for endotoxin-free plasmid DNA	MACHEREY-NAGEL GmbH & Co. KG	740424.1
PicoPure™ RNA Isolation Kit	Applied Biosystems™	KIT0204
Pierce™ BCA Protein Assay Kit	Thermo Scientific™	23225
QIAprep Spin Miniprep Kit	QIAGEN	27104
QIAquick Gel Extraction Kit	QIAGEN	28704
Qubit™ Protein Assay Kit	Invitrogen™	Q33211
RNase-Free DNase Set (50)	QIAGEN	79254
SuperScript™ IV VILO™ Master Mix	Invitrogen™	11756050

### 5.1.4 Reagents and buffers

**Table 5 | List of reagents and buffers**

<b>Reagent/Buffer</b>	<b>Supplier</b>	<b>Identifier</b>
10X RIPA Buffer	Abcam	ab156034
5-Fluorouracil	Sigma-Aldrich	F6627
AEBSF hydrochloride	Genaxxon bioscience	M6360.0500
Ampicillin	Sigma-Aldrich	A9393
Blasticidine S hydrochloride	Sigma-Aldrich	15205
Bovine Serum Albumin	CARL ROTH®	8076.4
Brilliant Stain Buffer	BD Horizon™	566349

## Materials and Methods

Ciprofloxacin hydrochloride monohydrate	Thermo Scientific Chemicals	J61970.06
Clarity Max Western ECL Substrate	Bio-Rad	1705062
DMEM, low glucose, GlutaMAX™ Supplement, pyruvate	Gibco™	21885025
Dulbecco's Phosphate Buffered Saline	Sigma-Aldrich	D8537
EcoRI-HF®	NEB	R3101S
EDTA (0.5 M), pH 8.0	Thermo Scientific™	R1021
Ethidium bromide solution 1 %, 10 ml, glass, 1 x 10 ml	CARL ROTH®	2218.1
Fetal Bovine Serum	Gibco™	10270106
GranuCult® plus LB agar (MILLER)	MERCK	1.10283
Halt™ Phosphatase Inhibitor Cocktail	Thermo Scientific™	78420
Halt™ Phosphatase Inhibitor Single-Use Cocktail	Thermo Scientific™	78428
Halt™ Protease Inhibitor Cocktail (100x)	Thermo Scientific™	78429
Ham's F-12 Nutrient Mix	Gibco™	11765-054
HBSS, no calcium, no magnesium, no phenol red	Gibco™	14175095
HEPES Solution	Sigma-Aldrich	H0887
Hexadimethrine bromide	Sigma-Aldrich	H9268
Insulin-Transferrin-Selenium-Ethanolamin (ITS-X) (100x)	Gibco™	51500-056
Kanamycin sulfate	Sigma-Aldrich	k1377
L-Glutamine (200 mM)	Thermo Scientific™	25030024
LB Broth (Miller)	Sigma-Aldrich	L3522
Liberase™ TL Research Grade	Roche® Life Science Products	5401020001
Mouse IFN $\alpha$ , research grade	Miltenyi Biotec	130-093-131
Nilotinib, Free Base, >99%	LC Laboratories®	N-8207
NuPAGE™ LDS Sample Buffer (4X)	Invitrogen™	NP0008
NuPAGE™ Sample Reducing Agent (10X)	Invitrogen™	NP0004
Penicillin-Streptomycin	Sigma-Aldrich	P4458
Percoll®	Sigma-Aldrich	P4937
pl:C HMW	InvivoGen	tlrl-pic-5
PMSF Protease Inhibitor	Thermo Scientific™	36978
Poly(vinyl alcohol)	Sigma-Aldrich	P8136
Power SYBRTM Green PCR Master Mix	Applied Biosystems™	4367659
Primocin®	InvivoGen	ant-pm-1
Puromycin Dihydrochloride	Gibco™	A1113803
Recombinant Murine Flt3-Ligand	PEPROTECH®	250-31L
Recombinant Murine IL-3	PEPROTECH®	213-13
Recombinant Murine IL-6	PEPROTECH®	216-16
Recombinant Murine SCF	PEPROTECH®	250-03
Recombinant Murine TPO	PEPROTECH®	315-14
RetroNectin® Recombinant Human Fibronectin Fragment	Takara Bio	T100B
RPMI – 1640 Medium	Sigma-Aldrich	R8758

## Materials and Methods

Shrimp Alkaline Phosphatase (rSAP)	NEB	M0371S
Spectra™ Multicolor Broad Range Protein Ladder	Thermo Scientific™	26623
StemSpan™ SFEM	STEMCELL™ TECHNOLOGIES	9650
T4 DNA Ligase	NEB	M0202S
TheraPEAK™ ACK Lysing Buffer (1x)	LONZA	BP10-548E
Tris Buffer pH 7.5, 1 M solution	SERVA	37180
Trypsin – EDTA Solution	Sigma-Aldrich	T3924
Tween® 20	Sigma-Aldrich	P1379
UltraPure™ DNase/RNase-Free Distilled Water	Invitrogen™	10977-035

### 5.1.5 Additional Material

**Table 6 | List of additional material**

<b>Additional Materials</b>	<b>Supplier</b>	<b>Identifier</b>
4-20% Criterion TGX™ Precast Midi Protein Gel	Bio-Rad	5671094
Centrifuge tube, 50 mL	MERCK	T2318
Costar® 48-well Clear TC-treated Multiple Well Plates, Individually Wrapped, Sterile	Corning®	3548
Costar® 6-well Clear TC-treated Multiple Well Plates, Bulk Packed, Sterile	Corning®	3506
DNA LoBind® Tubes 1.5mL	eppendorf	30108051
EasySep™ Magnet	STEMCELL™ TECHNOLOGIES	18000
EASYstrainer™, 40 µm, green	Greiner BIO-ONE	542040
EASYstrainer™, 70 µm, blue	Greiner BIO-ONE	542070
Falcon® 5mL Round Bottom Polystyrene Test Tube, with Cell Strainer Snap Cap	neoLab®	GF-0058
Microvette® 500 EDTA K3E, 500 µL	SARSTEDT	20.1341
One Shot™ Stbl3™ chemically competent E. coli	Invitrogen™	C737303
Open-Top Thinwall Ultra-Clear Tube	Beckman Coulter	344058
PCR Plate, 384-well, standard, white	Thermo Scientific™	AB1384
PCR SingleCap 8-pack SoftStrips 0.2 ml, colorless	Biozym®	710970X
Primaria™ 75 cm <sup>2</sup> Rectangular Straight Neck Cell Culture Flask	Corning®	353810
Reusable Feeding Needles Round Tip	F.S.D	18061-22
Size-exclusion chromatography columns	IZON	Single qEV, 35 nm
TPP® syringe filter	Faust Labscience GmbH	TPP99722
TPP® tissue culture dishes, 9.2 cm <sup>2</sup>	MERCK	Z707651
TPP® tissue culture flasks, 75 cm <sup>2</sup>	MERCK	Z707503
TPP™ centrifuge tubes (15mL)	Fisher Scientific	11391694
Trans-Blot® Turbo™ Midi 0.2 µm PVDF Transfer Packs	Bio-Rad	1704157
UltraPure™ Agarose-1000	Invitrogen™	16550100

### 5.1.6 Cell lines and plasmids

**Table 7 | List of cell lines and plasmids**

Name	Supplier	Identifier
Cell lines		
NIH/3T3	ATCC®	CRL-1658™
reivigorating mesenchymal stem cells (rMSCs)	in house	
Platinum-E (Plat-E) Retroviral Packaging Cell Line	CELL BIOLABS, INC.	RV-101
Plasmids		
NGFR P210	Addgene	27486
pMSCV-IRES-mCherry FP	Addgene	52114

### 5.1.7 Equipment

**Table 8 | List of equipment**

Equipment	Supplier	Model
Agilent 2100 Bioanalyzer Instrument	Agilent	G2939BA
BD FACSAria™ Fusion II Cell Sorter	BD Biosciences	FACSAria™
BD FACSAria™ I Cell Sorter	BD Biosciences	FACSAria™
BD FACSAria™ II Cell Sorter	BD Biosciences	FACSAria™
BD LSRFortessa™ cell Analyzer	BD Biosciences	Fortessa™
BD® LSR II Flow Cytometer	BD Biosciences	BD® LSR
ChemiDoc™ Touch Imaging System	Bio-Rad	6517
Heracell™ 240i CO <sub>2</sub> Incubator	Thermo Scientific™	51032875
NanoSight	Malvern Instruments	LM10
Optima L-90K Floor Ultracentrifuge	Beckman Coulter	365672
Primovert Inverted Routine Microscope	Zeiss	491206-0001-000
QuantStudio™ 5 Real-Time PCR System, 384-well	Applied Biosystems™	A28140
Qubit™ 4 Fluorometer	Invitrogen™	Q33238
SW 32 Ti Swinging-Bucket Rotor	Beckman Coulter	369650
Trans-Blot® Turbo™ Transfer System	Bio-Rad	1704150
Transmission electron microscope (TEM)	Zeiss	EM 910/912
Vi-CELL XR Cell Viability Analyzer	Beckman Coulter	731196

**5.1.8 Programs and software****Table 9 | List of programs and software**

<b>Program</b>	<b>Developer</b>
BD FACSDiva™ v8.0	BD Biosciences
FlowJo™ v10	BD Biosciences
GraphPad Prism v10.1.0 (264)	GraphPad Software, Inc.
Image Lab 6.1	Bio-Rad
MaxQuant (v 1.6.14.0)	Max Plank Insitute of Biochemistry
Primer-Blast (Using Primer3 and BLAST)	NCBI
QIAGEN Ingenuity Pathway Analysis (IPA)	QIAGEN
SnapGene	Dotmatics

### 5.2 Methods

#### 5.2.1 Mice

##### 5.2.1.1 Mouse strains

In adherence to the German Law for Protection of Animals and the National Institute of Health Guidelines for Care and Use of Laboratory Animals, the experimental procedures involving animals were conducted under the following licenses: DKFZ355, TVA G285/21, and TVA G194/21. The mice utilized in this study were housed in individually ventilated cages (IVC) within a pathogen-free environment at the Central Animal Laboratory, German Cancer Research Center (DKFZ), located in Heidelberg, Germany.

All mice involved in the experiments shared a C57BL/6 background, were aged between 8 and 13 weeks, and weighed above 20g at the start of any experiment or protocol. CD45.2 C57BL/6 mice, denoted as WT or CD45.2 WT, were obtained from Janvier Laboratories. In-house breeding was conducted for B6.SJL-*Ptprc<sup>a</sup>-Pepc<sup>b</sup>*/BoyJ mice, identified as CD45.1 WT mice. The CD45.1/2 mice were generated through in-house crosses between CD45.2 WT and CD45.1 WT mice.

*ISRE-eGFP* (Tovey et al., 2006) and *Ifnar<sup>-/-</sup>* mice (IFNAR KO) are CD45.2. Euthanasia and sacrifice were carried out by cervical dislocation as per German guidelines. For genotyping purposes, DNA was extracted from either ear punches or tail biopsies.

##### 5.2.1.2 Organ dissection and preparation of cell suspensions

###### 5.2.1.2.1 Blood

Blood collection was performed by submandibular bleeding of the vena facialis into Microvette<sup>®</sup> 500 EDTA K3E, 500 µl (SARSTEDT). Subsequently, red blood cells (RBCs) were lysed by incubation in TheraPEAK<sup>™</sup> ACK Lysing Buffer (LONZA) for a duration of 10 minutes. Following the lysis step, the samples were stained and analyzed using flow cytometry.

### 5.2.1.2.2 Spleen

Spleens were extracted from sacrificed mice, and their weights were recorded. Subsequently, a single-cell suspension of splenocytes was obtained by mechanically disaggregating the spleen through a 40 µm EASYstrainer™ (Greiner bio-one) and washing it with RPMI-1640 medium (Sigma-Aldrich) supplemented with 2% Fetal Bovine Serum (FBS, Gibco™). RBC lysis was carried out, and cell counts were determined using the Vi-CELL XR Cell Viability Analyzer (Beckman Coulter).

### 5.2.1.2.3 Bone marrow

BM was harvested from the tibia, femur, and hips, by either crushing or flushing techniques in RPMI-1640 supplemented with 2% FBS. RBCs were lysed, and the samples were passed through a 40 µm strainer before determining cell counts using Vi-CELL XR Cell Viability Analyzer.

For sorting experiments, lineage deletion was achieved through the utilization of the EasySep™ Mouse Hematopoietic Progenitor Cell Isolation Kit in conjunction with the EasySep™ Magnet (both from STEMCELL™ TECHNOLOGIES), following the manufacturer's protocol.

### 5.2.1.3 ISG-CML mouse model

#### 5.2.1.3.1 Isolation of BM from *ISRE-eGFP* mice

BM was obtained from CD45.2 donor *ISRE-eGFP* or WT mice aged between 8 to 13 weeks. Collection involved flushing the BM using a 21G needle and a 1 mL syringe with Dulbecco's Phosphate Buffered Saline (PBS, Sigma-Aldrich) supplemented with 2% FBS. Pooled BM underwent RBC lysis, washed with PBS+2%FCS, and cell counts were determined using the Vi-CELL XR Cell Viability Analyzer.

#### 5.2.1.3.2 *In vitro* pre-stimulation

Collected BM cells were plated in pre-stimulation medium at the density of  $3.5 \times 10^6$  cells/mL in Costar® 6-well plate (Corning®), with a maximum volume of 5 mL per well, for 24 hours. Pre-stimulation medium consisted of DMEM, low glucose, GlutaMAX™ Supplement,

pyruvate (Gibco™) supplemented with 20% FBS, 1% Penicillin-Streptomycin (P/S, Sigma-Aldrich), and 0.1 mg/mL Kanamycin (Sigma-Aldrich), 10 ng/mL murine IL-3 (PEPROTECH®), murine IL-6 (PEPROTECH®), 100 ng/mL murine stem cell factor (mSCF, PEPROTECH®), and 1 µg/mL Ciprofloxacin hydrochloride monohydrate (Thermo Scientific Chemicals).

For 100% chimeras, samples underwent lineage deletion and cells were then stained with lineage markers. Lin<sup>-</sup> cKit<sup>+</sup> (LK) cells were sorted based on their eGFP signal into eGFP<sup>low</sup> or eGFP<sup>high</sup> LK cells. Sorted cells were cultured in pre-stimulation medium as mentioned above.

### 5.2.1.3.3 Viral transduction and transformation

After pre-stimulation, cell counts were determined, and cells were replated at a density of  $7.5 \times 10^5$  cells/mL of infection media in 6-well plates with a maximum of 4 mL/well. The infection media comprised pre-stimulation media supplemented with 8 µg/mL Hexadimethrine bromide (Sigma-Aldrich) and BCR::ABL1 viral supernatant at appropriate dilutions to achieve a multiplicity of infection (MOI) of 0.3. Cells were centrifuged at 32°C for 2 hours, followed by placement in a CO<sub>2</sub> incubator. After 4 hours, half of the media was aspirated and replaced with 2 mL fresh pre-stimulation medium. This process was repeated the next day, with harvested and counted cells resuspended in Hank's Balanced Salt Solution (HBSS) for transplantation. Samples for 100% chimeras were processed similarly but in separate plates.

### 5.2.1.3.4 Transplantation

Recipient mice were lethally irradiated (2x500 Rad) 24 hours before transplantation by the Central Animal Laboratory, DKFZ. The following day, irradiated mice were transplanted with  $2.5 \times 10^5$  *in vitro* transformed cells in 150 µL Hank's Balanced Salt Solution (HBSS, Gibco™) intravenously (i.v.). 100% chimeras were generated similarly, transplanting transformed eGFP<sup>low</sup> or eGFP<sup>high</sup> cells into different recipient groups. If empty vector viral supernatant was used, an additional transplantation of  $3 \times 10^5$  CD45.1/.2 rescue total BM cells was also performed. Leukemia engraftment was monitored by blood sampling starting at day 6. Engraftment was confirmed by the presence of more than 1% mCherry<sup>+</sup> cells in the peripheral blood of all recipients.

### 5.2.1.3.5 Secondary transplantation

For secondary transplantations, untreated leukemic mice were sacrificed at day 14, and  $5 \times 10^6$  RBC-lysed splenocytes were intravenously transplanted into sub-lethally irradiated (600 Rad) secondary recipients. Secondary transplantation of nilotinib-treated mice was performed similarly after the treatment duration of 21 days.

### 5.2.1.4 Forward and reverse Chimeras

Forward chimeras (WT/*Ifnar*<sup>-/-</sup>) were generated by transplanting lethally irradiated (2x500 Rad) CD45.1 WT mice with  $3 \times 10^6$  total BM from CD45.2 *Ifnar*<sup>-/-</sup> i.v. Reverse chimeras (*Ifnar*<sup>-/-</sup>/WT) were generated by transplanting lethally irradiated (2x500 Rad) CD45.2 *Ifnar*<sup>-/-</sup> mice with  $3 \times 10^6$  total BM from CD45.1 WT mice. Chimerism was assessed by blood sampling 8 weeks post-transplantation. Experimental procedures on these mice were initiated at week 12 post-transplantation. Irradiation of recipient mice was performed 24 hours before transplantation by the staff of the Central Animal Laboratory, DKFZ.

### 5.2.1.5 *In vivo* treatments

To induce an inflammatory response, intraperitoneal (i.p.) administration of pl:C (InvivoGen) treatment was carried out at a dose of 5 mg/kg in a total volume of 200  $\mu$ L PBS (Sigma-Aldrich). Control mice received a comparable injection of 200  $\mu$ L PBS. For both forward and reverse chimeras, the treatment was initiated 12 weeks post-transplantation. Treated mice were subsequently sacrificed at either 3-, 9-, 18-, or 24-hour time points.

For 5-FU experiments, a 50 mg/mL stock solution of 5-FU (Sigma-Aldrich) was prepared in 1M ammonium hydroxide, filtered through 0.22 $\mu$ m filters (Faust Labscience GmbH), and stored in lightproof containers. The working solution of 5-FU was created by diluting the stock solution in PBS and administered i.v. at either 100 or 200 mg/kg, with a maximum injection volume of 150  $\mu$ L. Mice were sacrificed 96 hours post-treatment.

For Nilotinib (LC Laboratories<sup>®</sup>) treatment, a 50 mg/mL stock solution was prepared in dimethyl sulfoxide (DMSO, Sigma-Aldrich) and stored at -20°C. The working solution was then diluted in PBS and administered orally via gavage (O.G.) using reusable feeding needles (F.S.D.) at a dose of 75 mg/kg daily for a duration of 21 days.

For sEV treatments, 25µg, 50µg, or 100µg of pl:C sEVs were transplanted i.v. in 150 µL PBS. Recipient mice were analyzed 18 hours after transplantation.

### 5.2.2. Flow cytometry and cell sorting

Samples designated for flow cytometry analysis or fluorescence-activated cell sorting (FACS) underwent initial staining with fixable viability stain 780 (FVS78, BD Horizon™) in PBS, following the manufacturer's instructions. Subsequently, the samples were washed in PBS + 2% FBS and stained with a staining medium (RPMI-1640 + 2% FBS) containing antibodies specific to desired surface markers (Table 10) for 40 minutes at 4°C in the dark.

**Table 10 | Cell population surface markers**

Population	Surface markers
CMP	Lin <sup>-</sup> Sca-1 <sup>+</sup> cKit <sup>-</sup> CD16/32 <sup>low</sup> CD34 <sup>+</sup>
GMP	Lin <sup>-</sup> Sca-1 <sup>+</sup> cKit <sup>-</sup> CD16/32 <sup>+</sup> CD34 <sup>+</sup>
HSC	Lin <sup>-</sup> Sca-1 <sup>+</sup> cKit <sup>+</sup> CD150 <sup>+</sup> CD48 <sup>-</sup> CD34 <sup>-</sup>
LPM	B220 <sup>-</sup> CD45 <sup>+</sup> CD11b <sup>+</sup> CD115 <sup>+</sup> F4/80 <sup>high</sup> MHCII <sup>low</sup> TIM-4 <sup>+</sup>
LSK	Lin <sup>-</sup> Sca-1 <sup>-</sup> cKit <sup>+</sup>
LSKs	Lin <sup>-</sup> Sca-1 <sup>+</sup> cKit <sup>+</sup>
macrophages (MΦ)	B220 <sup>-</sup> CD4 <sup>-</sup> CD8 <sup>-</sup> CD11b <sup>+</sup> Ly6G <sup>-</sup> Siglec-F <sup>-</sup> F4/80 <sup>+</sup>
MDMs	CD11b <sup>+</sup> CD45 <sup>high</sup> Tmem119 <sup>-</sup> CX3CR1 <sup>-</sup> CCR2 <sup>+</sup>
Microglia	CD11b <sup>+</sup> CD45 <sup>med</sup> Tmem119 <sup>+</sup> CX3CR1 <sup>+</sup> CCR2 <sup>-</sup>
neutrophils	B220 <sup>-</sup> CD4 <sup>-</sup> CD8 <sup>-</sup> CD11b <sup>+</sup> Ly6G <sup>+</sup>
SPM	B220 <sup>-</sup> CD45 <sup>+</sup> CD11b <sup>+</sup> CD115 <sup>+</sup> F4/80 <sup>low</sup> MHCII <sup>high</sup> TIM-4 <sup>-</sup>

*Lin* refers to lineage committed cells (CD220<sup>+</sup>, CD11b<sup>+</sup>, CD4<sup>+</sup>, CD8<sup>+</sup>, Gr-1<sup>+</sup>, Ter-119<sup>+</sup>)

In cases where more than two antibodies were conjugated with brilliant dyes, the staining medium was adjusted to include 25% Brilliant Stain Buffer (BD Horizon™). For panels necessitating secondary staining, samples underwent two washes in PBS + 2% FBS, followed by counterstaining in the staining medium with the respective secondary antibody for 40 minutes at 4°C in the dark. All antibodies utilized were monoclonal (Table 1) and used at concentrations determined through prior titration against BM or spleen samples.

In the context of the *in vitro* proliferation assay, FACS-sorted LSKs were stained using the Cell Trace™ Violet (CTV) Cell Proliferation Kit (Invitrogen™) per the manufacturer's instructions and subsequently plated in 96-well plates. The cells were treated with sEVs, either alone or in combination with 100 units/ml of IFNα, and harvested at specified time points for subsequent flow cytometric analyses.

To assess apoptosis, stained cells were washed in PBS and subjected to apoptosis staining using the Annexin V-APC Assay Kit (Abcam) according to the manufacturer's instructions. The analysis was carried out using flow cytometry.

All samples designated for flow cytometry were passed through Falcon® 5mL Round Bottom Polystyrene Test Tubes with Cell Strainer Snap Caps (neoLab®) before acquisition on either BD LSR Fortessa or LSRII (BD Biosciences) equipped with 350nm, 205nm, 488nm, 561nm, and 640 lasers. FACS was conducted using BD FACSAria™ I, II, or Fusion II (BD Biosciences). Post-acquisition data analysis was performed using FlowJo™ v10 software (BD Biosciences).

### 5.2.3 Cell cycle analysis

Cell cycle analysis was conducted using the DNA dye DAPI (Thermo Scientific™) in conjunction with the proliferation marker Ki-67. In a concise overview, samples were initially stained for surface markers, followed by fixation and permeabilization using the Fixation/Permeabilization Kit (BD Cytotfix/Cytoperm™) in accordance with the manufacturer's instructions. Subsequently, samples were stained with anti-Ki-67 coupled with Alexa Fluor® 647, which was prepared in Permash wash buffer and incubated overnight at 4°C, shielded from light. Finally, cells were stained with 1µg/mL DAPI for 10 minutes immediately prior to flow cytometry analysis. Different phases of the cell cycle were determined as follows: G<sub>0</sub> (Ki-67<sup>neg</sup> DAPI<sup>low</sup>), G<sub>1</sub> (Ki-67<sup>high</sup> DAPI<sup>low</sup>) and G<sub>2</sub>SM (Ki-67<sup>high</sup> DAPI<sup>high</sup>)

### 5.2.4 Isolation of macrophages

To isolate peritoneal macrophages, mice were euthanized using cervical dislocation. The peritoneal cavity was accessed by carefully removing the overlying skin, and 3 mL of PBS + 2% FBS solution was gently injected, ensuring the avoidance of any internal organ puncture. Subsequently, the abdominal wall was massaged for 10-25 seconds to facilitate optimal recovery of peritoneal cells. The injected fluid was then aspirated using a new 25-gauge needle and syringe, transferring the collected sample into sterile TPP™ centrifuge tubes (15mL, Fisher Scientific) pre-chilled on ice. Cell counts were determined using Vi-CELL XR Cell Viability Analyzer. Following cell counting, the isolated peritoneal cells were washed with PBS+2% FBS and prepared for flow cytometry analysis.

For the isolation of CNS macrophages, the brain and spinal cord were carefully excised from the euthanized animal using precision scissors and placed into DNA LoBind<sup>®</sup> Tubes (1.5 mL). A digestion cocktail composed of PBS with 1.6 Wunsch/mL Liberase<sup>™</sup> TL Research Grade (Roche<sup>®</sup> Life Science Products) and 0.5 mg/mL DNase (RNase-Free DNase Set kit, QIAGEN) was prepared, and the brain and spinal cord were finely minced with the same scissors. The samples were then incubated at 37°C for 30 minutes, and the reaction was halted by adding 20 µL of 0.5M EDTA (Thermo Scientific<sup>™</sup>). Following incubation, the samples were passed through an EASYstrainer<sup>™</sup>, 70 µm, blue (Greiner BIO-ONE) into a 50 mL tube, and the cells were washed with 20 mL of PBS+2% FBS. The cells were resuspended in 4 mL of 30% Percoll<sup>®</sup> (Sigma-Aldrich) density gradient medium and transferred into 15 mL tubes. A Pasteur pipette was positioned at the tube bottom, and 4 mL of 37% Percoll<sup>®</sup> density gradient medium was slowly underlaid using a 1 mL pipette. Subsequently, 4 mL of 70% Percoll<sup>®</sup> density gradient medium was similarly underlaid with the same Pasteur pipette. The tubes were then centrifuged for 40 minutes at 800 x *g* and 18 °C with no brake. After centrifugation, 3-4 mL of the 70%-37% density gradient interphase containing the macrophages was carefully collected into a clean 15 mL tube. The isolated cells were washed three times with PBS+2% FBS. Cell counts were determined using the Vi-CELL XR Cell Viability Analyzer. Following cell counting, the isolated cells were prepared for flow cytometry analysis.

### 5.2.5 Cell culture

rMSCs were cultured and expanded in Primaria<sup>™</sup> 75 cell culture flasks (Corning<sup>®</sup>), utilizing Dulbecco's Modified Eagle Medium (DMEM) (Gibco<sup>™</sup>) supplemented with 15% FBS, 1% P/S, 1% L-glutamine (Thermo Scientific<sup>™</sup>), and 1% Primocin (InvivoGen). These cells were maintained under hypoxic conditions (5% O<sub>2</sub>, 5% CO<sub>2</sub>) at 37°C.

NIH/3T3 (ATCC<sup>®</sup>) cells were cultured in T75 cell culture flasks (MERK) with complete DMEM (cDMEM) comprising DMEM supplemented with 10% FBS, 1% P/S, and 0.1 mg/mL Kanamycin. Platinum-E cells (Plat-E, CELL BIOLABS, INC.) were cultured in T75 cell culture flasks in cDMEM supplemented with 1µg/mL Puromycin Dihydrochloride (Gibco<sup>™</sup>) and 10µg/mL Blastidine S hydrochloride (Sigma-Aldrich). NIH/3T3 and Plat-E cells were maintained under normoxic conditions (20% O<sub>2</sub>, 5% CO<sub>2</sub>) in a humidified incubator at 37°C.

Cell passaging was performed using trypsin-EDTA (Sigma-Aldrich) when cells reached 70% confluency. Cells were not passaged beyond six passages, and a fresh batch was introduced thereafter to ensure optimal cellular characteristics.

### 5.2.6 Generation of MSCV-BCR::*ABL1*-IRES-mCherry by restriction cloning

1 µg each of NGFR P210 (Addgene plasmid #27486) and pMSCV-IRES-mCherry FP (Addgene plasmid #52114) were digested separately using *EcoRI*-HF® (NEB) following the manufacturer's instructions. After digestion, the pMSCV-IRES-mCherry FP was additionally treated with Shrimp Alkaline Phosphatase (rSAP, NEB) to prevent re-circularization of the digested plasmid backbone. The resulting reactions were separated on a 1% standard UltraPure™ Agarose-1000 gel (Invitrogen™), and the 7005-bp *EcoRI* fragment corresponding to the *BCR>::ABL1* sequence from the NGFR P210 reaction and the entire pMSCV-IRES-mCherry FP reaction were excised from the gel. The fragments were then purified using the QIAquick Gel Extraction Kit (QIAGEN) as per the manufacturer's instructions. A ligation reaction was performed using a 1:3 ratio of pMSCV-IRES-mCherry FP to *BCR>::ABL1* fragments with T4 DNA Ligase (NEB) following the manufacturer's recommendations.

### 5.2.7 Bacterial transformation

1 µL of the ligation reaction was transformed into 20 µL One Shot™ Stbl3™ chemically competent *E. coli* (Invitrogen™). The competent cell/DNA mixture was incubated on ice for 20-30 mins, followed by a heat shock at 42°C for 30-60 secs, and then placed back on ice for 2 minutes. Subsequently, 250-1,000 µL LB (Sigma-Aldrich) was added to the samples, which were then placed in a 37°C shaking incubator for 45 minutes. The transformed bacteria were plated on GranuCult® plus LB agar (MERK) plates with 100 µg/mL ampicillin (Sigma Aldrich) and incubated overnight at 37°C.

The next day, a few colonies were selected, and a mini prep was performed (5 mL culture in LB broth with 100 µg/mL ampicillin). Plasmids were extracted using the QIAprep Spin Miniprep Kit (QIAGEN). The samples were sent for plasmid sequencing, and positive samples were subsequently amplified by performing a maxi prep (500 mL culture in LB broth with 100 µg/mL ampicillin). Finally, the plasmids were purified using the NucleoBond Xtra Maxi EF, Maxi kit for endotoxin-free plasmid DNA (MACHEREY-NAGEL GmbH & Co. KG).

### 5.2.8 Generation of viral supernatant

Plat-E cells were seeded at a density of  $1.25 \times 10^6$  cells overnight in 100 mm cell culture dishes (MERK), in DMEM supplemented with 1 µg/mL Puromycin Dihydrochloride and 10 µg/mL Blasticidine S hydrochloride. Four hours before transfection, the media was replaced

with cDMEM. Following this 4-hour pre-transfection period, 10, 15, or 20 µg of MSCV-BCR::ABL1-IRES-mCherry or MSCV-IRES-mCherry retroviral DNA constructs were added to each dish using the Calcium Phosphate Transfection Kit (Invitrogen™) in accordance with the manufacturer's instructions. Following a 24-hour incubation period, the cell culture media were removed, the plates were washed with PBS, and fresh cDMEM was added. The viral supernatant, now present in the media, was collected at 48 hours post-transfection, and the process was repeated with another collection at the 72-hour mark. The Plat-E cells were ultimately harvested and subjected to analysis for transfection efficiency (% mCherry<sup>+</sup>) using flow cytometry.

### 5.2.9 Determination of viral titer

To determine viral titer,  $5 \times 10^4$  NIH/3T3 cells were initially seeded in 6-well plates using cDMEM. After 24 hours, the media was replaced with viral supernatants that were appropriately diluted in cDMEM at concentrations of 1:2, 1:10, 1:50, 1:100, 1:200, 1:400, 1:1000, 1:2000, and 1:10000, supplemented with 8µg/mL Hexadimethrine bromide. Each dilution was performed in at least two technical replicates.

To assess the cell number in each well at the time of infection, cells from two untreated wells were collected using Trypsin-EDTA solution and subsequently counted. The following day, the infection medium was replaced with 1 mL of fresh medium. 48 hours post-infection, cells from all wells were harvested and analyzed by flow cytometry to determine transduction efficiency (%mCherry<sup>+</sup>). The viral titer (units/mL) was calculated using the formula:

$$IU/mL = \frac{\text{Dilution factor} \times \text{frequency of mCherry labelled cells} \times \text{inital cell number}}{\text{volume}}$$

### 5.2.10 Viral infectibility studies

To assess the infectivity of eGFP<sup>low</sup> and eGFP<sup>high</sup> HSCs, cells were isolated by FACS from the BM of *ISRE-eGFP* mice. The sorted cells were collected in DNA LoBind® Tubes (1.5 mL) containing StemSpan™ SFEM (STEMCELL™ TECHNOLOGIES), supplemented with 1% P/S and 1% L-glutamine.

The cells were plated at a density of  $5 \times 10^4$  HSCs per well in a 48-well plate coated with RetroNectin® (Takara Bio) in 250 µL stimulation medium. The coating was achieved by

incubating the plate with 25 µg/mL RetroNectin® in a humidified CO<sub>2</sub> incubator for 3 hours. Stimulation media consisted of StemSpan™ SFEM supplemented with 1% P/S, 1% L-glutamine, 50 ng/ml mSCF, 50 ng/ml TPO, and 50 ng/ml recombinant murine Flt3-Ligand (PEPROTECH®).

On the following day, the media was aspirated, and the cells were exposed to the infection medium, which consisted of the stimulation medium supplemented with 4 µg/mL hexadimethrine bromide and viral supernatant at appropriate dilutions to achieve the desired MOIs. The subsequent day, the medium was aspirated, and 300 µL of stimulation medium was added for another 24 hours. Finally, the cells were harvested from the wells and stained for flow cytometry analysis.

### **5.2.11 Generation of sEV-free FBS**

FBS was ultracentrifugation at 100,000x *g* for 2 hours at 4°C using an Optima L-90K ultracentrifuge (Beckman Coulter) equipped with a SW27 Swinging Bucket Rotor (both from Beckman Coulter). The resulting FBS supernatant was filtered through a 0.22µm filter and subsequently employed to establish a culture environment devoid of sEVs.

### **5.2.12 Collection of sEVs**

To isolate sEVs from rMSCs, an initial seeding of 2 x 10<sup>5</sup> rMSCs per Primaria T75 cell culture flask was performed. The following day, the culture medium was replaced with DMEM supplemented with 15% sEV-free FBS, 1% P/S, 1% L-glutamine, and 1% Primocin, and either 100 units/mL IFNα or PBS (as a treatment control) was added. After 48 hours from the medium change, the cell culture supernatant was collected for the isolation and purification of sEVs.

For BM sEV isolation, WT mice treated with either pl:C or PBS were sacrificed at various time points. The hips, femur, and tibiae were flushed in 0.22 µm-filtered PBS using a 1 mL syringe fitted with a 21G needle. The murine BM supernatant was then subjected to sEV purification

### **5.2.13 Purification of sEVs**

Supernatants from rMSCs and murine BM underwent a multi-step centrifugation process for sEV isolation. Initially, centrifugation at 300x *g* was employed to remove cells,

followed by a subsequent step at 2,000x *g* to eliminate cellular debris, dead cells, and larger apoptotic bodies. The third step involved centrifugation at 10,000x *g* to remove larger vesicles. Each of these centrifugations was conducted for 20 minutes at 4°C.

The resulting 10,000x *g* supernatants were then transferred to Open-Top Thinwall Ultra-Clear Tubes (Beckman Coulter) for the final ultracentrifugation at 100,000x *g*, performed for 2 hours at 4°C using an Optima L-90K ultracentrifuge with a SW27 Swinging Bucket Rotor. Subsequently, the final 100,000x *g* pellets were resuspended in 150 µL of 0.22 µm-filtered PBS and underwent SEC using single qEV 35 nm columns (IZON). The columns were allowed to equilibrate for 30 minutes at room temperature before introducing the resuspended pellet fraction. Once the sample volume was absorbed, 0.22 µm-filtered PBS was added to the column top, and fractions were collected: F0 (600 µL, representing the void volume of the column) and F1 to F10 (150 µL each), following the manufacturer's instructions.

### **5.2.14 Treatment of HSPC with sEV *in vitro***

HSC or LSKs were obtained by FACS from BM of WT mice and cultured *ex vivo*. The culture medium comprised serum-free Ham's F12 medium (Gibco™) supplemented with 1% P/S, 1% ITS-X (Gibco™), 1% L-glutamine, 10 mM HEPES (Sigma-Aldrich), 100 ng/mL murine thrombopoietin (TPO) (PEPROTECH®), 0.1% PVA (Sigma-Aldrich), and 10 ng/mL mSCF. The culture conditions were maintained at a hypoxic environment (5% O<sub>2</sub>, 5% CO<sub>2</sub>) at 37°C.

For short-term treatments, 2 x 10<sup>4</sup> LSKs per well were plated in a 96-well plate. The following day, cells were treated with sEVs at specified concentrations, either alone or in combination with 100 units/mL of IFNα, for the designated time intervals. Subsequently, flow cytometry was employed for cellular analysis.

In the case of long-term treatments, 2 x 10<sup>3</sup> HSCs were plated per well in a 96-well plate. Cells received sEV treatments at the specified concentrations on the subsequent day, as well as on days three and six post-initial treatment. Media change occurred prior to the second and third treatments on the same day. Following ten days of culture, cells were analyzed by flow cytometry.

### 5.2.15 Nanoparticle tracking analysis (NTA)

The size and concentration of sEV fractions were assessed using a NanoSight LM10 (Malvern Instruments) equipped with a 405 nm laser. In the NTA analysis, samples were appropriately diluted (1:500 to 1:1000) in 0.22 µm-filtered PBS. Camera level and detection threshold were optimized at 13 and 5, respectively. The absence of background interference was confirmed using 0.22 µm-filtered PBS. Each sample underwent three 30-second video recordings, and the data were analyzed using NTA 3.0 software.

### 5.2.16 Transmission electron microscopy (TEM)

Electron microscopy was conducted with the full technical assistance of the Imaging and Cytometry Core Facility, DKFZ. Briefly, sEV fractions were adsorbed onto glow-discharged carbon-coated grids, washed in distilled water, and negatively stained using a 2% aqueous solution of uranyl acetate. Imaging was performed using Zeiss EM 910 or EM 912 transmission electron microscopes.

### 5.2.17 Protein extraction and western blot

For the analysis of sEV fractions and their respective parental cells, lysates were prepared using RIPA buffer (Abcam), supplemented with 5 mM EDTA, 1x AEBSF hydrochloride (Genaxxon bioscience), 1x Halt™ Protease Inhibitor, 1x Halt™ Phosphatase Inhibitor, and 1 mM PMSF Protease Inhibitor (all from Thermo Scientific™). The lysates were incubated for 30 minutes on ice with intermittent vortexing, followed by centrifugation at 14,000x g for 20 minutes at 4°C. The resulting supernatants were transferred to new collection tubes.

Protein lysates from parental cells were quantified using the Pierce™ BCA Protein Assay Kit (Thermo Scientific™) and sEV protein quantification was performed with the Qubit™ protein assay kit (Thermo Scientific™), following the manufacturer's instructions for each. Equal amounts of protein from each sample, as determined by these assays, were combined with NuPAGE™ LDS sample buffer and NuPAGE™ sample reducing agent (both from Invitrogen™). Subsequently, the samples were loaded onto 4-20% Criterion TGX™ Precast Midi Protein Gels (Bio-Rad) with Spectra™ Multicolor Broad Range Protein Ladder (Thermo Scientific™).

Following SDS-PAGE, protein transfer to 0.2  $\mu\text{m}$  PVDF membranes was performed using Trans-Blot Turbo™ Midi Transfer Packs and the Trans-Blot Turbo™ Transfer System (both from Bio-Rad). Membranes were blocked in 5% bovine serum albumin (BSA) (CARL ROTH®) in Tris-buffered saline with 0.1% Tween 20 (TBS-T) for 1 hour at room temperature.

Primary antibodies against CD81, Flotillin-1, TSG101, Calnexin, Cytochrome C, and GM130 were used in the manufacturer's recommended concentrations in 5% BSA in TBS-T and incubated overnight at 4°C. Subsequently, membranes were washed three times with TBS-T before incubation with secondary antibodies. After three additional washes with TBS-T, signals were visualized using the Clarity™ Max Western ECL Substrate and the ChemiDoc™ Touch Imaging System (both from Bio-Rad).

### 5.2.18 RNA extraction, cDNA synthesis, and qRT-PCR

RNA isolation was performed on cell pellets using the PicoPure™ RNA Isolation Kit (Applied Biosystems™) as per the manufacturer's guidelines. The optional step of DNase treatment was performed using the RNase-Free DNase Set kit (QIAGEN) according to manufacturer's instructions and each sample was eluted in 16  $\mu\text{L}$  elution buffer.

cDNA synthesis was performed on 14  $\mu\text{L}$  of the eluted RNA by using the SuperScript™ IV VILO™ Master Mix kit (Invitrogen™) according to manufacturer's recommendations.

For quantitative real-time polymerase chain reaction (qRT-PCR), the cDNA was appropriately diluted with UltraPure™ DNase/RNase-Free Distilled Water (Invitrogen™) to meet the minimum required volume. Primer sequences were designed using Primer-BLAST (NCBI), and gene sequences were obtained from NCBI. Each qRT-PCR reaction comprised 14  $\mu\text{L}$ , consisting of 6  $\mu\text{L}$  diluted cDNA, 7  $\mu\text{L}$  Power SYBR™ Green PCR Master Mix (Applied Biosystems™), 0.1  $\mu\text{L}$  forward primer, 0.1  $\mu\text{L}$  reverse primer, and 0.8  $\mu\text{L}$  H<sub>2</sub>O. The qRT-PCR reactions were conducted in a 384-well plate (Thermo Scientific™) using the QuantStudio™ 5 Real-Time PCR System (Applied Biosystems™), with a minimum of three technical replicates for each gene. *Sadh*,  *$\beta$ -actin*, and *Oaz1* were employed as housekeeping genes to normalize gene expression. Relative gene expression levels were determined utilizing the  $\Delta\Delta\text{CT}$  method.

### 5.2.19 Microarray

The assessment of RNA sample quality for microarray analysis was conducted using the Agilent RNA 6000 Pico Kit (Agilent), following the manufacturer's guidelines. The determination of RNA integrity number (RIN) and sample concentration was executed using the Agilent 2100 Bioanalyzer Instrument (Agilent). Samples exhibiting RIN values of 8 or above were subsequently forwarded to the Genomics and Proteomics Core facility, DKFZ. There, global gene expression analysis was performed utilizing the Clariom™ S mouse chip. An initial analysis of the results was provided by the core facility. Briefly, microarray scanning was performed using an iScan array scanner. Data extraction included individual bead-level assessment, with outlier removal using a 2.5 times Median Absolute Deviation (MAD) threshold. Remaining bead-level data points underwent quantile normalization. Gene expression significance was determined using the student's *t*-test, with Benjamini-Hochberg correction applied to all *p*-values (Benjamini & Hochberg, 1995). Average expression values were calculated as the mean of measured bead expressions, accompanied by standard deviation. The analysis, conducted in R, utilized raw data files. Procedures included outlier removal (expression value > 20 before the 2.5 MAD rule), mean calculations, and *t*-tests over all beads in the original scale. Benjamini-Hochberg correction was uniformly applied (Benjamini & Hochberg, 1995). To generate bead-level matrices, ProbesIDs with expression values > 20 were averaged, and resulting lists were randomly filled with NAs. Quantile normalization was applied using R and Bioconductor packages: multicore, preprocessCore, affy, oligo, pd.hugene.2.0.st, pd.ragene.2.0.st, pd.mogene.1.0.st.v1.

The resulting data was filtered for 404 mouse-specific ISGs (Wu et al., 2018) (Table 11), and a core analysis was performed by Ingenuity Pathway Analysis (IPA), with  $-\log(p\text{-value})$  cutoff set at 10, to identify canonical pathways associated with the expression profiles.

### 5.2.20 Proteomic analysis

A total of 20 µg of proteins isolated from sEVs underwent proteomic analysis at the Genomics and Proteomics Core Facility of the DKFZ. Briefly, prior to liquid chromatography with tandem mass spectrometry (LC-MS/MS) analysis, dried peptides were dissolved in 2.5% hexafluoroisopropanol (HFIP) in 1% trifluoroacetic acid (TFA) (v/v). The separation and analysis of peptides were conducted using a nanoHPLC system (Ultimate 3000 RSLCnano; Thermo Scientific™) coupled with an Orbitrap Exploris 480 mass spectrometer in data-dependent acquisition (DDA) mode.

## Materials and Methods

MaxQuant (version 1.6.14.0) was employed for data analysis, identifying proteins and peptides by querying the Uniprot database with a false discovery rate (FDR) threshold set at 1%. Default settings, including the match between runs option, were selected. Intensity-based absolute quantification (iBAQ) facilitated comparison between samples and normalization to the number of theoretical peptides for each protein (Schwanhäusser et al., 2011). R package "limma" was used for data analysis, and missing values were imputed based on quantile normalization. *p*-values were adjusted using the Benjamin-Hochberg method (Benjamini & Hochberg, 1995).

Significant differences between PBS sEVs and pl:C sEVs were determined using a non-parametric Wilcoxon signed-rank test. Gene ontology (GO) analysis of proteins significantly upregulated in pl:C sEVs compared to PBS sEVs, detected in all samples, was performed using the PANTHER classification system based on "biological processes." Additionally, the top 100 exosome proteins from ExoCarta were employed to assess the percentage of proteins identified in our proteomic experiment (Keerthikumar et al., 2016).

## 6. Appendix

## 6.1 Supplementary tables

Table 11| List of mouse-specific ISGs (Wu et al., 2018)

Symbol	Entrez Gene ID	Description
ABCA9	217262	ATP-binding cassette, sub-family A (ABC1), member 9
ABCE1	24015	ATP-binding cassette, sub-family E (OABP), member 1
ABLIM3	319713	actin binding LIM protein family, member 3
ABTB2	99382	ankyrin repeat and BTB (POZ) domain containing 2
ACSL1	14081	acyl-CoA synthetase long-chain family member 1
ADAMDEC1	58860	ADAM-like, decysin 1
ADAR	56417	adenosine deaminase, RNA-specific
ADM	11535	adrenomedullin
AGPAT9	231510	1-acylglycerol-3-phosphate O-acyltransferase 9
AIM2	383619	absent in melanoma 2
AKT3	23797	v-akt murine thymoma viral oncogene homolog 3
ALDH1A1	11668	aldehyde dehydrogenase 1 family, member A1
ALYREF	21681	Aly/REF export factor
AMPH	218038	amphiphysin
ANGPTL1	72713	angiopoietin-like 1
ANKRD22	52024	Ankyrin Repeat Domain 22
APOL2	239552	apolipoprotein L, 2
APOL6	71939	apolipoprotein L, 6
AQP9	64008	apolipoprotein L, 9
ARG2	11847	arginase 2
ARHGEF3	71704	Rho guanine nucleotide exchange factor (GEF) 3
ARNTL	11865	aryl hydrocarbon receptor nuclear translocator-like
ATF2	11909	activating transcription factor 2
ATF3	11910	activating transcription factor 3
B2M	12010	beta-2-microglobulin
BAG1	12017	BCL2-associated athanogene
BAK1	12018	BCL2-antagonist/killer 1
BANF1	23825	barrier to autointegration factor 1
BATF2	74481	basic leucine zipper transcription factor, ATF-like 2
BAX	12028	BCL2-associated X protein
BCL2	12043	B cell leukemia/lymphoma 2
BCL2L1	12048	BCL2-like 1
BCL3	12051	B cell leukemia/lymphoma 3
BIRC2	11797	baculoviral IAP repeat-containing 2
BIRC3	11796	baculoviral IAP repeat-containing 3
BLVRA	109778	biliverdin reductase A
BLZF1	66352	basic leucine zipper nuclear factor 1
BST2	69550	bone marrow stromal cell antigen 2
BUB1	12235	BUB1 mitotic checkpoint serine/threonine kinase
C10orf10	213393	chromosome 10 open reading frame 10
C15orf48	433470	chromosome 15 open reading frame 48
C1S	317677	complement component 1, s subcomponent
C22orf28	28088	chromosome 22 open reading frame 28
C4orf32	70617	chromosome 4 open reading frame 32
C4orf33	73852	chromosome 4 open reading frame 33
C9orf91	230279	chromosome 9 open reading frame 91
CALR	12317	calreticulin
CANX	12330	calnexin
CASP1	12362	caspase 1

## Appendix

CASP7	12369	caspase 1, apoptosis-related cysteine peptidase
CCDC75	53951	caspase 7, apoptosis-related cysteine peptidase
CCL11	20292	C-C Motif Chemokine Ligand 11
CCL2	20293	C-C Motif Chemokine Ligand 2
CCL22	20299	C-C Motif Chemokine Ligand 22
CCL4	20303	C-C Motif Chemokine Ligand 4
CCL5	20304	C-C Motif Chemokine Ligand 5
CCNA1	12427	cyclin A1
CCR1	12768	chemokine (C-C motif) receptor 1
CCR7	12775	chemokine (C-C motif) receptor 7
CD163	93671	CD163 molecule
CD274	60533	CD274 molecule
CD38	12494	CD38 molecule
CD40	21939	CD40 molecule
CD69	12515	CD69 molecule
CD74	16149	CD74 molecule
CD9	12527	CD9 molecule
CDK17	237459	cyclin-dependent kinase 17
CDK18	18557	cyclin-dependent kinase 18
CDKN1A	12575	cyclin-dependent kinase inhibitor 1A (p21, Cip1)
CES1	12623	carboxylesterase 1
CFB	14962	complement factor B
CHMP5	76959	charged multivesicular body protein 5
CHUK	12675	conserved helix-loop-helix ubiquitous kinase
CIITA	12265	class II transactivator
CLEC4D	17474	C-type lectin domain family 4, member D
CLEC4E	56619	C-type lectin domain family 4, member E
CLEC5A	23845	C-type lectin domain family 5, member a
CNP	12799	2',3'-cyclic nucleotide 3' phosphodiesterase
COMMD3	12238	COMM domain containing 3
CPT1A	12894	carnitine palmitoyltransferase 1A (liver)
CREB3L3	208677	cAMP responsive element binding protein 3-like 3
CREBBP	12914	CREB binding protein
CREBZF	233490	CREB/ATF bZIP transcription factor
CRP	12944	C-Reactive Protein
CRY1	12952	cryptochrome circadian clock 1
CSRNP1	215418	cysteine-serine-rich nuclear protein 1
CX3CL1	20312	chemokine (C-X3-C motif) ligand 1
CXCL10	15945	C-X-C Motif Chemokine Ligand 10
CXCL9	17329	C-X-C Motif Chemokine Ligand 9
CXCR4	12767	chemokine (C-X-C motif) receptor 4
CYP1B1	13078	cytochrome P450, family 1, subfamily B, polypeptide 1
CYTH1	19157	cytohesin 1
DCP1A	75901	Decapping MRNA 1A
DDIT4	74747	DNA-damage-inducible transcript 4
DDX58	230073	DEAD (Asp-Glu-Ala-Asp) box polypeptide 58
DDX60	234311	DEAD (Asp-Glu-Ala-Asp) box polypeptide 60
DHX58	80861	DEXH (Asp-Glu-X-His) box polypeptide 58
DTX3L	209200	deltex 3 like, E3 ubiquitin ligase
DUOX2	214593	dual oxidase 2
DUSP5	240672	dual specificity phosphatase 5
DYNLT1	100040 531	dynein, light chain, Tctex-type 1
EHD4	98878	EH-domain containing 4
EIF2AK2	19106	eukaryotic translation initiation factor 2-alpha kinase 2
EIF3L	223691	eukaryotic translation initiation factor 3, subunit L
ELF1	13709	E74-like factor 1 (ets domain transcription factor)
ENPP1	18605	ectonucleotide pyrophosphatase/phosphodiesterase 1
EPAS1	13819	endothelial PAS domain protein 1

Appendix

ERLIN1	226144	ER lipid raft associated 1
ETV6	14011	ets variant 6
EXT1	14042	exostosin glycosyltransferase 1
FADD	14082	Fas (TNFRSF6)-associated via death domain
FAM125B	72543	family with sequence similarity 125, member B
FAM134B	66270	family with sequence similarity 134, member B
FAM46A	212943	family with sequence similarity 46, member A
FAM46C	74645	family with sequence similarity 46, member C
FAM70A	245386	family with sequence similarity 70, member A
FBXO6	50762	F-box protein 6
FCGR1A	14129	Fc fragment of IgG, high affinity Ia, receptor (CD64)
FFAR2	233079	free fatty acid receptor 2
FGR	14191	FGR proto-oncogene, Src family tyrosine kinase
FKBP5	14229	FK506 binding protein 5
FLT1	14254	fms-related tyrosine kinase 1
FNDC3B	72007	fibronectin type III domain containing 3B
FNDC4	64339	fibronectin type III domain containing 4
FOSL1	14283	fos-like antigen 1
FUT4	14345	fucosyltransferase 4 (alpha (1,3) fucosyltransferase, myeloid-specific)
Fv1	14349	Friend virus susceptibility 1
FZD5	14367	frizzled class receptor 5
G6PC	14377	Glucose-6-Phosphatase Catalytic Subunit
GAK	231580	cyclin G associated kinase
GALNT2	108148	polypeptide N-acetylgalactosaminyltransferase 2
GBP2	14468	guanylate binding protein 2, interferon-inducible
GBP4	55932	guanylate binding protein 4
GBP5	229898	guanylate binding protein 5
GCA	227960	granulocitin, EF-hand calcium binding protein
GCH1	14528	GTP cyclohydrolase 1
GEM	14579	GTP binding protein overexpressed in skeletal muscle
GJA4	14612	gap junction protein, alpha 4, 37kDa
GK	14933	glycerol kinase
GLIPR2	384009	GLI pathogenesis-related 2
GLRX	93692	glutaredoxin (thioltransferase)
GMPR	66355	guanosine monophosphate reductase
GPX2	14776	glutathione peroxidase 2
GTPBP2	56055	GTP binding protein 2
GZMB	14939	Granzyme B
HBXIP	68576	late endosomal/lysosomal adaptor, MAPK and MTOR activator 5
HEG1	77446	heart development protein with EGF-like domains 1
HERC6	67138	HECT and RLD domain containing E3 ubiquitin protein ligase family member 6
HESX1	15209	HESX homeobox 1
HK2	15277	hexokinase 2
HLA-F	100529 082	major histocompatibility complex, class I, F
HLA-G	14991	major histocompatibility complex, class I, G
HNRNPUL1	232989	heterogeneous nuclear ribonucleoprotein U-like 1
HPSE	15442	heparanase
HSH2D	209488	hematopoietic SH2 domain containing
HYAL1	15586	hyaluronoglucosaminidase 1
HYAL2	15587	hyaluronoglucosaminidase 2
HYAL3	109685	hyaluronoglucosaminidase 3
IDO1	15930	indoleamine 2,3-dioxygenase 1
IFI27L2	76933	interferon, alpha-inducible protein 27-like 2
IFI30	65972	interferon, gamma-inducible protein 30
IFI35	70110	interferon, gamma-inducible protein 35
IFI44	99899	interferon, gamma-inducible protein 44
IFI44L	15061	interferon-induced protein 44-like

Appendix

IFIH1	71586	interferon induced with helicase C domain 1
IFIT1	112419	interferon-induced protein with tetratricopeptide repeats 1
IFIT2	15958	interferon-induced protein with tetratricopeptide repeats 2
IFIT3	667370	interferon-induced protein with tetratricopeptide repeats 3
IFITM1	68713	interferon induced transmembrane protein 1
IFITM2	80876	interferon induced transmembrane protein 2
IFITM3	66141	interferon induced transmembrane protein 3
IFNE	230405	interferon epsilon
IGFBP2	16008	insulin-like growth factor binding protein 2, 36kDa
IKBKB	16150	Inhibitor Of Nuclear Factor Kappa B Kinase Subunit Beta
IKBKE	56489	Inhibitor Of Nuclear Factor Kappa B Kinase Subunit Epsilon
IKBKG	16151	Inhibitor Of Kappa Light Polypeptide Gene Enhancer In B-Cells, Kinase Gamma
IL10	16153	interleukin 10
IL12B	16160	interleukin 12,B
IL12RB1	16161	interleukin 12 receptor B1
IL15	16168	interleukin 15
IL15RA	16169	interleukin 15 receptor, alpha
IL17RB	50905	interleukin 17 receptor B
IL1R1	16177	Interleukin 1 Receptor Type 1
IL1RN	16181	interleukin 1 receptor antagonist
IL23A	83430	interleukin 23,A
IL23R	209590	interleukin 23 receptor,
IL28RA	242700	interleukin 28 receptor, alpha
IL6	16193	interleukin 6
IL6ST	16195	interleukin 6 signal transducer
IMPA2	114663	inositol(myo)-1(or 4)-monophosphatase 2
IRF1	16362	interferon regulatory factor 1
IRF2	16363	interferon regulatory factor 2
IRF3	54131	interferon regulatory factor 3
IRF7	54123	interferon regulatory factor 7
IRF9	16391	interferon regulatory factor 9
ISG15	100038 882	ISG15 ubiquitin-like modifier
ISG20	57444	interferon stimulated exonuclease gene 20kDa
ITCH	16396	itchy, E3 ubiquitin protein ligase
IVNS1ABP	117198	influenza virus NS1A binding protein
JAK2	16452	Janus kinase 2
JUN	16476	jun proto-oncogene
JUNB	16477	jun B proto-oncogene
LAMP3	239739	lysosomal-associated membrane protein 3
LAP3	66988	leucine aminopeptidase 3
LCN2	16819	lipocalin 2
LEPR	16847	leptin receptor
LGALS3	16854	lectin, galactoside-binding, soluble, 3
LGALS9	16859	lectin, galactoside-binding, soluble, 9
LGMN	19141	legumain
LIPA	16889	legumain
LMO2	16909	lipase A, lysosomal acid, cholesterol esterase
LTA	16992	LIM domain only 2 (rhombotin-like 1)
LY6E	17069	lymphocyte antigen 6 complex, locus E
MAB21L2	23937	mab-21-like 2 (C. elegans)
MAFB	16658	v-maf avian musculoaponeurotic fibrosarcoma oncogene homolog B
MAFF	17133	v-maf avian musculoaponeurotic fibrosarcoma oncogene homolog F
MAP3K14	53859	mitogen-activated protein kinase kinase kinase 14
MAP3K5	26408	mitogen-activated protein kinase kinase kinase 5
MAPKAPK2	17164	MAP kinase-activated protein kinase 2
MASTL	67121	microtubule associated serine/threonine kinase-like
MAVS	228607	mitochondrial antiviral signaling protein

## Appendix

MAX	17187	MYC associated factor X
MB21D1	214763	Mab-21 domain containing 1
MCL1	17210	Mab-21 domain containing 1
MED14	26896	myeloid cell leukemia 1
MFN1	67414	mitofusin 1
MICB	243864	MHC I like leukocyte 2
MKX	210719	mohawk homeobox
MOV10	17454	Mov10 RISC complex RNA helicase
MS4A4A	666907	membrane-spanning 4-domains, subfamily A, member 4A
MST1R	19882	macrophage stimulating 1 receptor (c-met-related tyrosine kinase)
MT1H	17750	metallothionein 1H
MTHFD2L	665563	methylenetetrahydrofolate dehydrogenase (NADP+ dependent) 2-like
MYD88	17874	myeloid differentiation primary response 88
MYOF	226101	myoferlin
N4BP1	80750	NEDD4 binding protein 1
NAMPT	59027	nicotinamide phosphoribosyltransferase
NAPA	108124	N-ethylmaleimide-sensitive factor attachment protein, alpha
NCF1	17969	neutrophil cytosolic factor 1
NCOA3	17979	nuclear receptor coactivator 3
NDC80	67052	NDC80 kinetochore complex component
NFIL3	18030	nuclear factor, interleukin 3 regulated
NLRX1	270151	N-myc (and STAT) interactor
NMI	64685	nucleotide-binding oligomerization domain containing 2
NOD2	257632	nitric oxide synthase 2, inducible
NOS2	18126	neuronal PAS domain protein 2
NPAS2	18143	neuronal PAS domain protein 2
NT5C3	107569	5'-nucleotidase, cytosolic III
NUP50	18141	nucleoporin 50kDa
OAS1	23960	2'-5'-oligoadenylate synthetase 1, 40/46kDa
Oas1b	23961	2'-5'-oligoadenylate synthetase 1B
OAS2	246728	2'-5'-oligoadenylate synthetase 2, 69/71kDa
OAS3	246727	2'-5'-oligoadenylate synthetase 3, 100kDa
OASL	231655	2'-5'-oligoadenylate synthetase-like
ODC1	18263	ornithine decarboxylase 1
OGFR	72075	opioid growth factor receptor
OPTN	71648	optineurin
OTUB1	107260	OTU domain, ubiquitin aldehyde binding 1
OTUB2	68149	OTU domain, ubiquitin aldehyde binding 2
P2RY6	233571	pyrimidinerbic receptor P2Y, G-protein coupled, 6
PABPC4	230721	poly(A) binding protein, cytoplasmic 4 (inducible form)
PADI2	18600	peptidyl arginine deiminase, type II
PDGFRL	68797	platelet-derived growth factor receptor-like
PDIA3	14827	protein disulfide isomerase associated 3
PDK1	228026	pyruvate dehydrogenase kinase, isozyme 1
PFDN6	14976	prefoldin subunit 6
PFKFB3	170768	6-phosphofructo-2-kinase/fructose-2,6-biphosphatase 3
PHF15	76901	PHD finger protein 15
PI4K2B	67073	phosphatidylinositol 4-kinase type 2 beta
PIAS1	56469	protein inhibitor of activated STAT 1
PIM3	223775	Pim-3 proto-oncogene, serine/threonine kinase
PIN1	23988	protein (peptidyl-prolyl cis/trans isomerase) NIMA-interacting 1
PLEKHA4	69217	pleckstrin homology domain containing, family A (phosphoinositide binding specific) member 4
PLIN2	11520	perilipin 2
PLP1	18823	Proteolipid Protein 1
PLSCR1	22038	phospholipid scramblase 1
PML	18854	promyelocytic leukemia
PMM2	54128	phosphomannomutase 2
PNPT1	71701	polyribonucleotide nucleotidyltransferase 1

Appendix

PNRC1	108767	proline-rich nuclear receptor coactivator 1
PPM1K	243382	protein phosphatase, Mg <sup>2+</sup> /Mn <sup>2+</sup> dependent, 1K
PRKD2	101540	protein kinase D2
PRKRA	23992	protein kinase, interferon inducible double stranded RNA dependent activator
PSMB5	19173	proteasome (prosome, macropain) subunit, beta type, 5
PSMB6	19175	proteasome (prosome, macropain) subunit, beta type, 6
PSMB8	16913	proteasome (prosome, macropain) subunit, beta type, 8
PSMB9	16912	proteasome (prosome, macropain) subunit, beta type, 9
PTPN2	19255	protein tyrosine phosphatase, non-receptor type 2
PTPN6	15170	protein tyrosine phosphatase, non-receptor type 6
PUS1	56361	pseudouridylate synthase 1
PXK	218699	PX domain containing serine/threonine kinase
RAB27A	11891	RAB27A, member RAS oncogene family
RAF1	110157	v-raf-leukemia viral oncogene 1
RASGEF1B	320292	RasGEF domain family, member 1B
RASSF4	213391	Ras association (RalGDS/AF-6) domain family member 4
RBCK1	24105	RanBP-type and C3HC4-type zinc finger containing 1
RBM25	67039	RNA binding motif protein 25
RELA	19697	v-rel reticuloendotheliosis viral oncogene homolog A (avian)
RGS1	50778	regulator of G-protein signaling 1
RIPK1	19766	receptor-interacting serine-threonine kinase 2
RNASE4	58809	Ribonuclease A Family Member 4
RNASEL	24014	ribonuclease L (2', 5'-oligoadenylate synthetase-dependent)
RNF114	81018	ring finger protein 114
RNF216	108086	ring finger protein 216
RPL22	19934	ribosomal protein L22
RPS15A	267019	ribosomal protein S15A
RSAD2	58185	radical S-adenosyl methionine domain containing 2
RTP4	67775	Receptor Transporter Protein 4
S100A8	20201	S100 calcium binding protein A8
SAA1	20209	serum amyloid A1
SAMD4A	74480	sterile alpha motif domain containing 4A
SAMHD1	56045	SAM domain and HD domain 1
SAT1	20229	spermidine/spermine N1-acetyltransferase 1
SCARB2	12492	scavenger receptor class B, member 2
SCO2	100126 824	SCO2 cytochrome c oxidase assembly protein
SECTM1	209588	secreted and transmembrane 1
SERPINB9	20723	serpin peptidase inhibitor, clade B (ovalbumin), member 9
SERPINE1	18787	serpin peptidase inhibitor, clade E (nexin, plasminogen activator inhibitor type 1), member 1
SERPING1	12258	serpin peptidase inhibitor, clade G (C1 inhibitor), member 1
SIKE1	66641	suppressor of IKBKE 1
SIRPA	19261	signal-regulatory protein alpha
SLC15A3	65221	solute carrier family 15 (oligopeptide transporter), member 3
SLC16A1	20501	solute carrier family 16 (monocarboxylate transporter), member 1
SLC1A1	20510	solute carrier family 1 (neuronal/epithelial high affinity glutamate transporter, system Xag), member 1
SLC25A28	246696	solute carrier family 25 (mitochondrial iron transporter), member 28
SLC25A30	67554	solute carrier family 25, member 30
SLFN5	327978	schlafen family member 5
SMAD3	17127	SMAD family member 3
SNN	20621	stannin
SOCS1	12703	suppressor of cytokine signaling 1
SOCS2	216233	suppressor of cytokine signaling 2
SOCS3	12702	suppressor of cytokine signaling 3
SP110	109032	SP110 nuclear body protein
SPACA3	75622	sperm acrosome associated 3

Appendix

SPN	20737	sialophorin
SPSB1	74646	splA/ryanodine receptor domain and SOCS box containing 1
SPTLC2	20773	serine palmitoyltransferase, long chain base subunit 2
SSBP3	72475	single stranded DNA binding protein 3
STAP1	56792	signal transducing adaptor family member 1
STARD5	170460	StAR-related lipid transfer (START) domain containing 5
STAT1	20846	signal transducer and activator of transcription 1, 91kDa
STAT2	20847	signal transducer and activator of transcription 2, 113kDa
STAT3	20848	signal transducer and activator of transcription 3
STEAP4	117167	STEAP family member 4
SUN2	223697	Sad1 and UNC84 domain containing 2
TAGAP	72536	T-cell activation RhoGTPase activating protein
TANK	21353	TRAF family member-associated Nf-kappa B activator
TAP1	21354	transporter 1, ATP-binding cassette, sub-family B (MDR/TAP)
TAP2	21355	transporter 2, ATP-binding cassette, sub-family B (MDR/TAP)
TAPBP	21356	TAP binding protein
TBK1	56480	TANK-binding kinase 1
TBX3	21386	T-box 3
TCF7L2	21416	transcription factor 7-like 2 (T-cell specific, HMG-box)
TDRD7	100121	tudor domain containing 7
TFEC	21426	transcription factor EC
THBD	21824	thrombomodulin
TICAM1	106759	toll-like receptor adaptor molecule 1
TIMP1	21857	TIMP metalloproteinase inhibitor 1
TLK2	24086	tousled-like kinase 2
TLR3	142980	toll-like receptor 3
TLR7	170743	toll-like receptor 7
TLR8	170744	toll-like receptor 8
TMEM140	68487	transmembrane protein 140
TMEM173	72512	transmembrane protein 173
TMEM51	214359	transmembrane protein 51
TNF	21926	tumor necrosis factor
TNFAIP3	21929	tumor necrosis factor, alpha-induced protein 3
TNFRSF10A	21933	tumor necrosis factor receptor superfamily, member 10a
TNFRSF9	21942	tumor necrosis factor, alpha-induced protein 9
TNFSF10	22035	tumor necrosis factor (ligand) superfamily, member 10
TRAF2	22030	TNF Receptor Associated Factor 2
TRAF3	22031	TNF Receptor Associated Factor 4
TRAF6	22034	TNF Receptor Associated Factor 6
TRAFD1	231712	TRAF-type zinc finger domain containing 1
TREX1	22040	three prime repair exonuclease 1
TRIM14	74735	tripartite motif containing 14
TRIM21	20821	tripartite motif containing 21
TRIM25	217069	tripartite motif containing 25
TRIM38	214158	tripartite motif containing 38
TRIM5	667823	tripartite motif containing 5
TRIM56	384309	tripartite motif containing 56
TXNIP	56338	Thioredoxin Interacting Protein
TYK2	54721	Tyrosine Kinase 2
TYMP	72962	thymidine phosphorylase
UBA7	74153	ubiquitin-like modifier activating enzyme 7
UBE2L6	56791	ubiquitin-conjugating enzyme E2L 6
ULK4	209012	unc-51 like kinase 4
UNC93B1	54445	unc-93 homolog B1 (C. elegans)
UPP2	76654	Uridine Phosphorylase 2
URI1	19777	URI1, prefoldin-like chaperone
USP18	24110	ubiquitin specific peptidase 18
VAMP5	53620	vesicle-associated membrane protein 5
VAV1	22324	vav 1 oncogene

## Appendix

VEGFC	22341	vascular endothelial growth factor C
VMP1	75909	vacuole membrane protein 1
WARS	22375	tryptophanyl-tRNA synthetase
WHAMM	434204	WAS protein homolog associated with actin, golgi membranes and microtubules
XAF1	327959	XIAP associated factor 1
XCL1	16963	chemokine (C motif) ligand 1
XPR1	19775	xenotropic and polytropic retrovirus receptor 1
ZBP1	58203	Z-DNA Binding Protein 1
ZC3HAV1	78781	zinc finger CCCH-type, antiviral 1
ZNF295	114565	zinc finger protein 295
ZNF385B	241494	zinc finger protein 385B

## 6.2 Abbreviations

<b>1<sup>ry</sup></b>	Primary
<b>2<sup>ry</sup></b>	Secondary
<b>5-FU</b>	5-Fluorouracil
<b>ABL1</b>	Abelson leukemia virus
<b>ALIX</b>	ALG-2-interacting protein X
<b>AML</b>	Acute myeloid leukemia
<b>ATP</b>	Adenosine triphosphate
<b>BCR</b>	Breakpoint cluster region
<b>BM</b>	Bone marrow
<b>CH</b>	Clonal hematopoiesis
<b>circRNA</b>	Circular RNA
<b>CML</b>	Chronic myeloid leukemia
<b>CMPs</b>	Common myeloid progenitors
<b>CNS</b>	Central nervous system
<b>CTLA-4</b>	Cytotoxic T-lymphocyte-associated protein 4
<b>CTV</b>	Cell trace violet
<b>D</b>	Day
<b>DNA</b>	Deoxyribonucleic acid
<b>E</b>	Embryonic day
<b>eGFP</b>	Enhanced green fluorescent protein
<b>EHT</b>	Endothelial-to-hematopoietic transition
<b>EMP</b>	Erythroid and myeloid progenitor
<b>ER</b>	Endoplasmic reticulum
<b>ESEs</b>	Early-sorting endosomes
<b>EVs</b>	Extracellular vesicles
<b>F</b>	Fraction
<b>FACS</b>	Fluorescence-activated cell sorting
<b>FBS</b>	Fetal bovine serum
<b>FDR</b>	False discovery rate
<b>G-CSF</b>	Colony-stimulating factor
<b>GAS</b>	Gamma ( $\gamma$ )-activated sequence
<b>GMP</b>	Granulocyte-monocyte progenitors
<b>GO</b>	Gene ontology
<b><math>\gamma</math></b>	Gamma
<b>HMGB1</b>	High-mobility group box 1
<b>HSC</b>	Hematopoietic stem cell
<b>HSPCs</b>	Hematopoietic stem and progenitor cells
<b>i.p.</b>	Intraperitoneal
<b>i.v.</b>	Intravenously
<b>IAHC</b>	Intra-aortic hematopoietic cluster
<b>ICAM</b>	Intercellular adhesion molecule
<b>ICAM-1</b>	Intercellular adhesion molecule-1
<b>IFN</b>	Interferon
<b>IFNAR1</b>	IFN alpha/beta receptor 1
<b>IFNAR2</b>	IFN alpha/beta receptor 2
<b>IL-3</b>	Interleukin 3
<b>IL-6</b>	Interleukin 6
<b>ILVs</b>	Intraluminal vesicles
<b>IPA</b>	Ingenuity pathway analysis
<b>IRF9</b>	IFN-regulatory factor 9
<b>ISEV</b>	International Society for Extracellular Vesicles
<b>ISG</b>	IFN-stimulated genes
<b>ISGF3</b>	IFN-stimulated gene factor 3
<b>ISRE</b>	IFN-stimulated response elements
<b>IVC</b>	Individually ventilated cages
<b>JAK1</b>	Janus-activated kinase 1
<b>KO</b>	Knock out
<b>LK</b>	Lin-ckit+
<b>lncRNA</b>	Long non-coding RNA

## Appendix

<b>LPMs</b>	Large peritoneal macrophages
<b>LPS</b>	Lipopolysaccharide
<b>LS<sup>-</sup>K</b>	Lin <sup>-</sup> Sca-1 <sup>-</sup> ckit <sup>+</sup>
<b>LSC</b>	Leukemia stem cell
<b>LSEs</b>	Late-sorting endosomes
<b>LSK</b>	Lin <sup>-</sup> Sca-1 <sup>+</sup> ckit <sup>+</sup>
<b>MDMs</b>	Monocyte-derived macrophages
<b>MFI</b>	Median fluorescence intensity
<b>MHC-II</b>	Histocompatibility complex class II
<b>miRNAs/miRs</b>	Micrnas
<b>MISEV</b>	Minimal Information for Studies of Extracellular Vesicles
<b>MOI</b>	Multiplicity of infection
<b>MPN</b>	Myeloproliferative neoplasm
<b>MPNs</b>	Myeloproliferative neoplasms
<b>mRNA</b>	Messenger RNA
<b>mSCF</b>	Murine stem cell factor
<b>MSCs</b>	Mesenchymal stem cells
<b>MSCV</b>	Murine stem cell vector
<b>MSigDB</b>	Molecular signature database
<b>MVBs</b>	Multivesicular bodies
<b>MVs</b>	Microvesicles
<b>MΦ</b>	Macrophages
<b>N</b>	Nilotinib treatment day
<b>ncRNAs</b>	Non-coding rnas
<b>NTA</b>	Nanoparticle tracking analysis
<b>O.G.</b>	Oral gavage
<b>PB</b>	Peripheral blood
<b>PBS</b>	Phosphate buffer saline
<b>PCA</b>	Principal component analysis
<b>PCR</b>	Polymerase chain reaction
<b>PD-L1</b>	Programmed death-ligand 1
<b>Ph</b>	Philadelphia chromosome
<b>pl:C</b>	Polyinosinic:polycytidylic acid
<b>Plat-E</b>	Platinum-E
<b>qRT-PCR</b>	Real-time quantitative reverse transcription PCR
<b>R</b>	Relapse day
<b>rMSCs</b>	Reinvigorating mesenchymal stem cells
<b>RNA</b>	Deoxyribonucleic acid
<b>SEC</b>	Size exclusion chromatography
<b>sEVs</b>	Small extracellular vesicles
<b>SPMs</b>	Small peritoneal macrophages
<b>STAT</b>	Signal transducers and activators of transcription
<b>TEM</b>	Transmission electron microscope
<b>TFR</b>	Tumor-free remission
<b>TGF-β</b>	Transforming growth factor
<b>TGN</b>	Trans-Golgi network
<b>TGS101</b>	Tumor susceptibility gene 101
<b>TKIs</b>	Tyrosine kinase inhibitors
<b>TNF-α</b>	Tumor necrosis factor-alpha
<b>TRMs</b>	Tissue-resident macrophages
<b>TYK2</b>	Tyrosine kinase 2
<b>VCAM-1</b>	Vascular cell adhesion molecule-1
<b>WT</b>	Wildtype
<b>α</b>	Alpha
<b>β</b>	Beta

### 6.3 List of figures

Figure 1   IFN type I and type II signaling pathway. ....	5
Figure 2   Intrinsic IFN signaling heterogeneity represents a powerful indicator of stemness in the hematopoietic system. ....	7
Figure 3   Stem cell based intrinsic IFN signaling heterogeneity in the hematopoietic system. ....	8
Figure 4   The biogenesis of sEVs. ....	12
Figure 5   The composition and cargo of sEVs. ....	13
Figure 6   <i>ISRE-eGFP</i> reporter mouse model reveals intrinsic IFN signaling heterogeneity in HSCs. ....	18
Figure 7   Identification of tissue resident macrophages in WT mice. ....	19
Figure 8   IFN signaling heterogeneity in tissue resident macrophages in <i>ISRE-eGFP</i> mice. ....	20
Figure 9   IFN signaling heterogeneity in TRMs confirmed by transcriptional profiling of ISGs. ....	22
Figure 10   No difference in baseline infectibility of eGFP <sup>low</sup> and eGFP <sup>high</sup> HSCs with murine stem cell vector (MSCV) retrovirus. ....	25
Figure 11   No difference in the response to <i>in vivo</i> 5-FU treatment between eGFP <sup>low</sup> and eGFP <sup>high</sup> HSCs. ....	27
Figure 12   No difference between eGFP <sup>low</sup> and eGFP <sup>high</sup> HSC response to <i>in vitro</i> cytokine pre-stimulation and viral transduction. ....	29
Figure 13   Transplantation of BCR::ABL1 transduced BM induced a CML-like disease <i>in vivo</i> . ....	31
Figure 14   Mice transplanted with BM transduced with control MSCV-IRES-mCherry exhibit a normal phenotype <i>in vivo</i> . ....	33
Figure 15   Clonal expansion advantage of eGFP <sup>low</sup> neutrophils in PB of leukemic mice. ....	35
Figure 16   Leukemic eGFP <sup>low</sup> HSCs show increased chimerism and quiescence. ....	37
Figure 17   Clonal expansion advantage of eGFP <sup>low</sup> leukemic cells in 2 <sup>ry</sup> ISG-CML mice. ....	39
Figure 18   Effective leukemia progression control with frontline nilotinib TKI therapy. ....	41
Figure 19   eGFP <sup>low</sup> leukemic cells expand in mice generated by 2 <sup>ry</sup> transplantation from nilotinib treated mice. ....	43
Figure 20   Absence of apparent relapse in nilotinib-treated ISG-CML mice up to 32 days post-treatment cessation. ....	45
Figure 21   Faster rate of leukemia progression in eGFP <sup>low</sup> chimeric ISG-CML mice. ....	47
Figure 22   Expression of <i>BCR::ABL1</i> in eGFP <sup>low</sup> HSCs promotes aggressive leukemogenesis <i>in vivo</i> . ....	49
Figure 23   Isolation of sEVs through sequential centrifugation and SEC. ....	51
Figure 24   Incorporating SEC to sEV isolation enhances purity. ....	53
Figure 25   Isolation of <i>in vitro</i> -generated exosome-enriched rMSC sEVs. ....	55
Figure 26   Variations in particle and protein quantities of sEVs derived from from PBS and IFN $\alpha$ treated stromal cells. ....	56
Figure 27   rMSC derived sEVs do not affect proliferation or differentiation potential of HSPCs <i>in vitro</i> . ....	58
Figure 28   Isolation of exosome-enriched sEVs from murine BM. ....	59

## Appendix

Figure 29   Inflammatory stress induces changes in the size distribution and abundance of BM sEVs <i>in vivo</i> . .....	60
Figure 30   <i>In vitro</i> suppression of HSPC proliferation by BM pl:C-induced sEVs. ....	63
Figure 31   Dynamic increase in sEV production during inflammation is predominantly orchestrated by hematopoietic cells <i>in vivo</i> . .....	65
Figure 32   Optimization of the <i>in vivo</i> treatment dose of inflammatory BM sEVs .....	66
Figure 33   Inflammatory sEV administration impacts the myeloid compartment <i>in vivo</i> . .....	67
Figure 34   Alterations in the proteomic composition of sEVs isolated from murine BM in response to inflammatory stress. ....	69

**6.4 list of tables**

Table 1   List of flow cytometry antibodies and stains .....	85
Table 2   List of Western Blot antibodies .....	86
Table 3   List of qRT-PCR primers and sequences .....	87
Table 4   List of kits.....	90
Table 5   List of reagents and buffers .....	90
Table 6   List of additional material .....	92
Table 7   List of cell lines and plasmids .....	93
Table 8   List of equipment .....	93
Table 9   List of programs and software .....	94
Table 10   Cell population surface markers .....	99
Table 11  List of mouse-specific ISGs (Wu et al., 2018) .....	110

### 7. Contributions

This doctoral thesis represents the research conducted during my time in Marieke Essers's laboratory. While the majority of the work is the result of my efforts, it is essential to acknowledge the collaborative nature of certain experiments. I extend my appreciation to those who contributed to the following aspects of this research:

#### 7.1 Technical support and expertise

Andrea Kuck offered comprehensive technical support throughout the experiments, aiding in various aspects of mouse experiments such as experiment setup, animal bleeding, bone extraction, cell harvesting, staining protocols, and antibody titrations. Additionally, she provided valuable technical assistance in the purification of sEVs, as well as protein extraction and quantification. Franziska Pilz contributed to maintaining mouse lines, ordering mice, genotyping, setting up matings, and translating animal protocols.

The Central Animal Laboratory of the DKFZ supported animal husbandry and irradiation protocols. The Flow Cytometry Core Facility at the DKFZ offered valuable technical support and training for the operation of flow cytometry sorters and analyzers. The Electron Microscopy Core Facility at the DKFZ provided full technical support for performing TEM experiments. The Genomics and Proteomics Core facility at the DKFZ provided full technical support for performing microarrays and proteomic analysis.

#### 7.2 Collaborative research efforts

As part of her master's thesis work conducted in the Essers lab under the co-supervision of Marieke and myself, Marie-Elen Tuchel made contributions to the execution of experiments related to Aim 3: "Develop a reliable and reproducible method for isolating exosome-enriched sEVs". This included purification of sEVs, conducting western blots, employing NTA, protein extraction, preparing samples for TEM, and comprehensive data analysis. Additionally, our collaborative efforts extended to conducting *in vitro* experiments for Aim 4: "Investigate the role of sEV signaling in regulating system response to inflammatory stress". This involved cell cultures, qRT-PCR analyses, sample preparation for TEM and proteomic analysis, flow cytometry procedures, and data analysis.

## Contributions

Kalliopi-Anna Penteskoufi, a lab rotation student under co-supervision of Marieke and myself, assisted in some of the experiments related to aim 2: “Investigate the impact of IFN signaling in LSC on clonal expansion and disease progression in CML”. This included assistance in generating viral supernatants, viral titer quantifications, and performing first control *in vitro* transduction experiments.

### **8. Acknowledgment**

With profound gratitude and a heart full of thanks, I extend my deepest appreciation to the remarkable individuals who have played pivotal roles in my academic journey.

First and foremost, I express my sincere appreciation to Marieke Essers, whose impact on my life is indelible. I am incredibly fortunate for the opportunity you provided to pursue my doctorate in your lab. Your guidance created the perfect environment for my growth as a scientist and as an individual. Your embodiment of professionalism, class, and empathy has set a standard that I aspire to uphold throughout my career. Thank you for your unwavering support, genuine care for my research, career development, and well-being. Your presence, always there when needed, will be eternally remembered and appreciated.

I extend my gratitude to my Thesis Advisory Committee (TAC) members, Ralf Bartenschlager and Steve Boulant, for their invaluable advice and support.

Andrea Kuck, the pillar of our lab, deserves a special acknowledgment. Your warmth, love, and exceptional partnership have made you the best lab partner one could ask for. Your contagious enthusiasm and bright spirit infused life and energy into every aspect of our research project. I am immensely grateful for your role in my success and motivation.

To Sarah Geiger, my ally and best friend in the lab, your unwavering support, as my secret keeper, attitude checker, eating partner, and true buddy, has been a constant source of strength. Our friendship has become one of the cornerstones of my doctoral journey, and I eagerly anticipate the lasting bond we share.

Nirmeen Elmadany, though our time together in Germany was brief, your influence was profound. Your intelligence, kindness, and genuine nature have left an everlasting impact on me. I am thankful for your support, engaging backgammon games, and meaningful conversations.

Johnna, your unique spirit has been a comforting presence, and I always felt reassured in your company. It is an absolute privilege to call you my friend.

To Stephi, your time in the lab may have flown by swiftly, but your friendship is forever. I consider myself fortunate to have you as one of my dearest friends, and I eagerly look forward to witnessing the great things that lie ahead for you.

## Acknowledgment

Tasneem and Martha, your presence made Germany feel like home. Tasneem, with your perfect smile, and Martha, with your very German spirit, you both provided a sense of belonging that eased the distance from home.

Mohamed Abdalla, my dearest friend and confidant, you hold a special place in my heart. Your kindness, resilience, and genuine nature have made a lasting impact on me. I feel incredibly fortunate to have you by my side. Witnessing your personal and academic growth has been a privilege. I am proud to be part of your journey, just as you are an essential part of mine. Thank you for being a great companion—I look forward to the continued adventures we share. My heartfelt appreciation and love go out to you.

To my family back home—Farah, Abeer, Imad, Sameer, Myriam, and Amira—thank you for your unwavering love and support. I am truly blessed to have the best family anyone could ask for. Mama, I love you.

Ghada, I can't believe I pulled this off without you! The countless hours spent on the phone made this journey more manageable, and I eagerly await the day I can call you Dr. to your face.

Lastly, to Nour, my love, every achievement is dedicated to us. Your unwavering belief in me has been my driving force, and I hope to make you proud with this accomplishment and those that follow.

## 9. Bibliography

- Ahn, S. H., Ryu, S. W., Choi, H., You, S., Park, J., & Choi, C. (2022). Manufacturing Therapeutic Exosomes: from Bench to Industry. *Mol Cells*, *45*(5), 284-290. doi:10.14348/molcells.2022.2033
- Annunziata, M., Bonifacio, M., Breccia, M., Castagnetti, F., Gozzini, A., Iurlo, A., . . . Specchia, G. (2020). Current Strategies and Future Directions to Achieve Deep Molecular Response and Treatment-Free Remission in Chronic Myeloid Leukemia. *Frontiers in oncology*, *10*(883). doi:10.3389/fonc.2020.00883
- Anthony, B. A., & Link, D. C. (2014). Regulation of hematopoietic stem cells by bone marrow stromal cells. *Trends in immunology*, *35*(1), 32-37.
- Asare-Werehene, M., Nakka, K., Reunov, A., Chiu, C.-T., Lee, W.-T., Abedini, M. R., . . . Tsang, B. K. (2020). The exosome-mediated autocrine and paracrine actions of plasma gelsolin in ovarian cancer chemoresistance. *Oncogene*, *39*(7), 1600-1616. doi:10.1038/s41388-019-1087-9
- Baccarani, M. (2017). Treatment-free remission in chronic myeloid leukemia: floating between expectation and evidence. *Leukemia*, *31*(4), 1015-1016. doi:10.1038/leu.2017.20
- Belzile, J. P., Stark, T. J., Yeo, G. W., & Spector, D. H. (2014). Human cytomegalovirus infection of human embryonic stem cell-derived primitive neural stem cells is restricted at several steps but leads to the persistence of viral DNA. *Journal of Virology*, *88*(8), 4021-4039. doi:10.1128/JVI.03492-13
- Benjamini, Y., & Hochberg, Y. (1995). Controlling the False Discovery Rate: A Practical and Powerful Approach to Multiple Testing. *Journal of the Royal Statistical Society: Series B (Methodological)*, *57*(1), 289-300. doi:<https://doi.org/10.1111/j.2517-6161.1995.tb02031.x>
- Benz, C., Copley, M. R., Kent, D. G., Wohrer, S., Cortes, A., Aghaeepour, N., . . . Eaves, C. J. (2012). Hematopoietic stem cell subtypes expand differentially during development and display distinct lymphopoietic programs. *Cell Stem Cell*, *10*(3), 273-283. doi:10.1016/j.stem.2012.02.007
- Berumen Sánchez, G., Bunn, K. E., Pua, H. H., & Rafat, M. (2021). Extracellular vesicles: mediators of intercellular communication in tissue injury and disease. *Cell Communication and Signaling*, *19*(1), 104. doi:10.1186/s12964-021-00787-y
- Bogeska, R., Mikecin, A. M., Kaschutnig, P., Fawaz, M., Büchler-Schäff, M., Le, D., . . . Milsom, M. D. (2022). Inflammatory exposure drives long-lived impairment of hematopoietic stem cell self-renewal activity and accelerated aging. *Cell Stem Cell*, *29*(8), 1273-1284.e1278. doi:10.1016/j.stem.2022.06.012
- Bowman, R. L., Busque, L., & Levine, R. L. (2018). Clonal Hematopoiesis and Evolution to Hematopoietic Malignancies. *Cell Stem Cell*, *22*(2), 157-170. doi:<https://doi.org/10.1016/j.stem.2018.01.011>
- Branford, S. (2020). Why is it critical to achieve a deep molecular response in chronic myeloid leukemia? *Haematologica*, *105*(12), 2730-2737. doi:10.3324/haematol.2019.240739
- Bruns, I., Czibere, A., Fischer, J. C., Roels, F., Cadeddu, R. P., Buest, S., . . . Haas, R. (2009). The hematopoietic stem cell in chronic phase CML is characterized by a transcriptional profile resembling normal myeloid progenitor cells and reflecting loss of quiescence. *Leukemia*, *23*(5), 892-899. doi:10.1038/leu.2008.392

## Bibliography

- Buenrostro, J. D., Wu, B., Chang, H. Y., & Greenleaf, W. J. (2015). ATAC-seq: A Method for Assaying Chromatin Accessibility Genome-Wide. *Curr Protoc Mol Biol*, *109*, 21.29.21-21.29.29. doi:10.1002/0471142727.mb2129s109
- Bührer, E. D., Amrein, M. A., Forster, S., Isringhausen, S., Schürch, C. M., Bhatte, S. S., . . . Ochsenbein, A. F. (2022). Splenic red pulp macrophages provide a niche for CML stem cells and induce therapy resistance. *Leukemia*, *36*(11), 2634-2646. doi:10.1038/s41375-022-01682-2
- Burgelman, M., Vandendriessche, C., & Vandembroucke, R. E. (2021). Extracellular Vesicles: A Double-Edged Sword in Sepsis. *Pharmaceuticals (Basel)*, *14*(8). doi:10.3390/ph14080829
- Butler, J. T., Abdelhamed, S., & Kurre, P. (2018). Extracellular vesicles in the hematopoietic microenvironment. *Haematologica*, *103*(3), 382-394. doi:10.3324/haematol.2017.183335
- Buzas, E. I. (2023). The roles of extracellular vesicles in the immune system. *Nature Reviews Immunology*, *23*(4), 236-250. doi:10.1038/s41577-022-00763-8
- Caiado, F., Pietras, E. M., & Manz, M. G. (2021). Inflammation as a regulator of hematopoietic stem cell function in disease, aging, and clonal selection. *J Exp Med*, *218*(7). doi:10.1084/jem.20201541
- Cain, D. W., O'Koren, E. G., Kan, M. J., Womble, M., Sempowski, G. D., Hopper, K., . . . Kelsoe, G. (2013). Identification of a Tissue-Specific, C/EBP $\beta$ -Dependent Pathway of Differentiation for Murine Peritoneal Macrophages. *The Journal of Immunology*, *191*(9), 4665-4675. doi:10.4049/jimmunol.1300581
- Cain, D. W., Snowden, P. B., Sempowski, G. D., & Kelsoe, G. (2011). Inflammation triggers emergency granulopoiesis through a density-dependent feedback mechanism. *PLoS One*, *6*(5), e19957. doi:10.1371/journal.pone.0019957
- Carrelha, J., Meng, Y., Kettyle, L. M., Luis, T. C., Norfo, R., Alcolea, V., . . . Jacobsen, S. E. W. (2018). Hierarchically related lineage-restricted fates of multipotent haematopoietic stem cells. *Nature*, *554*(7690), 106-111. doi:10.1038/nature25455
- Carter, B. Z., Mak, P. Y., Mu, H., Zhou, H., Mak, D. H., Schober, W., . . . Andreeff, M. (2016). Combined targeting of BCL-2 and BCR-ABL tyrosine kinase eradicates chronic myeloid leukemia stem cells. *Sci Transl Med*, *8*(355), 355ra117. doi:10.1126/scitranslmed.aag1180
- Caruso Bavisotto, C., Scalia, F., Marino Gammazza, A., Carlisi, D., Bucchieri, F., Conway de Macario, E., . . . Campanella, C. (2019). Extracellular Vesicle-Mediated Cell-Cell Communication in the Nervous System: Focus on Neurological Diseases. *Int J Mol Sci*, *20*(2). doi:10.3390/ijms20020434
- Cassado, A. d. A., D'Império Lima, M. R., & Bortoluci, K. R. (2015). Revisiting Mouse Peritoneal Macrophages: Heterogeneity, Development, and Function. *Frontiers in Immunology*, *6*. doi:10.3389/fimmu.2015.00225
- Challen, G. A., Boles, N., Lin, K. K., & Goodell, M. A. (2009). Mouse hematopoietic stem cell identification and analysis. *Cytometry A*, *75*(1), 14-24. doi:10.1002/cyto.a.20674
- Chen, Y. S., Lin, E. Y., Chiou, T. W., & Harn, H. J. (2020). Exosomes in clinical trial and their production in compliance with good manufacturing practice. *Ci Ji Yi Xue Za Zhi*, *32*(2), 113-120. doi:10.4103/tcmj.tcmj\_182\_19
- Clayton, A., Court, J., Navabi, H., Adams, M., Mason, M. D., Hobot, J. A., . . . Jasani, B. (2001). Analysis of antigen presenting cell derived exosomes, based on immuno-magnetic

## Bibliography

- isolation and flow cytometry. *J Immunol Methods*, 247(1-2), 163-174. doi:10.1016/s0022-1759(00)00321-5
- Copelan, E. A. (2006). Hematopoietic stem-cell transplantation. *N Engl J Med*, 354(17), 1813-1826. doi:10.1056/NEJMra052638
- Cosgun, K. N., Rahmig, S., Mende, N., Reinke, S., Hauber, I., Schäfer, C., . . . Waskow, C. (2014). Kit regulates HSC engraftment across the human-mouse species barrier. *Cell Stem Cell*, 15(2), 227-238. doi:10.1016/j.stem.2014.06.001
- Craver, B. M., El Alaoui, K., Scherber, R. M., & Fleischman, A. G. (2018). The Critical Role of Inflammation in the Pathogenesis and Progression of Myeloid Malignancies. *Cancers*, 10(4), 104. Retrieved from <https://www.mdpi.com/2072-6694/10/4/104>
- Craver, B. M., El Alaoui, K., Scherber, R. M., & Fleischman, A. G. (2018). The Critical Role of Inflammation in the Pathogenesis and Progression of Myeloid Malignancies. *Cancers (Basel)*, 10(4). doi:10.3390/cancers10040104
- Crisan, M., & Dzierzak, E. (2016). The many faces of hematopoietic stem cell heterogeneity. *Development*, 143(24), 4571-4581. doi:10.1242/dev.114231
- D'Hondt, L., Lambert, J. F., Damon, J., Benoit, B. O., Cerny, J., Carlson, J. E., . . . Quesenberry, P. J. (2002). Engraftment of post 5-fluorouracil murine marrow into minimally myeloablated (100 cGy) murine hosts. *J Hematother Stem Cell Res*, 11(3), 483-490. doi:10.1089/15258160260090942
- De Luca, L., Trino, S., Laurenzana, I., Simeon, V., Calice, G., Raimondo, S., . . . Musto, P. (2016). MiRNAs and piRNAs from bone marrow mesenchymal stem cell extracellular vesicles induce cell survival and inhibit cell differentiation of cord blood hematopoietic stem cells: a new insight in transplantation. *Oncotarget*, 7(6), 6676-6692. doi:10.18632/oncotarget.6791
- Decker, T., Müller, M., & Stockinger, S. (2005). The yin and yang of type I interferon activity in bacterial infection. *Nat Rev Immunol*, 5(9), 675-687. doi:10.1038/nri1684
- Demerdash, Y., Kain, B., Essers, M. A. G., & King, K. Y. (2021). Yin and Yang: The dual effects of interferons on hematopoiesis. *Exp Hematol*, 96, 1-12. doi:10.1016/j.exphem.2021.02.002
- Diaz, G., Bridges, C., Lucas, M., Cheng, Y., Schorey, J. S., Dobos, K. M., & Kruh-Garcia, N. A. (2018). Protein Digestion, Ultrafiltration, and Size Exclusion Chromatography to Optimize the Isolation of Exosomes from Human Blood Plasma and Serum. *J Vis Exp*(134). doi:10.3791/57467
- Donnelly, D. S., Zelterman, D., Sharkis, S., & Krause, D. S. (1999). Functional activity of murine CD34+ and CD34- hematopoietic stem cell populations. *Exp Hematol*, 27(5), 788-796. doi:10.1016/s0301-472x(99)00032-6
- Dragovic, R. A., Gardiner, C., Brooks, A. S., Tannetta, D. S., Ferguson, D. J., Hole, P., . . . Sargent, I. L. (2011). Sizing and phenotyping of cellular vesicles using Nanoparticle Tracking Analysis. *Nanomedicine*, 7(6), 780-788. doi:10.1016/j.nano.2011.04.003
- Dzierzak, E., & Bigas, A. (2018). Blood Development: Hematopoietic Stem Cell Dependence and Independence. *Cell Stem Cell*, 22(5), 639-651. doi:10.1016/j.stem.2018.04.015
- Eaves, C. J. (2015). Hematopoietic stem cells: concepts, definitions, and the new reality. *Blood*, 125(17), 2605-2613. doi:10.1182/blood-2014-12-570200
- Ehninger, A., & Trumpp, A. (2011). The bone marrow stem cell niche grows up: Mesenchymal stem cells and macrophages move in. *Journal of Experimental Medicine*, 208(3), 421-428. doi:10.1084/jem.20110132

## Bibliography

- El Eit, R., Itani, A. R., Nassar, F., Rasbieh, N., Jabbour, M., Santina, A., . . . Nasr, R. (2019). Antitumor efficacy of arsenic/interferon in preclinical models of chronic myeloid leukemia resistant to tyrosine kinase inhibitors. *Cancer*, *125*(16), 2818-2828. doi:10.1002/cncr.32130
- El Eit, R. M., Iskandarani, A. N., Saliba, J. L., Jabbour, M. N., Mahfouz, R. A., Bitar, N. M., . . . Nasr, R. R. (2014). Effective targeting of chronic myeloid leukemia initiating activity with the combination of arsenic trioxide and interferon alpha. *Int J Cancer*, *134*(4), 988-996. doi:10.1002/ijc.28427
- Essers, M. A., Offner, S., Blanco-Bose, W. E., Waibler, Z., Kalinke, U., Duchosal, M. A., & Trumpp, A. (2009). IFNalpha activates dormant haematopoietic stem cells in vivo. *Nature*, *458*(7240), 904-908. doi:10.1038/nature07815
- A focus on single-cell omics. (2023). *Nature Reviews Genetics*, *24*(8), 485-485. doi:10.1038/s41576-023-00628-3
- Gao, X., Wan, Z., Wei, M., Dong, Y., Zhao, Y., Chen, X., . . . Liu, L. (2019). Chronic myelogenous leukemia cells remodel the bone marrow niche via exosome-mediated transfer of miR-320. *Theranostics*, *9*(19), 5642-5656. doi:10.7150/thno.34813
- García-Gutiérrez, V., & Hernández-Boluda, J. C. (2019). Tyrosine Kinase Inhibitors Available for Chronic Myeloid Leukemia: Efficacy and Safety. *Frontiers in oncology*, *9*, 603. doi:10.3389/fonc.2019.00603
- Gautheron, F., Georgievski, A., Garrido, C., & Quéré, R. (2023). Bone marrow-derived extracellular vesicles carry the TGF- $\beta$  signal transducer Smad2 to preserve hematopoietic stem cells in mice. *Cell Death Discovery*, *9*(1), 117. doi:10.1038/s41420-023-01414-0
- Gavrilescu, L. C., & Van Etten, R. A. (2008). Murine retroviral bone marrow transplantation models for the study of human myeloproliferative disorders. *Curr Protoc Pharmacol*, *Chapter 14*, Unit14.10. doi:10.1002/0471141755.ph1410s43
- Ghosn, E. E. B., Cassado, A. A., Govoni, G. R., Fukuhara, T., Yang, Y., Monack, D. M., . . . Herzenberg, L. A. (2010). Two physically, functionally, and developmentally distinct peritoneal macrophage subsets. *Proceedings of the National Academy of Sciences*, *107*(6), 2568-2573. doi:doi:10.1073/pnas.0915000107
- Ginhoux, F., Greter, M., Leboeuf, M., Nandi, S., See, P., Gokhan, S., . . . Merad, M. (2010). Fate mapping analysis reveals that adult microglia derive from primitive macrophages. *Science*, *330*(6005), 841-845. doi:10.1126/science.1194637
- Ginhoux, F., Greter, M., Leboeuf, M., Nandi, S., See, P., Gokhan, S., . . . Merad, M. (2010). Fate Mapping Analysis Reveals That Adult Microglia Derive from Primitive Macrophages. *Science*, *330*(6005), 841-845. doi:doi:10.1126/science.1194637
- Goloviznina, N. A., Verghese, S. C., Yoon, Y. M., Taratula, O., Marks, D. L., & Kurre, P. (2016). Mesenchymal Stromal Cell-derived Extracellular Vesicles Promote Myeloid-biased Multipotent Hematopoietic Progenitor Expansion via Toll-Like Receptor Engagement. *J Biol Chem*, *291*(47), 24607-24617. doi:10.1074/jbc.M116.745653
- Ha, D., Yang, N., & Nadithe, V. (2016). Exosomes as therapeutic drug carriers and delivery vehicles across biological membranes: current perspectives and future challenges. *Acta Pharm Sin B*, *6*(4), 287-296. doi:10.1016/j.apsb.2016.02.001
- Haas, S., Hansson, J., Klimmeck, D., Loeffler, D., Velten, L., Uckelmann, H., . . . Essers, M. A. (2015). Inflammation-Induced Emergency Megakaryopoiesis Driven by Hematopoietic Stem Cell-like Megakaryocyte Progenitors. *Cell Stem Cell*, *17*(4), 422-434. doi:10.1016/j.stem.2015.07.007

## Bibliography

- Haas, S., Trumpp, A., & Milsom, M. D. (2018). Causes and Consequences of Hematopoietic Stem Cell Heterogeneity. *Cell Stem Cell*, 22(5), 627-638. doi:10.1016/j.stem.2018.04.003
- Harrison, D. E., Astle, C. M., & Delaittre, J. A. (1978). Loss of proliferative capacity in immunohemopoietic stem cells caused by serial transplantation rather than aging. *J Exp Med*, 147(5), 1526-1531. doi:10.1084/jem.147.5.1526
- Harrison, D. E., Stone, M., & Astle, C. M. (1990). Effects of transplantation on the primitive immunohematopoietic stem cell. *J Exp Med*, 172(2), 431-437. doi:10.1084/jem.172.2.431
- Hazan-Halevy, I., Rosenblum, D., Weinstein, S., Bairey, O., Raanani, P., & Peer, D. (2015). Cell-specific uptake of mantle cell lymphoma-derived exosomes by malignant and non-malignant B-lymphocytes. *Cancer Lett*, 364(1), 59-69. doi:10.1016/j.canlet.2015.04.026
- Hijiya, N., Schultz, K. R., Metzler, M., Millot, F., & Suttorp, M. (2016). Pediatric chronic myeloid leukemia is a unique disease that requires a different approach. *Blood*, 127(4), 392-399. doi:10.1182/blood-2015-06-648667
- Ho, N. P., & Takizawa, H. (2022). Inflammation Regulates Haematopoietic Stem Cells and Their Niche. *Int J Mol Sci*, 23(3). doi:10.3390/ijms23031125
- Hodgson, G. S., & Bradley, T. R. (1979). Properties of haematopoietic stem cells surviving 5-fluorouracil treatment: evidence for a pre-CFU-S cell? *Nature*, 281(5730), 381-382. doi:10.1038/281381a0
- Hoffman, R., Benz, E. J., Furie, B., McGlave, P., & Heslop, H. (2008). *Hematology: Basic Principles and Practice*: Churchill Livingstone/Elsevier.
- Hu, Y. (2016). CML Mouse Model Generated from Leukemia Stem Cells. In (Vol. 1465, pp. 27-35).
- Huan, J., Hornick, N. I., Shurtleff, M. J., Skinner, A. M., Goloviznina, N. A., Roberts, C. T., Jr., & Kurre, P. (2013). RNA trafficking by acute myelogenous leukemia exosomes. *Cancer Res*, 73(2), 918-929. doi:10.1158/0008-5472.Can-12-2184
- Hughes, T. P., & Ross, D. M. (2016). Moving treatment-free remission into mainstream clinical practice in CML. *Blood*, 128(1), 17-23. doi:10.1182/blood-2016-01-694265
- Jabbour, E., & Kantarjian, H. (2022). Chronic myeloid leukemia: 2022 update on diagnosis, therapy, and monitoring. *Am J Hematol*, 97(9), 1236-1256. doi:10.1002/ajh.26642
- Jagannathan-Bogdan, M., & Zon, L. I. (2013). Hematopoiesis. *Development*, 140(12), 2463-2467. doi:10.1242/dev.083147
- Jia, Y., Yu, L., Ma, T., Xu, W., Qian, H., Sun, Y., & Shi, H. (2022). Small extracellular vesicles isolation and separation: Current techniques, pending questions and clinical applications. *Theranostics*, 12(15), 6548-6575. doi:10.7150/thno.74305
- Ju, Y. S., Martincorena, I., Gerstung, M., Petljak, M., Alexandrov, L. B., Rahbari, R., . . . Stratton, M. R. (2017). Somatic mutations reveal asymmetric cellular dynamics in the early human embryo. *Nature*, 543(7647), 714-718. doi:10.1038/nature21703
- Kalluri, R., & LeBleu, V. S. (2020). The biology, function, and biomedical applications of exosomes. *Science*, 367(6478). doi:10.1126/science.aau6977
- Kawai, T., & Akira, S. (2006). Innate immune recognition of viral infection. *Nat Immunol*, 7(2), 131-137. doi:10.1038/ni1303
- Kawakubo, K., Ohyashiki, K., Ohyashiki, J. H., Shimamoto, T., Fujimura, T., Iwama, H., & Toyama, K. (1996). A possible correlation between interferon-stimulated gene expression and cytogenetic responses in chronic myelogenous leukemia patients

## Bibliography

- treated with alpha-interferon. *Jpn J Clin Oncol*, 26(2), 59-64. doi:10.1093/oxfordjournals.jjco.a023185
- Keerthikumar, S., Chisanga, D., Ariyaratne, D., Al Saffar, H., Anand, S., Zhao, K., . . . Mathivanan, S. (2016). ExoCarta: A Web-Based Compendium of Exosomal Cargo. *J Mol Biol*, 428(4), 688-692. doi:10.1016/j.jmb.2015.09.019
- Kfoury, Y. S., Ji, F., Mazzola, M., Sykes, D. B., Scherer, A. K., Anselmo, A., . . . Scadden, D. T. (2021). tiRNA signaling via stress-regulated vesicle transfer in the hematopoietic niche. *Cell Stem Cell*, 28(12), 2090-2103.e2099. doi:10.1016/j.stem.2021.08.014
- Konoshenko, M. Y., Lekchnov, E. A., Vlassov, A. V., & Laktionov, P. P. (2018). Isolation of Extracellular Vesicles: General Methodologies and Latest Trends. *Biomed Res Int*, 2018, 8545347. doi:10.1155/2018/8545347
- Koschmieder, S., Göttgens, B., Zhang, P., Iwasaki-Arai, J., Akashi, K., Kutok, J. L., . . . Huettnner, C. S. (2005). Inducible chronic phase of myeloid leukemia with expansion of hematopoietic stem cells in a transgenic model of BCR-ABL leukemogenesis. *Blood*, 105(1), 324-334. doi:10.1182/blood-2003-12-4369
- Kumar, B., Garcia, M., Weng, L., Jung, X., Murakami, J. L., Hu, X., . . . Chen, C. C. (2018). Acute myeloid leukemia transforms the bone marrow niche into a leukemia-permissive microenvironment through exosome secretion. *Leukemia*, 32(3), 575-587. doi:10.1038/leu.2017.259
- Kwak, H.-J., Liu, P., Bajrami, B., Xu, Y., Park, S.-Y., Nombela-Arrieta, C., . . . Luo, Hongbo R. (2015). Myeloid Cell-Derived Reactive Oxygen Species Externally Regulate the Proliferation of Myeloid Progenitors in Emergency Granulopoiesis. *Immunity*, 42(1), 159-171. doi:<https://doi.org/10.1016/j.immuni.2014.12.017>
- Landt, S. G., Marinov, G. K., Kundaje, A., Kheradpour, P., Pauli, F., Batzoglou, S., . . . Snyder, M. (2012). ChIP-seq guidelines and practices of the ENCODE and modENCODE consortia. *Genome Res*, 22(9), 1813-1831. doi:10.1101/gr.136184.111
- Lazear, H. M., Schoggins, J. W., & Diamond, M. S. (2019). Shared and Distinct Functions of Type I and Type III Interferons. *Immunity*, 50(4), 907-923. doi:10.1016/j.immuni.2019.03.025
- Lehrich, B. M., Liang, Y., Khosravi, P., Federoff, H. J., & Fiandaca, M. S. (2018). Fetal Bovine Serum-Derived Extracellular Vesicles Persist within Vesicle-Depleted Culture Media. *Int J Mol Sci*, 19(11). doi:10.3390/ijms19113538
- Lerner, C., & Harrison, D. E. (1990). 5-Fluorouracil spares hemopoietic stem cells responsible for long-term repopulation. *Exp Hematol*, 18(2), 114-118.
- Li, W., Wang, J., Yin, X., Shi, H., Sun, B., Ji, M., . . . Zhang, Y. (2022). Construction of a mouse model that can be used for tissue-specific EV screening and tracing in vivo. *Front Cell Dev Biol*, 10, 1015841. doi:10.3389/fcell.2022.1015841
- Liberzon, A., Birger, C., Thorvaldsdóttir, H., Ghandi, M., Mesirov, J. P., & Tamayo, P. (2015). The Molecular Signatures Database (MSigDB) hallmark gene set collection. *Cell Syst*, 1(6), 417-425. doi:10.1016/j.cels.2015.12.004
- Lötvall, J., Hill, A. F., Hochberg, F., Buzás, E. I., Di Vizio, D., Gardiner, C., . . . Théry, C. (2014). Minimal experimental requirements for definition of extracellular vesicles and their functions: a position statement from the International Society for Extracellular Vesicles. *J Extracell Vesicles*, 3, 26913. doi:10.3402/jev.v3.26913
- Lu, H., Yuan, Z., Tan, T., Wang, J., Zhang, J., Luo, H. J., . . . Gao, F. (2015). Improved tagmentation-based whole-genome bisulfite sequencing for input DNA from less than 100 mammalian cells. *Epigenomics*, 7(1), 47-56. doi:10.2217/epi.14.76

## Bibliography

- Makhijani, P., & McGaha, T. L. (2022). Myeloid Responses to Extracellular Vesicles in Health and Disease. *Front Immunol*, *13*, 818538. doi:10.3389/fimmu.2022.818538
- Marcoux, G., Laroche, A., Hasse, S., Bellio, M., Mbarik, M., Tamagne, M., . . . Boilard, E. (2021). Platelet EVs contain an active proteasome involved in protein processing for antigen presentation via MHC-I molecules. *Blood*, *138*(25), 2607-2620. doi:10.1182/blood.2020009957
- Matatall, K. A., Shen, C.-C., Challen, G. A., & King, K. Y. (2014). Type II Interferon Promotes Differentiation of Myeloid-Biased Hematopoietic Stem Cells. *STEM CELLS*, *32*(11), 3023-3030. doi:<https://doi.org/10.1002/stem.1799>
- McNab, F., Mayer-Barber, K., Sher, A., Wack, A., & O'Garra, A. (2015). Type I interferons in infectious disease. *Nature Reviews Immunology*, *15*(2), 87-103. doi:10.1038/nri3787
- Meldolesi, J. (2018). Exosomes and Ectosomes in Intercellular Communication. *Current Biology*, *28*(8), R435-R444. doi:<https://doi.org/10.1016/j.cub.2018.01.059>
- Miyawaki, K., Kusumoto, H., Iino, T., Kohno, K., Tsuzuki, H., Shima, T., . . . Akashi, K. (2013). The Expansion Of CML Clones Initiates At The CMP Stage, and Is Associated With The Down-Regulation Of IRF8 and GFI1. *Blood*, *122*(21), 1477-1477. doi:10.1182/blood.V122.21.1477.1477
- Morita, Y., Ema, H., & Nakauchi, H. (2010). Heterogeneity and hierarchy within the most primitive hematopoietic stem cell compartment. *Journal of Experimental Medicine*, *207*(6), 1173-1182.
- Morita, Y., Iseki, A., Okamura, S., Suzuki, S., Nakauchi, H., & Ema, H. (2011). Functional characterization of hematopoietic stem cells in the spleen. *Exp Hematol*, *39*(3), 351-359.e353. doi:10.1016/j.exphem.2010.12.008
- Morrison, S. J., & Scadden, D. T. (2014). The bone marrow niche for haematopoietic stem cells. *Nature*, *505*(7483), 327-334.
- Muthu, S., Bapat, A., Jain, R., Jeyaraman, N., & Jeyaraman, M. (2021). Exosomal therapy-a new frontier in regenerative medicine. *Stem Cell Investig*, *8*, 7. doi:10.21037/sci-2020-037
- Negishi, H., Taniguchi, T., & Yanai, H. (2018). The Interferon (IFN) Class of Cytokines and the IFN Regulatory Factor (IRF) Transcription Factor Family. *Cold Spring Harb Perspect Biol*, *10*(11). doi:10.1101/cshperspect.a028423
- Niu, R., Pan, P., Li, C., Luo, B., Ma, H., Hao, H., . . . Chen, J. (2023). Bone mesenchymal stromal cell-derived small extracellular vesicles inhibit inflammation and ameliorate sepsis via delivery of microRNA-21a-5p. *Cytotherapy*, *25*(6), 625-639. doi:<https://doi.org/10.1016/j.jcyt.2023.02.002>
- Osawa, M., Hanada, K., Hamada, H., & Nakauchi, H. (1996). Long-term lymphohematopoietic reconstitution by a single CD34-low/negative hematopoietic stem cell. *Science*, *273*(5272), 242-245. doi:10.1126/science.273.5272.242
- Passegué, E., Wagers, A. J., Giuriato, S., Anderson, W. C., & Weissman, I. L. (2005). Global analysis of proliferation and cell cycle gene expression in the regulation of hematopoietic stem and progenitor cell fates. *Journal of Experimental Medicine*, *202*(11), 1599-1611. doi:10.1084/jem.20050967
- Patel, N. J., Ashraf, A., & Chung, E. J. (2023). Extracellular Vesicles as Regulators of the Extracellular Matrix. *Bioengineering (Basel)*, *10*(2). doi:10.3390/bioengineering10020136
- Pauklin, S., & Vallier, L. (2013). The cell-cycle state of stem cells determines cell fate propensity. *Cell*, *155*(1), 135-147.

## Bibliography

- Pear, W. S., Miller, J. P., Xu, L., Pui, J. C., Soffer, B., Quackenbush, R. C., . . . Baltimore, D. (1998). Efficient and rapid induction of a chronic myelogenous leukemia-like myeloproliferative disease in mice receiving P210 bcr/abl-transduced bone marrow. *Blood*, *92*(10), 3780-3792.
- Pinho, S., & Frenette, P. S. (2019). Haematopoietic stem cell activity and interactions with the niche. *Nature Reviews Molecular Cell Biology*, *20*(5), 303-320. doi:10.1038/s41580-019-0103-9
- Pitt, J. M., Kroemer, G., & Zitvogel, L. (2016). Extracellular vesicles: masters of intercellular communication and potential clinical interventions. *The Journal of clinical investigation*, *126*(4), 1139-1143. doi:10.1172/jci87316
- Ramkumar, C., Gerstein, R. M., & Zhang, H. (2013). Serial transplantation of bone marrow to test self-renewal capacity of hematopoietic stem cells in vivo. *Methods Mol Biol*, *976*, 17-24. doi:10.1007/978-1-62703-317-6\_2
- Rana, S., Yue, S., Stadel, D., & Zöller, M. (2012). Toward tailored exosomes: the exosomal tetraspanin web contributes to target cell selection. *Int J Biochem Cell Biol*, *44*(9), 1574-1584. doi:10.1016/j.biocel.2012.06.018
- Raposo, G., & Stoorvogel, W. (2013). Extracellular vesicles: exosomes, microvesicles, and friends. *J Cell Biol*, *200*(4), 373-383. doi:10.1083/jcb.201211138
- Sanderson, R. D., Bandari, S. K., & Vlodavsky, I. (2019). Proteases and glycosidases on the surface of exosomes: Newly discovered mechanisms for extracellular remodeling. *Matrix Biology*, *75-76*, 160-169. doi:<https://doi.org/10.1016/j.matbio.2017.10.007>
- Schneider, W. M., Chevillotte, M. D., & Rice, C. M. (2014). Interferon-stimulated genes: a complex web of host defenses. *Annu Rev Immunol*, *32*, 513-545. doi:10.1146/annurev-immunol-032713-120231
- Scholar, E. (2007). Chronic Myelogenous Leukemia. In S. J. Enna & D. B. Bylund (Eds.), *xPharm: The Comprehensive Pharmacology Reference* (pp. 1-5). New York: Elsevier.
- Schreiber, G. (2017). The molecular basis for differential type I interferon signaling. *J Biol Chem*, *292*(18), 7285-7294. doi:10.1074/jbc.R116.774562
- Schubert, C., Allhoff, M., Tillmann, S., Maié, T., Costa, I. G., Lipka, D. B., . . . Koschmieder, S. (2019). Differential roles of STAT1 and STAT2 in the sensitivity of JAK2V617F- vs. BCR-ABL-positive cells to interferon alpha. *J Hematol Oncol*, *12*(1), 36. doi:10.1186/s13045-019-0722-9
- Schwanhäusser, B., Busse, D., Li, N., Dittmar, G., Schuchhardt, J., Wolf, J., . . . Selbach, M. (2011). Global quantification of mammalian gene expression control. *Nature*, *473*(7347), 337-342. doi:10.1038/nature10098
- Shaikh, A., Bhartiya, D., Kapoor, S., & Nimkar, H. (2016). Delineating the effects of 5-fluorouracil and follicle-stimulating hormone on mouse bone marrow stem/progenitor cells. *Stem Cell Research & Therapy*, *7*(1), 59. doi:10.1186/s13287-016-0311-6
- Sieburg, H. B., Cho, R. H., Dykstra, B., Uchida, N., Eaves, C. J., & Muller-Sieburg, C. E. (2006). The hematopoietic stem compartment consists of a limited number of discrete stem cell subsets. *Blood*, *107*(6), 2311-2316. doi:10.1182/blood-2005-07-2970
- Subramanian, A., Tamayo, P., Mootha, V. K., Mukherjee, S., Ebert, B. L., Gillette, M. A., . . . Mesirov, J. P. (2005). Gene set enrichment analysis: a knowledge-based approach for interpreting genome-wide expression profiles. *Proc Natl Acad Sci U S A*, *102*(43), 15545-15550. doi:10.1073/pnas.0506580102

## Bibliography

- Sun, J., Ramos, A., Chapman, B., Johnnidis, J. B., Le, L., Ho, Y. J., . . . Camargo, F. D. (2014). Clonal dynamics of native haematopoiesis. *Nature*, *514*(7522), 322-327. doi:10.1038/nature13824
- Takeuchi, O., Fisher, J., Suh, H., Harada, H., Malynn, B. A., & Korsmeyer, S. J. (2005). Essential role of BAX, BAK in B cell homeostasis and prevention of autoimmune disease. *Proc Natl Acad Sci U S A*, *102*(32), 11272-11277. doi:10.1073/pnas.0504783102
- Takov, K., Yellon, D. M., & Davidson, S. M. (2019). Comparison of small extracellular vesicles isolated from plasma by ultracentrifugation or size-exclusion chromatography: yield, purity and functional potential. *J Extracell Vesicles*, *8*(1), 1560809. doi:10.1080/20013078.2018.1560809
- Tanaka, Y., Takeda, R., Fukushima, T., Mikami, K., Tsuchiya, S., Tamura, M., . . . Kitamura, T. (2022). Eliminating chronic myeloid leukemia stem cells by IRAK1/4 inhibitors. *Nature Communications*, *13*(1), 271. doi:10.1038/s41467-021-27928-8
- Taverna, S., Flugy, A., Saieva, L., Kohn, E. C., Santoro, A., Meraviglia, S., . . . Alessandro, R. (2012). Role of exosomes released by chronic myelogenous leukemia cells in angiogenesis. *Int J Cancer*, *130*(9), 2033-2043. doi:10.1002/ijc.26217
- Théry, C., Amigorena, S., Raposo, G., & Clayton, A. (2006). Isolation and characterization of exosomes from cell culture supernatants and biological fluids. *Curr Protoc Cell Biol*, Chapter 3, Unit 3.22. doi:10.1002/0471143030.cb0322s30
- Théry, C., Witwer, K. W., Aikawa, E., Alcaraz, M. J., Anderson, J. D., Andriantsitohaina, R., . . . Zuba-Surma, E. K. (2018). Minimal information for studies of extracellular vesicles 2018 (MISEV2018): a position statement of the International Society for Extracellular Vesicles and update of the MISEV2014 guidelines. *J Extracell Vesicles*, *7*(1), 1535750. doi:10.1080/20013078.2018.1535750
- Thompson, K. K., & Tsirka, S. E. (2017). The Diverse Roles of Microglia in the Neurodegenerative Aspects of Central Nervous System (CNS) Autoimmunity. *Int J Mol Sci*, *18*(3). doi:10.3390/ijms18030504
- Toda, Y., Takata, K., Nakagawa, Y., Kawakami, H., Fujioka, S., Kobayashi, K., . . . Ashihara, E. (2015). Effective internalization of U251-MG-secreted exosomes into cancer cells and characterization of their lipid components. *Biochemical and Biophysical Research Communications*, *456*(3), 768-773. doi:<https://doi.org/10.1016/j.bbrc.2014.12.015>
- Tovey, M. G., Lallemand, C., Meritet, J. F., & Maury, C. (2006). Adjuvant activity of interferon alpha: mechanism(s) of action. *Vaccine*, *24* Suppl 2, S2-46-47. doi:10.1016/j.vaccine.2005.01.117
- Trinchieri, G. (2010). Type I interferon: friend or foe? *J Exp Med*, *207*(10), 2053-2063. doi:10.1084/jem.20101664
- Uchida, N., Fleming, W. H., Alpern, E. J., & Weissman, I. L. (1993). Heterogeneity of hematopoietic stem cells. *Curr Opin Immunol*, *5*(2), 177-184. doi:10.1016/0952-7915(93)90002-a
- Uckelmann, H., Blaszkiewicz, S., Nicolae, C., Haas, S., Schnell, A., Wurzer, S., . . . Essers, M. A. G. (2016). Extracellular matrix protein Matrilin-4 regulates stress-induced HSC proliferation via CXCR4. *Journal of Experimental Medicine*, *213*(10), 1961-1971.
- Van Zant, G. (1984). Studies of hematopoietic stem cells spared by 5-fluorouracil. *J Exp Med*, *159*(3), 679-690. doi:10.1084/jem.159.3.679
- Wang, Y., Zhao, R., Jiao, X., Wu, L., Wei, Y., Shi, F., . . . Xiong, L. (2021). Small Extracellular Vesicles: Functions and Potential Clinical Applications as Cancer Biomarkers. *Life (Basel)*, *11*(10). doi:10.3390/life11101044

## Bibliography

- Weisberg, E., Manley, P. W., Breitenstein, W., Brügggen, J., Cowan-Jacob, S. W., Ray, A., . . . Griffin, J. D. (2005). Characterization of AMN107, a selective inhibitor of native and mutant Bcr-Abl. *Cancer Cell*, 7(2), 129-141. doi:<https://doi.org/10.1016/j.ccr.2005.01.007>
- Wen, S. W., Lima, L. G., Lobb, R. J., Norris, E. L., Hastie, M. L., Krumeich, S., & Möller, A. (2019). Breast Cancer-Derived Exosomes Reflect the Cell-of-Origin Phenotype. *Proteomics*, 19(8), e1800180. doi:10.1002/pmic.201800180
- Wertheim, J. A., Miller, J. P., Xu, L., He, Y., & Pear, W. S. (2002). The biology of chronic myelogenous leukemia: mouse models and cell adhesion. *Oncogene*, 21(56), 8612-8628. doi:10.1038/sj.onc.1206089
- Wiklander, O. P. B., Brennan, M. Á., Lötvall, J., Breakefield, X. O., & EL Andaloussi, S. (2019). Advances in therapeutic applications of extracellular vesicles. *Science Translational Medicine*, 11(492), eaav8521. doi:doi:10.1126/scitranslmed.aav8521
- Wilkinson, A. C., Ishida, R., Kikuchi, M., Sudo, K., Morita, M., Crisostomo, R. V., . . . Yamazaki, S. (2019). Long-term ex vivo haematopoietic-stem-cell expansion allows nonconditioned transplantation. *Nature*, 571(7763), 117-121. doi:10.1038/s41586-019-1244-x
- Wilkinson, A. C., & Yamazaki, S. (2018). The hematopoietic stem cell diet. *Int J Hematol*, 107(6), 634-641. doi:10.1007/s12185-018-2451-1
- Wilson, A., Laurenti, E., Oser, G., van der Wath, R. C., Blanco-Bose, W., Jaworski, M., . . . Trumpp, A. (2008). Hematopoietic stem cells reversibly switch from dormancy to self-renewal during homeostasis and repair. *Cell*, 135(6), 1118-1129. doi:10.1016/j.cell.2008.10.048
- Wilson, A., Laurenti, E., Oser, G., van der Wath, R. C., Blanco-Bose, W., Jaworski, M., . . . Trumpp, A. (2008). Hematopoietic Stem Cells Reversibly Switch from Dormancy to Self-Renewal during Homeostasis and Repair. *Cell*, 135(6), 1118-1129. doi:<https://doi.org/10.1016/j.cell.2008.10.048>
- Wintrobe, M. M., & Greer, J. P. (2014). *Wintrobe's clinical hematology*.
- Wolf, D., & Goff, S. P. (2009). Embryonic stem cells use ZFP809 to silence retroviral DNAs. *Nature*, 458(7242), 1201-1204. doi:10.1038/nature07844
- Wu, X., Dao Thi, V. L., Huang, Y., Billerbeck, E., Saha, D., Hoffmann, H. H., . . . Rice, C. M. (2018). Intrinsic Immunity Shapes Viral Resistance of Stem Cells. *Cell*, 172(3), 423-438.e425. doi:10.1016/j.cell.2017.11.018
- Wu, X., Kwong, A. C., & Rice, C. M. (2019). Antiviral resistance of stem cells. *Curr Opin Immunol*, 56, 50-59. doi:10.1016/j.coi.2018.10.004
- Yona, S., Kim, K. W., Wolf, Y., Mildner, A., Varol, D., Breker, M., . . . Jung, S. (2013). Fate mapping reveals origins and dynamics of monocytes and tissue macrophages under homeostasis. *Immunity*, 38(1), 79-91. doi:10.1016/j.immuni.2012.12.001
- Yu, V. W. C., Yusuf, R. Z., Oki, T., Wu, J., Saez, B., Wang, X., . . . Scadden, D. T. (2016). Epigenetic Memory Underlies Cell-Autonomous Heterogeneous Behavior of Hematopoietic Stem Cells. *Cell*, 167(5), 1310-1322.e1317. doi:<https://doi.org/10.1016/j.cell.2016.10.045>
- Zhang, H. G., & Grizzle, W. E. (2014). Exosomes: a novel pathway of local and distant intercellular communication that facilitates the growth and metastasis of neoplastic lesions. *Am J Pathol*, 184(1), 28-41. doi:10.1016/j.ajpath.2013.09.027
- Zhang, J. M., & An, J. (2007). Cytokines, inflammation, and pain. *Int Anesthesiol Clin*, 45(2), 27-37. doi:10.1097/AIA.0b013e318034194e

## Bibliography

- Zhang, Z., Li, N., Liu, S., Jiang, M., Wan, J., Zhang, Y., . . . Le, A. (2020). Overexpression of IFIT2 inhibits the proliferation of chronic myeloid leukemia cells by regulating the BCR-ABL/AKT/mTOR pathway. *Int J Mol Med*, 45(4), 1187-1194. doi:10.3892/ijmm.2020.4500
- Zhao, J. L., & Baltimore, D. (2015). Regulation of stress-induced hematopoiesis. *Curr Opin Hematol*, 22(4), 286-292. doi:10.1097/moh.0000000000000149
- Zhou, F., Li, X., Wang, W., Zhu, P., Zhou, J., He, W., . . . Liu, B. (2016). Tracing haematopoietic stem cell formation at single-cell resolution. *Nature*, 533(7604), 487-492. doi:10.1038/nature17997
- Zink, F., Stacey, S. N., Norrdahl, G. L., Frigge, M. L., Magnusson, O. T., Jonsdottir, I., . . . Stefansson, K. (2017). Clonal hematopoiesis, with and without candidate driver mutations, is common in the elderly. *Blood*, 130(6), 742-752. doi:10.1182/blood-2017-02-769869

### Papers in preparation:

- BJ Bouman, Y Demerdash, S Sood, F Grünschläger, F Pilz, AR Itani, A Kuck, S Haas, L Haghverdi, MAG Essers. (2023) Single-cell time series analysis reveals the dynamics of *in vivo* HSPC responses to inflammation. BioRxiv. doi: 10.1101/2023.03.09.531881
- S Sood, L Klein, F Pilz, R Mascaro, P Albert, MAG. Essers. (2023) Long term ex vivo growth system for hematopoietic stem cells using reinvigorating mesenchymal stem cells allows for clinical translation. In preparation for submission
- P Werner, C Hirche, S Haas, AI Schnell, C Sönmezer, J Langstein, S Wurzer, S Blaszkiewicz, F Pilz, M Thier, P Werner, D Brocks, M Tovey, C Plass, M Milsom, A Trumpp, D Lipka, U Kalinke, MAG Essers. (2023) Inherited stem cell based Interferon signaling heterogeneity primes response of hematopoietic cells to stress. In preparation for submission